Structural Dissonance in Galaxy Decomposition: The red sequence and evolutionary pathways in the Coma Cluster

HEAD, JACOB,THOMAS,CHRISTOPHER

Structural Dissonance in Galaxy Decomposition:

The red sequence and evolutionary pathways in the Coma Cluster

Jacob Thomas Christopher George Head

A thesis submitted to Durham University in accordance

with the regulations for admittance to the Degree of

Doctor of Philosophy

Department of Physics

Durham University

United Kingdom

2014

Abstract

The structural and photometric properties of 'red-and-dead' early-type galaxies provide vital clues about the evolutionary pathway which lead to their formation. Here, I use deep Canada-France-Hawaii Telescope image data to explore the multi-component internal structures of red sequence galaxies in the Coma cluster, with a particular focus on disk-dominated early-type galaxies (i.e. *S0*s). Galaxies are investigated across a wide range of luminosities ($-17 > M_g > -22$) and cluster-centric radii ($0 < r_{\rm cluster} < 1.3\ r_{200}$). I present the 2D structural decomposition of u, g, i imaging via `GALFIT`. Rigorous filtering is applied to ensure that the measured best-fit models are the most meaningful descriptions of their galaxy's underlying stellar structures.

A sample of Coma cluster members ($N = 200$) was identified as well described by an 'archetypal' *S0* structure (central bulge + outer disk). Internal bulge and/or disk colour gradients were implemented by allowing component sizes to vary between bands. Such gradients are required for 30% of archetypal *S0* galaxies. Bulges are characterised by $n \sim 2$ profiles with half-light radii, $R_e \sim 1$ kpc, remaining consistent in size for all but the brightest galaxies ($M_g < -20.5$). *S0* disks are brighter (at fixed size, or smaller at fixed luminosity) than those of star-forming spirals. Similar colour-magnitude relations are found for both bulges and disks. The global red sequence for *S0*s in Coma hence results from a combination of both component trends. The average bulge $-$ disk colour difference is 0.09 ± 0.01 mag in $g - i$, and 0.16 ± 0.01 mag in $u - g$. Using simple stellar population models, bulges are either $\sim$ 2-3$\times$ older, or $\sim$ 2$\times$ more metal-rich than disks. The trend towards bluer global *S0* colours observed further from Coma's core is driven by a significant correlation of disk colour with cluster-centric radius. An equivalent trend is detected in bulge colours at a marginal significance level. An environment-mediated mechanism of disk fading is favoured as the dominant factor in *S0* formation.

The decomposition analysis was then extended to encompass a wider range of structural models. This revealed a large sample of reliably-fit, symmetric multi-component galaxies in Coma ($N = 478$). $42 \pm 3\%$ of Coma cluster galaxies ($N = 201$) are best described by a 3(+) component structure. In addition, 11% of galaxies ($N = 52$) feature a break in their outer profiles, indicating truncated or anti-truncated disks. Beyond the break radius, truncated disks are consistent in structure with untruncated disks, disfavouring a formation mechanism via physical truncation of exponential disks. The sizes/luminosities of bulges in anti-truncated galaxies correlate strongly with galaxy luminosity, indicating a bulge-enhancement formation mechanism for anti-truncated disks. Both types of broken disk are found overwhelmingly ($> 70\%$) in barred galaxies, suggesting that galaxy bar play an important role in formation of such structures. The wide variety of galaxy structures detected in Coma highlights the naïveté of the simple 'bulge + disk' or 'single spheroid' morphological paradigm for early-type galaxies.

Contents

List of Figures

List of Tables

Acknowledgements

I would like to thank John Lucey for his help and guidance over the years: You were never afraid to make me feel like an idiot, but were polite enough not to call me one. I owe my success to you. I am also very grateful to Russell Smith for his patient (unofficial) co-supervision, and Alan Lotts for keeping the IT network running smoothly. Apologies to Alan and the Pan-STARRS consortium for crashing panstarrs-a with `AGONII` that one time.

Big thanks to everyone in the physics department, particularly my R311 officemates (past and present), my graduating cohort, and Lynne, whose steady supply of tea has kept me functioning for the last four years. Thanks also to the unofficial astro-badminton group who have somehow managed to keep me fit (and somewhat competent at the sport).

I would also like to thank my family for setting me on this long and winding path, and the friends I've met along the way. Finally and most importantly, unending thanks to Em for her support, reassurance, and sympathetic ear. I honestly don't think I could have made it this far without you.

- Jacob Head

Declaration

The work described in this thesis was undertaken between October 2010 and September 2014 while the author was a postgraduate student supervised by Dr. John Lucey at the Department of Physics, Durham University. This work has not been submitted for any other degree at this (or any other) university.

Chapters 2 - 6 of this thesis are based on work previously published as Head J. T. C. G., Lucey J. R., Hudson M. J., Smith R. J., 2014, MNRAS, 440, 1690.

This work is based on observations obtained with MegaPrime/MegaCam, a joint project of CFHT and CEA/DAPNIA, at the Canada-France-Hawaii Telescope (CFHT) which is operated by the National Research Council (NRC) of Canada, the Institute National des Sciences de l'Univers of the Centre National de la Recherche Scientifique of France, and the University of Hawaii. This work is based in part on data products produced at TERAPIX with the expert assistance of Partick Hudelot and Yannick Mellier. Observational data used in this paper are available from the CFHT archive http://www3.cadc-ccda.hia-iha.nrc-cnrc.gc.ca/cfht/cfht.html

This work uses data from SDSS-III. Funding for SDSS-III has been provided by the Alfred P. Sloan Foundation, the Participating Institutions, the National Science Foundation, and the U.S. Department of Energy Office of Science. The SDSS-III web site is http://www.sdss3.org/.

SDSS-III is managed by the Astrophysical Research Consortium for the Participating Institutions of the SDSS-III Collaboration including the University of Arizona, the Brazilian Participation Group, Brookhaven National Laboratory, Carnegie Mellon University, University of Florida, the French Participation Group, the German Participation Group, Harvard University, the Instituto de Astrofisica de Canarias, the Michigan State/Notre Dame/JINA Participation Group, Johns Hopkins University, Lawrence Berkeley National Laboratory,

Max Planck Institute for Astrophysics, Max Planck Institute for Extraterrestrial Physics, New Mexico State University, New York University, Ohio State University, Pennsylvania State University, University of Portsmouth, Princeton University, the Spanish Participation Group, University of Tokyo, University of Utah, Vanderbilt University, University of Virginia, University of Washington, and Yale University.

Statement of Copyright

Chapter 1

Introduction

1.1 Early-Type Galaxies and the Red Sequence

Galaxy morphologies are categorised as either 'early' or 'late' type based on their location on the Hubble sequence (Hubble, 1926; Figure 1.1). Early-type galaxies (ETGs) comprise elliptical and lenticular morphologies, while late type galaxies are primarily spirals. The giant elliptical morphology is traditionally considered to encompass a single spheroid of stars following dynamically hot orbits (i.e. randomised, rather than coplanar). This observed structure can be spherical ('*E0*'), but becomes increasingly flattened along the Hubble sequence ('*E1*'-'*E7*', where the number corresponds to $10(1-q)$ for the galaxy minor/major axis ratio, q). An equivalent spheroidal 'bulge' is present in spiral galaxies. Galaxies of this type also possess a flat, rotating disk, and the characteristic pattern of spiral arms for which the morphology is named. Along the Hubble sequence ('*Sa*'-'*Sd*'), galaxies become bluer (Roberts & Haynes, 1994), their bulges decrease in luminosity (relative to the spiral/disk; Simien & de Vaucouleurs, 1986), and their spiral arms become less tightly-wound. Intermediate to these two morphologies, lenticular ('*S0*') galaxies possess both a spheroidal bulge, and a smooth disk devoid of any spiral features. *S0* bulges are larger (Dressler, 1980b), and brighter (relative to their disks) than *Sa* bulges (Simien & de Vaucouleurs, 1986). Both spiral and *S0* galaxies can also possess a stellar bar (designated as '*SB0*' or '*SBa*'-'*SBc*'), which distinguishes the two parallel sequences of spiral morphologies.

Hubble's 'early'/'late' notation is frequently (mis)interpreted as the assumption of a particular sequence of galaxy evolution: elliptical galaxies grow stellar disks around their

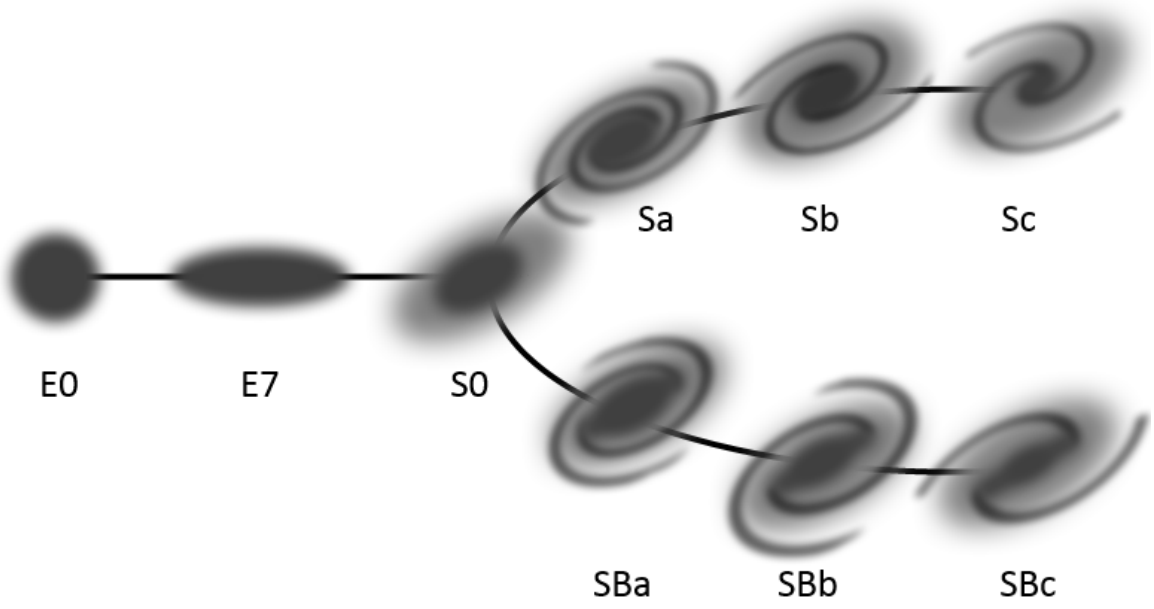

Figure 1.1: The Hubble sequence of galaxy morphologies (also known as the 'Hubble tuning fork'), illustrating the structures of early-type galaxies (*En*, *S0*) and barred/unbarred spirals.

spheroids (forming *S0*s), which would then unwind into spiral arms and brighten over time relative to the bulges. However, this nomenclature was intended to reflect the increase in observed morphological complexity across the Hubble sequence (similar to the 'early' and 'late' typing of stellar spectra), rather than to carry any serious temporal connotations (see footnotes in Hubble, 1926). Indeed, recent analyses of stellar populations reveal that late-type galaxies have significant ongoing star formation, and hence posses young stellar populations. Conversely, ETGs are mostly old and quiescent (typical specific star formation rate $< 1/(3t_H)\ M_\odot\ \mathrm{yr}^{-1}$, where t_H is the Hubble time; e.g. Damen et al., 2009). Thus, the arrow of time points from right to left on the Hubble sequence *on average* (Figure 1.1; i.e. 'early-types' evolve from 'late-types'), rather than left to right.

The evolution of late-type galaxies to early-type morphologies is illustrated photometrically by the colour-magnitude diagram (Fig. 1.2). Late-type spirals occupy a broad (i.e. high scatter) parameter space with bluer average galaxy colours (the 'blue cloud'). This indicates the presence of massive, but short-lived stars in the galaxy (i.e. a younger stellar population), and hence ongoing star formation. Conversely, ETGs are significantly redder on average, and follow a tight correlation of redder colours for more luminous galaxies (the

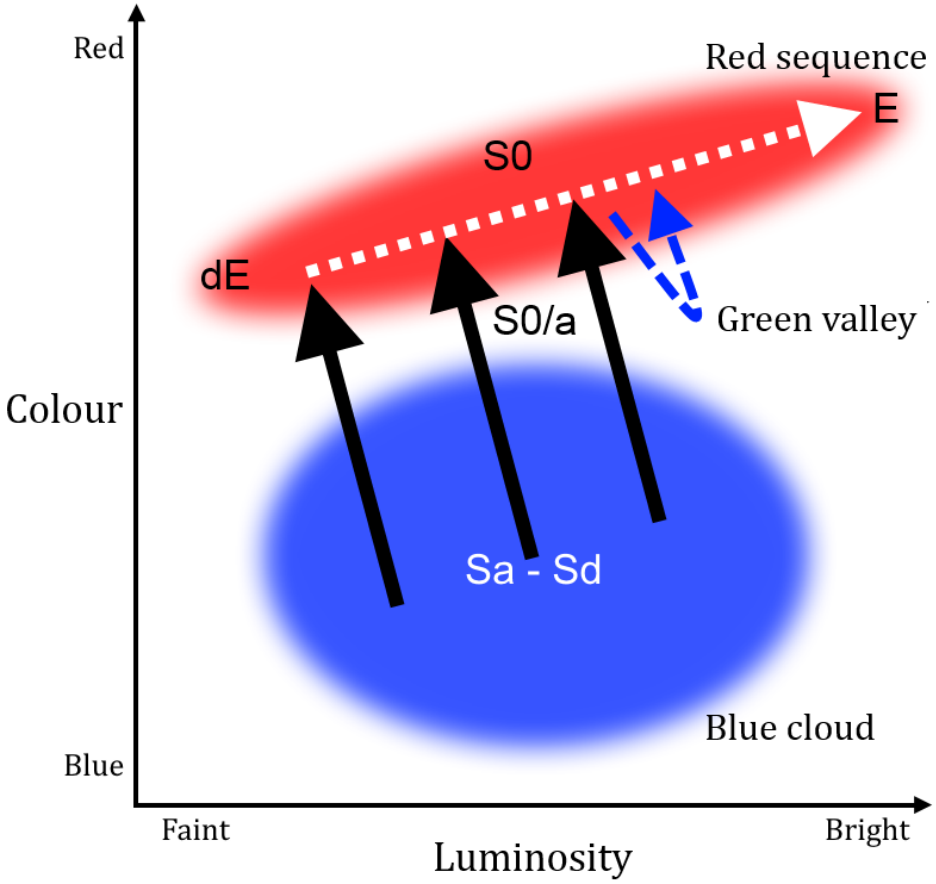

Figure 1.2: Cartoon of the global colour-magnitude diagram for galaxies highlighting the blue cloud, red sequence, and green valley. Arrows mark the expected pathway for galaxies experiencing various evolutionary processes: **Solid black arrows:** Quenching of star-forming spirals. **Dotted white arrow:** Passive evolution via dry mergers. **Dashed blue arrow:** Temporary renewed star formation of a red sequence galaxy. Characteristic locations of various morphologies - including spiral-lenticular transitions ('*S0/a*') and dwarf ellipticals ('*dE*') - are also indicated.

'red sequence'; Bower et al., 1992). If star formation is curtailed in a late-type galaxy (hereafter 'quenching'), its stellar populations will redden and fade with time, as its massive (O, B, and A-type) stars leave the main sequence. This causes the galaxy to transition from the blue cloud to the red sequence over a period of ~ 1 Gyr (i.e. an A-star's main sequence lifetime) or longer if quenching is gradual. The relatively low number of objects observed with colours intermediate to the blue cloud and red sequence (the 'green valley') thus correspond to quenched galaxies transitioning between the two populations. However, the bright end of the red sequence contains galaxies more luminous than the brightest blue cloud galaxies. Passive evolution (and hence fading) of blue cloud galaxies is therefore insufficient to populate the entire red sequence. Instead, quenched red sequence galaxies must gain mass (and hence luminosity) passively via merger events. However, since a 'wet' (i.e. gas-rich) merger would fuel further star formation (and thus move the galaxy back to the blue cloud), this passive evolution must involve 'dry' (i.e. gasless) mergers.

The apparent morphologies of observed galaxies do not necessarily reflect their true structures. Image resolution limits the detection of fine details such as bars, inner (subdominant) disks, or spiral features. Likewise, the magnitude limit and dynamic range of an observation inhibits the detection (or distinction between) low surface brightness features. Furthermore, the inclination of a galaxy on the sky can mask its true shape. For example, an elongated elliptical, En, can be detected as any morphology in the range *E0* to *E7* depending on its observed orientation. By-eye differentiation between *E* and *S0* morphologies is also difficult in cases where such galaxies are viewed face-on due to the central concentration of light in elliptical galaxies (equivalent to *S0* bulges). Similarly, the distinction between *S0*s and the most elongated (*E5*-*E7*) elliptical galaxies may be purely an observational bias (van den Bergh, 2009b).

Simple one/two-component profiles do not reflect the true complexity of elliptical/*S0* morphologies respectively. Multi-component (2+) structures for ETGs are consistent with the predictions of photometric modeling (e.g. disks in elliptical galaxies; Rix & White, 1990), and have been detected in nearby ellipticals (Huang et al., 2013). Recent work studying galaxy kinematics (e.g. Emsellem et al., 2011 for an *S0*-dominated ETG sample) has indicated that rapidly rotating ETGs are dominant. Through conservation of angular mo-

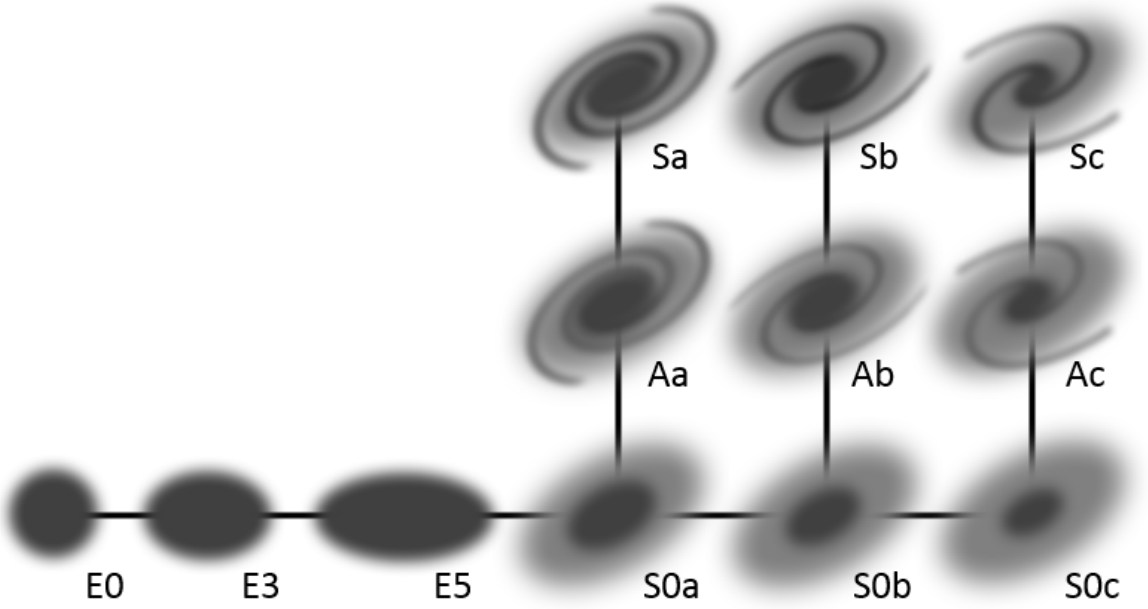

Figure 1.3: Cartoon of the ATLAS^{3D} comb illustrating the evolution of morphology from spiral to *S0* (*Sa-c* to *S0a-c*) via an anemic spiral stage (*Aa-c*).

mentum, any rotating, self-gravitating system will collapse to form a coplanar disk. Hence, weak disks (and other structures) may be present in most galaxies, but imaging signal-to-noise (S/N) limits their detection.

The proposed paradigm for galaxy evolution (van den Bergh, 1976; Cappellari et al., 2011; Kormendy & Bender, 2012) places elliptical and lenticular galaxies on a continuous sequence of rotating, quiescent galaxies (Fig. 1.3). Galaxy specific angular momentum, λ_R, increases in magnitude from *E* ('slow rotators', $\lambda_R < 0.31\sqrt{\epsilon}$ for apparent ellipticity, ϵ) to *S0* ('fast rotators', $\lambda_R > 0.31\sqrt{\epsilon}$). Here, the *S0* morphology encompasses multiple distinct classes, *S0a-S0c*, differing in luminosity, relative bulge dominance, and evolutionary pathway (van den Bergh, 1990, 2009a). These *S0* subtypes are analogous to the *Sa - Sc* spiral morphologies, suggesting evolution from *Sx* to *S0x* via anemic (red) spiral intermediates (*Aa - Ac*, van den Bergh, 1976; Masters et al., 2010), rather than gradual evolution through each Hubble type. This direct quenching of the spiral subtypes is equivalent to the transition to the red sequence for blue cloud galaxies with different total luminosities. Equivalently, moving right to left along the comb 'handle' (*S0c - E*) is equivalent to the passive evolution which builds mass/light along the red sequence.

In this thesis, I analyse the structures and structural component photometry of ETGs on the red sequence in order to investigate the physical mechanisms which mediated their quenching and evolution. Analysis was carried out on a sample of Coma cluster-members over a broad range of clustercentric radii (and hence local environment densities), enabling investigation of the importance of the cluster environment (relative to secular processes) in galaxy evolution.

In the following sections, I first provide details of the physical mechanisms which may drive the quenching and morphological evolution with emphasis on the processes which act in the cluster environment. Secondly, I discuss trends in structural and stellar population properties relevant to ETGs. Thirdly, the properties of ETG surface brightness profiles are introduced, including a thorough discussion of the analytical profiles used to model them in a decomposition analysis. Lastly, I provide an overview of the motivation and content of subsequent chapters within this thesis.

1.2 Mechanisms for Quenching

Structural and kinematic similarities between *S0*s and spiral galaxies (van den Bergh, 1976; Aragón-Salamanca et al., 2006; Bekki & Couch, 2011; Rawle et al., 2013) imply a evolutionary scenario in which spiral-like progenitors are transformed into ETGs. Such a transformation would require the erasure of any prominent spiral pattern, and truncation of the galaxy's star formation. Without continued star formation, the galaxy would then fade and redden as its stellar populations age. Additionally, as *S0*s have brighter bulges (relative to their disks) than spiral galaxies (Dressler, 1980b), transformation must also enhance the galaxy's bulge-to-total ratio,

$$\mathrm{B/T} = \frac{f_B}{(f_B + f_D)}, \tag{1.1}$$

where f_B and f_D are the luminosities of the bulge and disk components respectively. The resulting 'red and dead' descendant galaxy would be bulge-dominated, with a smooth, rotating disk.

Within galaxy clusters, strong radial trends are observed in galaxy morphology such that with increasing local density (or decreasing distance from the cluster core), the fraction of

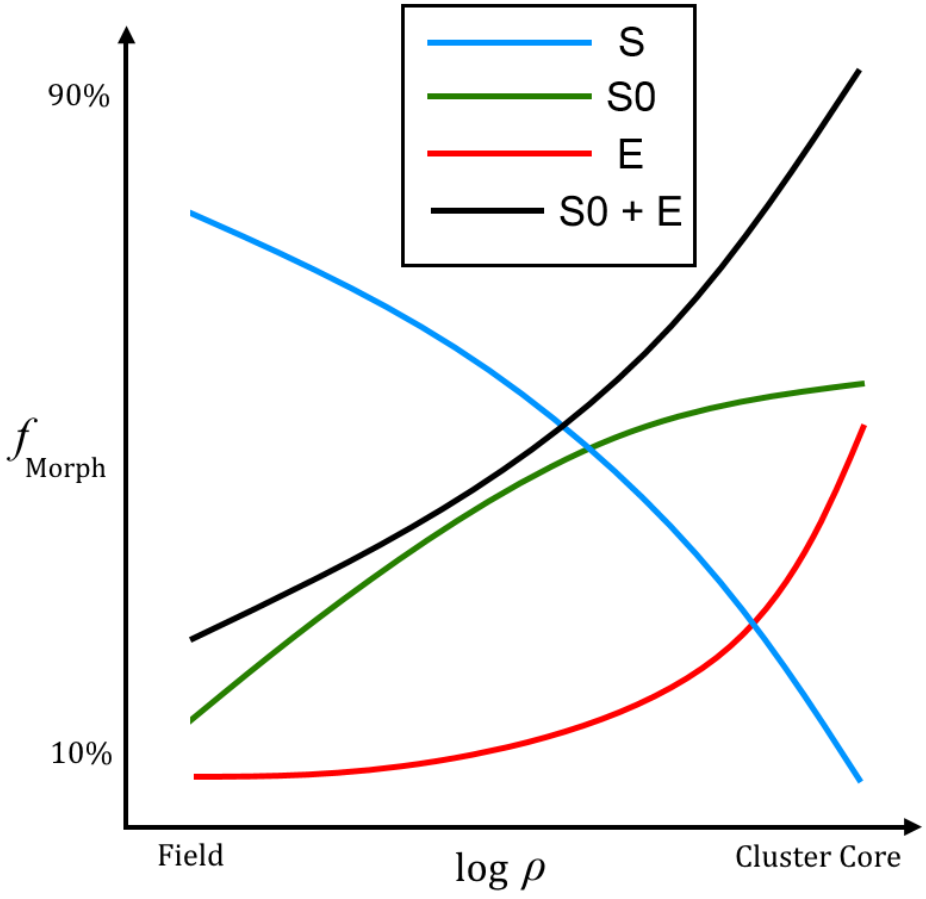

Figure 1.4: Cartoon of the morphology fractions of elliptical, lenticular, and spiral galaxies as a function of local environment density (the 'morphology-density' relation). Based on Figure 4 of Dressler (1980b).

spiral galaxies decreases with a proportional increase in the fraction of ETGs (Fig. 1.4; the 'morphology-density' relation, Dressler, 1980b; Dressler et al., 1997). Likewise, with increasing local environment density, a galaxy's star formation rate decreases (the 'colour-density' relation, Balogh et al., 2000; Lewis et al., 2002; Balogh et al., 2004; Hogg et al., 2004). This builds a picture in which a galaxy is driven from late- to early-type morphology during accretion onto a cluster due to environment-mediated processes. The current position of a galaxy within a cluster is correlated with its infall time (Gao et al., 2004; Smith et al., 2012; De Lucia et al., 2012; Taranu et al., 2014) and velocity (Oman et al., 2013). Therefore, variations of galaxy structure and colour with clustercentric radius offer insight into the physical mechanisms which acted during cluster infall, precipitating morphological evolution.

The environment-mediated mechanisms proposed to drive morphological transformation can be broadly categorised as either 'bulge enhancing' or 'disk fading' depending on how the increase in B/T is achieved. In both cases, the primary cause for quenching is the removal of a galaxy's gas reserves which fuel its star formation (Larson et al., 1980).

In a 'bulge enhancement' scenario, the galaxy's cold gas is rapidly consumed in strong bursts of centrally-concentrated star formation. Additionally, driving the gas towards the galaxy's centre may feed a supermassive black hole, quenching star formation through active galactic nucleus (AGN) feedback (Silk & Rees, 1998; Schawinski et al., 2006, 2007; Brodwin et al., 2013). Mergers (in groups or the field) and galaxy harassment (in clusters, Moore et al., 1996) are the most widely studied mechanisms of this type, both of which show the potential to form *S0*s (Bekki, 1998; Governato et al., 2009; Moore et al., 1998, 1999). Stellar disks of galaxies are typically disrupted by these processes, however, requiring specific environmental conditions for disk survival (Hopkins et al., 2009) or a long period of disk regrowth (Kannappan et al., 2009).

A 'disk fading' scenario involves either the direct stripping of cold gas from the galaxy's disk (e.g. due to ram pressure Gunn & Gott, 1972; Quilis et al., 2000), or removal of its hot halo gas reservoir over a long period of strangulation (Larson et al., 1980; Balogh et al., 2000). These mechanisms act preferentially on gas, causing little or no disruption to the galaxy's stellar disk. Additionally, disk fading mechanisms are triggered by interactions be-

tween a galaxy and an external medium, such as a hot intra-cluster medium (ICM). This precludes disk fading in low density environments, requiring that such a transformation would have had to occur since accretion into a group (or denser) environment.

Alternatively, secular processes driven by a galaxy's internal astrophysics may also be an important factor in the transformation of spirals to ETGs. Mechanisms of this type modify the structure and star formation of a galaxy, without the need for external causes. Instead, the galaxy's intrinsic dynamics mediate changes to stellar orbits or internal gas reservoirs. Galaxy bars, for instance can induce strong gravitational torques, potentially causing stellar migration into the bulge, or triggering central starbursts (Zhang, 1998, 1999; Coelho & Gadotti, 2011). Given the strong environmental dependences of morphology and star formation, secular mechanisms are unlikely to be the primary cause for ETG formation. However, secular processes may influence the variety of galaxy morphologies and structures.

In the following subsections I present the theory describing the mechanisms which may precipitate *S0* (trans)formation. A particular emphasis is placed on the importance of the cluster environment, and the morphology-density relation in general.

1.2.1 Disk Fading

Disk fading transformation mechanisms operate via the direct removal of the galactic gas supply, thus robbing the galaxy of the fuel for star formation. Affected spirals will subsequently fade as their stellar populations age, becoming increasingly red in colour as their short-lived, massive blue stars die off. As gas-stripping mechanisms act preferentially on the weakly-bound outer regions of galaxies, the disk is faded in preference to the bulge. This outside-in galaxy fading would yield a boosted B/T relative to its progenitor.

The morphology distributions for quiescent galaxies as a function of parent halo mass (analogous to environment density) supports environment-mediated disk fading (van der Wel et al., 2010). For galaxies with masses $M < 10^{11}\ M_{\odot}$, the high halo mass environment exhibits a significant excess of disk-like galaxies relative to the low halo mass environment (see Figure 4 in van der Wel et al., 2010). However, by adding an additional population of 'quenched' L_* spiral galaxies to a low halo mass quiescent sample, the distributions in both environments become consistent (see Fig. 5 in van der Wel et al., 2010). This is equivalent to

truncation of star formation in a late-type galaxy without disrupting its disk-like 'morphology'. However, an additional population of quenched spirals is insufficient to reconcile the high and low halo mass distributions for galaxies more massive than $M = 10^{11}\ M_{\odot}$. This disparity supports bimodal evolutionary pathways for high and low mass galaxies.

The detection of a significant population of field *S0*s (Dressler, 1980b) disfavours a simple disk fading scenario for *S0* formation. In the field environment, the gas temperature and density would have been insufficient for ablative gas-stripping processes to have driven morphological transformations. Furthermore, the morphology-density relations observed in regular and irregular clusters were equivalent, despite gas-stripping only acting in virialised, regular clusters. Structurally, the bulges of *S0* galaxies were found to be systematically brighter than the bulges of spiral galaxies. Assuming that late morphologies are the progenitors for *S0*s, a simple disk fading mechanism cannot account for this trend. However, this structural trend could simply be a result of observational biases associated with classifying morphology by eye. Furthermore, local ETGs could not have evolved from *local* late-type galaxies; rather, both local populations evolved from a primordial spiral-like progenitor population. Thus, this structural disparity between local spirals and ETGs does not necessarily impede a disk-fading evolutionary pathway.

In the following sections, I describe two main themes of disk fading: ram pressure stripping due to a hot external medium, and 'strangulation' of a galaxy's hot gas reservoir.

Ram Pressure/Viscous Stripping

As a spiral galaxy falls into a cluster with a hot, ionised ICM, the motion of the galaxy's interstellar medium (ISM) past the ICM causes a build up of ram pressure (P_r) ahead of the galaxy. This is described by the equation

$$P_r \approx \rho_e v^2, \tag{1.2}$$

where ρ_e is the density external to the galaxy, and v is the galaxy's propagation velocity through the ICM.

For the typical ICM density of a cluster ($\sim 10^3$ atoms m^{-3}), ram pressure will strip all of the cold gas from a Milky Way-like galaxy within ~ 100 Myr (Gunn & Gott, 1972; Quilis

et al., 2000). This abrupt removal of gas would lead to a rapid truncation of the star formation within the galaxy similar to the predictions for *S0*s based on spectroscopic observations. The increase in pressure that the ISM would experience during stripping could also lead to a starburst in the central regions of the galaxy. Quilis et al. (2000) propose that this temporarily boosted star formation rate would explain the presence of enhanced hydrogen absorption lines in *S0* spectra.

There has been substantial observational evidence for ongoing, or past Ram Pressure Stripping (RPS) events in clusters and groups (e.g. Irwin et al., 1987; Vollmer et al., 2004; van der Wel et al., 2010; in Coma: Smith et al., 2010), nevertheless, the extent to which ram pressure/viscous stripping influences *S0* evolution is disputed. Simulations performed by Abadi et al. (1999) suggested that RPS would only result in a loss of $\sim 80\%$ of gas mass. This would represent a significant truncation, but not total removal of the disk gas. Additionally, Abadi et al. found that a galaxy with orbital inclination relative to their motion through a cluster would lose substantially less gas ($\sim 50\%$) than those interacting with the ICM face-on. However, this result has been disputed by Quilis et al. (2000), whose simulations indicated total gas removal in even moderately inclined ($i = 20°$) galaxies. Additionally, they argue that a galaxy's motion within a cluster is such that it will be appropriately inclined for stripping at some point during its orbit.

More recently, Tecce et al. (2010) have examined RPS using a hybrid of Smoothed Particle Hydrodynamics (SPH) and semi-analytical methods to calculate the ram pressure experienced by galactic gas. They find that ram pressure depends on both cluster virial mass and redshift, increasing by an order of magnitude between $z = 1$ and 0. Including redshift-dependent RPS, the simulated fraction of gas-depleted galaxies within a cluster's virial radius (r_{200}) increases by $\sim 60\%$ relative to simulations excluding a treatment of RPS (see Fig 8 in Tecce et al., 2010). Even at the cluster outskirts ($\sim 2r_{200}$), there remains a significant increase in the gas-depleted galaxy fraction with decreasing redshift, implying a significant amount of pre-processing (see Section 1.2.4) via RPS in subgroups accreted by the cluster.

Clearly, ram pressure would have a significant effect on any gas-rich spiral galaxy entering a cluster's virial radius. Until typical conditions, this can drive the abrupt star formation truncation necessary to form an *S0*. Nevertheless, the existence of a significant population

of field *S0*s (Dressler, 1980b) challenges the dominance of RPS as the major mechanism of *S0* formation. It is possible that RPS only influences galaxies that remain unquenched prior to entering the cluster's virial radius. Furthermore, partial, or ongoing transformations could be supplemented by RPS upon entering the virial radius. This would cause a density-dependent acceleration of star formation truncation which may explain the observed morphology-density relation.

Strangulation

In a simple, closed-box model of gas evolution, a steady rate of star formation would be sufficient to consume all of the available cold gas within a few Gyr (Larson et al., 1980). Therefore, spiral galaxies require a means of replenishing their gas content from their surroundings (i.e. via accretion of gas-rich satellites in their halo or cooling of hot halo gas). Strangulation (Balogh et al., 2000) is a mechanism for spiral transformation based on the sweeping of gas content from a galaxy's halo, thus starving it of the fuel for future gas accretion and star formation. Although this removal of halo gas may proceed via the same physical mechanisms discussed earlier in this section, strangulation would result in a distinctly different star formation history. Specifically, removal of the halo gas reservoir would cause a gradual reduction of the star formation rate, rather than a rapid truncation.

Kawata & Mulchaey (2008) demonstrated that the ram pressure in a low-mass group environment could strip hot halo gas, but would be insufficient to permanently disturb the cold galactic gas (see Figure 4 in Kawata & Mulchaey, 2008). Hence, strangulation of star formation alone should be sufficient to explain the star formation history and morphological transformation of spirals into *S0*s. Additionally, as strangulation can proceed even in relatively low-mass groups, it counters the assertion of Dressler (1980b) that gas-stripping mechanisms could not drive spiral transformations due to the presence of field *S0*s.

Feldmann et al. (2010) followed the evolution of a simulated group, noting that galaxies identified as present-day *S0*s entered the group environment earlier than the spirals that maintained star formation up to $z = 0$. Hence, they conclude that the group environment drives the morphological transformation into *S0*s for infalling gas-rich spirals. This transformation follows the pattern expected for strangulation, with the stripping of the galaxies' hot

halo gas driving the quenching of star formation. Nevertheless, additional RPS accelerates the removal of cold gas relative to a pure strangulation scenario ($\sim 90 \pm 10\%$ of galactic cold gas within ~ 1 Gyr).

For satellite galaxies accreted into approximately equal-mass halos, quenching must be driven by processes which change colour, but not concentration (i.e. strangulation or RPS; van den Bosch et al., 2008). However, differences in colour and concentration were found to be independent of host halo mass, implying that environment-dependent mechanisms such as RPS are disfavoured. It is also noted that for galaxies with stellar mass, $M_\star \sim 10^9 h^{-2}$ $M_\odot$, roughly 30% of red sequence satellite galaxies were red prior to accretion into a larger mass halo. The proportion increases to $\sim 100\%$ for galaxies of stellar mass $M_\star \geq 10^{11} h^{-2}$ $M_\odot$. This mass-dependence for transformation time appears to suggest a dichotomy of transformation mechanisms for high and low mass galaxies. Potentially, this correlates with the observed trend that the most massive galaxies are more likely to have undergone a major merger (Robaina et al., 2010).

Weinmann et al. (2006) found that semi-analytical models implementing strangulation do not correctly reproduce the observed fraction of blue galaxies. Specifically, models produce too few blue satellite galaxies, even without a treatment of RPS further truncating their star formation. Hester (2010), however, suggests that this discrepancy can be solved by gas inflow in a galaxy's neutral hydrogen (HI) disk, following a partial quenching event. This inflow of gas would feed star formation, prolonging the galaxy's star forming lifetime and thus producing a higher fraction of blue galaxies at late times on average.

Overall, strangulation presents a robust picture of star formation truncation for disk galaxies entering a higher density environment. In combination with RPS, strangulation is consistent with most observed trends in colour and morphology, and appears to be the dominant mechanism for transformation of disk galaxies up to around $M_\star = 10^9 h^{-2}$ $M_\odot$. Strangulation doesn't, however, explain the evolution of those galaxies that had their star formation truncated prior to entering the group environment, nor does it account for the increased B/T ratio of *S0*s relative to unquenched spirals.

1.2.2 Bulge Enhancement

In a bulge-enhancement scenario, the larger B/T for ETGs results from a build-up of mass (and hence luminosity) in galaxy bulges. Galaxy quenching in this scenario involves the rapid consumption of star-forming gas in a burst of accelerated star formation, rather than via physical expulsion of gas. These starbursts occur as a result of increased central gas density induced when disk gas loses angular momentum during a dynamic interaction, and falls towards the bulge (Barnes & Hernquist, 1991; Mihos & Hernquist, 1994). In addition, the inflow of gas to the galaxy centre can feed the Supermassive Black Hole (SMBH) expected in most giant galaxies (Magorrian et al., 1998; Ferrarese & Merritt, 2000). The resulting increase in AGN activity can cause gas to be expelled from the galaxy, causing a truncation of ongoing star formation.

The proposed initiators of bulge enhancement (interactions between galaxies, or with a cluster's tidal field) are both more likely to occur in high density environments, hence providing a potential link with the morphology-density relation. As disks are typically disrupted or destroyed by these interactions, the progenitors of a bulge-enhancement *S0* formation scenario must be disk-like in structure. Furthermore, the interacting system must be gas-rich to fuel a starburst. Thus, *S0*s must evolve from disk-dominated, late-type galaxies. However, the ages of stars in *S0* bulges and inner thick disks typically exceed 10 Gyr (Stewart et al., 2008; Rawle et al., 2010). These old central stellar populations contradict a *recent* starburst formation mechanism.

A bulge enhancement scenario is supported by Christlein & Zabludoff (2004), who examined trends in B/T for *S0* galaxies, parametrised by the Schechter parameter, M^* (Schechter, 1976), of the bulge and disk luminosity functions. A weakly negative gradient in M^* with increasing B/T was evident for disk components, while the equivalent gradient for bulge components was strongly negative. Using Monte Carlo analysis, Christlein & Zabludoff found that only a bulge enhancement scenario explains the observed gradients, and only for a subset of the total range of B/T values (see Figure 5 in Christlein & Zabludoff, 2004).

It is worth highlighting that the Monte Carlo models of Christlein & Zabludoff (2004) are based on the assumption that early-type galaxies share a common progenitor population with late-types. Relaxation of this assumption might improve the extent to which a disk

fading null hypothesis could account for the observed trends in M^* for a limited B/T range. Nevertheless, their conclusions support the importance of bulge-enhancement mechanisms for the formation of *S0*s.

In the following section, I address three main themes of bulge formation: galaxy mergers (in field/group environments), galaxy harassment (in clusters), and feedback from AGN.

Mergers

Galaxy mergers occur when gravitational interaction causes two (or more) galaxies to collide, and eventually coalesce. For a simple two-body merger, this process will take place over multiple orbits, during which the close proximity of the merging systems causes significant alteration to their internal orbital dynamics. Galaxy mergers are well-characterised by the mass ratio of their constituent interacting galaxies. Major mergers (mass ratios 1:1 to 4:1) represent a unification of (approximately) equal-mass galaxies, such as the eventual collision of the Milky Way with Andromeda. Conversely, minor mergers (mass ratios 5:1 to 10:1) correspond to the accretion of a satellite by the more massive primary galaxy.

Mergers result in increased B/T and bulge n (Aguerri et al., 2001), and grow the bulge $R_{e,B}$ proportional to the mass growth, M^{α} (Naab et al., 2009; Hilz et al., 2012). For major mergers, this results in an approximately linear growth in bulge size relative to mass growth ($\alpha = 0.8-1.0$; Boylan-Kolchin et al., 2005; Hilz et al., 2012). In addition, disk structures are disrupted or destroyed by major mergers (Barnes & Hernquist, 1991; Bendo & Barnes, 2000; Bois et al., 2011), yielding a (kinematically) elliptical-like remnant (Toomre & Toomre, 1972). For minor mergers, the bulge size growth is predicted to be significantly larger ($\alpha = 2.0 - 2.4$; van Dokkum et al., 2010; Hilz et al., 2012). However, not all simulations agree on this point; for example, Eliche-Moral et al. (2012) suggest that dry, minor mergers can provide the B/T growth necessary for *S0* formation while causing no significant change to either bulge or disk scale lengths.

Minor mergers are less disk-disruptive; remnant disk structures are thickened (Quinn et al., 1993), but retain the kinematic and (radial) size properties of their progenitors (Bournaud et al., 2005). Consequently, individual minor merger events may be insufficient to completely drive the evolution in morphology (Walker et al., 1996). Instead, multiple minor

mergers drive galaxy morphology from spiral to *S0* to spheroidal, and eventually to elliptical (Bournaud et al., 2007). In this case, *S0*s represent true intermediates of late- and early-type galaxies in a multi-step evolution scenario.

The gas content of the progenitor galaxies plays a large role in determining the star-formation properties of the resulting merger remnant. 'Dry' (dissipationless) mergers involve the interaction of gas-poor (e.g. *E*/*S0*) systems, producing a massive remnant with little or no additional star formation. While this may explain the formation of some of the most massive ETGs (Tran et al., 2005), it does not address the issue of the origin of these quenched early-type progenitors. By contrast, 'wet' mergers of gas-rich galaxies, or 'mixed' mergers of a gas-rich object with a gas-poor system are expected to drive strong (central) starbursts in the remnant galaxy. This epoch of heightened star formation follows the inward radial migration of disk gas (due to tidally-induced asymmetries) and/or the accretion of a gas rich satellite. It has been demonstrated that the majority ($\sim 75\%$) of a progenitor's disk gas can be consumed during merger-induced starbursts, resulting in a remnant with distinct spheroid, thick disk, and thin bar structures (i.e. a *SB0* galaxy; Bekki, 1998).

In order to satisfy the conditions of *S0* formation, a merger must be sufficiently gas-rich to drive the bulge growth of the remnant while being of a low enough mass ratio that the disk structure of the remnant is preserved. However, N-body simulations suggest that $\sim 95\%$ of galaxies experience a major merger between $z = 2$ and 0 (Stewart et al., 2008). Hence, the observed fraction of local disk-dominated ETGs cannot be reproduced unless mergers with mass ratios up to 5:1 do not always destroy disks. For instance, the most efficient mode of angular momentum loss for gas is due to merger-induced asymmetries in the galaxy's internal stellar disk (Hopkins et al., 2009). Hence, galaxies with a high disk gas fraction (low mass stellar disk) or high stellar winds (driving gas to large radii) will lose very little angular momentum and thus potentially survive the merger (see Figure 1 in Hopkins et al., 2009).

SPH simulations have demonstrated the regrowth of a thin disk following a wet merger event at $z = 0.8$ (Governato et al., 2009; e.g. their Figure 1). Disk regrowth has been identified observationally within blue ETGs in modest to low density environments (Kannappan et al., 2009). The dynamics of these galaxies indicate a past (unequal-mass) merger event,

with regrowth assembling a stellar disk over the early-type remnant. This regrowth process would require abundant cold gas (either within the merger progenitors or acquired via cold flow accretion) and efficient star formation (i.e. lower mass). However, renewed star formation on a scale sufficient to reform a dominant disk would move the remnant galaxy back to the blue cloud. Thus, in order to form red, quiescent *S0*s in this manner, it is necessary to invoke additional gas-stripping effects (Roediger et al., 2010).

Overall, gas-rich mergers seem a likely candidate for driving the formation of *S0*s from late-type progenitors through central starburst events. Although major mergers tend to form elliptical-like remnants, the expected merger rate between $z = 2$ and the present day does not necessarily pose a problem, as disk-regrowth or survival could preserve *S0* morphology. However, neither gas-poor mergers nor disk regrowth can explain the final quenching of star formation, and supplementary gas-stripping mechanisms may thus be required.

Harassment

Within virialised clusters, the relative velocities of any two galaxies is usually too large for a direct merger to occur. Even if the galaxies collided head-on, the entire interaction would be too brief for the gas to react dynamically. Due to the relatively high galaxy density within the cluster environment, however, each cluster galaxy is likely to experience many brief tidal interactions over its lifetime. The cumulative effect of these repeated encounters with other galaxies and the host cluster's tidal field is termed 'galaxy harassment'.

Acting on typical spiral galaxies, harassment causes heating of the stellar disk and loss of gas angular momentum to its dark matter halo (Moore et al., 1996). Similar to the effect induced by direct mergers, this will prompt funneling of gas towards the galaxy centre, where it could fuel a central starburst. Additionally, as the disk of the infalling galaxy is disturbed by the cluster's tidal field, large 'tails' of stellar and gaseous matter (as observed by Haynes et al., 2007) would form. Loss of stellar matter in this manner can remove as much as 50% of a galaxy's stars, which would account for the diffuse intracluster light (ICL) observed in clusters (Moore et al., 1998).

Harassment has a far lesser effect on a more densely concentrated system, such as a galactic core or giant elliptical galaxies. Hence, the overall influence of harassment differs

depending on the surface brightness of the target galaxy (Moore et al., 1999). Low surface brightness (LSB) galaxies - as characterised by large disk scale lengths and slowly rising rotation curves - can lose up to 90% of their stellar mass to repeated tidal shocks, resulting in a dwarf elliptical remnant. High surface brightness (HSB) galaxies, however, can react adiabatically to tidal shocks. Thus, HSB galaxies will experience disk heating and thickening, but will otherwise remain stable to harassment (see Figure 5 in Moore et al., 1999). Dwarf galaxies are similarly stable to harassment due to their high mass concentration (Smith et al., 2010), losing only $\sim 10\%$ of their stellar mass in most cases. These harassed dwarfs remained disk dominated, with some gaining tidally-induced spirals.

Harassment would not be sufficient to drive the *complete* morphological transformation of HSB galaxies. However, this process is sufficient to erase the spiral features of an infalling galaxy within a few Gyr. Therefore, these harassed remnants are ideal *S0* precursor candidates, requiring an additional gas-stripping event to complete their transformation to early-type morphologies.

Harassment is a more relevant morphological transformation mechanism in the cluster environment than direct mergers. Acting on a mid-to-high surface brightness galaxy, it can cause transformation to an *S0*-like morphology within a few Gyr. The highest surface brightness galaxies are more stable, however, requiring gas-stripping to supplement harassment.

AGN Feedback

The velocity dispersion of a galaxy's bulge (and therefore its mass) correlates strongly with the mass of the SMBH it hosts, $M_{\rm BH}$ (the 'Magorrian relation'; Magorrian et al., 1998; Ferrarese & Merritt, 2000). Thus, the properties of the stellar bulge and SMBH are directly inter-related. As these objects differ in mass and physical size by factors of $\sim 10^3$ and $\sim 10^8$ respectively, this causal link cannot result from gravitational effects. Instead, the kinetic or radiative activity of the galactic nucleus on accretion of mass must influence the galaxy's stellar properties.

AGN eject collimated jets of ionised matter perpendicular to the plane of their accretion disk due to interaction between black hole rotation and the magnetic field of the disk itself (Rees et al., 1982; Begelman et al., 1984; Semenov et al., 2004). These jets (supplemented

by radiation pressure from the AGN, and existing wind from supernovae) impart significant kinetic energy to the host galaxy's ISM. If the accretion rate is sufficiently high (i.e. 'quasar mode'), these AGN winds can cause kpc-scale outflows of gas (Springel et al., 2005; King, 2005; Di Matteo et al., 2005; Harrison et al., 2012), suppressing star formation via removal of the galaxy's cold gas supply. While such outflows would not exist for lower accretion rates ('Radio mode'), the transfer of kinetic energy would nevertheless cause mechanical heating of the galaxy's cold gas reserves. This mechanism can also cause galaxy quenching by preventing gas from cooling and collapsing to form stars (Best et al., 2005, 2006; Danielson et al., 2012). Additional gas heating can result from the emission of ionising radiation or the production of energetic particles (cosmic rays etc.) by the AGN (Ferland et al., 2008, 2009).

AGN activity and star formation appears to be correlated on average (e.g. Chen et al., 2013). This reflects that both processes are triggered by the same conditions (i.e. increased gas density). However, a causal connection between AGN feedback and galaxy quenching is disputed observationally: red (i.e. quenched) galaxies are not more likely to host AGN (Aird et al., 2012), while AGN-hosting galaxies do not exhibit significant deviation from expected star formation rates (Harrison et al., 2012). Further studies suggest that AGN regulate star formation via both negative (i.e. star formation suppressing) and positive (i.e. star formation triggering) feedback (Zinn et al., 2013; Karouzos et al., 2014). In this scenario, the dominant feedback mechanism in a particular galaxy depends on the properties of the AGN it hosts. However, the resulting star formation suppression would not necessarily be sufficient to fully quench a galaxy.

Feedback from AGN is of particular relevance for bulge-enhancing evolutionary mechanisms due to the potential for tidal interactions to feed gas to the central black hole. However, the morphological signatures of major merger events have been detected in only a minority of AGN-host galaxies (Liu et al., 2011; Kocevski et al., 2012). Such observational evidence is limited by imaging depth, with deeper data yielding significantly higher fractions of post-merger AGN (Schawinski et al., 2010; Imanishi & Saito, 2014). Furthermore, AGN fed by tidal harassment in clusters would be unlikely to host detectable morphological features (see earlier in this section).

1.2.3 Secular Processes

Galaxy evolution via secular (i.e. internal) processes provides a means of forming ETGs in environments in which most quenching mechanisms do not occur. However, the existence of strong environmental trends in colour and morphology suggest that this is not the primary evolutionary pathway. Secular mechanisms can nevertheless supplement the environment-mediated evolutionary mechanisms discussed above. In this way, the apparent discrepancies between bulge-enhancing or disk-fading processes and the observed properties of ETGs may be reconciled by invoking additional secular effects (e.g. increasing bulge size in disk-faded galaxies, or providing additional star formation truncation in post-merger starburst galaxies).

Most secular processes relevant to disk-dominated late-type galaxies involve the interaction of disk stars or gas with structural density perturbations. Galaxy bars are ellipsoidal/rectangular structures consisting of stars on elongated orbits due to orbital resonances and/or disk instabilities (see review in Sellwood & Wilkinson, 1993). As the bar pattern rotates, disk gas is accelerated, forming shocks. Outside the radius of corotation (where stars are at rest on average with respect to the bar), angular momentum is transferred from the bar to disk gas, potentially forming an outer stellar ring. Inside corotation, the gas *loses* angular momentum and falls towards the galaxy centre. The increased central gas density thus leads to the formation of an inner ring and/or stellar bulge[1](Kormendy & Kennicutt, 2004). Central gas concentration can similarly be induced by the galaxy's spiral pattern. However, the effect is weaker in this case due to non-incident interaction of spiral-induced shocks with the gas.

As with the bulge-enhancement mechanisms discussed in Section 1.2.2, AGN activity can be fed by secularly-driven gas inflow (Knapen et al., 2000; Orban de Xivry et al., 2011). A secular AGN mode explains observations of AGN hosts without indications of previous merger events. AGN feedback can therefore provide a quenching mechanism independent of local environmental conditions. This self-quenching could also supplement environment-mediated quenching to produce the observed quenching timescales (e.g. accelerating a gradual quenching via strangulation), or age gradients (e.g. centralised quenching for disk-quenching mechanisms).

[1]Bulges formed via secular processes are termed 'pseudobulges', distinct from the 'classical bulges' formed via mergers.

Secular interactions with galaxy structures can also directly influence disk stars. Scattering due to spiral patterns can cause thickening/heating of the stellar disk (Sellwood, 2014), and explain the observation that older stars (as detected in the Solar neighbourhood) have greater velocity dispersions (Wielen, 1977). More generally, radial redistribution of disk stars due to secular processes leads to a build up of bulge stellar mass (Zhang, 1998, 1999) and production of thickened outer disks (Roškar et al., 2013). As these processes can lead to a change in bulge fraction without additional star formation, they are of particular relevance for the morphological evolution of galaxies post-quenching. Furthermore, migration of stars from their radius of formation can lead to compositional mixing (e.g. as stars formed in metal-rich regions move to metal poor regions). This may explain the radial gradients in stellar metallicity detected in ETGs (Di Matteo et al., 2013, see Section 1.3).

Galaxy bars are apparent in only $\sim 30\%$ of galaxies in optical surveys of the local Universe (Masters et al., 2011), but have been detected in $\sim 70\%$ of Coma *S0*s (Lansbury et al., 2014). Orientation/inclination effects (Erwin & Debattista, 2013) and dust obscuration (Marinova & Jogee, 2007) significantly limit the detected bar fraction. Furthermore, bars are intrinsically unstable to the central mass build-up they induce (see Kormendy & Kennicutt, 2004), decaying to lens-like remnants (Kormendy, 1979). Therefore, many galaxies are expected to have hosted a bar at some point since $z \sim 1$, even where these structures are not detected in the present day. Thus, bar-driven secular evolution is a relevant consideration for a large proportion of galaxies.

1.2.4 Pre-Processing

Within a hierarchical model of galaxy evolution, most galaxies assemble in groups prior to entering a cluster at low/intermediate redshift. 'Pre-processing' refers to a scenario in which galaxies within groups are subjected to local environmental effects prior to entering the clusters they inhabit at $z = 0$. Pre-processed galaxies are subjected to incremental shift to earlier-type morphologies, and/or have their star formation rate partially truncated. Hence, these galaxies are more susceptible to environment-driven quenching when their parent groups enter a cluster potential.

In most cases, pre-processing corresponds to an early truncation of the galaxy's star

formation rate via gas stripping processes. This earlier, group-based stripping would help explain the prevalence of *S0*s beyond the virialised clusters best suited to RPS. Additionally, gradual truncation mechanisms (e.g. strangulation) initiated at the group stage would be more likely to fully quench star formation by the time at which such galaxies are observed in the cluster. This would yield a star formation history more consistent with observations of *S0* truncation times ($\gtrsim$ 1 Gyr; Fujita, 2004).

Despite the decreasing mass of a hierarchically grown group with redshift, the increasing mass *density* of the group at earlier times would make RPS increasingly effective. Thus, if ram pressure is present in pre-cluster groups, it would have a non-negligible (if not dominant) effect on star formation. Nevertheless, there exists doubt that RPS can act in groups: Fujita argues that non-gravitational heating of the group's intergalactic medium (e.g. by AGN feedback) would prevent ram pressure stripping from occurring at high redshift ($z \sim$ 2-3), and at lower redshifts if tidal acceleration (of the group by its parent cluster) is significant.

Pre-processing is also an important consideration for bulge enhancement processes. Close galaxy pairs in intermediate density environments ($\equiv$ infalling galaxy groups) have a larger fraction of red galaxies than lone galaxies regardless of host halo mass (Perez et al., 2009). This reflects the increased probability that group galaxies will experience mergers relative to isolated field galaxies. By contrast, high and low-density environments (clusters and the field respectively) both exhibit strongly mass dependent red sequence fractions. This suggests a higher frequency and/or increased efficiency of morphology-transforming galaxy-galaxy interactions within group environments.

Although the fraction of red galaxies in a cluster would increase as it accretes more merger-enriched groups over time, merger pre-processing simultaneously poses a problem in terms of *S0* survival. As discussed in Section 1.2.2, subsequent mergers (or major mergers) can destroy disks, driving the evolution to elliptical morphologies. Thus, the high merger frequency in intermediate-density groups would reduce the number of surviving *S0* galaxies observed in the cluster potential. Group-based disk destruction can be counteracted, however, by disk regrowth. Relative to mergers/harassment occurring at low-redshift in the cluster environment, the remnant of a merger within a group would spend a significantly longer period of time in a (relatively) cold, gas-rich environment. Thus, these galaxies will

have a larger chance of fully reconstructing their disks. However, as discussed above, disk regrowth necessitates an additional quenching event to produce red sequence *S0*s.

To summarise, pre-processing represents an important stage in galaxy evolution at intermediate redshifts. Typically, this acts as an initiating stage for transformation mechanisms that will conclude after the galaxy group is accreted by its parent cluster. Although relatively few *S0*s are formed within groups in this manner (thus meaning that pre-processing cannot be the primary driver of *S0* formation), pre-processing provides an explanation of the existence of 'field' *S0*s.

1.3 Stellar Populations and Scaling Relations

Using observations of stars in the Milky Way and models of their astrophysics, synthetic spectra can be produced for stars of any given mass, age, and composition. Assuming stars form with a particular distribution of masses (the initial mass function, IMF), synthetic stellar population (SSP) models can be used to predict the spectra (and photometric colours) of stellar populations. Hence, the ages and metallicities (the compositional fraction of metals) of distant galaxies' stellar populations can be interpolated from either spectroscopic or photometric (colour) observations.

Early-type galaxies possess old, 'red-and-dead' stellar populations, lacking the emission lines indicative of active star formation. Spectroscopic studies of cluster ETGs have revealed strong negative internal gradients in metallicity and α-enrichment, strongly anti-correlated with equivalent gradients in stellar population age (Rawle et al., 2010; Bedregal et al., 2011; Sil'chenko, 2011; Johnston et al., 2012). Hence, stars in an ETG's outer regions are metal-poor, but older than the stellar populations close to the galaxy centre. This indicates an 'outside-in' quenching scenario where the outskirts ceased forming stars first, while star formation (and thus metal enrichment) persisted in the core until later times.

The (central) stellar population ages of giant red sequence galaxies vary minimally as a function of local environment, but depend strongly on total galaxy mass (Smith et al., 2012). Conversely, the trends for red sequence dwarf galaxies are inverted, with stellar population age depending strongly on environment, but not mass. Dwarf galaxies are thus predicted to be quenched by a high-efficiency environment-driven mechanism. Any environmental

trends for giant galaxies would therefore be removed by environment-independent, secular processes. Spectroscopic bulge-disk decompositions (Johnston et al., 2012) detected negative component colour gradients (i.e. increasingly blue component colours with radius) in both the bulges and disks of *S0*s, but no corresponding gradients in compositional line strengths. Johnston et al. therefore attribute the *component* colour gradients to decreasing dust obscuration, rather than stellar population gradients.

For disk-dominated (late-type) galaxies, a galaxy's maximum rotational velocity is strongly correlated with its total luminosity (the 'Tully-Fisher relation', TFR; Tully & Fisher, 1977). The TFR was measured spectroscopically for the Coma cluster in Rawle et al. (2013). For a fixed rotational velocity (i.e. for equivalent disks), *S0*s were found to be systematically fainter than cluster spirals by 1.1 ± 0.2 mag in the g band. This offset was found to be consistent with *S0* formation via an abrupt quenching of spirals at intermediate redshift.

1.4 The Sérsic Profile

Data analysis in this thesis focuses on surface brightness profile fitting using the Sérsic function (Sérsic, 1963, see also Cen, 2014), a model profile whose shape is characterised by the Sérsic index, n. For $n = 4$, the Sérsic function is identical to the de Vaucouleur's profile (de Vaucouleurs, 1948), which is typically considered to be a good fit for most giant ellipticals, and 'classical' bulges. At large n, the Sérsic function peaks strongly in the centre, with slowly decaying outer wings. Conversely, at small n, the Sérsic function has a suppressed core and decays rapidly at large radii. Hence, n can be used as a measure of light concentration, with higher n indicating more centrally-concentrated models (see Figure 1.5).

For a Sérsic model with arbitrary n, the intensity (counts pixel^{-2}), Σ, at a radial distance, r, along the profile major axis is given by,

$$\Sigma(r) = \Sigma_e \exp\left[-\kappa\left(\left(\frac{r}{R_e}\right)^{\frac{1}{n}} - 1\right)\right] \tag{1.3}$$

where R_e is the effective half-light radius, Σ_e is the effective intensity at $r = R_e$, and κ is a constant whose value is determined by the Sérsic index such that half the model flux is contained within R_e. This constant can be approximated as $\kappa \approx 1.9992n - 0.3271$ (for

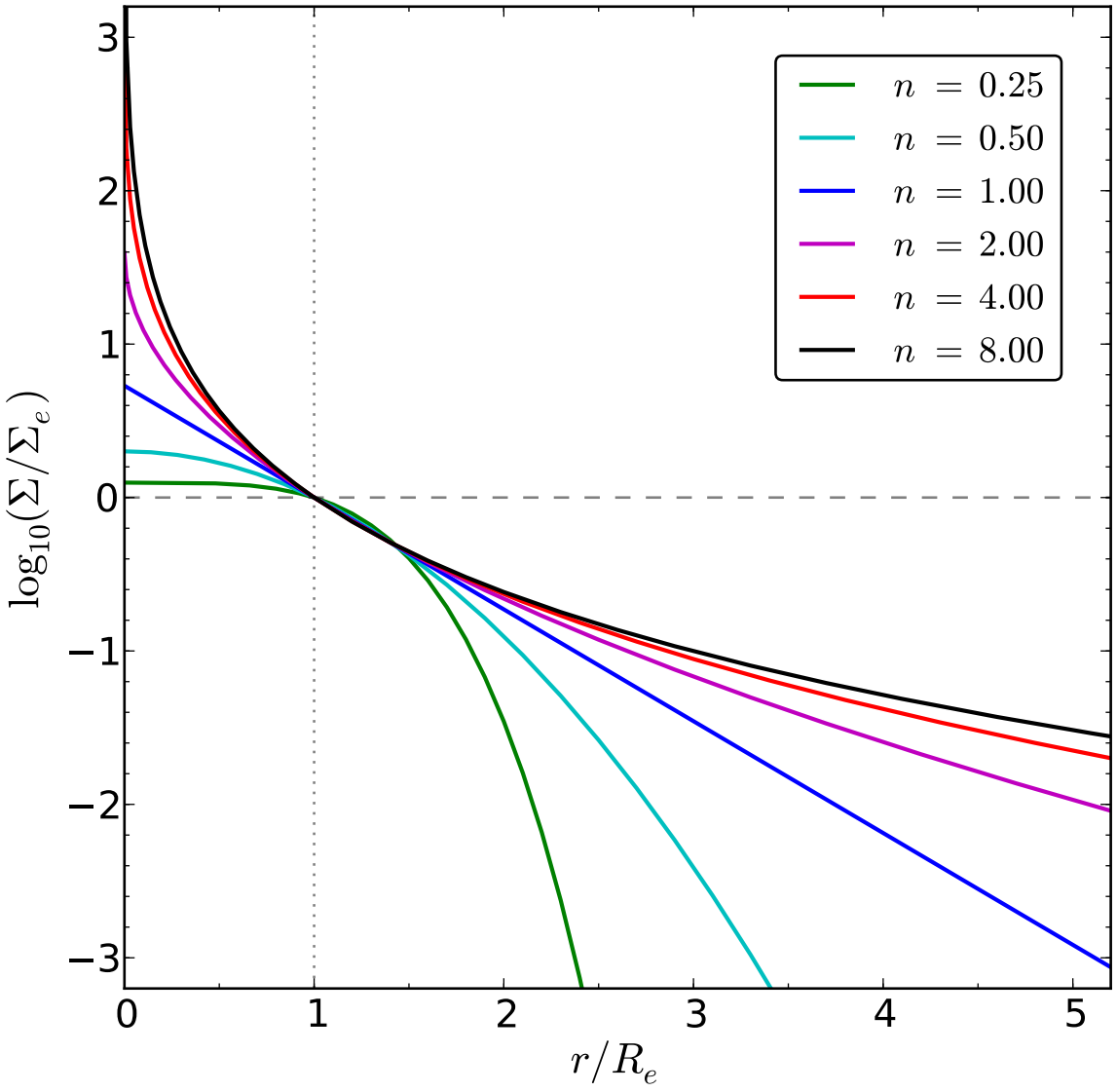

Figure 1.5: Plot of Sérsic profile intensity, Σ, as a function of radius, r, for models with different Sérsic index, n. Grey dotted and dashed lines indicate R_e and Σ_e respectively.

$0.5 < n < 10$; Capaccioli, 1989).

An important special case of the Sérsic function is the exponential profile ($n = 1$), which has been determined empirically to provide a good description for galaxy disks (Freeman, 1970). In this case, the equivalent intensity profile, $\Sigma_{\rm exp}$, at r can be written simply as,

$$\Sigma_{\rm exp}(r) = \Sigma_0 \exp\left(\frac{-r}{R_s}\right) \tag{1.4}$$

where R_s is the exponential scale length, and Σ_0 is the central surface brightness (at $r = 0$). For direct size comparison with Sérsic components, the exponential effective radius can be calculated as $R_e = 1.678R_s$ (since $\kappa(n = 1) = 1.678$).

Other notable applications for the Sérsic function include galaxy bars (Gaussian-like profiles $n \sim 0.5$), and so-called 'pseudobulges' ($1 < n < 3$; see Section 1.2.3). High n profiles ($n > 8$) generally represent underfit multi-component systems (i.e. concentrated central + outer profiles) rather than a single coherent structure.

When analysing galaxy colours and luminosities, it is convenient to describe components using total magnitudes, rather than effective or central surface brightnesses. Integrating the above expressions for Σ and $\Sigma_{\rm exp}$ over the model area (to $r = \infty$) yields the total model flux,

$$F_{\rm tot} = 2\pi R_e^2 \Sigma_e {\rm exp}(\kappa) n \kappa^{-2n} \Gamma(2n) q \tag{1.5}$$

$$F_{\rm tot} = 2\pi R_s^2 \Sigma_0 q \ \ ({\rm for}\ n = 1) \tag{1.6}$$

where q is the component axial ratio (b/a), and Γ is the gamma function (Graham & Driver, 2005). In either case, the units of R_e/R_s (pixels or arcseconds) and Σ_e/Σ_0 (counts/pixel^2 or counts/arcseconds^2) must be consistent to yield F in counts. Hence, the total model apparent magnitude can be evaluated as

$$m_{\rm ser} = m_{\rm zp} - 2.5{\rm log}_{10}[2\pi R_e^2 \Sigma_e {\rm exp}(\kappa) n \kappa^{-2n} \Gamma(2n) q] \tag{1.7}$$

$$m_{\rm exp} = m_{\rm zp} - 2.5{\rm log}_{10}[2\pi R_s^2 \Sigma_0 q] \ \ ({\rm for}\ n = 1) \tag{1.8}$$

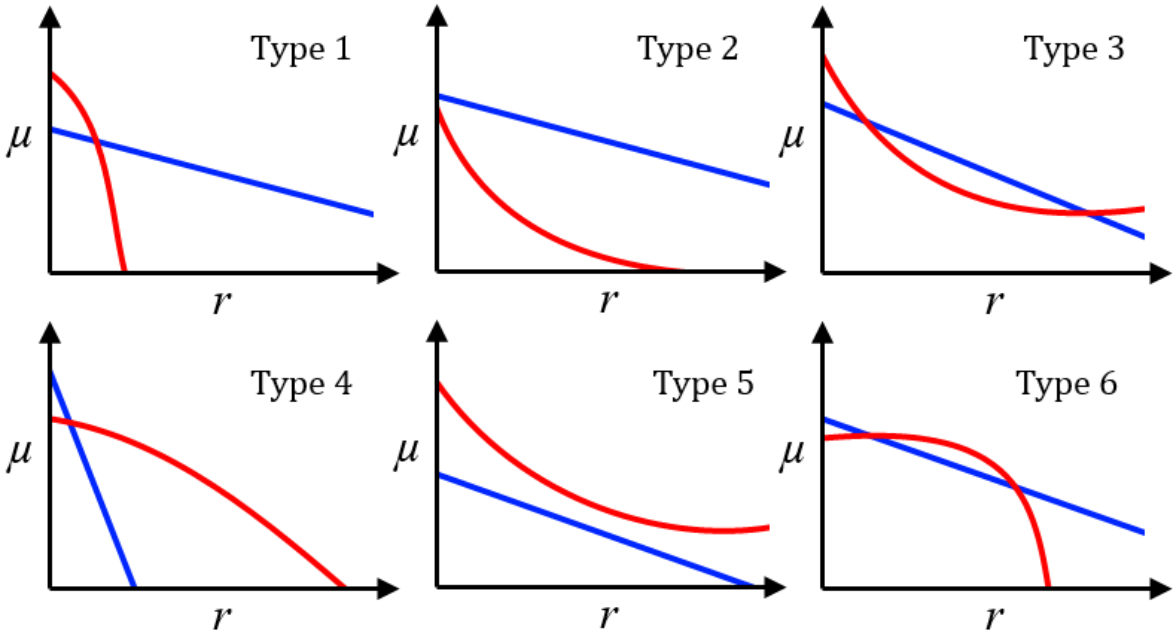

Figure 1.6: Cartoon surface brightness plots for Sérsic (red) + disk (blue) systems of each Allen type (Allen et al., 2006). Type 1 profiles are termed 'archetypal', while all other profiles are described as 'atypical'. Profile Types 4 and 6 are inversions of Types 1 and 3 (respectively), and may indicate erroneous fitting results.

where $m_{\rm zp}$ is the zero point of the magnitude scale.

It is useful to express Sérsic intensity profiles in terms of surface brightness, μ (magnitudes arcsec^{-2}), as the μ-radius plot for an exponential component is a straight line. The surface brightness profile can be expressed as

$$\mu(r) = m_{\rm zp} - 2.5\log_{10}[\Sigma(r)\theta^2] \tag{1.9}$$

where θ is the image pixel scale in arcseconds per pixel.

For a multi-component system, it is convenient to describe the combined model in terms of its component surface brightness profiles. Profile types for Sérsic + exponential models were first formalised in Allen et al. (2006) based on which component dominates at $r = 0$, and how many times the component profiles cross (see Fig. 1.6). Type 1 profiles correspond to the archetypal central bulge + outer disk of spirals and *S0*s. Type 2/Type 5 profiles represent dominant disks/bulges at all radii, with sub-dominant bulges/disks. Conversely, the centrally-dominant Sérsic component in Type 3 profiles re-dominates the model at large radii. These profiles may be non-physical representations of more complex (3+ component) systems. Profile Types 4 and 6 are equivalent to Types 1 and 3 with the roles of the Sérsic

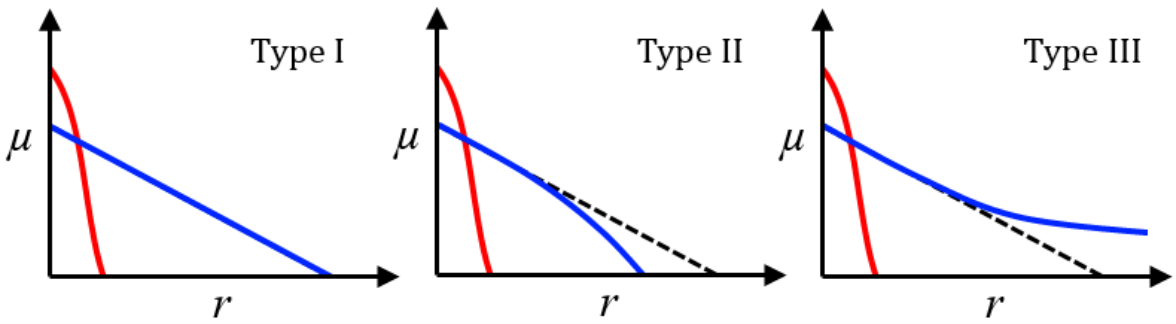

Figure 1.7: Cartoon surface brightness plots for bulge (red) + disk (blue) systems of each Erwin outer disk type (Erwin et al., 2008). **Left:** Non-truncated (Type I) disk. **Middle:** Truncated (Type II) disk. **Right:** Anti-truncated (Type III) disk. Black dashed lines corresponding to the non-truncated disk are included in the Types II and III profiles for comparison.

and exponential components swapped. As such, these inverted profiles may be symptoms of erroneous fitting pathways, rather than true physical structures.

The outer profiles of disk-dominated galaxies do not have to correspond to a classical exponential disk. 'Broken' disks have been observed for *S0* and spiral galaxies (Erwin et al., 2008), wherein surface brightness profiles beyond a break radius deviate either downwards (i.e. fainter; 'Type II') and upwards (i.e. brighter; 'Type III') relative to a simple exponential ('Type I') profile. A Type II profile corresponds to the truncation of an exponential disk due to, for example, the stripping of disk stars at large r, or inward radial migration. However, the physical interpretation of Type III profiles is less clear, and may indicate the renewed dominance of the central spheroid. Studies of outer *S0* profiles indicate an absence of Type II disks in the (Virgo) cluster environment, despite approximately even numbers of Types I, II, and III in the field (Erwin et al., 2012).

1.5 Thesis Overview and Aims

Measurements of broad-band colours can be used to probe a galaxy's star formation history. Using stellar population synthesis models, optical colours can constrain the ages and metallicities of the observed stellar populations, albeit with degeneracies due to the common bias towards redder colours caused by both properties. Many photometric studies of galaxy evolution only investigated *global* colours (e.g. Gavazzi et al., 2010). While straightforward, this approach glosses over the rich variation of stellar population properties within and be-

tween component structures. Alternatively, bulge-disk decomposition of imaging data (e.g. Hudson et al., 2010, hereafter H10; Simard et al., 2011; Lackner & Gunn, 2012) separates the photometric contributions of the galaxy bulge and disk, and thus enables stellar population properties of these structures to be measured separately. An age difference between the bulge and disk would constrain the transformation mechanisms that drove the galaxy's evolution in the past.

First discovered in the late $18^{\rm th}$ century (Herschel, 1785), the Coma cluster (Abell 1656) possesses one of the richest, and most well-studied ETG populations in the local Universe ($z \approx 0.024$). As such, Coma is an excellent laboratory for studying the morphologies (e.g. Wolf, 1902; Shapley, 1934; Dressler, 1980b) and evolution of ETGs (e.g. Lucey et al., 1991; Bower et al., 1992; Jørgensen, 1999). In addition, Coma encompasses a wide range of local environment conditions ($\sim 100\times$ difference in galaxy density between the core and the virial radius; Rawle et al., 2013), allowing in-depth investigation of radial trends of environment-mediated processes (Gavazzi, 1989; Guzman et al., 1992; Carter et al., 2008; Gavazzi et al., 2010; Smith et al., 2012; Cappellari, 2013; Rawle et al., 2013; Lansbury et al., 2014).

In this thesis, multi-component (2+) model fitting is used to characterise the structural and photometric properties of red sequence galaxies in the Coma cluster. Galaxies are selected in an absolute magnitude range $-17 > M_g > -22$, yielding a large ($N \sim 600$) initial catalogue of ETGs over a wide range of local environment densities. Decomposition analysis yields insight into the morphological and star-formation histories of galaxies which reside in rich galaxy clusters in the present day. Thus, structural variation along the Hubble sequence and the nature of star-formation quenching (environment-mediated or otherwise) is investigated. Five main questions are addressed:

- Are progenitor bulge and/or disk structures preserved in present-day S0s?
- Do the bulges and disks of ETGs follow a common red sequence slope?
- How separated (in colour) are the stellar populations of these components?
- In what way do the observed colour distributions vary during cluster infall?
- Do the profiles of galaxy disks maintain an exponential profile to large radii?

The results of the study presented in this thesis are based on deep observations of Coma taken during March-June 2008 at the Canada-France Hawaii Telescope (CFHT) on Mauna Kea, Hawaii. In Chapter 2, these observations are described in detail, including discussion of the data pipeline and the data products derived from the initial imaging (e.g. noise maps, point spread functions). In addition, the sample selection criteria used to identify Coma cluster galaxies for analysis are described.

In Chapter 3, I first describe both the general principles of bulge-disk decomposition (including discussions of the models and software used), and the specific algorithm developed for this work to extend and automate this data reduction. Secondly, I present details of the sample filtering and model selection techniques used to isolate a sample of galaxies for analysis which provide meaningful bulge + disk fits. Thirdly, the reliability of results produced by this reduction pathway is discussed, along with a description of its limitations. Lastly, techniques for multi-band fitting (i.e. fitting using constraints derived from fits to another photometric band) of varying complexity are discussed and contrasted.

The results of the present decomposition analysis are contrasted to the equivalent studies of independent imaging data (SDSS, HST) in Chapter 4. This comparison investigates both literature decomposition catalogues, and the results of applying the present decomposition pipeline to equivalent data sources. This provides a valuable test of the fitting scatter and highlights the improved reliability of the present work relative to the decomposition of shallower imaging.

Rather than forcing a Sérsic bulge + exponential disk morphology on all galaxies regardless of model suitability, I focus exclusively on a sample of galaxies with *S0*-like structural morphologies (i.e. central bulge + outer disk; described as 'Classic'/Type 1 in Allen et al., 2006). The cherry-picked nature of this sample introduces selection biases as only symmetric galaxies with idealised morphologies are included. However, the aim of this work is to examine galaxies expected to be well-fit by a bulge + disk model, rather than to address a complete sample. The resulting distributions of component structural properties (i.e. size, shape, and orientation on the sky) are presented in Chapter 5, along with a discussion of trends with galaxy mass/luminosity or local environment.

Galaxy and component photometric results (luminosity and colour) are described in

Chapter 6. This chapter includes a full discussion of the component red sequences and environmental trends, and any variation therein caused by the choice of the multi-band fitting technique. The resulting component stellar population properties are then derived via simple stellar population models. In addition, this chapter investigates variations in the measured photometric properties if the sample is divided by (visually-classified) galaxy morphology.

In Chapter 7, I describe the extended decomposition routine for more complex multi-component galaxy analysis, highlighting pipeline, fitting, and filtering differences from Chapter 3. I also describe the broken disk model used during this analysis to identify deviations from a simple exponential profile in the outer regions of ETGs. The structural results of this analysis are described in Chapter 8. This includes discussion of multi-Sérsic galaxies, and the formation mechanism of truncated/anti-truncated disk structures.

Finally, in Chapter 9 I summarise the results of this work, and the final conclusions of this study are drawn.

Throughout this thesis, I make use of the following notation conventions: Galaxy morphologies (see Section 1.1) are indicated in italics (e.g. '*Sa*') to distinguish them from fitted model structures (see Section 7.2.3; e.g. 'S'). Disk break types (i.e. Freeman types; untruncated, truncated, anti-truncated, see Section 1.4) are denoted with Roman numerals (e.g. 'Type II'), and galaxies containing such structures are referred to as Type I, Type II, or Type III galaxies. Conversely, galaxy types using Arabic numerals (e.g. 'Type 2') refer to Allen et al. (2006) surface brightness profile types (see Sections 1.4 and 7.2.3). The Type 1 profile is a special case describing a central bulge and an outer disk, and is referred to as an 'archetypal *S0*' profile ('archetypal', or '*S0*' as shorthand). All other Allen et al. (2006) types are referred to as 'atypical *S0*' profiles (or simply 'atypical').

Furthermore, I use the WMAP7 cosmology: $H_0 = 70.4$ km s^{-1} Mpc^{-1} (i.e. $h_{70} = 1.01$), $\Omega_m = 0.272$, and $\Omega_\Lambda = 0.728$ (Komatsu et al., 2011). Using $z_{\rm CMB}({\rm Coma}) = 0.024$, the luminosity distance for the Coma cluster is 104.1 Mpc, and the distance modulus, $m - M = 35.09$. Equivalently, the angular size distance for Coma is 99.3 Mpc, and thus $1'$ corresponds to 28.9 kpc. Taking a value for velocity dispersion of $\sigma_{\rm Coma} = 1008$ km s^{-1} (Struble & Rood, 1999) and virial mass, $M_{200} = 5.1 \times 10^{14} h_{70}^{-1} M_\odot$ (Gavazzi et al., 2009), the virial radius, r_{200}, for Coma is 2.2 Mpc ($\sim 75'$).

Chapter 2

Data and Initial Sample

2.1 Introduction

In this chapter, I describe the optical imaging data used in this thesis to analyse red sequence ETGs in the Coma cluster. This encompasses a full description of the observations (including details of the detector, initial data processing, and observed fields), and the selection criteria used to define a sample of target galaxies for analysis. In addition, I discuss the data products derived from the (as-received) imaging for use in the decomposition analysis, along with the corrections applied to enable robust measurement of rest-frame photometry.

2.2 Observations and Initial Reduction Pipeline

Optical imaging of the Coma cluster was acquired in the u, g, and i bands at the 3.6 m Canada-France Hawaii Telescope (CFHT) during March - June 2008 (Run ID 2008AC24, PI: M. Hudson). These observations made use of the MegaCam instrument (Boulade et al., 2003), a 340 Megapixel optical/near infrared Charge-Coupled Device (CCD) detector with a square degree field of view. In total, a ~ 9 deg^2 area ($\equiv 5.2$ Mpc $\times 5.2$ Mpc, 2 $r_{200} \times$ 2 r_{200} for Coma) was observed, comprised of nine subfields (details in Table 2.1, illustrated in Fig 2.1). Total (coadded) exposure times of 300 s were obtained for the g and i bands, and 1360 s for the u band. Compared to Sloan Digital Sky Survey (SDSS; York et al., 2000) imaging (2.5 m telescope, 53 s exposures), these observations were $\sim 12\times$ deeper in the g and i bands,

Field	RA_{min} [deg]	RA_{max} [deg]	Dec_{min} [deg]	Dec_{max} [deg]
COMA-F1	193.30714	194.43549	+26.54732	+27.56709
COMA-F2	194.36464	195.49299	+26.54732	+27.56709
COMA-F3	195.42297	196.55133	+26.54732	+27.56709
COMA-F4	193.30245	194.44043	+27.48061	+28.50038
COMA-F5	194.35995	195.49793	+27.48061	+28.50038
COMA-F6	195.41828	196.55626	+27.48061	+28.50038
COMA-F7	193.29745	194.44570	+28.43056	+29.45033
COMA-F8	194.35495	195.50320	+28.43056	+29.45033
COMA-F9	195.41328	196.56154	+28.43056	+29.45033

Table 2.1: The maxima and minima in Right Ascension (RA) and Declination (Dec) for the nine Coma CFHT fields in degrees. These fields are illustrated graphically in Figure 2.1 by green boxes.

and $\sim 50\times$ deeper in the u band (from exposure time, $t_{\rm exp}$ and aperture size, D[1]). We note that the MegaCam u filter is shifted slightly redward relative to SDSS u. This difference is accounted for by calibrating the u band zero points with SDSS aperture photometry (see Section 2.4). The MegaCam point spread function (psf) full-width half-maximum (fwhm) was between $0.65''$ and $0.84''$. For comparison, the psf for SDSS imaging in the Coma region has a fwhm of $\sim 1''$. The pixel scale for all MegaCam imaging was ~ 0.186 arcseconds/pixel.

Each 1 deg^2 MegaCam field image was combined from four 75 second exposure frames (in g and i; 340 second exposures in u), each of which comprise 36 individual CCDs. The raw data frames were pre-processed via the Elixir pipeline (Magnier & Cuillandre, 2004), and subsequently stacked using the `TERAPIX` pipeline (Bertin et al., 2002). Elixir is a 2-3 stage pre-processing routine: First, biases and errors resulting from the optics/CCD system were corrected: this included bad pixel masking (setting their value to 0 ADU), and the removal of overscan (y-axis) gradients and ringing at the beginning of the pixel rows in each CCD. Flat-fielding was also carried out to correct for variation in optical transmission, filter bandwidth, and pixel scale across the detector. By normalising the gain/quantum efficiency ratio for each CCD, this also yielded a uniform zero point across the detector. Secondly, fringe correction was carried out in the i band based on a master fringe pattern generated from multiple fringed images (linearly-scaled to the same level). The scaling factor used for fringe correction was a median of the values computed for all 36 CCDs. Lastly, a correction was applied to all bands to remove an apparent increase in intensity towards the centre of the

[1] $(t_{\rm exp,CFHT}/t_{\rm exp,SDSS})(D_{\rm CFHT}/D_{\rm SDSS})^2$

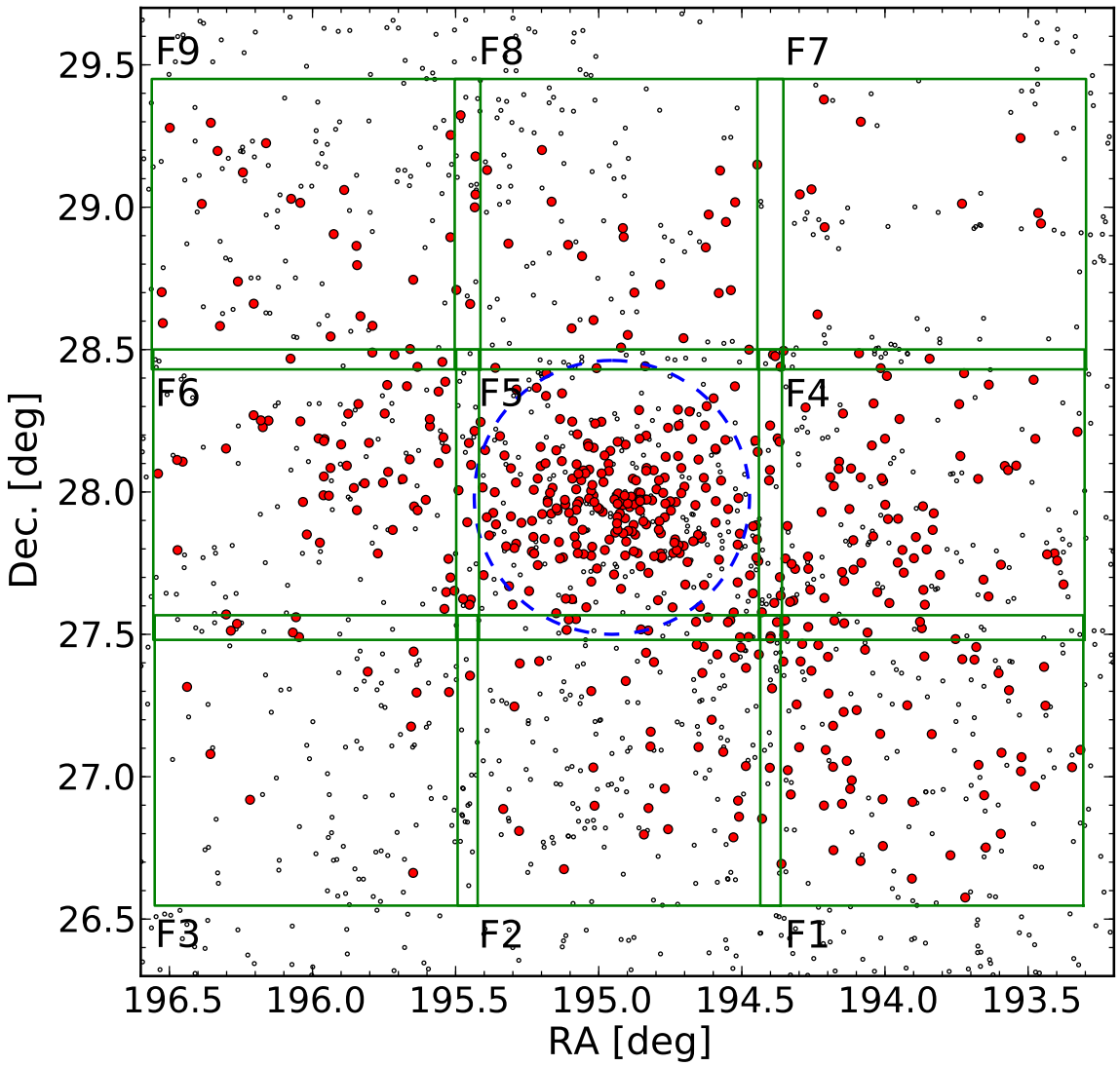

Figure 2.1: Plot of the Right Ascension (RA) and Declination (Dec.) of the CFHT Coma field of view, and the resulting galaxy sample used for analysis. The CFHT fields (see Table 2.1) are marked as green boxes. Galaxies which meet the selection criteria for analysis (the Coma sample) are plotted as filled red circles. All other galaxies (too faint, too blue, or non-cluster members) are plotted as small, unfilled circles. A dashed blue line indicates the area within 1 Mpc of the cluster centre.

frame introduced by the photometric flat-field image. Image astrometry was calibrated via a first-order fit ($\sim 1''$ error) to astrometeric catalogues based on rough World Coordinates System (WCS) data in the raw data frames. Band-wise photometric calibration was performed via repeated observation of standard star fields over the course of the observing run.

The TERAPIX pipeline was used to sky-subtract and stack the Elixir-processed data frames. In addition, TERAPIX provided an additional stage of astrometric and photometric calibration: Elixir astrometry is tuned up through iterative fitting of a global astrometric solution to the imaged fields (Astrometrix) via cost function minimisation. A similar routine (Photometrix) is used to calibrate the photometric zero-points. Calibrated frames were then stacked using SWarp, including automated sky-subtraction with a 64 pixel mesh.

In this section, I have described the MegaCam observations used in this thesis, including details of the target Coma fields, ugi observation depth, and the imaging data pre-processing. The resulting data products comprise 27 one deg^2 stacked, (photometrically + astrometrically) calibrated, and sky-subtracted images (u, g, and i for all nine Coma fields).

2.3 Coma Sample Selection

An initial sample of target galaxies in the 9 deg^2 area covered by the MegaCam observations (see Section 2.2) was taken from the SDSS Data Release 9 (DR9; Ahn et al., 2012) catalogue. In total, this initial sample comprised $N = 1449$ galaxies with SDSS photometry, and spectroscopic redshifts. A magnitude limit of $g < 18$ ($M_g < -17.1$) was applied to ensure sufficient signal-to-noise (S/N[2]) for reliable measurement of galaxy bulge and disk structures ($\lesssim 1\%$ uncertainty on model magnitude). This limit removes $N \sim 550$ galaxies from the initial SDSS galaxy sample. Likewise, an apparent colour limit of $(g-r) > 0.5$ (selected for consistency with Smith et al., 2012) was used to isolate red sequence galaxies ($N \sim 100$ removed). These photometric selection criteria are illustrated in Figure 2.2. Targets were also limited to the redshift range $0.015 < z < 0.032$ (heliocentric $v_{\rm Coma} \pm 2.5\sigma_{\rm 1D}$) to ensure that only cluster members were included ($N \sim 200$ removed). These selection criteria yield a sample of $N = 570$ red-sequence galaxies (hereafter 'Coma sample').

[2]Calculated as the sum of sky-subtracted pixel counts within the target ellipse (see Section 2.4), divided by the quadrature sum of the noise map in the same area.

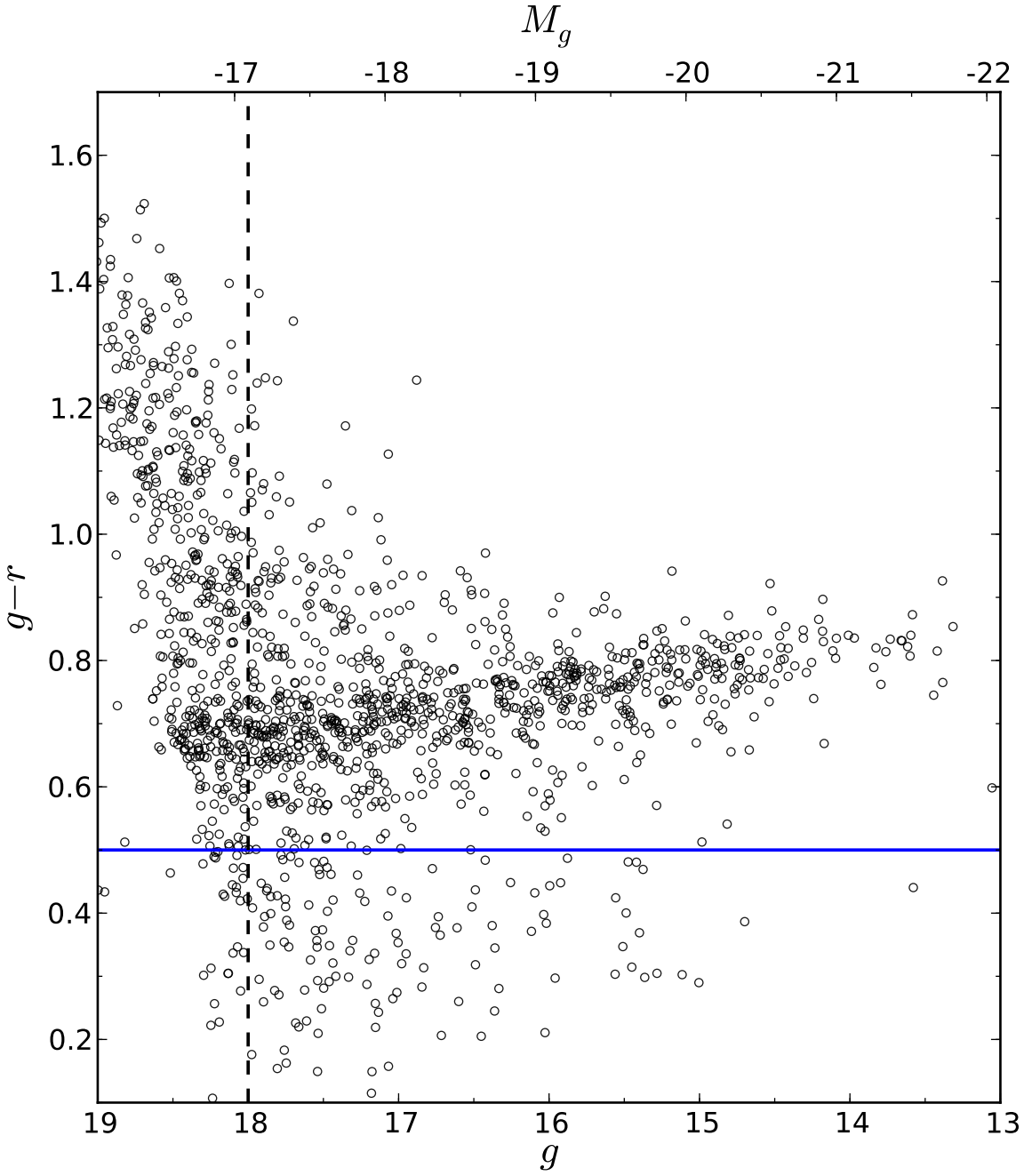

Figure 2.2: Colour-magnitude diagram for the Coma cluster, using total galaxy magnitudes from SDSS (DR9). The $(g-r)$ colour, and g band brightness limits used to define the Coma sample are included as a solid blue line and dashed black line respectively.

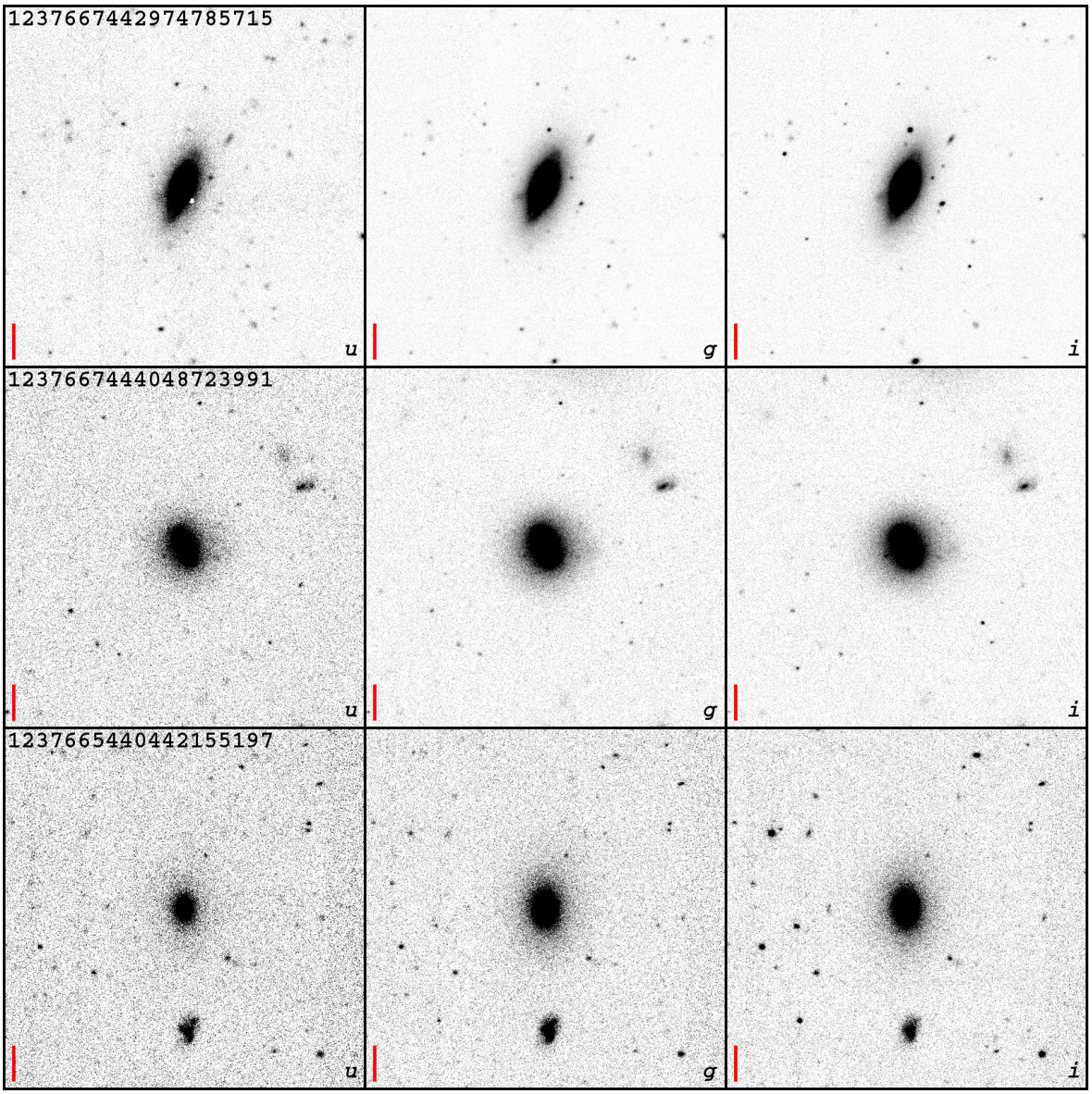

Figure 2.3: Example u, g, i image frames for galaxies with median, and first and third quartile (g band) S/N. **Upper:** SDSS DR8 ObjID 1237667442974785715; $M_g = -19.1$, S/N~ 1000. **Middle:** SDSS DR8 ObjID 1237667444048723991; $M_g = -18.9$, S/N~ 530. **Lower:** SDSS DR8 ObjID 1237665440442155197; $M_g = -18.2$, S/N~ 310. A red scale bar corresponding to $10''$ ($\equiv 4.8$ kpc) is included in each frame.

2.4 Input Analysis Data

2.4.1 Data images

For the primary data input, $\sim 100'' \times 100''$ (536 $\times$ 536 pixel) thumbnail images were extracted from the coadded MegaCam image frames, centred on each target galaxy (see Fig. 2.3). To ensure that no pixels contained negative values, a soft sky of 100 counts was added to each thumbnail. The resulting local background sky was then measured from the thumbnail using elliptical annuli: first, `SExtractor` (Bertin & Arnouts, 1996) was used to identify an ellipse enclosing all pixels containing flux from the target galaxy (at a $0.5\sigma_{\rm sky}$ threshold above the sky value; hereafter 'moments ellipse'). Next, the moments ellipse was doubled in radius (hereafter 'sky ellipse') to ensure the galaxy does not contaminate the measured sky value. This sky ellipse was then sequentially scaled up (by 10% in radius, preserving axis ratio and position angle)[3], and the median sky flux was measured within the resulting annuli (Figure 2.4). As no significant variation ($< 0.1\%$) was detected between sky measurement annuli, the sky value was assumed to remain constant for each thumbnail.

Galaxy thumbnails are masked during fitting to prevent the sky from dominating the value of chi-squared (χ^2) during fitting. The `SExtractor` moments ellipse was extended by $5''$ along the semi-major axis (with axis ratio fixed) to ensure that no target flux was omitted (hereafter 'target ellipse'). All pixels outside of the target ellipse were masked, except for $\sim 1''$ wide strips along its major and minor axes (see Figure 2.5). This unmasked cross area was included to avoid discontinuities at the mask boundary. In addition, `SExtractor` was used to detect and mask other sources or defects in the thumbnail ($> \sigma_{\rm sky}$ threshold).

2.4.2 Noise maps

The results of χ^2-minimisation fitting is highly dependent on the weighting of each image pixel. If pixels with high uncertainty (due to Poisson noise) and well-known brightnesses are assigned equal importance during fitting, then χ^2 struggles to distinguish between improvement/worsening of the goodness-of-fit. Therefore, in order to carry out model fitting reliably, a robust estimate of the underlying noise distribution is essential. This noise map

[3]Until the (outermost) ellipse radius exceeds $300/q$ pixels, where q is the ellipse axis ratio, to ensure a sufficient number of pixels per annulus.

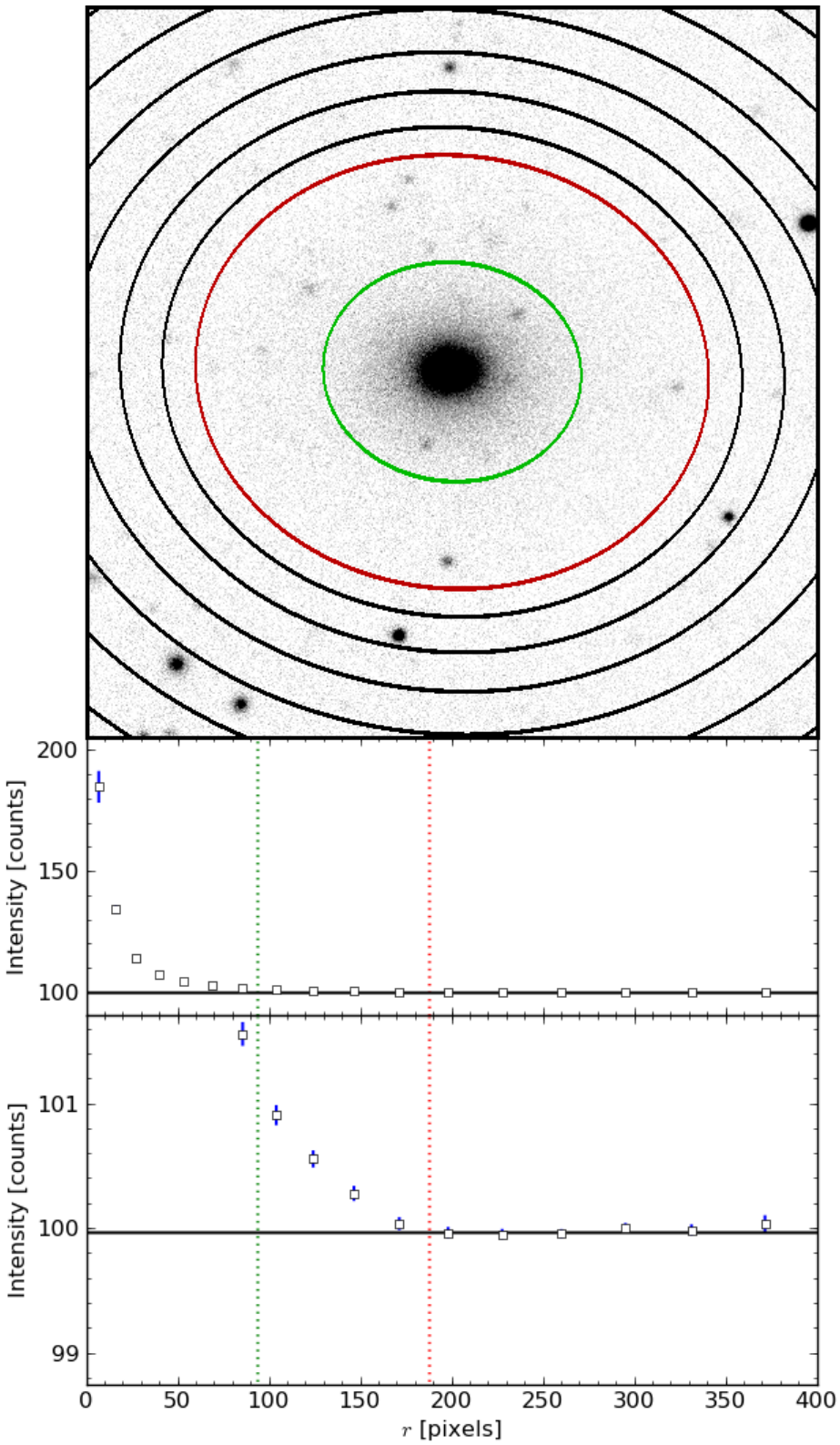

Figure 2.4: Sky determination for an example galaxy (SDSS DR8 ObjID: 1237667444048199866). **Upper panel:** g band galaxy thumbnail indicating the `SExtractor`-determined moments ellipse (green), and the corresponding sky ellipse (red) which is sequentially scaled up (by 10%; black ellipses) to form elliptical annuli for sky measurement. For clarity, neither the external source masking or annuli within the sky ellipse are indicated. **Middle/lower panels:** The median pixel intensity (in counts) in each elliptical annulus (square points) plotted against the median (major axis) radial distance from the galaxy centre. The radii of the moments and sky ellipses are indicated as green and red dotted lines (respectively), and the measured sky value is indicated by a solid black line.

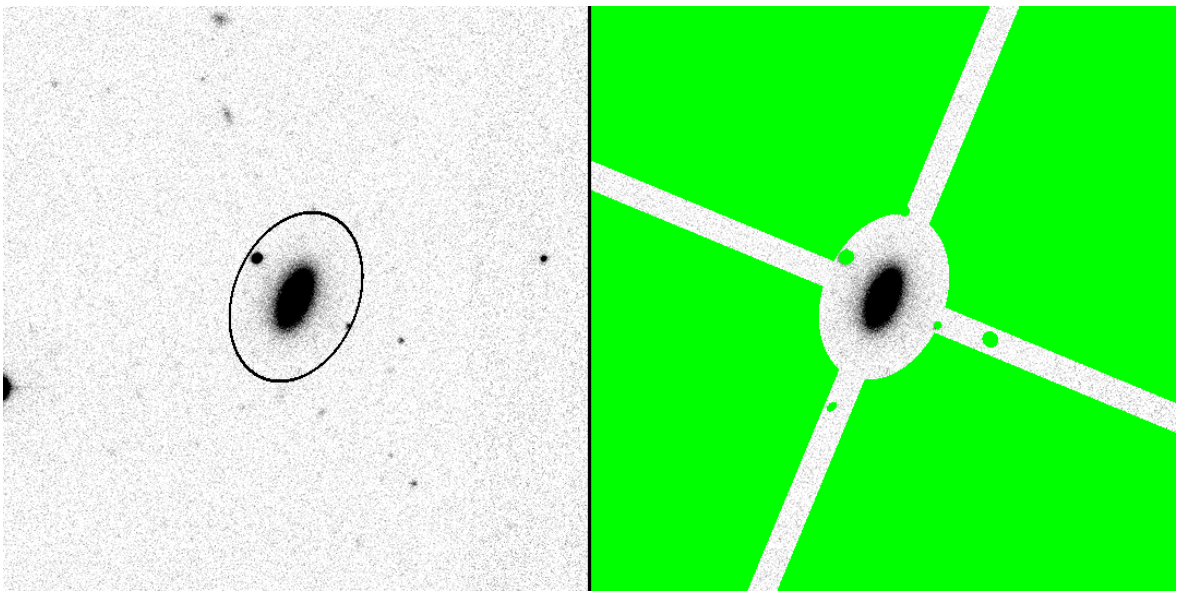

Figure 2.5: Example of image masking for SDSS DR8 ObjID 1237665427553321062. **Left:** Galaxy thumbnail with target ellipse overplotted in black. **Right:** Galaxy thumbnail with final cross mask (including neighbouring source masking) overlaid in green.

was estimated using

$$\sigma(x,y) = \left(\frac{|f(x,y) - f_{\rm sky}|}{\rm GAIN} + \sigma_{\rm sky}(x,y)^2 \right)^{\frac{1}{2}} \tag{2.1}$$

where $f(x,y)$ is the signal in analogue-to-digital units (ADU) for a pixel at position (x,y), $\sigma_{\rm sky}(x,y)^2$ is the root mean squared (RMS) sky variance in that pixel (in ADU^2), $f_{\rm sky}$ is the mean sky level (in ADU), and GAIN is the CCD gain in ADU/counts (Peng et al., 2010). However, the chosen fitting software (`GALFIT`, see Chapter 3) estimates the sky parameters by removing the faintest and brightest 20% of pixels and calculating a filtered median and RMS value from the remaining regions. This approach assumes that 60% of the image contains no source objects. If this is not the case, then the sky will be overestimated by sampling pixels corresponding to low surface brightness sources, and thus produce an incorrectly-weighted sigma image. Therefore, the mean sky flux and RMS sky variance were estimated independently. To avoid overestimates of the sky variance due to exposure frame mosaicing or faint unmasked sources, $\sigma_{\rm sky}$ is determined locally in 16 pixel $\times$ 16 pixel regions in the (source-masked) image frame. Where less than 50% of the pixels in a region are unmasked, a median value is calculated from valid surrounding regions.

2.4.3 PSF characterisation

Stars in the MegaCam frames were used to characterise the psf of the data images. Thumbnail images covering an area of $9.3'' \times 9.3''$ (50 $\times$ 50 pixels) were extracted from the sky-subtracted frames. These psf images were vetted via ellipse fitting to exclude saturated, binary, or contaminated star images. For each band, the closest five clean psf thumbnails (of sufficient S/N) were averaged using `KAPPA` and `MAKEMOS` (from the `Starlink` package, Giaretta et al., 2004) to produce an master psf image. Stars were sampled from no further than $5'$ from the target galaxy, as the psf varies across the detector CCD (see Figure 2.6). For the u, g, and i bands, fwhm of $\sim 0.8''$, $\sim 0.7''$, and $\sim 0.6''$ were typical.

2.4.4 Photometric zero point corrections

The photometric zero points were calibrated by comparing SDSS photometry ($7.43''$ aperture) with the magnitude measured in an equivalent radius aperture in the MegaCam images. To avoid erroneous zero points in cases where deblending is required, the median zero point correction for each MegaCam field (determined on a galaxy-by-galaxy basis) is applied to all galaxies within that field. The size of this correction was typically 0.35 mag, 0.15 mag, and 0.05 mag in the u, g, and i bands respectively (see Fig. 2.7). This correction allows direct comparison of this work's results with studies utilising the Sloan $ugriz$ magnitude system (Fukugita et al., 1996; Smith et al., 2002). To first order, this also accounts for the differences between MegaCam and SDSS u band filters. The zero point uncertainty was typically $\lesssim 0.01$ mag in the g and i bands, but $\sim$ 2-3$\times$ greater in the u band, due to sky determination issues in the (relatively shallow) SDSS imaging.

2.4.5 Conversion to rest-frame photometry

In this study, fitting results are considered primarily as a function of absolute galaxy luminosity. This approach is favoured over the prediction of galaxy stellar masses, as directly measurable parameters require the fewest number of assumptions (e.g. the choice of initial mass function). If galaxies luminosities *were* converted to stellar masses (e.g. via $\log_{10}(\mathrm{M/L}) = 0.914(g-i) - 0.379$ from Bell et al., 2003), then the Coma sample covers a 100$\times$ range ($\approx 10^9$-$10^{11}\ M_\odot$). However, given the small range of colours covered by the

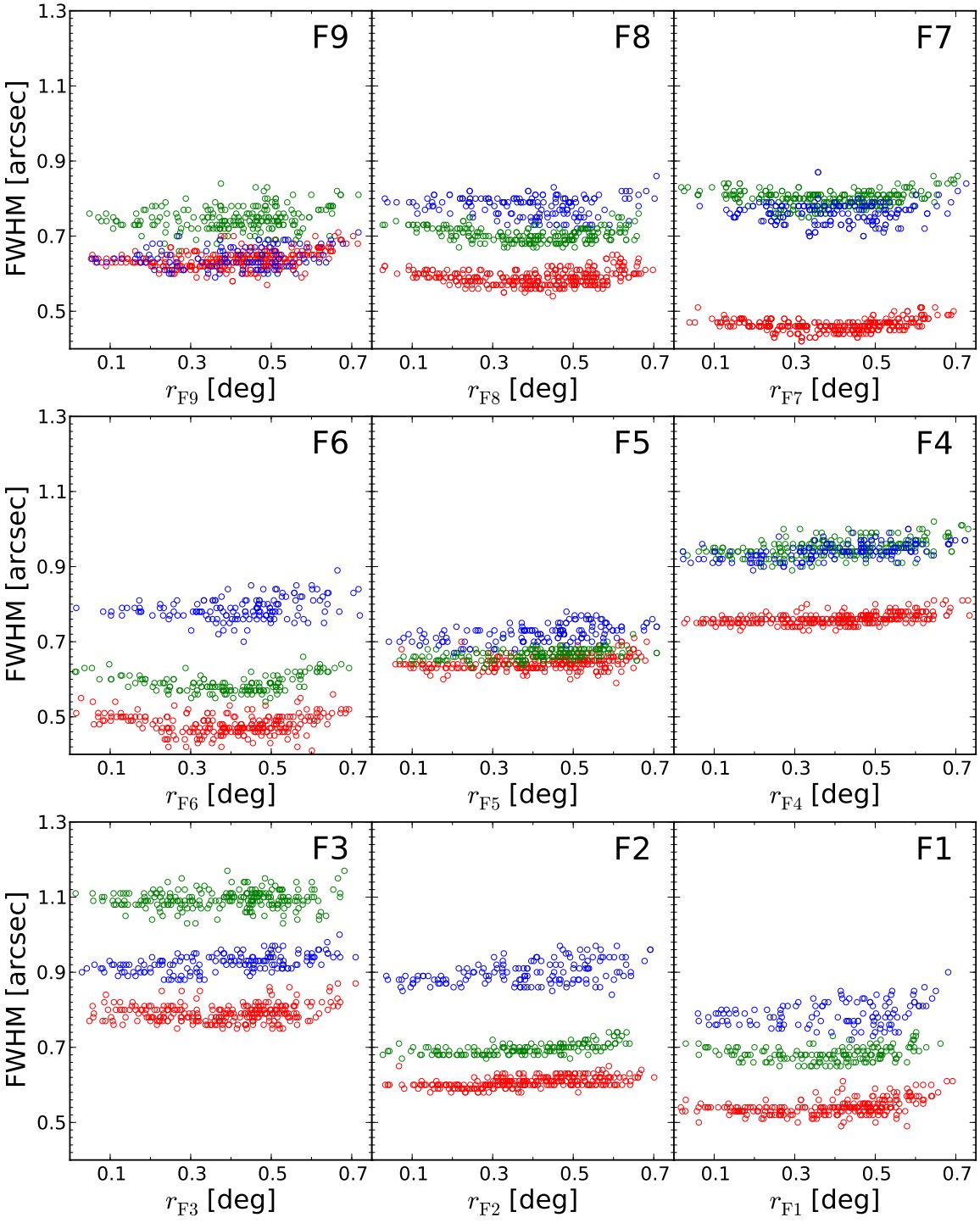

Figure 2.6: The point spread function FWHM (in arcseconds) as measured from stars in each MegaCam field (F1-F9) plotted against field-centric radius, r_{FN}. The u, g, and i band FWHM are plotted as blue, green, and red circles respectively.

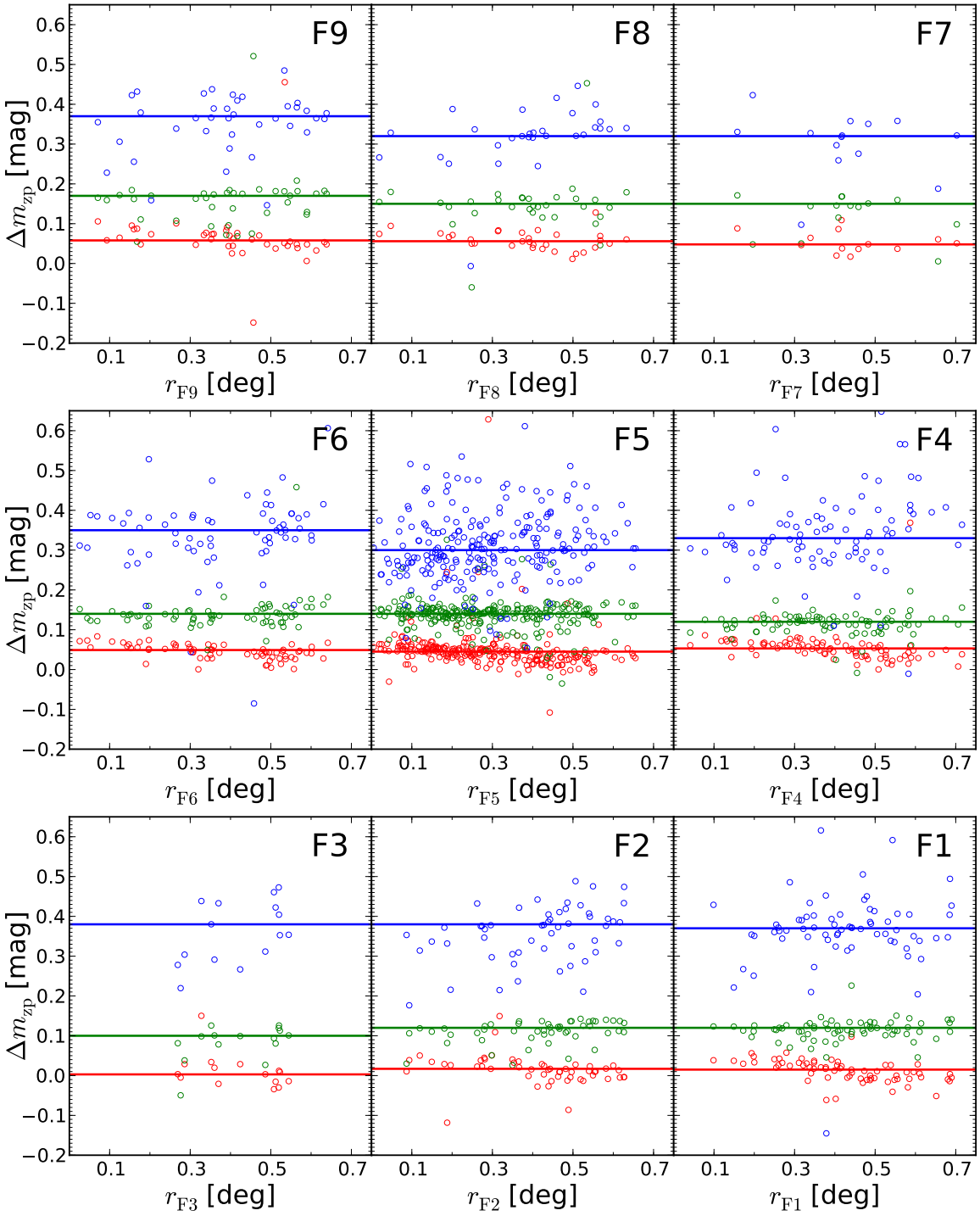

Figure 2.7: The correction to the MegaCam photometric zeropoints, $\Delta m_{\rm zp}$, in magnitudes plotted against field-centric radius, $r_{{\rm F}N}$ for galaxies within each MegaCam field (F1-F9). The u, g, and i band corrections calculated for each galaxy are plotted as blue, green, and red circles respectively. The field median corrections (applied to all galaxies in that field) are plotted as solid lines, using the same colour scheme for the three bands.

red sequence galaxies, a light-to-mass conversion would not significantly alter the measured trends (i.e. a constant offset, with only $\sim 10\%$ uncertainty in mass due to colour scatter).

Absolute rest-frame magnitudes were calculated by subtracting the distance modulus ($m - M = 35.09$), and applying galactic dust extinction- and k-corrections. Using the maps of Schlafly & Finkbeiner (2011), average galactic extinction corrections of 0.034, 0.026, and 0.014 mag were applied to the u, g, and i bands respectively. The k-correction was calculated using SDSS spectroscopic redshifts and 'the k-correction calculator' (Chilingarian et al., 2010; Chilingarian & Zolotukhin, 2012). This correction was typically 0.12, 0.05, and 0.01 mag in the u, g, and i bands.

Throughout this thesis, no formal correction is included for the presence of dust internal to the observed galaxies. Dust effects will contribute to the scatter in structural and photometric distributions presented below. This effect is pronounced in highly inclined galaxies, but will also influence face-on galaxies (Driver et al., 2007). However, dust-contaminated ETGs are rare in cluster environments (Kaviraj et al., 2012). By filtering the analysis sample to remove the few galaxies with strong dust lanes or asymmetries (see Section 3.5), the effects of dust on the conclusions of this thesis have been minimised.

2.5 Chapter Summary

In this chapter, I have described the preparation and calibration of the MegaCam imaging data for use in bulge - disk decomposition, and the selection of a sample of Coma cluster member galaxies.

Analysis thumbnails were extracted from the (pre-processed; astrometrically and photometrically calibrated) parent MegaCam frames with a $100'' \times 100''$ field of view. These thumbnails were then re-calibrated to SDSS magnitudes using aperture photometry, and their background sky fluxes were robustly measured. Maps of the pixelwise statistical noise were estimated from each thumbnail in order to correctly weight galaxy pixels during fitting analyses. In addition, the MegaCam psf was characterised by extracting (uncontaminated) star images from no further than $5'$ from each target galaxy.

The initial sample of Coma cluster galaxies was selected from the MegaCam fields using the SDSS DR9 catalogue. Red sequence target galaxies were selected where $g < 18$, and

$g-r > 0.5$. Cluster membership was determined using a (SDSS DR9 spectroscopic) redshift range of $0.015 < z < 0.032$. This yielded a sample of 570 galaxies.

In the next chapter, I will describe the galaxy decomposition pipeline used to measure the bulge and disk properties of Coma cluster galaxies. This includes a discussion of the model selection and sample filtering techniques used, and a description of the resulting galaxy subsamples.

Chapter 3

Bulge-disk Decomposition Techniques

3.1 Introduction

To measure the structural and photometric parameters of galaxy bulges and disks, galaxy decomposition has been carried out using GALFIT (version 3.0.4), a 2D fitting routine (Peng et al., 2010). Given a user-specified model (of arbitrary complexity), GALFIT varies parameters based on a non-linear chi-squared minimisation algorithm until no significant decrease in (reduced) chi-squared (χ^2_ν) is found. The parameter values of this best-fit model are used to estimate the underlying structure and photometry of the target galaxy.

In this chapter, I describe the bulge-disk decomposition methodology used to fit 2-component models (consisting of a Sérsic 'bulge' and exponential 'disk') to the Coma cluster galaxy sample described in Chapter 2. This includes a description and critical analysis of techniques for fitting consistent model structures across multiple photometric bands. In addition, the statistical tests and selection criteria used to filter out galaxies which are *not* well-described by a bulge + disk interpretation are presented.

3.2 Decomposition Routine - AGONII

AGONII (Automated Galfitting of Optical/Near Infrared Imaging) - a python wrap-around script for GALFIT - was developed for this work to automate and extend the fitting process. This circumvents the two major issues with running stand-alone GALFIT: a) sensitivity of fitting results to initial parameters, and b) inability to differentiate between local and

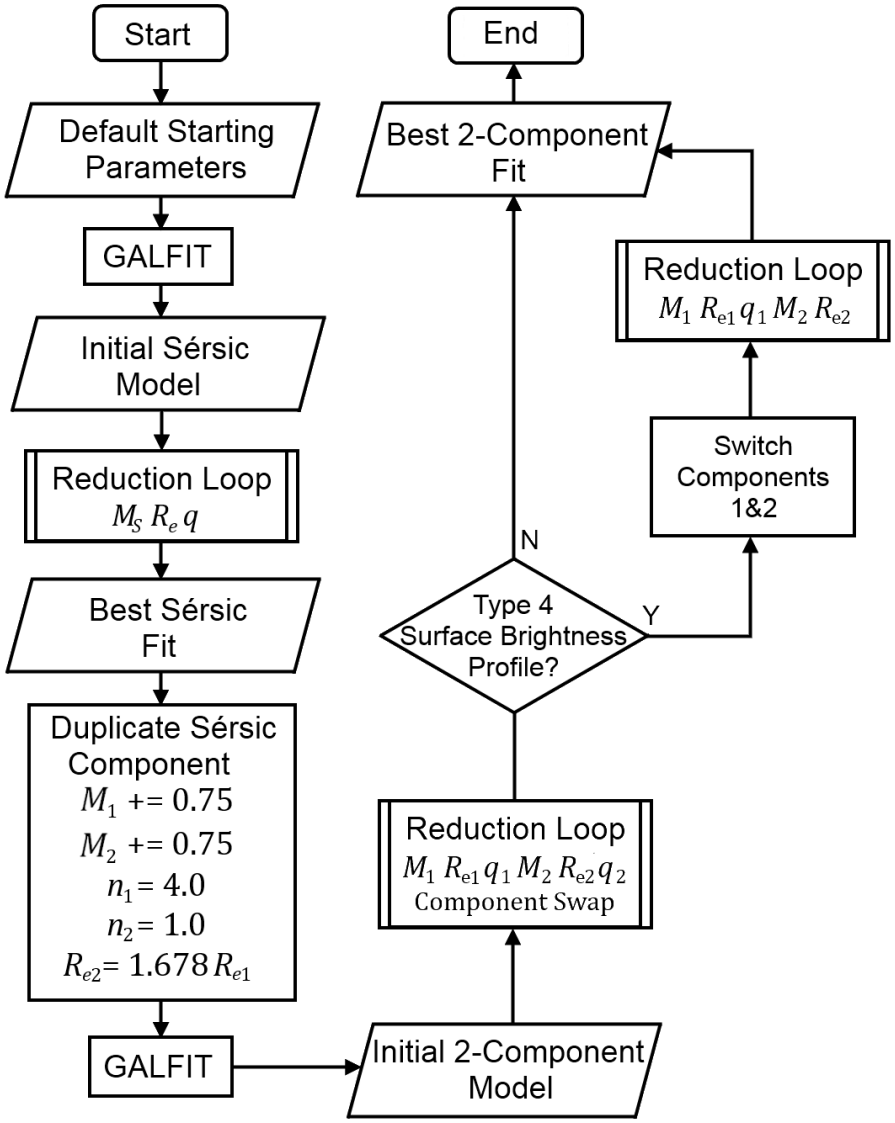

Figure 3.1: Flow chart: Overall fitting process for 1- and 2-component model fitting. The reduction loop process is described in Figure 3.2.

global χ^2 minima. Relative to other automated GALFIT wrap-arounds (e.g. GALAPAGOS; Barden et al., 2012), AGONII's extended search provides a more thorough exploration of the parameter-space. In addition, AGONII includes a prescription for multi-band decomposition (i.e. variation of model parameters between photometric bands). While complex multi-band approaches have been presented previously for Sérsic-only fits (e.g. GALFITM/MegaMorph; Vika et al., 2013), AGONII represents the first multi-wavelength application of bulge-disk decomposition. Furthermore, AGONII implements an additional stage of sample filtering to ensure applicability of the assumed bulge + disk model structure. This ensures that the resulting analysis data products are not contaminated by inappropriately-fit galaxies (i.e. dissonance between model and stellar structures).

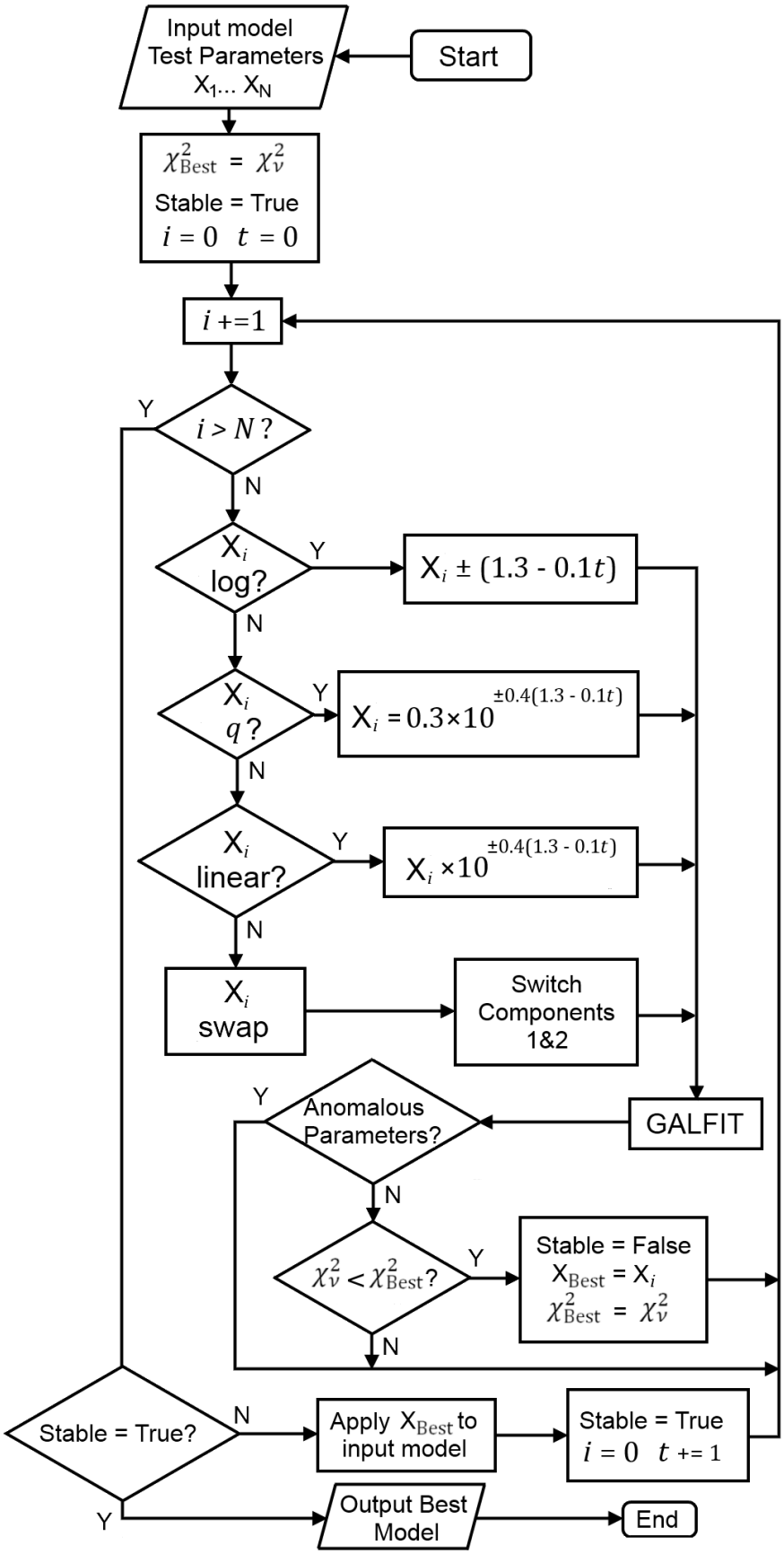

Figure 3.2: Flow chart: Reduction loop for a specified series of model parameters (X_1, X_2,..., X_N) to be varied. Variations are dependent on parameter type (e.g. logarithmic, linear, or ratio), and cycle number, t.

Parameter	Value
Total magnitude, m	10.0
Effective radius, R_e	24.0 pix
Sérsic index, n	4.0
Axis ratio, q	0.5
Position angle, PA	60.0°

Table 3.1: The initial fitting parameters used for a one component (Sérsic) galaxy model. Note that the pixel scale for all MegaCam images was 0.186 arcseconds/pixel.

AGONII's fitting extension (see Figures 3.1 and 3.2) is implemented by perturbing the GALFIT model parameters from their apparent best-fit positions and re-fitting. A large perturbation (a $3\times$ increase/decrease) will shift GALFIT out of any local minimum in χ^2_ν-space, thus improving the true global minimum detection rate. Extended fitting is carried out in cycles in which each parameter[1] is varied twice (increased/decreased) until a stable χ^2_ν minimum solution is found. In this context, 'stable' means that no improvement in χ^2_ν was found over an entire cycle. To avoid repeatedly testing the same parameter values from cycle to cycle, the magnitude of the variation decreases with cycle number.

In order to acquire realistic starting values for our fit parameters, model complexity is built up over subsequent stages of the analysis. Initially, a single Sérsic model is exhaustively fit to the galaxy using generic initial parameter values (see Table 3.1). The choice of these starting values has no effect on the final two-component results due to the low level of degeneracy and scatter in a single-component fit. The resulting best-fit is then used as the basis for the 2-component fit initial conditions: the Sérsic component is duplicated (increasing both components' magnitudes accordingly), and the Sérsic indices of the new 'bulge' and 'disk' are fixed at $n = 4$ and $n = 1$ respectively. GALFIT is run again for this input (Sérsic + exponential) model, and the resulting fit parameters are used as the initial values for exhaustive two-component fitting.

The influence of unrealistic models can be mitigated through use of fitting constraints to set upper and lower limits to the acceptable parameter values. Excessive use of constraints can introduce model biases, however, by limiting GALFIT's search of the parameter space, and thus preventing the true best-fit model from being found. In this study, constraints are

[1]Excluding Sérsic index due to covariance with R_e, and component PA, which is well determined without fitting extension.

Parameter	Constraint	Notes
x ordinates ($x_{\rm B}, x_{\rm D}$)	$x_{\rm B} = x_{\rm D}$	Component centres fixed
y ordinates ($y_{\rm B}, y_{\rm D}$)	$y_{\rm B} = y_{\rm D}$	〃
Bulge Sérsic index (n)	$0.15 < n < 10.0$	$\kappa(n < 0.15)$ poorly-defined
Bulge magnitude ($m_{\rm B}$)	$-100 < m_{\rm B} < 100$	Extreme value limits
Disk magnitude ($m_{\rm D}$)	$-100 < m_{\rm D} < 100$	〃
Bulge effective radius (R_e)	$1 < R_e < 500$ pix	Lower limit $\ll$ resolution,
Disk scale length (R_s)	$1 < R_s < 500$ pix	upper limit $\gg$ thumbnail
Disk axis ratio ($q_{\rm D}$)	$0.05 < q_{\rm D} < 1.0$	Model quantised if $q < 0.05$
Bulge axis ratio ($q_{\rm B}$)	$0.1 < q_{\rm B} < 1.0$	$> q_{\rm D}$ to deter BD swap
Position angles ($\rm PA_B$,$\rm PA_D$)	$-180^\circ < \rm PA < 180^\circ$	Extreme value limits

Table 3.2: The fitting constraints for a two component (Sérsic bulge + exponential disk) galaxy model. κ refers to the dimensionless normalisation parameter in the Sérsic profile (see Section 1.4). Note that the pixel scale for all MegaCam images was 0.186 arcseconds/pixel.

only used to provide extreme limits to model parameters (see Table 3.2). This minimally-constrained approach reduces the likelihood of parameter underflow errors[2] or unreasonable parameter values. By placing limits significantly in excess of the expected range of parameter values (e.g. $n \geq 0.15$ rather than $n \geq 1$), these constraints will not artificially restrict GALFIT's search through parameter space. In addition, a thorough *a posteriori* sample filter (as described in Section 3.5) is utilised to test applicability of the imposed (bulge + disk) model, thus ensuring reliable fitting results.

3.3 Fit parameter uncertainty

The statistical uncertainties associated with the fit parameters were estimated through the Monte Carlo fitting of synthetic model galaxies. Model Sérsic, and 2-component (bulge + disk) galaxies were generated external to GALFIT using the analytical forms of the Sérsic and exponential disk models (Equations 1.3 & 1.4), and convolved with a typical MegaCam psf. These noiseless models were then Poisson resampled to simulate photon noise, including treatments of sky RMS and CCD gain using values typical for the MegaCam imaging. This was repeated to produce 100 Monte Carlo realisations of each underlying model. AGONII's fitting analysis routine (see Section 3.2) was carried out for these model galaxies, the results of which were used to measure the uncertainty in each parameter value: The measurement scatter, $\sigma_{\rm s}$, was found from the ensemble standard deviation in parameter values, and the

[2]Wherein GALFIT iterates a parameter value below zero during fitting, yielding a non-physically large value.

Parameter	A	B	α	β	γ	Type
$M_{\rm S,s}$	0.0	+1	-1.202	0.0	$8.389\mathrm{E}-1$	Pow
$M_{\rm S,o}$	0.0	+1	-0.913	0.0	$7.104\mathrm{E}-1$	Pow
$R_{\rm e,S}$	0.0	+1	-1.126	0.0	$8.580\mathrm{E}-1$	Pow
$n_{\rm S,s}$	0.0	+1	-1.020	0.0	$4.397\mathrm{E}-1$	Pow
$q_{\rm S,s}$	0.0	+1	-1.092	0.0	$3.577\mathrm{E}-1$	Pow
$M_{\rm B,s}$	0.0	+1	-1.260	-1.012	1.392	Pow
$M_{\rm B,o}$	0.0	+1	-0.211	$-7.770\mathrm{E}-1$	-1.293	Pow
$R_{\rm e,B,s}$	0.0	+1	-1.316	-1.081	1.631	Pow
$n_{\rm B,s}$	0.0	+1	-1.059	$-9.961\mathrm{E}-1$	$7.429\mathrm{E}-1$	Pow
$q_{\rm B,s}$	0.0	+1	$-9.685\mathrm{E}-1$	$-9.353\mathrm{E}-1$	$2.237\mathrm{E}-1$	Pow
$M_{\rm D,s}$	0.0	+1	-1.074	$9.198\mathrm{E}-1$	$5.961\mathrm{E}-1$	Mix
$M_{\rm D,o,}u$	$-9.7\mathrm{E}-3$	+1	$-9.943\mathrm{E}-1$	$-5.152\mathrm{E}-1$	$7.902\mathrm{E}-1$	Mix
$M_{\rm D,o,}g$	$3.4\mathrm{E}-3$	-1	$-4.105\mathrm{E}-2$	$9.262\mathrm{E}-1$	-2.301	Mix
$M_{\rm D,o,}i$	0.0	-1	$-6.163\mathrm{E}-5$	1.261	-2.593	Exp
$R_{\rm s,D}$	0.0	+1	-1.143	$8.525\mathrm{E}-1$	$5.587\mathrm{E}-1$	Mix
$q_{\rm D}$	0.0	+1	-1.142	$7.912\mathrm{E}-1$	$6.958\mathrm{E}-1$	Mix

Table 3.3: Definition of the equations determined for the random scatter (subscript 's') and systematic offsets (subscript 'o') in parameter values for pure Sérsic (subscript 'S'), Sérsic bulge (subscript 'B'), and exponential disk (subscript 'D') components. Equation types are pure power law ('Pow'; $A + B(10^{\gamma}(\mathrm{S/N})^{\alpha}(\mathrm{B/T})^{\beta})$), pure exponential ('Exp'; $A + B10^{(\alpha(\mathrm{S/N})+\beta(\mathrm{B/T})+\gamma)}$), and mixed power law/exponential ('Mix'; $A + B((\mathrm{S/N})^{\alpha}10^{(\beta(\mathrm{B/T})+\gamma)})$). Uncertainties and offsets do not vary from band to band except as noted for $M_{\rm D}$.

systematic offset, $\sigma_{\rm o}$, was calculated from the difference between the ensemble average parameter value and the true input value.

To characterise the variation of parameter uncertainty with S/N, this Monte Carlo process was carried out for models with seven values of total magnitude (used as a simple proxy for total S/N). Parameter uncertainties for model components are dependent on their component magnitudes (i.e. the S/N when that component is considered in isolation). Thus, five different values for B/T are also considered for the Monte Carlo models. Linear regression was used to obtain expressions for each parameter's $\sigma_{\rm s}$ and $\sigma_{\rm o}$ as power-law or exponential functions of galaxy S/N (as measured within the target ellipse, see Section 2.3) and model B/T. These expressions are summarised in Table 3.3 for component magnitudes, effective radii, axis ratios, and Sérsic indices (where appropriate). Note that no significant variation in the functional forms of these expressions was noted between photometric bands, with the exception of disk magnitude offset. Corrections applied to the measured component photometry to account for systematic fitting bias was no more than ± 0.02 mag in most cases. These

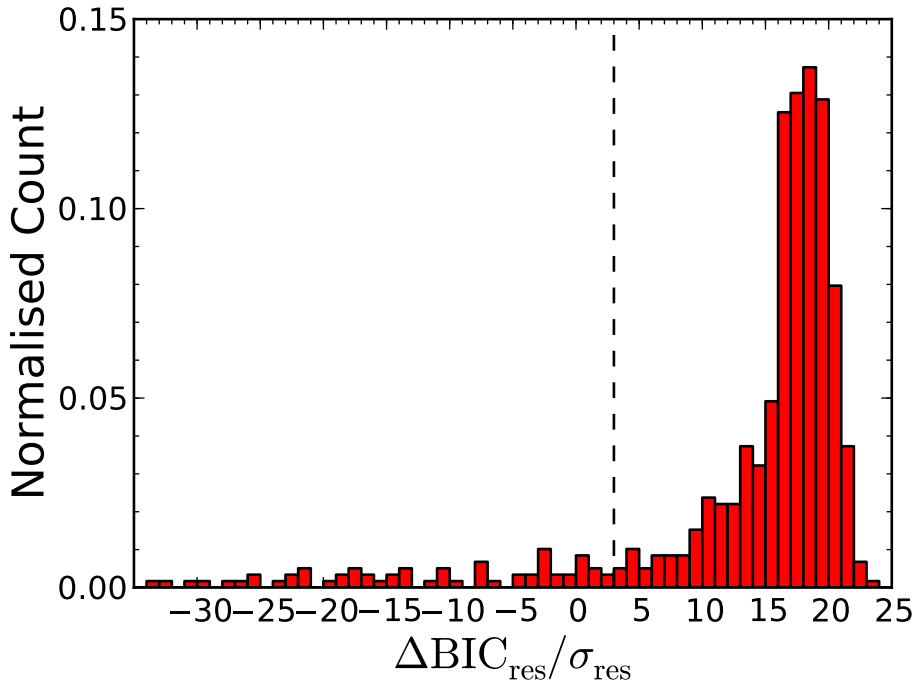

Figure 3.3: Distribution of $\Delta\mathrm{BIC}_{\mathrm{res}}$ (for comparison between Sérsic-only and Sérsic + disk models) plotted in bins of width σ_{res}, and normalised to the total Coma sample size ($N = 570$). A dashed line is given at the $3\sigma_{\mathrm{res}}$, below which the Sérsic-only model is preferred.

uncertainties are the minimum value for the error on a measured parameter value, under the assumption that the galaxy is perfectly represented by the fitting model.

While the fitting remains robust for thumbnails with low S/N ($m_g \sim 17$; S/N ~ 300), the uncertainty associated with bulge component photometry increases exponentially for low B/T galaxies. At B/T = 0.1, the bulge of a faint galaxy can only be measured to ± 0.1 magnitudes. Below B/T = 0.1, therefore, only a single (disk) component can be reliably fit. Similarly, disk magnitude measurement is limited (uncertainty > 0.1 mag) above B/T = 0.9.

3.4 Bayesian Model Selection

An important consideration for any study involving the fitting of multiple candidate models is the selection of a 'best fit' model. For example, pure Sérsic systems can be erroneously classified as possessing a disk due to weak ripples in their surface brightness profiles. Thus, it is necessary to apply a statistical test to identify true 2-component galaxies (e.g. an F-test, as performed by Simard et al., 2011). In this thesis, I use the Bayesian Information Criterion (BIC, Schwarz, 1978) to remove galaxies which would be overfit by a 2-component (Sérsic +

exponential) model. BIC modifies the standard χ^2 assessment of goodness-of-fit to penalise the addition of unnecessary free parameters. Thus, this statistic can be used to identify galaxies for which the addition of a (disk) component does not significantly improve the model fit. The general form of BIC is

$$\mathrm{BIC} = \chi^2 + k \cdot \ln(n) \tag{3.1}$$

where k is the number of model free parameters, and n is the number of independent data points. When comparing two fitting models, A and B, the fit which results in the lowest BIC is considered the preferred model. Thus, if $\Delta\mathrm{BIC} = \mathrm{BIC_A} - \mathrm{BIC_B} > 0$, model B provides a better fit than model A, regardless of any difference in number of free parameters.

A BIC test is selected over the similar Akaike Information Criterion (AIC, Akaike, 1974) as it more strongly penalises unnecessary model parameters. Thus, the BIC is a more thorough statistic for the identification of overfit models (e.g. bulge + disk fits to 1-component galaxies). As this work aims to provide a clean sample of 2-component galaxies, 'false-negative' detections of overfitting (i.e. 2-component galaxies categorised as 1-component) is preferable to 'false positive' detections (i.e. 1-component galaxies categorised as 2-component). Furthermore, in contrast to an F-test, the BIC allows 'non-nested' model comparison even where simpler models *cannot* be expressed in the form of more complex models (i.e. comparison of boxy Sérsic and Sérsic + exponential models).

Independence of data points is a key assumption of the BIC, however the individual pixels in the image thumbnails cannot be considered statistically independent. Instead, model selection must be evaluated from all independent *resolution* elements. Following the prescription of Simard et al. (2011), the number of pixels, n_{pix}, in Equation 3.1 is substituted for the number of resolution elements, $n_{\mathrm{res}} = n_{\mathrm{pix}}/N_{\mathrm{psf}}$, where N_{psf} is the size of the resolution element in pixels. As a practical method of determining the resolution element size, N_{psf} is calculated as the area within the psf half-width at half maximum (fwhm/2, as determined via fitting).

For consistency, the fitting χ^2 must also be evaluated across independent resolution elements. However, the identification of which pixels contribute to each resolution element is non-trivial. Instead, we approximate the resolution-chi-squared as, $\chi^2_{\mathrm{res}} \approx \chi^2_{\mathrm{pix}}/N_{\mathrm{psf}}$. This

approach is equivalent to evaluation of $\chi^2_{\rm res}$ via summation of the *average contributions* to χ^2 of each resolution element. The resolution-modified BIC, $\mathrm{BIC_{res}}$, is thus:

$$\mathrm{BIC_{res}} = \frac{\chi^2}{N_{\rm psf}} + k \cdot \ln\left(\frac{n_{\rm pix}}{N_{\rm psf}}\right). \tag{3.2}$$

Since measurement of $N_{\rm psf}$ has an associated error ($\lesssim 1\%$, determined from the individual star images used to produce the master psf), the use of $\mathrm{BIC_{res}}$ introduces uncertainty to the value of $\Delta\mathrm{BIC}$. This error, $\sigma_{\rm res}$, is estimated via Monte Carlo simulation. Thus, when comparing models we select the simpler model unless $\Delta\mathrm{BIC_{res}} > 3\sigma_{\rm res}$. This is illustrated in Figure 3.3, where the distribution of $\Delta\mathrm{BIC_{res}}$ is plotted in $\sigma_{\rm res}$ bins. The majority of galaxies possess a $\Delta\mathrm{BIC_{res}}$ significantly higher than 0, with a long tail towards negative values. Setting the acceptance limit for 2-component galaxies at $3\sigma_{\rm res}$ thus only affects a small minority of galaxies, but ensures an analysis sample uncontaminated by misclassified 1-component galaxies.

Model selection tests via $\mathrm{BIC_{res}}$ and pixel-wise BIC ($\mathrm{BIC_{pix}}$; i.e. Equation 3.1) were compared to visual model selection via inspection of 1D surface brightness profiles. For the majority ($\sim 83\%$) of (uncontaminated, symmetric) galaxies, all three tests select the same 'best-fit' model (e.g. upper panel of Figure 3.4). Where the test results *do not* agree, $\mathrm{BIC_{pix}}$ selects models which are overfit (relative to the visually-selected 'best-fit'; e.g. middle panel of Figure 3.4), while $\mathrm{BIC_{res}}$ selects an underfit model ($\sim 10\%$ and $\sim 3\%$ of cases respectively; e.g. lower panel of Figure 3.4). The remaining $\sim 4\%$ of cases are ambiguous.

As identification of a clean sample of well-fit 2-component (bulge + disk) galaxies is the primary goal of model selection in this work, the incorrect rejection of a small number of bulge + disk galaxies is preferable to contamination by overfit 1-component galaxies. Thus, I use $\mathrm{BIC_{res}}$ to distinguish between the goodness-of-fit of the Sérsic ($k = 7$), Sérsic + exponential ($k = 11$), and and boxy Sérsic ($k = 8$) models in this work.

A 1D BIC test is also used during multi-band fitting to select between component gradient models (see Section 3.7). Radial colour profiles (for the image and models) are measured in elliptical annuli (in the u and i bands) within the unmasked target ellipse. BIC is evaluated as per Equation 3.1, where n is the number of annuli, for $k = 8$ (no gradient), $k = 10$ ($\times 2$; disk or bulge gradient), and $k = 12$ (bulge and disk gradients).

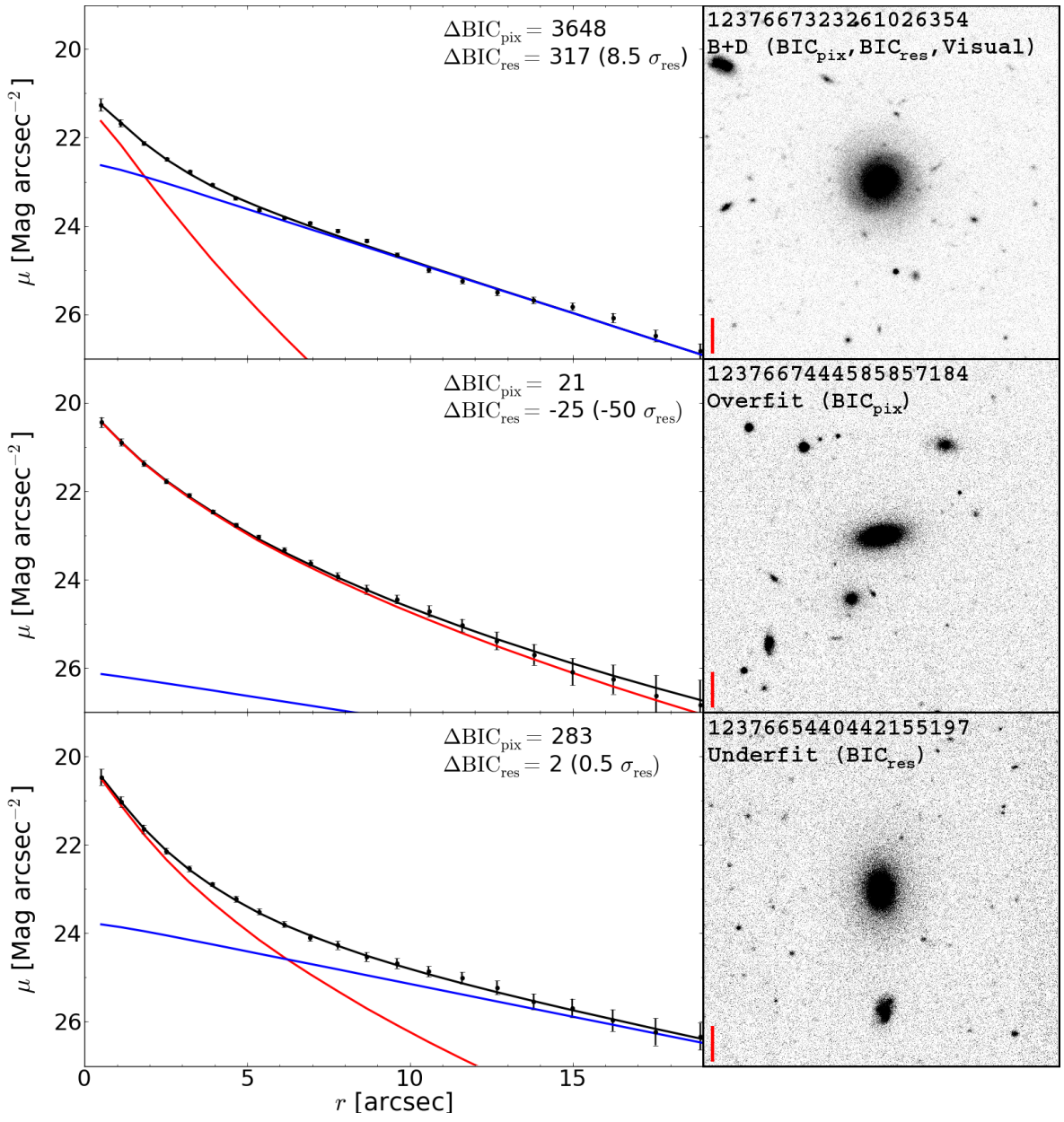

Figure 3.4: 1D surface brightness profiles and galaxy thumbnails (both g band) for three example galaxies. **Upper:** SDSS DR8 ObjID 1237667323261026354, for which $\mathrm{BIC_{res}}$, $\mathrm{BIC_{pix}}$, and visual classification all select a 2-component best fit. **Middle:** SDSS DR8 ObjID 1237667444585857184, incorrectly assigned a 2-component best fit by $\mathrm{BIC_{pix}}$ (overfit). **Lower:** SDSS DR8 ObjID 1237665440442155197, incorrectly assigned a 1-component best fit by $\mathrm{BIC_{res}}$ (underfit). Black data points indicate the galaxy surface brightnesses measured in elliptical annuli. The bulge/disk/total model surface brightnesses from the best 2-component fit are included as red/blue/black lines respectively. Values for $\Delta\mathrm{BIC_{pix}}$ and $\Delta\mathrm{BIC_{res}}$ (Sérsic model − Sérsic + exponential model) are indicated for each example. A red scale bar corresponding to $10''$ ($\equiv 4.8$ kpc) is displayed in each thumbnail.

3.5 Sample Filtering

The aim of this study is to characterise the photometric and structural properties of the bulges and disks of ETGs. The Coma sample (as defined in Section 2), however, contains many galaxies that are poorly described by an archetypal (centrally bulge-dominated, disk-dominated at large radii) *S0* morphology. It is necessary, therefore, to identify a sub-sample of galaxies which are well-fit by 2-component (Sérsic + exponential) models to ensure the applicability of a 'bulge + disk' interpretation.

A suitable sample of archetypal *S*0 models were selected for analysis via an *a posteriori* sample filter applied to the 2-component fitting results. This process involves a series of parameter cuts, and statistical tests which are described in detail in the following section. The overall filter is illustrated graphically in Figure 3.6, and the resulting filtered subsamples are described in Section 3.6.

3.5.1 Badly-fit galaxies

Asymmetric, contaminated, or poorly-fit galaxies (i.e. high χ^2) were removed from the sample. This includes cases where galaxy crowding (prominent towards the cluster core) would require additional deblending steps to accurately model. These fits do not yield reliable model parameters, and therefore cannot be considered accurate representations of the underlying galaxy structures. Hence, we remove any 2-component model fits with $\chi^2_\nu \geq 1.7$ as unstable. This cut was calibrated on visual inspection of fit residuals. However, galaxies with significant contamination or strong asymmetrical features may yield artificially low values of χ^2 (e.g. due to overzealous masking). Therefore, an upper limit to permitted values of χ^2 is insufficient to selectively remove all unstable galaxies.

Contamination of the galaxy thumbnails was parametrised via the fraction of masked pixels (due to `SExtractor`-detected sources; see Section 2.4), $f_{\rm mask}$. For an ellipse with semi-major axis, a, and axis ratio, q, this masked fraction is calculated as,

$$f_{\rm mask}(a,q) = \frac{n_{\rm mask}(a,q)}{n_{\rm pix}(a,q)}, \tag{3.3}$$

where $n_{\rm pix}$ is the total number of pixels contained in the ellipse, and $n_{\rm mask}$ is the number of

masked pixels. If the fraction of masked pixels within the target ellipse (see Section 2.4), $f_{\rm mask}(a_{\rm target}, q_{\rm target}) \geq 0.4$, then the thumbnail is considered contaminated. Additionally, since contamination at small galaxy-centric radii is more disruptive to fitting, galaxies are also removed as contaminated if the fraction within the inner quarter of the target ellipse, $f_{\rm mask}(a_{\rm target}/2, q_{\rm target}) \geq 0.3$.

Thumbnails were tested for asymmetric features using the asymmetry parameter, A (Homeier et al., 2006). A is defined as

$$A = \frac{1}{2}\left[\Sigma(|I - I_{180}|) - B_{\rm corr}\right]\frac{1}{I_t}, \tag{3.4}$$

where I is the flux in a particular pixel, I_{180} is the flux in the same pixel after rotating the image by 180° around the galaxy centre, and I_t is the sum of flux in all pixels. $B_{\rm corr}$ is a correction for uncorrelated noise (equivalent to calculating $\Sigma(|I - I_{180}|)$ for a empty region of sky). If a galaxy image has $A > 0.2$ (as calculated in the *unmasked* target ellipse), then it is removed from analysis as unstable. The galaxy is also removed if the asymmetry calculated for the Sérsic + exponential model-subtracted residual, $A_{\rm res} > 0.3$.

3.5.2 Single component galaxies

Galaxies best fit by a single-component model were excluded. These Sérsic-only galaxies were identified where the addition of the exponential disk component provided no significant improvement to the model fit. The comparative goodness-of-fit of the models was assessed using the Bayesian Information Criterion (see Section 3.4). Furthermore, model fits which yielded extreme values of B/T were considered indistinguishable from pure Sérsic systems due to high fitting parameter uncertainty ($> 10\%$) in components contributing $\leq 10\%$ of the total galaxy luminosity (i.e. B/T > 0.9 or B/T < 0.1).

3.5.3 Surface brightness profiles

Surface brightness profile types (see Section 1.4) were used to separate archetypal *S0* galaxies (Type 1; i.e. inner bulge, outer disk) from those with all other (atypical) morphologies. These surface brightness profiles were calculated analytically in the g band out to the edge

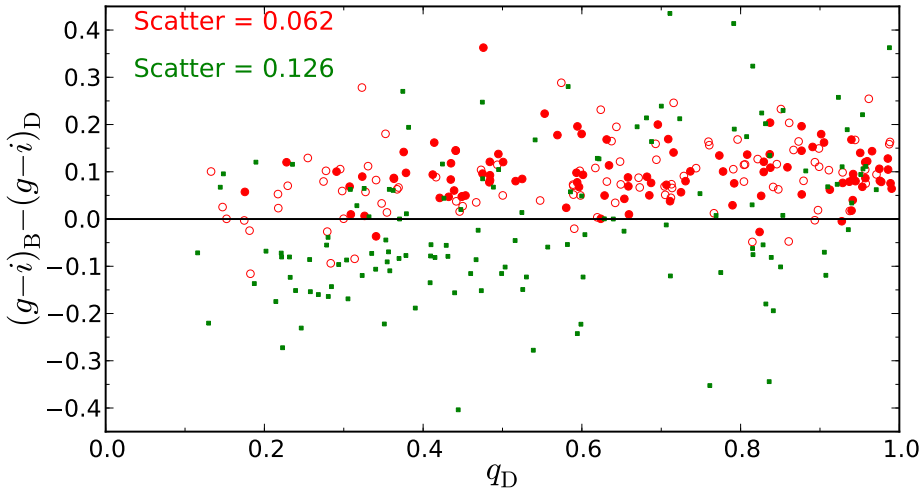

Figure 3.5: The measured $g-i$ colour separation (bulge - disk) of two component model fits plotted against the axis ratio of the disk component ($q_{\rm D}$). 'Archetypal' (Type 1) bulge + disk systems are plotted as red circles (unfilled circles indicate less reliable fits), while all other profile types (2, 3, 4, 5 and 6) are plotted as green squares. A line at $(g-i)_{\rm bulge} = (g-i)_{\rm disk}$ is plotted for clarity.

of the target ellipse (see Section 2.4).

Profile Types 4 (exponential-dominated at small radii, Sérsic-dominated at large radii) and 6 (exponential-dominated at small *and* large radii, Sérsic-dominated at intermediate radii) are inappropriate for a 'bulge + disk' interpretation and are removed from the sample. As these profiles are centrally disk-dominated, such models may result from artificial swapping of the 'bulge' and 'disk' roles of the Sérsic and exponential components. It is possible to recover a fraction of the inverted fits by manually swapping the parameter values of each component and re-fitting. When the re-fitted model yields a Type 1 profile, that galaxy is returned to the analysis sample. However, as a forced parameter swap may result in a higher value of χ^2_ν ($\lesssim 0.01$), galaxies recovered in this way are flagged as potentially unreliable. Such galaxies may be better fit by a double Sérsic model.

Profile Types 2 (exponential-dominated at all radii), 3 (Sérsic-dominated at small *and* large radii, exponential-dominated at intermediate radii), and 5 (Sérsic-dominated at all radii) can be considered as 'bulge + disk' systems, however, galaxies with these types are not archetypal *S0*s (i.e. non-central bulges and/or non-outer disks), and hence are removed from the sample. While genuine galaxies with sub-dominant disks (Types 3 and 5) exist within the Coma sample, fits of these types can also result from the underfitting of more complex morphologies (e.g. barred or ring galaxies). Including underfit models would render a pho-

tometric analysis unreliable, as measured photometry would not necessarily cleanly probe the intended structures. An example of this issue is displayed in Figure 3.5, which shows bulge - disk ($g - i$) colour separation as a function of the apparent disk model axial ratio. While the majority of model bulges are ~ 0.1 mag redder than their disks, a subsample of (predominantly Type 3 and Type 5) models have high ellipticity disks ~ 0.1 mag redder than their bulges. Here, the exponential components are following bar structures, while large-n Sérsic components account for both the bulge and the outer disk. The introduction of a second Sérsic component to account for a bar corrects the photometric swap of the bulge and disk. This issue is investigated in detail in Chapters 7 and 8.

3.5.4 Blue core galaxies

Galaxies were removed from the sample based on their radial colour profiles, as measured for use during multi-band fitting (see Section 3.7.2). A two-component model is insufficient to reproduce a galaxy colour profile which includes a significant downturn towards bluer colours in the core. Thus, if the innermost colour data point (as measured from the galaxy thumbnails) is more than 0.01 mag bluer than the adjacent measurement, that galaxy is considered unsuitable for bulge-disk decomposition analysis.

3.5.5 Flagged sample

A fraction of archetypal galaxies were highlighted as stable but lower-quality fits. Although selecting galaxies with Type 1 model profiles ensures that the Sérsic and exponential components measure inner and outer structures respectively, bars can still distort the photometry of the Sérsic component: Models in which the Sérsic component follows a bar rather than the bulge are also identified by flagging 'bulges' with low Sérsic indices ($n < 1.0$). Bar-like disks are flagged if the exponential component is smaller ($R_{e,D}/R_{e,B} > 0.8$) and narrower ($q_D < q_D$) than the Sérsic component. A large PA misalignment between the two model components ($|\mathrm{PA_D} - \mathrm{PA_B}| > 45°$) also indicates a bar-like structure, so such galaxies are flagged unless one or both components are circular ($q > 0.9$). Furthermore, a cut at $\chi^2_\nu > 1.2$ is used to flag fits which suggest the presence of additional (unfit) structural components which would distort interpretation of bulge and disk component colours.

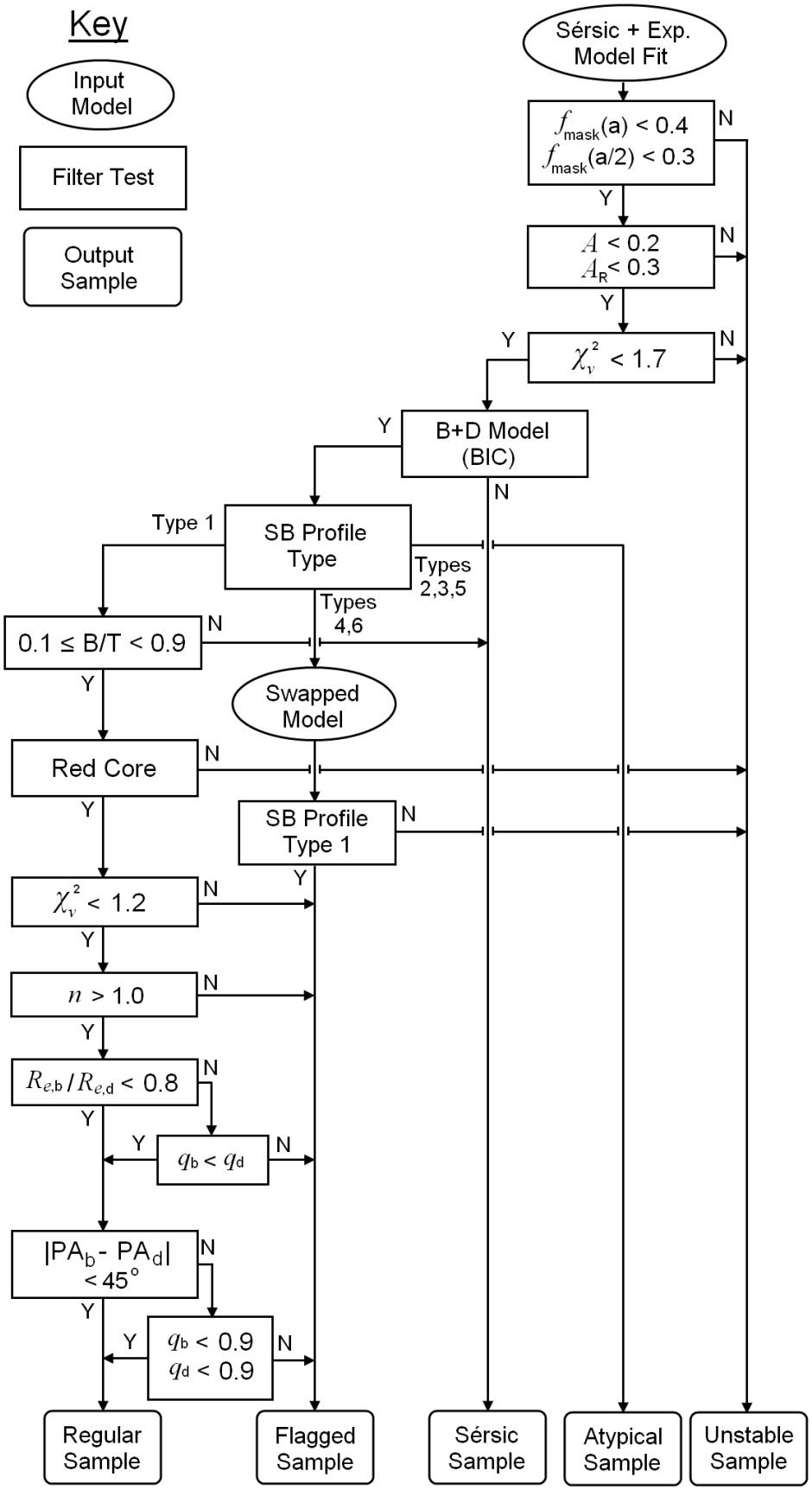

Figure 3.6: Flow chart for sample filtering following Sérsic + exponential fitting. For profile type definitions, refer to Section 1.4 and Allen et al. (2006).

3.5.6 Overview of sample filtering

To summarise, the results of bulge-disk decomposition are filtered to select a sub-sample of well-fit, archetypal 2-component galaxies from which bulge and disk properties can be measured reliably. Galaxies with high χ^2_ν , asymmetry, or contamination are removed as poorly-fit (hereafter 'unstable sample'). Pure Sérsic galaxies are identified and removed where one component is either not a significant improvement to the model, or has significant parameter uncertainty (hereafter 'Sérsic sample'). The remaining galaxies are all well-fit 2-component systems (hereafter 'stable sample'). However, 2-component models which do not exhibit 'central bulge + outer disk' surface brightness profiles (hereafter 'atypical sample') are not representative of *S0* morphologies, and are also removed. The remaining galaxies (hereafter 'archetypal sample') are subdivided into high and moderate-quality fits (hereafter 'regular sample' and 'flagged sample' respectively). The latter category includes galaxies with weak indications of additional components (e.g. bars), and fits which require manual adjustment to produce archetypal profiles.

3.6 Filtering Results

Galaxies are assigned to different subsamples depending on when and how each galaxy was removed from the filtering process. In this section, I describe the properties and statistics of the resulting filtered samples in detail. The samples are presented graphically in Figure 3.7, and summarised in Table 3.4.

From the 570 galaxies initially contained in the Coma sample (see Section 2.3), 127 (22%) galaxies are classified as unstable fits, having no adequate Sérsic-only or Sérsic + disk model solution. These fits are distorted by the presence of additional strong and/or elliptically asymmetric structures (e.g. spiral patterns, isophotal twists, peanut-shaped bulges), or possess colour profiles with blue cores. Contamination of the galaxy images by neighbouring stars, galaxies, or dust is also a contributing factor. Additionally, the fitting accuracy is very limited for the minority of galaxies with highly-inclined (edge-on) disks. In such cases, the infinitely thin exponential profile is a poor representation of a true structure of the disk.

A further 106 (19%) are identified as having no significant disk component. While the

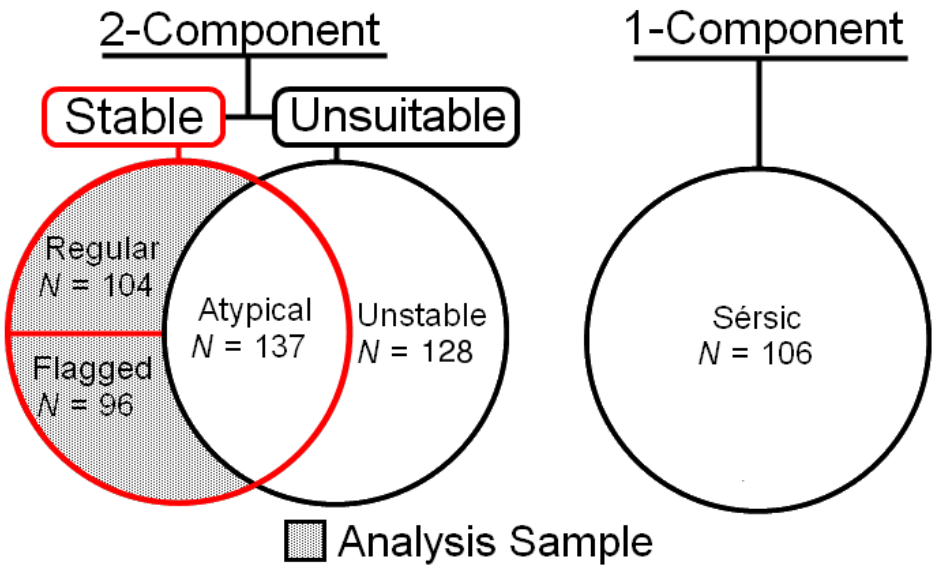

Figure 3.7: Venn diagram describing the main filtering samples and sub-samples (see Table 3.4) for galaxies best fit by Sérsic + disk or Sérsic-only models.

majority of these galaxies can be considered pure Sérsic systems, six are best represented by a boxy Sérsic profile. These boxy structures imply an underlying triaxial 3D galaxy shape.

The remaining 337 galaxies (59%) are better fit by two-component models. Of these, 137 (24%) possess an atypical *S0* surface brightness profile type (Types 2, 3, 4, 5 or 6; see Sections 1.4 & 3.5). As the Sérsic and exponential components of atypical fits cannot be reliably interpreted as bulge and disk structures, these galaxies are not considered for further analysis.

200 galaxies (35%) are found to be well-fit by an archetypal (bulge + disk) model. Of these, 96 (17%) are flagged as potentially unreliable fits due to the presence of (weak) additional structures (hereafter 'flagged sample'), but are not removed from the analysis sample. 12 galaxies are included in the analysis sample due to forcibly inverting a Type 4 model. As such inversions are only necessary when the corresponding Type 1 model yields a slightly higher χ^2_ν ($\lesssim 0.02$), these galaxies are also flagged. The remaining 104 (18%) galaxies are considered good fits which robustly represent the underlying stellar structures. Example galaxy (g band) thumbnails for each subsample are presented in Figures 3.8 and 3.9.

The global (bulge + disk) colour-magnitude properties of the 'Sérsic', 'unstable', 'atypical', and 'archetypal' filtering samples are presented in Figure 3.10. 'Regular' and 'flagged' subsample galaxies are plotted in the lower panel as filled and unfilled points (respectively) to highlight the results of lower-quality fits.

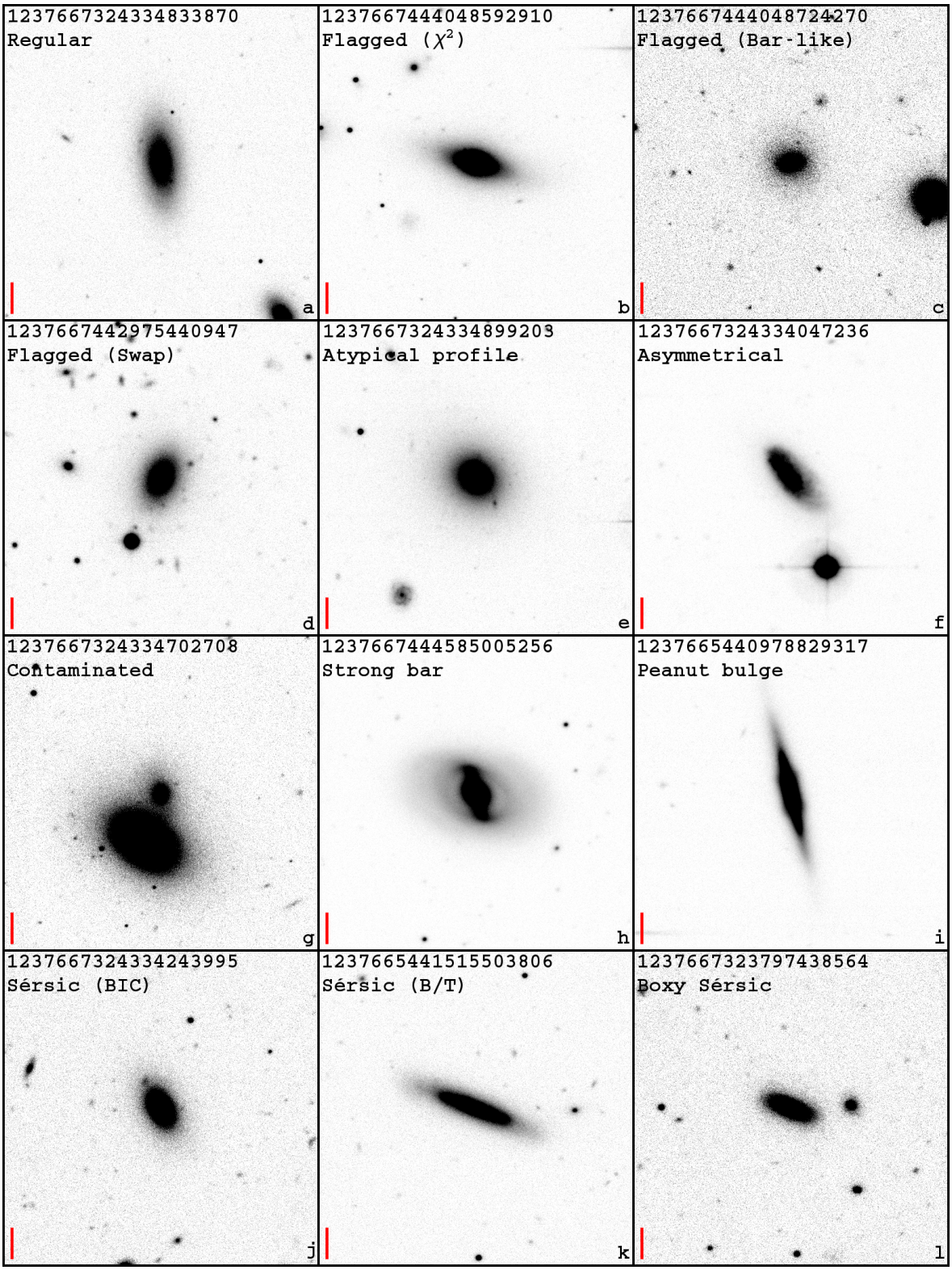

Figure 3.8: Example (g band) thumbnail images of galaxies illustrating the filter subsamples described in Table 3.4. Each thumbnail includes the SDSS (DR8) ObjID of the example galaxy, and a red scale bar corresponding to $10''$ ($\equiv 4.8$ kpc).

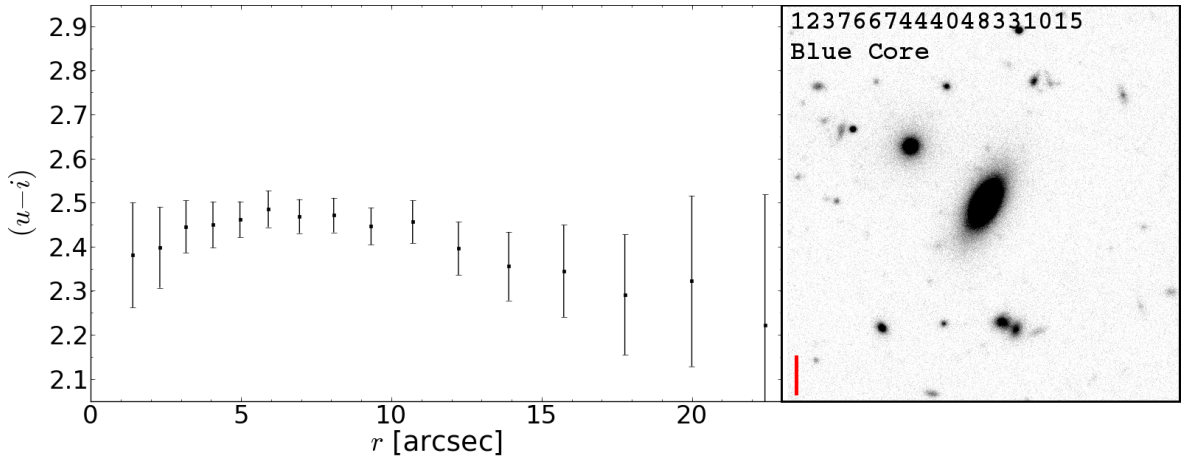

Figure 3.9: Example (g band) thumbnail and radial ($u - i$) colour data (as measured in elliptical annuli) for a 'blue core' galaxy (SDSS DR8 ObjID 1237667444048331015). A red scale bar corresponding to $10''$ ($\equiv 4.8$ kpc) is included in the thumbnail.

Sample	Subsample	Fig.	N
Initial	All Galaxies Fitted		570 (100%)
Analysis	Regular Fit	3.8a	104 (18.2%)
Sample	Flagged (High χ^2)	3.8b	52 (9.1%)
$N = 200$	Flagged (Bar Component)	3.8c	33 (5.8%)
(35.1%)	Flagged (Swapped Profile)	3.8d	11 (1.9%)
	Atypical Profile	3.8e	137 (24.0%)
Unsuitable	Asymm./Spiral/Dust Struct.	3.8f	55 (9.6%)
B+D Fits	Contaminated/Defective	3.8g	23 (4.0%)
$N = 264$	Bar/Twist/Edge-on	3.8h	17 (3.0%)
(46.3%)	Ring/Peanut Structure	3.8i	16 (2.8%)
	Blue Core Col. Profile	3.9	16 (2.8%)
Sérsic Sample	Sérsic (BIC)	3.8j	88 (15.4%)
$N = 106$	Sérsic (B/T)	3.8k	12 (2.1%)
(18.6%)	Sérsic (Boxy)	3.8l	6 (1.1%)

Table 3.4: The samples (and subsamples) of galaxies resulting from applying the logical filter to the fitting results. The number of galaxies occupying each sample, N, is given along with the percentage fraction of the initial data sample. For each subsample, the corresponding example thumbnail (Figs. 3.8 & 3.9) is indicated.

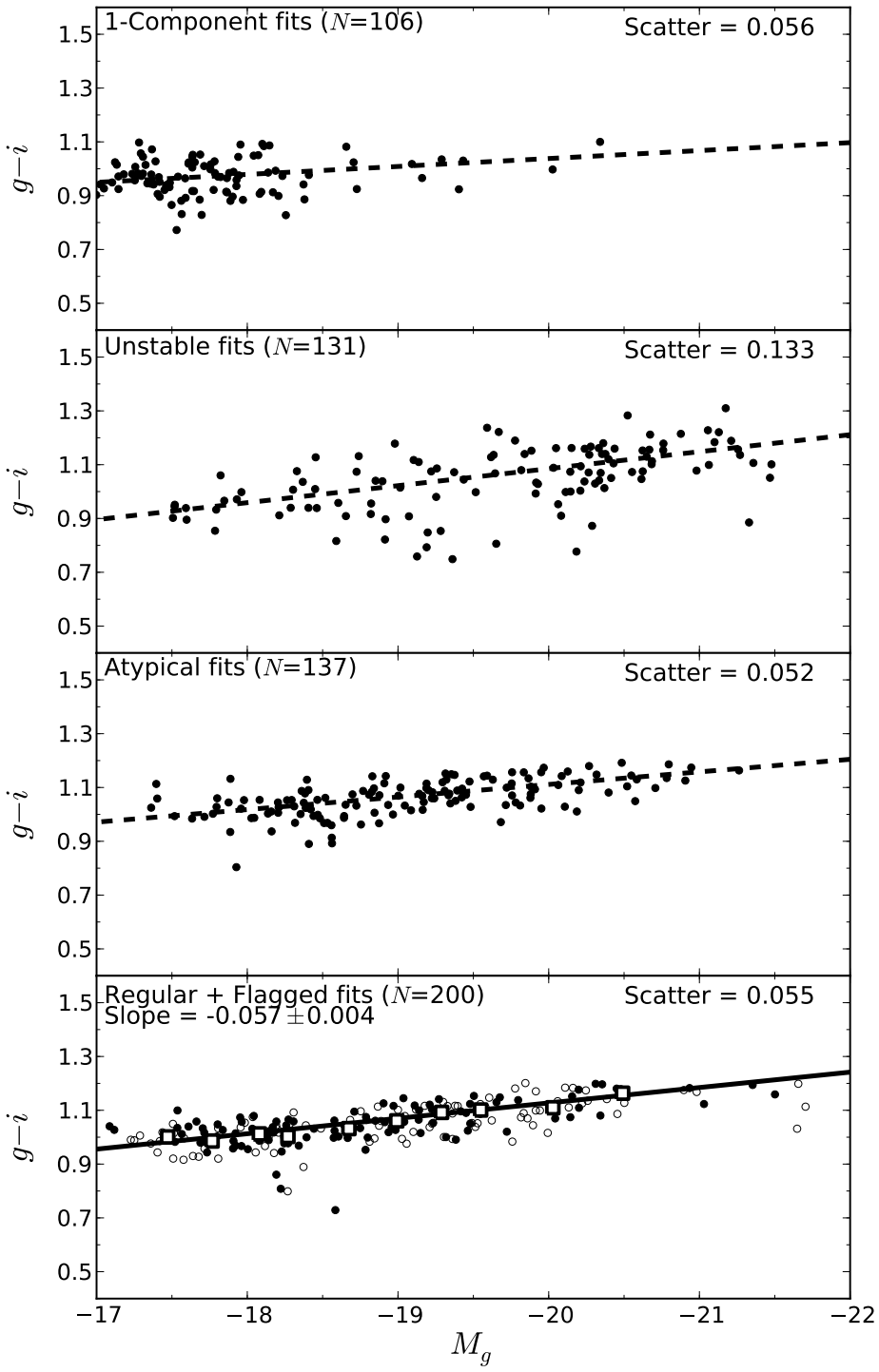

Figure 3.10: The measured (GALFIT) model $g - i$ colours plotted against their absolute (bulge + disk) g band magnitudes. **Top Panel:** Galaxies best fit with a Sérsic-only model. **Upper-middle Panel:** Galaxies with no stable 1 or 2-component fit. **Lower-middle Panel:** 2-component galaxies which do not possess an archetypal central bulge + outer disk morphology. **Bottom Panel:** Regular (filled points) and flagged (unfilled points) fits. The large square points indicate median colour values calculated in magnitude bins, to which a linear trend (solid line) is fitted. The slope uncertainty is calculated from bootstrap fitting the unbinned data. This best fit line is plotted for comparison as a dashed line in the other three panels.

D80 Morph.	No Stable Solution	2-Component Model					Sérsic-only Model	Total
		Type 1	Type 2	Type 3	Type 4	Type 5		
E, *E/S0*	8 12.3%	**20** **30.8%**	-	15 23.1%	-	20 30.8%	2 3.1%	65
S0, *S0/E*, *S0/a*	33 27.5%	**54** **45.0%**	1 0.8%	21 17.5%	2 1.7%	8 6.7%	1 0.8%	120
S, *S/S0*	11 57.9%	**6** **31.6%**	-	-	1 5.3%	-	1 5.3%	19

Table 3.5: The number of unstable, 1-component, and 2-component galaxies (of differing surface brightness profile types) separated by Dressler (1980a) morphological classification. Archetypal *S0* galaxies (central bulge + outer disk) are highlighted in bold.

Galaxies in both the 'regular' and 'flagged' samples follow a common red sequence, with similar scatter in both samples (0.058 mag and 0.054 mag respectively). Atypical galaxies exhibit a consistent red sequence slope and scatter. Thus, while a forced bulge + disk interpretation of atypical galaxies would yield incorrect component photometry, their global properties are consistent with archetypal galaxies. 'Unstable' sample galaxies, by contrast, appear bluer on average (e.g. due to the prevalence of spiral morphologies), and possess a far larger scatter in colour.

Galaxies classified as pure Sérsics ($n = 1.9 \pm 0.1$ on average) are mainly found at $M_g > -18.5$. This result partly reflects the prevalence of *dE* and *dS0* galaxies at the faint end of the magnitude range, as detected in Virgo ($M_g > -18$, Sandage et al., 1985) and Coma ($M_R > -19.5 \approx M_g > -18.5$, Aguerri et al., 2005). Misclassification of faint 2-component galaxies due to the low S/N remains a possibility, however, especially for highly bulge- or disk-dominated galaxies. Nevertheless, the absence of classic (1-component) giant ellipticals supports a multi-component structure paradigm for ellipticals (see e.g. Huang et al., 2013). These additional components are not necessarily classical disks, and may require additional model components to be fully characterised. The scatter of 'Sérsic' sample galaxy colours is similar to the 'archetypal' sample (0.056 mag vs. 0.055 mag).

3.6.1 Morphological fractions

Morphology classifications for Coma cluster galaxies are drawn from the Dressler (1980a) catalogue (hereafter 'D80'). These classifications are based on visual inspection of photometric plates (103a-O emulsion; $10.9''$ mm^{-1} plate scale) taken at the 2.5m du Pont telescope

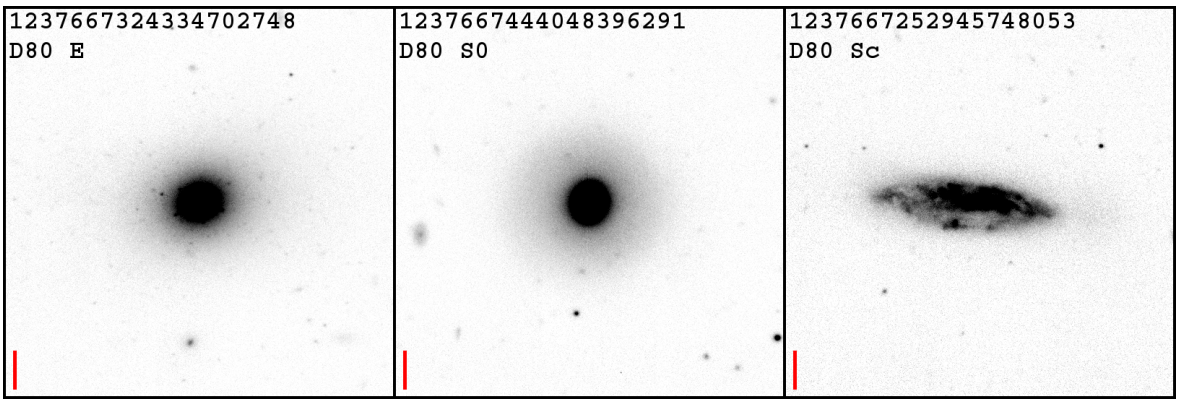

Figure 3.11: Example (g band) thumbnail images for example galaxies illustrating the D80 morphological types. **Left:** Elliptical (*E*); SDSS DR8 ObjID 1237667324334702748 (D80 A1656:143). **Middle:** Lenticular (*S0*); SDSS DR8 ObjID 1237667444048396291 (D80 A1656:163). **Right:** Spiral (*Sc*); SDSS DR8 1237667252945748053 (D80 A1656:247).

(Las Campanas Observatory, Chile). From the 247 galaxies classified in the 2.1 deg^2 D80 Coma field, 204 are present in the initial Coma sample of the present work. Note that nine galaxies from the original D80 catalogue lack SDSS DR9 spectroscopy, 12 are not within the Coma redshift range ($0.015 < z < 0.032$), and 22 are removed due to galaxy colour.

Of the 204 valid D80 galaxies, 65 are classified as *E* or *E/S0*, 120 are classified as *S0*, *S0/E* or *S0/a* (including barred variants), and 19 are classified as *Sa-d* or *S/S0*. A significant second component is found in 55 (85%) of D80 'ellipticals'. 20 (31%) of these 2-component ellipticals are archetypal bulge + disks, while the remaining 35 exhibit atypical structures (54%; Type 5, and some Type 3). 86 D80 '*S0*s' have a second component (72%), of which 53 are archetypal (44%), and 33 are atypical (28%; Type 3, and some Type 5). Only seven (37%) D80 'spirals' have a stable, significant 2-component solution, all but one of which are archetypal bulge-disk systems. If galaxies with unstable fitting solutions are excluded, the fractions of general/archetypal 2-component models increase to 96%/35% for elliptical D80 morphologies, 99%/62% for D80 *S0*s, and 88%/75% for D80 spirals. The morphologies of filtering subsample galaxies are summarised in Table 3.5, and example galaxy thumbnails are presented in Figure 3.11.

3.6.2 Summary of filtering samples

To summarise, a stable fitting solution (either a Sérsic-only or Sérsic + exponential model) is found for 443 of the 570 galaxies in the initial Coma sample. Evidence for a significant

second structural component is found in 76% ($N = 337$) of these galaxies. 'Archetypal' *S0* (central) bulge + (outer) disk structures are found in 59% of 2-component galaxies ($N = 200$). The remaining 41% represent 'atypical' 2-component structural morphologies (e.g. centre-dominating bulges which re-dominate the outer regions, dominant or sub-dominant disks at all radii, or inverted disk-bulge structures). Across the entire Coma sample, stable 2-component structures (of any type) are detected in 59% of galaxies, while 35% correspond to stable, 'archetypal' galaxies.

In the following analysis, we exclude 'unstable' and 'atypical' fits (hereafter 'unsuitable' sample), and the pure Sérsic sample. The remaining 200 'archetypal' Sérsic + exponential galaxies in the 'regular' and 'flagged' samples are described as the 'analysis sample' hereafter.

3.7 Multi-band Fitting

ETGs (particularly ellipticals) are well-known to possess internal radial gradients in colour (e.g. Vader et al., 1988; Franx & Illingworth, 1990). These colour gradients result from variation of stellar population properties; primarily metallicity. Gradients of -0.1 mag dex^{-1} in $B - R$ ($\approx g - i$) and -0.2 mag dex^{-1} in $U - R$ are typical (Wu et al., 2005).

For a 2-component galaxy model, galaxy colour gradients can be interpreted as the transition between inner- and outer-dominating structures with differing component colours. The detection of bluer outer disks than inner bulges thus reflects the typical negative galaxy colour gradients (i.e. bluer with increasing galaxy radius). Alternatively (or in addition), the structural components may possess internal colour gradients due to variation of stellar population properties with galaxy radius.

3.7.1 Fixed Multi-band Fitting

A straightforward method of fitting a galaxy across multiple photometric bands would be to fit each band entirely independently (e.g. Gadotti, 2009). In practice however, model degeneracies often yield inconsistent model structures if the fitting is not appropriately constrained. In order to ensure that the photometry is being measured reliably, consistent structures must

be fit to the galaxy in each band.

The most basic method of implementing multi-band fitting is to adopt a common structure for the models of all fitted bands. This 'fixed multi-band' approach is carried out by determining the structural parameters (Sérsic effective radius, R_e, Sérsic index, n, exponential scale length, Rs, position angle, PA, component axis ratio, q) from one freely-fit band, and fixing their values for fits to other bands. These 'dependent' fits allow only the component magnitudes to vary, with both components sharing a common centre. Here, the g band is selected for 'free' fitting (i.e. all structural parameters unfixed).

The limitation of fixed multi-band fitting is that no allowance is made for variation in surface brightness profile shape from band to band, and thus internal colour gradients in the bulge or disk are precluded. This is equivalent to the dual-band mode of GIM2D (Simard et al., 2002), wherein a single average model is fit to images in two bands. Where a fixed approach fails to adequately describe a galaxy's colour information, fitting can be improved by introducing band-dependent variation of structural parameters.

3.7.2 Component Gradients

If fixed multi-band fitting is not sufficient to reproduce the overall colour gradient of a galaxy, internal component colour gradients may be necessary. In this section, I describe the use of bulge and/or disk colour gradients to more accurately model the galaxy across the u, g, and i bands.

The goodness-of-fit of galaxy colour gradients resulting from multi-band fitting was assessed using observed 1D radial colour profiles. Free fitting was carried out in the g band to determine the model structure. Colour profiles are measured numerically from the thumbnails and model images of the dependent u and i bands. For robust measurement of the colour profile, identical annuli and a consistent resolution must be used across all photometric bands. Resolution-matching was carried out by smoothing each band's psf image such that the modified fwhm was equal to the largest (unmodified) value from the three band's psfs. The same smoothing was then applied to the data and model images in each band.

Colour gradients are added to the model components by allowing systematic band-to-band variations in R_e for bulge gradients, or R_s for disk gradients. As R_e and n are covariant,

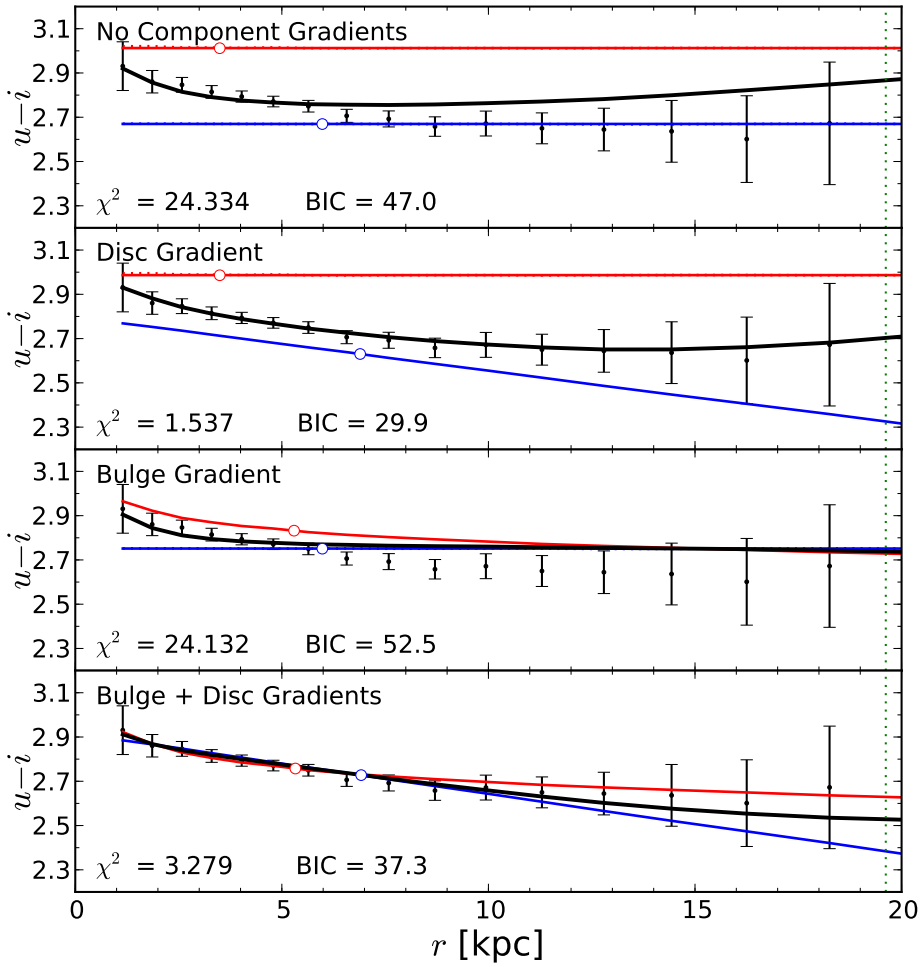

Figure 3.12: $u - i$ colour profiles for a typical galaxy (SDSS DR8 ID: 1237665440979026019) as measured in elliptical annuli. Black error bars indicate the colour measured from the galaxy thumbnail, while the derived model bulge, disk, and total colour profiles are plotted as red, blue and black solid lines. Unfilled red and blue points are plotted at the bulge and disk $R_{\rm e}$, indicating their global average colours. From top to bottom, the different panels show colour profile models with no component gradients, disk gradients only, bulge gradients only, and both bulge and disk gradients. For each profile, the (non-reduced) 1D chi-squared, and corresponding BIC statistic are included. Vertical green dotted lines indicate the edges of the object ellipses used during masking.

n is held fixed where bulge gradients are included to avoid this degeneracy. Increasing the number of free parameters in the 'dependent' bands reduces the reliability of the fit by introducing additional model degeneracy. To minimise this problem, a 1D BIC is calculated to select the simplest model (i.e. fewest free parameters) that sufficiently represents the underlying colour profile (see Section 3.4 for details).

Example colour profiles (with and without component gradients) for a typical galaxy are presented in Figure 3.12. In this case, the measured galaxy colour information in the disk-dominated region of the galaxy ($r > 6$ kpc) is only reproduced when a disk gradient is permitted. The 1D BIC shows no significant further improvement if both bulge and disk gradients are included. Alternatively, this outer region of the galaxy colour profile could be reproduced if the disk of the model with no component gradients (Figure 3.12, top panel) was shifted to a bluer colour. However, this shift would worsen the fit to the more precisely known inner region of the profile ($2 < r < 6$ kpc), yielding a poorer fit overall.

A total of 200 galaxies are found to be well-fit by an archetypal bulge + disk morphology, including 96 galaxies (48%) flagged as lower-quality fits (see Section 3.5). Of these archetypal galaxies, 60 (30%) require the inclusion of colour gradients in at least one model component (see Section 3.7.2). Nine (4.5%) require bulge gradients, 40 (20%) require disk gradients, and 11 (5.5%) require both bulge and disk gradients.

The ratios of measured R_e in the u:g:i bands in models requiring bulge gradients were 1.14:1.00:0.94 on average. The equivalent average u:g:i ratios of R_s in models requiring disk gradients were 1.03:1.00:0.98. Kelvin et al. (2012) presented wavelength-dependent variation of structural parameters for single Sérsic fits of disk- and spheroid-dominated galaxies. Calculating R_e and R_s using median passband wavelengths yields u:g:i ratios of 1.08:1.00:0.87 and 1.05:1.00:0.92 respectively. Thus, the internal component gradients included in this work are similar to previous measurement of size variations for bulge- and disk-dominated galaxies. The component size variations are systematically smaller than global size variations measured by Kelvin et al. (with the exception of the u band bulge R_e). This reflects the shallower colour gradients of bulge and disk components relative to their parent galaxy as a whole.

3.8 Summary

In this chapter, I have introduced and discussed the main techniques used in the (bulge + disk) decomposition analysis of this thesis. The AGONII decomposition pipeline has been detailed, including a description of the extended parameter space search and the use of fitting constraints. In addition, the extensive sample filtering/model selection process used to isolate a sample of well-fit, 'archetypal' (central bulge + outer disk) 2-component galaxies was discussed.

The results of sample filtering is summarised as follows:

i) From an initial sample of 570 Coma cluster member galaxies, a 'stable' fitting solution (i.e. symmetric, uncontaminated, with low χ^2) was measured for 443 galaxies (78%).

ii) A significant additional structural component was identified (via Bayesian model selection) in 337 (76%) of these stable fits. Hence, 106 galaxies (24%) were best-fit by a pure Sérsic model.

iii) The bulge-disk structure was deemed 'atypical' (the bulge does not dominate *only* at the galaxy's centre and/or the disk does not *only* dominate its outer regions) in 137 galaxies (41% of 2-component fits). The remaining 200 bulge + disk galaxies (59%) were considered archetypal *S0*s, and define the sample used for analysis in later chapters.

Finally, I have described techniques for ensuring that bulge-disk decomposition is carried out consistently across multiple bands. Two such 'multi-band fitting' methods have been implemented: i) where model structure does not vary from band-to-band ('fixed multi-band' fitting); ii) where bulge R_e and/or disk R_s is allowed to vary in order to incorporate internal component colour gradients. The latter (internal gradients) approach provides a significant improvement to the colour profile fitting for 30% of the analysis sample galaxies. The fraction of galaxies requiring component gradients decreases with luminosity, suggesting that the detection of internal component gradients is magnitude limited.

In the next chapter, the pure Sérsic, bulge, and disk measurements obtained via application of AGONII to the Coma MegaCam imaging data will be contrasted with the equivalent results of published decomposition studies covering the Coma cluster. The detailed structural

and photometric properties of Coma *S0*s, as measured in the present work, will be discussed in Chapters 5 and 6. The extension of the decomposition techniques presented in the present chapter to include a broader range of multi-component candidate models is discussed in Chapter 7.

Chapter 4

Comparison with Studies of Independent Imaging Data

4.1 Introduction

Decomposition studies using imaging data of varying quality (i.e. observation depth, and seeing) have been previously carried out for Coma cluster galaxies (e.g. Gutiérrez et al., 2004; Aguerri et al., 2005), and from SDSS data (Simard et al., 2011; Meert et al., 2014). As imaging S/N decreases, detection of faint features in a galaxy's surface brightness profile are inhibited. Hence, the reliability of galaxy parameters measured from galaxy fitting decreases for shallower imaging (particularly for the degenerate Sérsic + exponential model). Likewise, increased psf fwhm limits the accurate separation of distinct galaxy structural components. In particular, bulge measurements become highly sensitive to psf effects as seeing becomes comparable to size of the galaxy bulge. While better seeing (smaller fwhm) allows additional profile features (e.g. stellar bars) to be resolved, these structures can distort the parameters determined from simple 1- or 2-component models.

In this chapter, I compare measurements from the main decomposition analysis of the CFHT data with equivalent decomposition studies using both lower-quality (SDSS), and higher resolution (Hubble Space Telescope) image data. This analysis provides a valuable test for the decomposition results presented in this thesis using independent imaging data. For consistency, I also apply my decomposition pipeline (`AGONII`; described in Chapter 3) to these alternate imaging data sources where possible.

The structure of this chapter is as follows: first, the MegaCam decomposition results are compared to equivalent analyses of SDSS imaging. This entails both application of AGONII to SDSS Data Release 8 (DR8) data, and comparison with independent studies based on SDSS Data Release 7 (DR7) data (Simard et al., 2011, hereafter 'S11'; and Meert et al., 2014; hereafter 'M14'). Secondly, the MegaCam measurements are compared with Hubble Space Telescope (HST) fitting results for a subsample of Coma cluster galaxies from the ACS Coma Cluster Treasury survey (Weinzirl et al., 2014). Finally, I summarise the key results of these comparisons.

Note that sample filtering (see Section 3.5) used in this Chapter is based on the MegaCam results *only*. Thus, reference to the 'analysis sample' refers to the filtered sample defined from MegaCam decomposition. Furthermore, filtering in this Chapter is for illustrative purposes only: comparison analyses are carried out using all galaxies contained in both datasets (unless noted otherwise). Hence, the bin medians in Figures 4.1 - 4.14 are calculated from both the MegaCam analysis sample (filled data points), and filtered galaxies (unfilled data points).

4.2 SDSS

Due to its availability and large sky coverage, SDSS data has been used extensively in previous galaxy decomposition studies (e.g. Simard et al., 2011; Lackner & Gunn, 2012, 2013; Meert et al., 2014). A relatively small (2.5 m) telescope aperture, and short exposure times (53.9 s in all bands), however, result in considerably shallower imaging than the CFHT MegaCam data used throughout the present work. Consequently, structural component detection is less robust for SDSS-based decomposition, particularly for the lower surface brightness features. In addition, in the direction of the Coma cluster, the SDSS image data seeing ($\sim 1''$) is worse than CFHT ($\sim 0.8''$).

In this Section, I compare the Sérsic-only and 2-component (Sérsic+exponential) measurements of Coma cluster galaxies as presented in this thesis to equivalent measurements from decomposition studies using SDSS imaging. First, MegaCam decomposition measurements are compared with the results of applying the data reduction methodology described in Chapter 3 directly to SDSS DR8 image data. Comparisons with the Simard et al. (2011)

and Meert et al. (2014) measurements are then made, providing tests of model consistency independent of the analysis pipeline used in the present work.

4.2.1 SDSS AGONII

The AGONII pipeline (including independent sky determination) was used to analyse thumbnails of Coma galaxies drawn from g and i band SDSS DR8 imaging (psf $\sim 1''$). Galaxies were selected for analysis from the MegaCam fields area, however to ensure sufficient S/N for decomposition, the magnitude limit[1] for the SDSS sample was set at $m_g < 17$. In addition, galaxies were removed from the comparisons where global or component sizes were measured at the GALFIT constraint minimum (due to increased plate scale for the SDSS images). The resulting SDSS AGONII sample contains $N = 237$ galaxies, of which 84 galaxies are also contained in the MegaCam analysis sample (i.e. well-fit, archetypal bulge + disk galaxies from fitting MegaCam data).

The total (g band) apparent galaxy magnitudes, as measured from 1-component Sérsic model fits to data from both sources are presented in Figure 4.1. Strong agreement is found (Pearson' correlation coefficient, $\rho = 0.95$), with low scatter (0.08 mag), and a small average systematic offset (SDSS - MegaCam; $\tilde{\Delta} = -0.02$). This result is unsurprising, given that MegaCam magnitude zeropoints are calibrated from SDSS (aperture) photometry.

Comparison of component (g band) apparent magnitudes (Figure 4.2) indicates a strong correlation between MegaCam and SDSS measures of bulge ($\rho = 0.91$) and disk ($\rho = 0.83$) magnitudes. Nevertheless, bulge magnitudes are systematically fainter when measured from MegaCam data ($\tilde{\Delta} = -0.08$ mag), with a factor of $\sim 4\times$ greater scatter (~ 0.3 mag) than measures of total galaxy magnitude. Conversely, disk magnitudes are systematically brighter on average from MegaCam ($\tilde{\Delta} = 0.03$ mag), with $\sim 2.5\times$ greater scatter than global magnitudes. The increased component magnitude scatter indicates the reduced reliability of disk measurement from shallower imaging data. Here, light from the poorly-determined disk was traded to the bulge component, yielding systematically brighter bulges and fainter disks than MegaCam. These disk-determination issues are a major limitation for decomposition studies using the relatively shallow SDSS data.

[1] From SDSS DR9 modelMag.

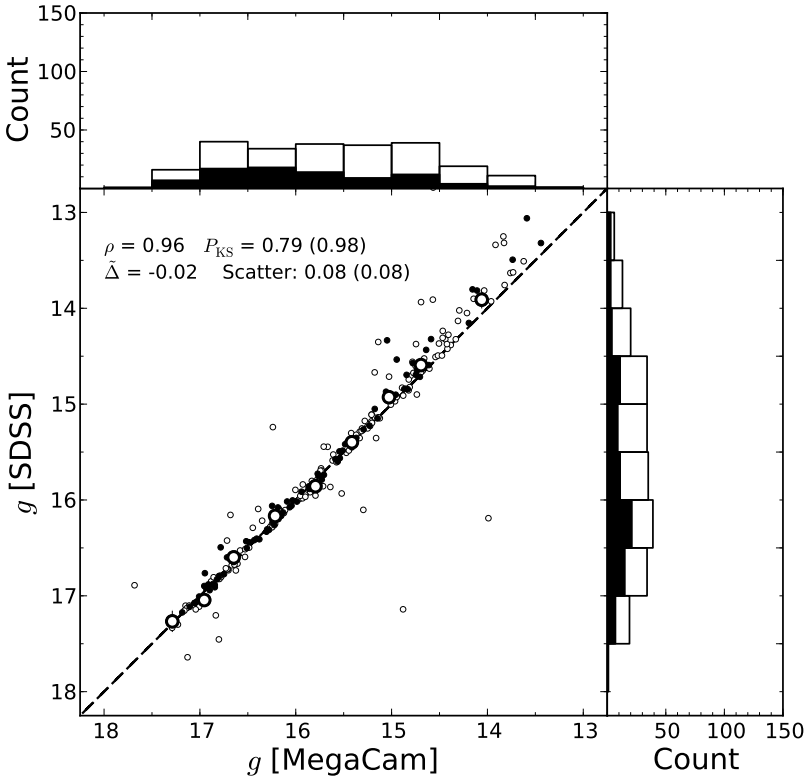

Figure 4.1: Plot comparing the total apparent (g band) magnitudes measured from MegaCam (x) and SDSS DR8 (y) imaging of Coma cluster galaxies, and histograms of the resulting magnitude distributions. Analysis sample galaxies, and galaxies removed by sample filtering (see Section 3.5) are indicated by small filled, and unfilled data points respectively (and filled/unfilled portions of the histograms). Large round points represent median values calculated in magnitude bins, with error bars indicating the robust standard error in each bin. A dashed line corresponding to $y = x$ is plotted for comparison. The Pearson's correlation coefficient, ρ, and the median $(y - x)$ offset, $\tilde{\Delta}$, (measured from all plotted points) are included. In addition, the overall scatter in galaxy magnitude and the K-S probability, $P_{\rm KS}$, are presented for analysis sample galaxies (and all galaxies).

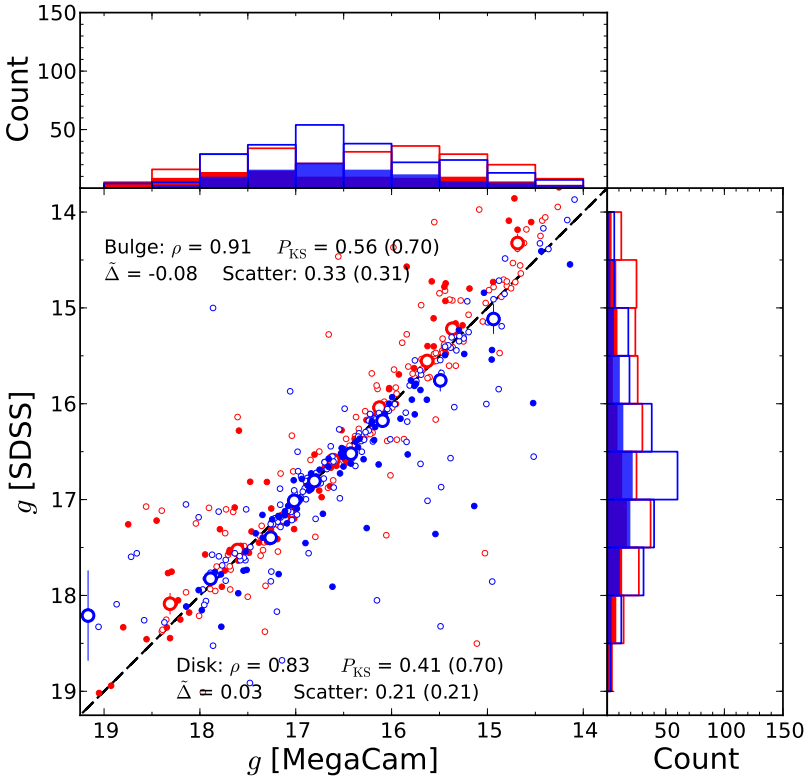

Figure 4.2: As Figure 4.1, displaying the (g band) apparent magnitudes for 2-component model bulges (red) and disks (blue), as obtained from decomposition of MegaCam (x) and SDSS DR8 (y) imaging of Coma cluster galaxies. Regions of the histograms where both component distributions overlap are indicated in purple.

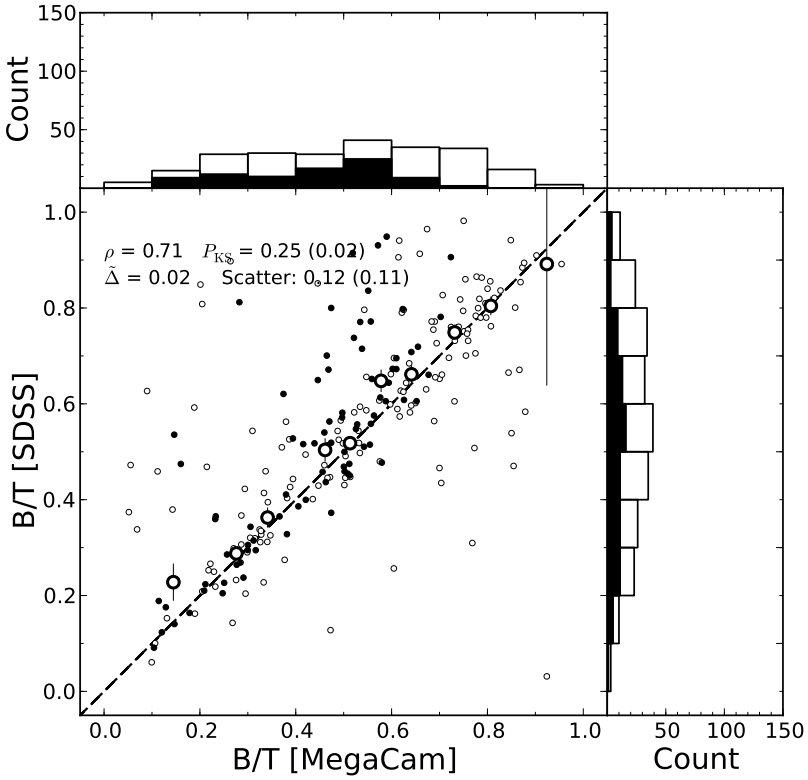

Figure 4.3: As Figure 4.1, displaying the (g band) galaxy bulge fractions (B/T) obtained from decomposition of MegaCam (x) and SDSS DR8 (y) imaging of Coma cluster galaxies.

The galaxy g band bulge fractions (B/T) as measured from the MegaCam and SDSS data are compared in Figure 4.3. As with the bulge colours, the bulge fractions agree reasonably well ($r_{\rm pearson} = 0.71$), although a small bias towards larger B/T is evident in the SDSS results ($\tilde{\Delta} = 0.02$). This amplified bulge fraction is further evidence for poor disk detection in SDSS, which results in weaker disks relative to the well-measured bulges. Moderate scatter is detected in B/T measurements (0.12 for analysis sample galaxies, 0.11 for all galaxies), however this scatter is significantly increased above (MegaCam-measured) B/T values ~ 0.6. These bulge-dominated galaxies almost all have atypical profiles and faint, sub-dominant disks. Such galaxies are thus vulnerable to disk measurement issues, and/or inversion of the bulge and disk model components.

The measured g band Sérsic model, and bulge Sérsic indices are compared in Figure 4.4. Note that here, the GALFIT constraints on n have been lowered (to $n \leq 8.5$) for consistency with literature SDSS decomposition studies[2]. Global galaxy n shows high agreement between both data sources ($\rho = 0.84$), and no net offset ($\tilde{\Delta} = 0.00$). Bulge n is equally-well

[2]The limit is placed at 8.5, rather than 8.0 as in Simard et al. (2011) to avoid excessive limitation of the fitting range.

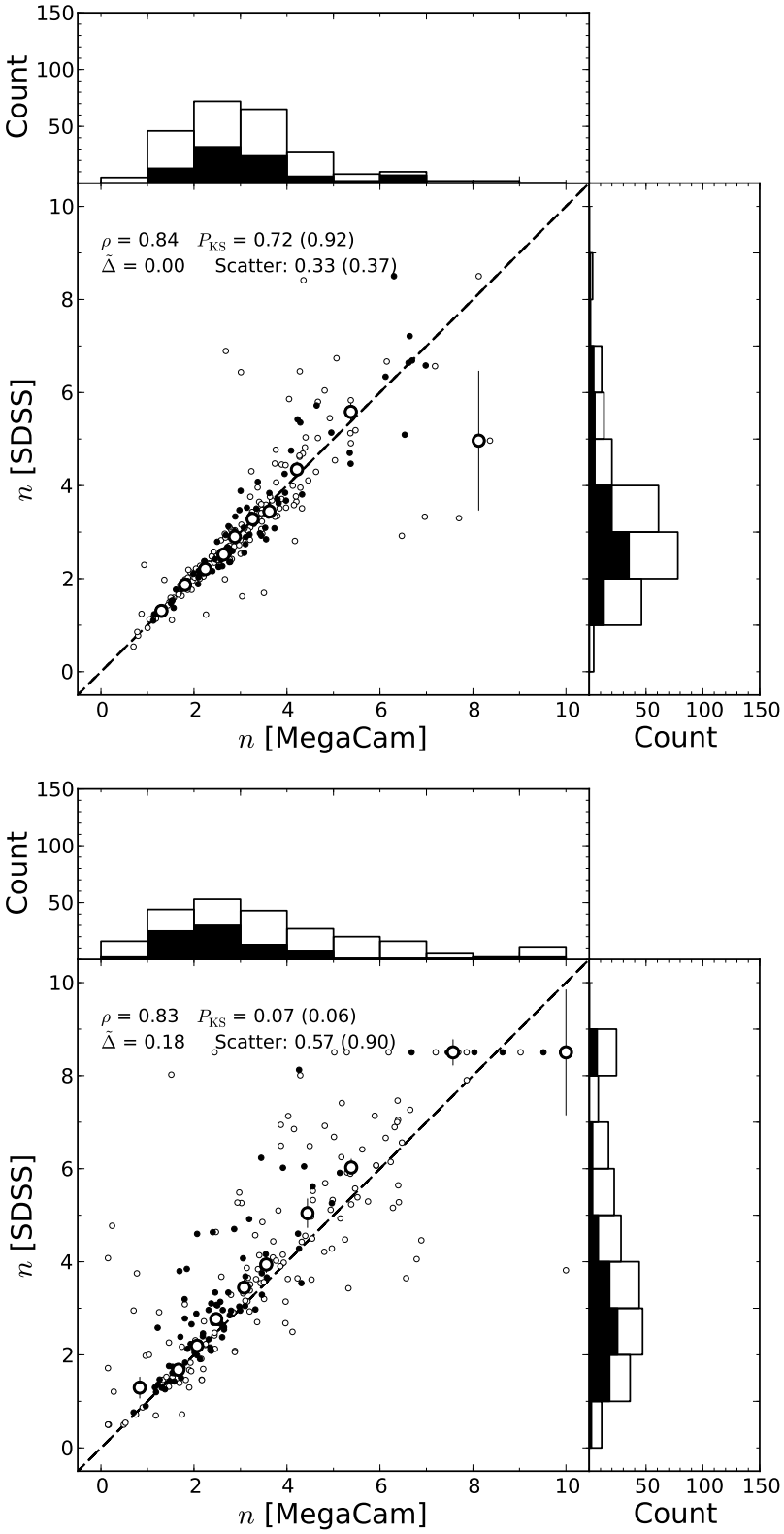

Figure 4.4: As Figure 4.1, displaying n for the Sérsic model (upper plot) and 2-component model bulge (lower plot) obtained from fitting MegaCam (x) and SDSS DR8 (y) imaging of Coma cluster galaxies.

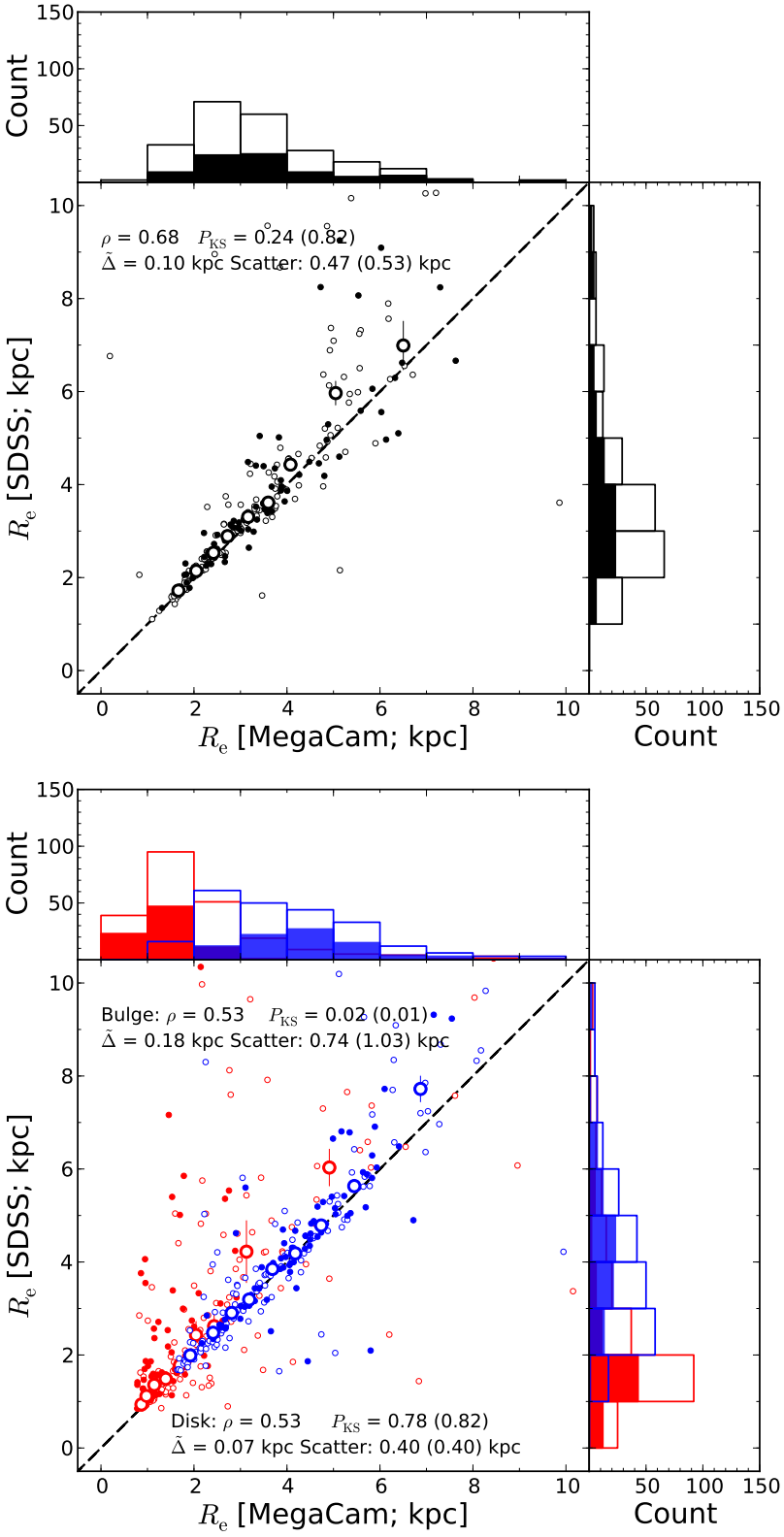

Figure 4.5: As Figure 4.1, displaying R_e for the Sérsic model (upper plot) and 2-component model bulge and disk (red and blue; lower plot) obtained from fitting MegaCam (x) and SDSS DR8 (y) imaging of Coma cluster galaxies.

correlated ($\rho = 0.83$), however a factor of $\sim 2\times$ higher scatter is measured for the analysis sample ($\sim 3\times$ for all galaxies). In addition, a bias towards higher n is noted for SDSS models ($\tilde{\Delta} = 0.18$), indicating more centrally-concentrated bulges. This lopsided scatter is particularly evident for low-n (< 3) Sérsic objects detected from the MegaCam imaging, suggesting a bias against disk-like bulge detection when fitting SDSS data. Such a bias would be expected if outer galaxy profiles were fit by the wings of high-n Sérsic profiles, rather than the exponential component.

Effective half-light radii for the bulge and disk components, and galaxy R_e from single Sérsic fits are presented in Figure 4.5. The global (Sérsic-only) R_e are correlated ($\rho = 0.68$), with a small offset ($\tilde{\Delta} = 0.10$ kpc). Disks are measured to be systematically larger than bulges (by a factor of ~ 3) from both data sources, even for atypical (i.e. not central bulge + outer disk) galaxies not included in the analysis sample. As noted for n, however, component half light radii exhibit weaker correlation between SDSS and MegaCam measurements ($\rho = 0.53$ for both bulges and disks). Nevertheless, disk sizes exhibit a similar level of scatter to global size measurements (~ 0.4 kpc), and a smaller systematic size offset ($\tilde{\Delta} = 0.07$ kpc). Bulges exhibit fundamentally distinct parameter distributions from MegaCam and SDSS ($P_{\rm KS} \sim 0$), reflecting a $\sim 1.5\times$ increase in scatter relative to global R_e measurements, and a systematic bias towards larger bulges ($\tilde{\Delta} = 0.18$ kpc) from SDSS decomposition. Note that for $R_e \lesssim 2$ kpc (MegaCam), there exists a population of bulges with strong scatter towards larger sizes in SDSS. This offset is partially a consequence of increased sensitivity to psf effects as R_e becomes comparable with the seeing ($1'' \approx 0.5$ kpc for SDSS), but also indicates cases where poor disk detection trades more outer profile (i.e. disk) light to the bulge, yielding a larger bulge with higher B/T and n.

In summary, while global (Sérsic-only model fit) galaxy properties are measured consistently from MegaCam and SDSS data, component (bulge and disk) parameters measured from each dataset are only moderately correlated ($\rho \lesssim 0.6$), exhibiting greater measurement scatter and/or significant systematic parameter differences. Decomposition of SDSS data results in larger, more centrally concentrated bulges, and less dominant, weakly constrained disks. This is interpreted as a consequence of less robust disk-detection for decomposition of the shallower SDSS imaging. However, increased bulge size scatter at low R_e also reflects

psf effects as bulges become comparable in size to the (larger) SDSS psf.

4.2.2 Comparison with Simard et al. (2011; S11)

S11 used GIM2D (Simard et al., 2002) to perform automated decomposition of a large sample of galaxies ($\gtrsim 10^6$) from the SDSS DR7 catalogue. Decomposition was performed on g and r band DR7 imaging data using a fixed multi-band approach[3]. A total of 455 galaxies are common to the S11 and MegaCam Coma samples, of which 167 are contained in the MegaCam analysis sample. Here, the colour cut ($g - r > 0.5$) was removed from the MegaCam Coma sample, as no such sample selection criterion is applied for S11 galaxies.

A comparison of the resulting (g band) total Sérsic model apparent magnitudes for S11 and MegaCam is given in Figure 4.6 (upper panel). The galaxy magnitudes measured from both data sources are very well correlated ($\rho = 0.94$). However, relative to the equivalent comparison of MegaCam with AGONII SDSS (Figure 4.1), measurement scatter was increased by a factor of four (to $\sim$0.3 mag). Here, the median magnitude offset (S11 $-$ MegaCam, $\tilde{\Delta} = 0.05$) indicates that galaxies are systematically fainter on average when measured in S11 (relative to MegaCam). Therefore, S11 does not detect $\sim 5\%$ of galaxy light (on average), indicating poor characterisation of outer galaxy profiles.

Component apparent magnitude measurements (lower panel of Figure 4.6) are less well-correlated than global magnitudes ($\rho = 0.74$ for bulges, $\rho = 0.65$ for disks), with a factor of $\sim$2-3$\times$ greater scatter. This component magnitude scatter between S11 and MegaCam is also $\sim 2\times$ larger than the equivalent comparison for SDSS AGONII (Figure 4.2). Furthermore, both components are measured to be 0.07 mag fainter on average in S11, reflecting the systematic bias in global magnitudes noted above. Hence, S11 component magnitudes are highly unreliable, and suffer from serious outer-profile (i.e. disk) measurement issues.

The corresponding (g band) B/T measurements from S11 and MegaCam are poorly correlated ($\rho = 0.38$), with a small offset on average ($\tilde{\Delta} = 0.02$; Figure 4.7). However, for B/T < 0.5, both estimates are moderately well correlated, with a significant offset ($\Delta = 0.09$; S11 B/T is systematically larger than for MegaCam on average) and substantial scatter (~ 0.2). For more bulge-dominated galaxies, SDSS B/T is weakly correlated with MegaCam B/T,

[3]Note that while DR7 imaging contains significantly overestimated sky levels for galaxies close to other bright sources, Simard et al. independently determine the mean sky flux via GIM2D fitting of sky pixels.

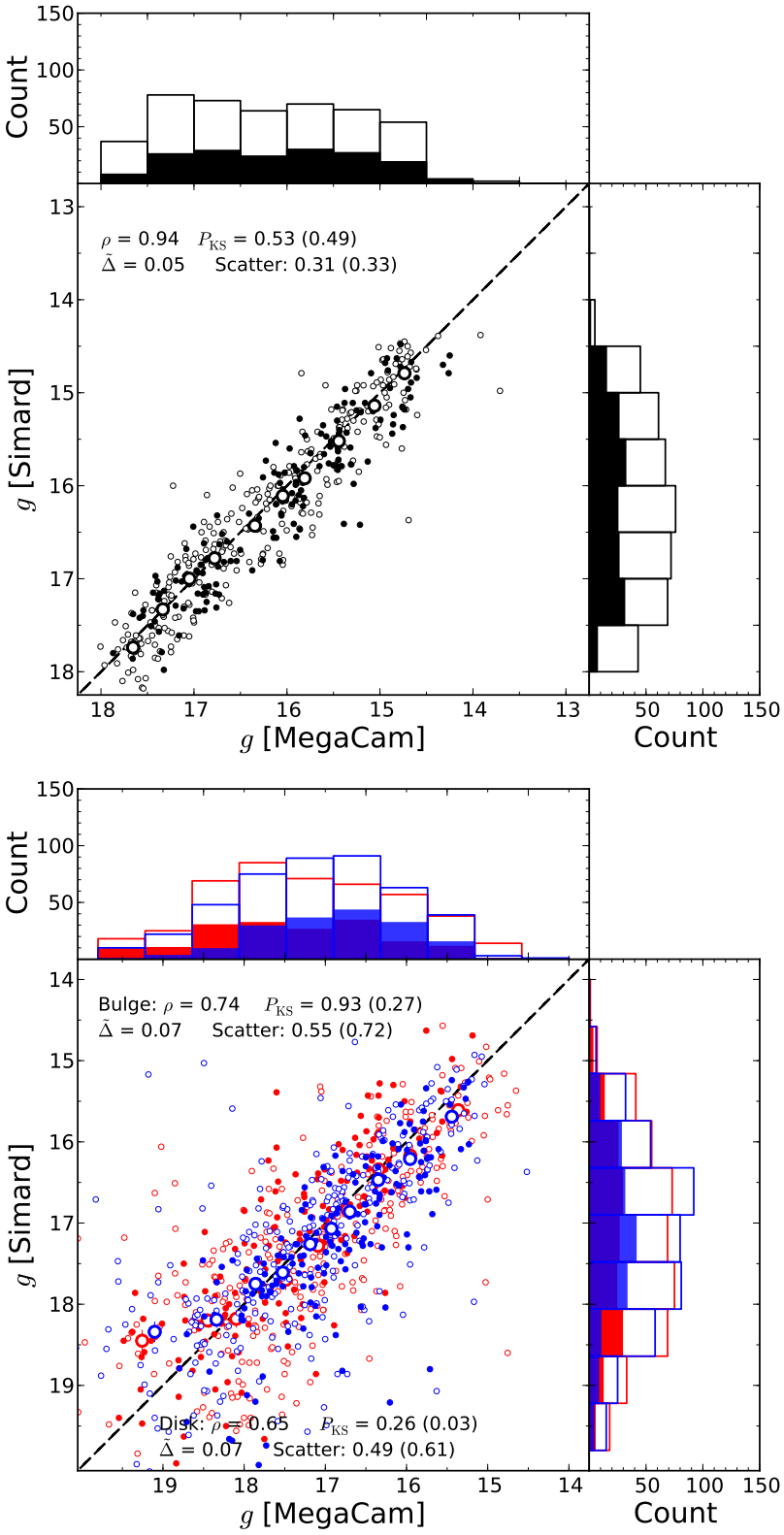

Figure 4.6: As Figure 4.1, displaying apparent (g band) Sérsic model magnitudes (**upper panel**), and 2-component model bulges and disks (**lower panel**; red and blue) for Coma cluster galaxies as measured in the present work from MegaCam imaging (x), and from SDSS DR7 imaging (y) as presented in Simard et al. (2011). Regions of the lower plot histograms where both component distributions overlap are indicated in purple.

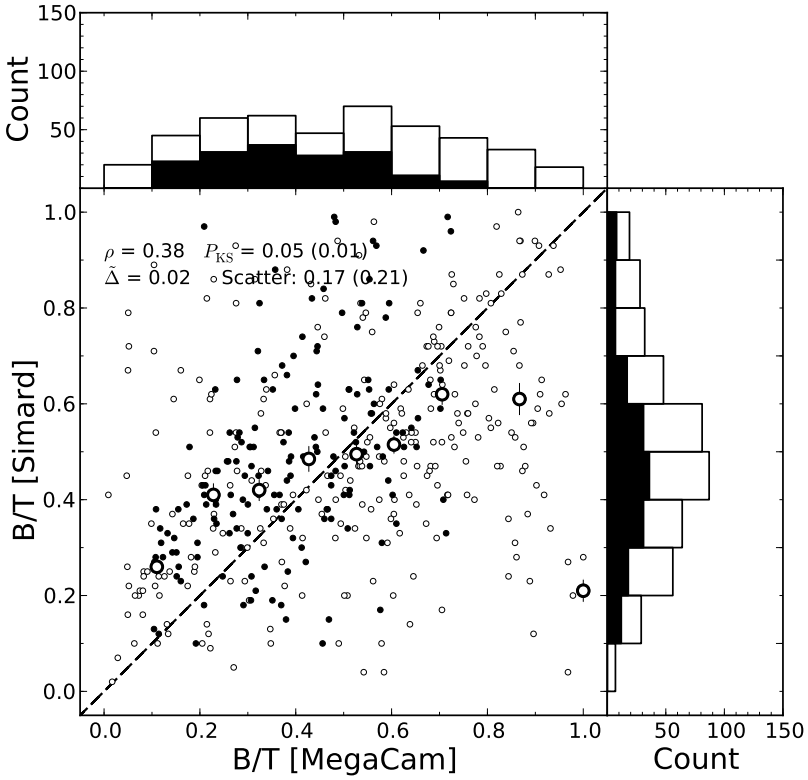

Figure 4.7: As Figure 4.1, displaying the (g band) B/T for Coma cluster galaxies as measured in the present work from MegaCam imaging (x), and from SDSS DR7 imaging (y) as presented in Simard et al. (2011).

and offset in the opposite direction ($\Delta = -0.15$; S11 B/T systematically smaller than MegaCam). This apparent bimodality (as evident from the weakly double-peaked distribution for MegaCam B/T) reflects the difference between archetypal (low B/T) and atypical ($\equiv$ traditional giant ellipticals; high B/T) galaxy fits in our sample.

Measurements of (single Sérsic fit, and component bulge) Sérsic indices from MegaCam and S11 are presented in Figure 4.8. Global n measured from MegaCam data is well correlated with S11 ($\rho = 0.87$), but bulge n shows poor agreement ($\rho = 0.39$), and high scatter (~ 1.4). However, the distribution of S11 bulge n is broader, and more strongly offset from the MegaCam results ($\tilde{\Delta} = 0.80$) than results measured from SDSS data using `AGONII`. Thus, while disk-detection issues exist in both SDSS-based decomposition studies (yielding more dominant bulges at large profile radii), S11 includes a further bias towards higher n bulges.

Figure 4.9 displays the (half-light) sizes of galaxies, bulges, and disks for MegaCam and S11. As seen previously for colour and n, global R_e measurements exhibit reasonable agreement ($\rho = 0.68$) between both measurements. However, unlike the equivalent analysis in

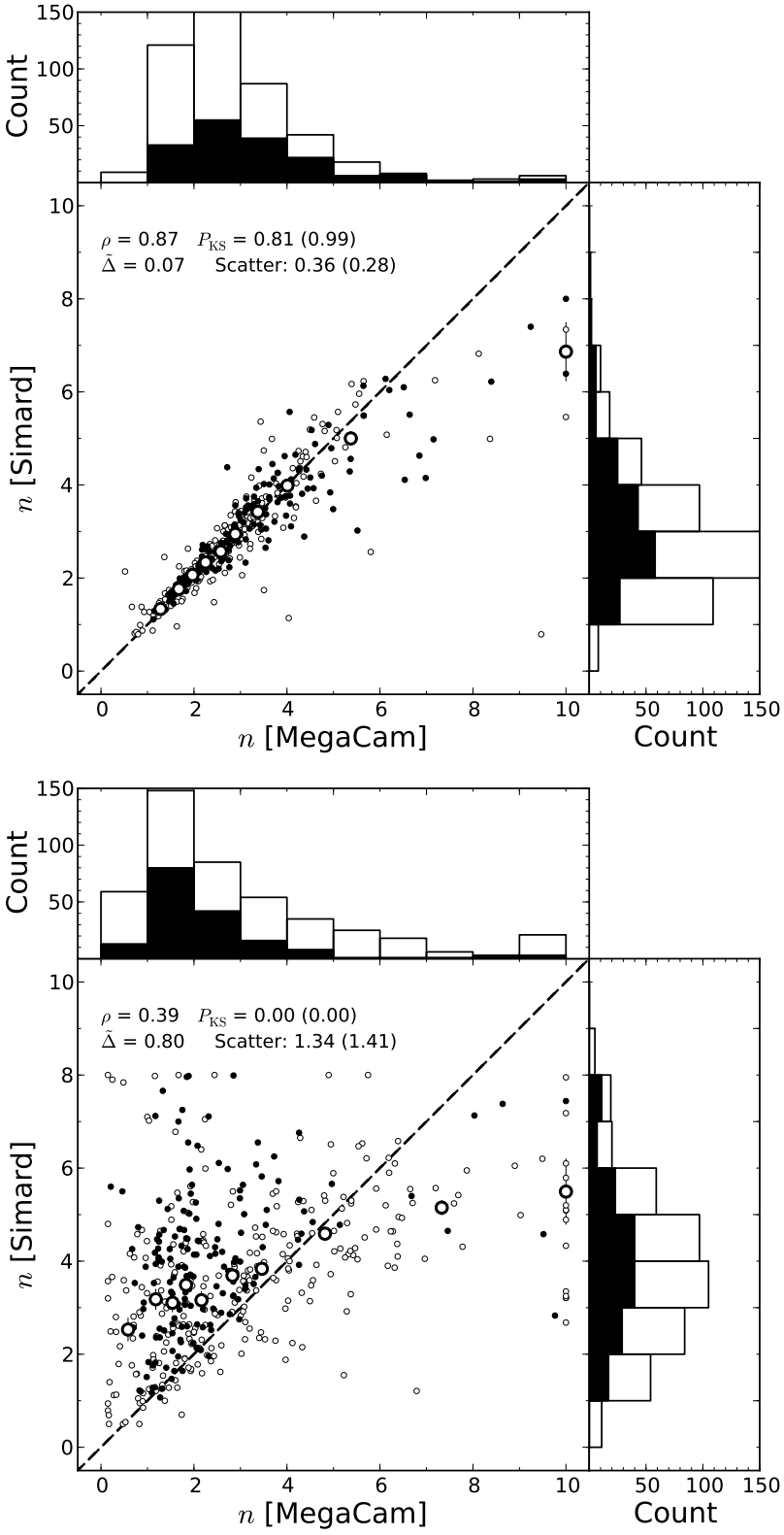

Figure 4.8: As Figure 4.1, displaying n for the Sérsic model (upper plot) and 2-component model bulge component (lower plot) for Coma cluster galaxies as measured in the present work from MegaCam imaging (x), and from SDSS DR7 imaging (y) as presented in Simard et al. (2011).

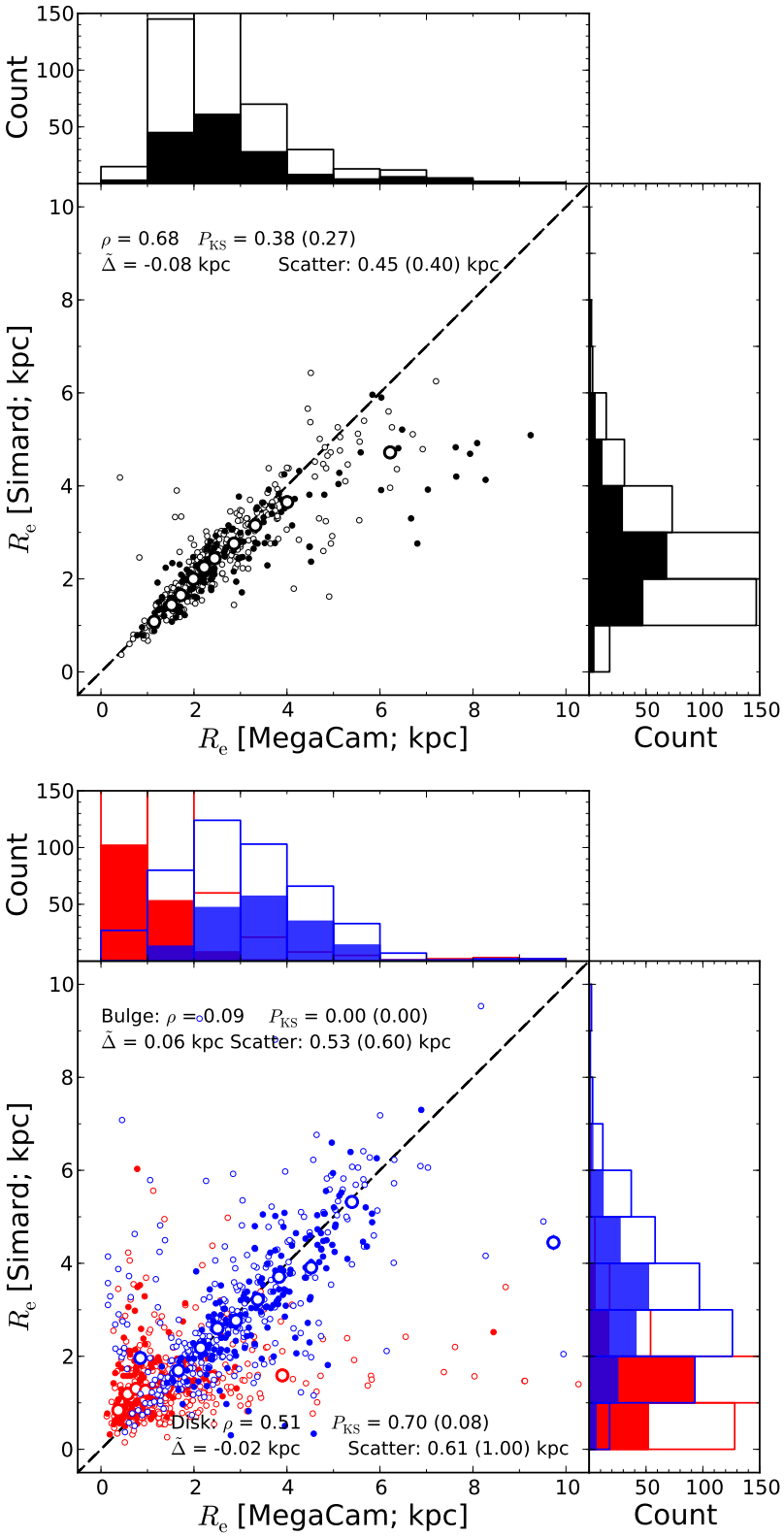

Figure 4.9: As Figure 4.1, displaying R_e for Sérsic model fits (upper plot) and 2-component model bulges and disks (red and blue; lower plot) for Coma cluster galaxies as measured in the present work from MegaCam imaging (x), and from SDSS DR7 imaging (y) as presented in Simard et al. (2011).

Section 4.2.1 (Figure 4.5), galaxy sizes are measured to be systematically *smaller* on average when measured in S11 ($\tilde{\Delta} = -0.08$ kpc). Likewise, disk components are systematically smaller in S11 (to a lesser degree; $\tilde{\Delta} = -0.02$ kpc). This difference is small for both disks and galaxies as a whole, but may result from sky determination issues in the DR7 imaging (i.e. over-subtracted sky yielding artificial truncation of the outer galaxy profiles).

Galaxy bulges measured from SDSS data (in S11) are larger than MegaCam, however the average offset is a factor of three times smaller than that reported in Figure 4.5 ($\tilde{\Delta} = 0.06$ kpc relative to 0.19 kpc). This implies that bulges are also affected by underestimation due to sky-subtraction errors, but remain larger than MegaCam measurements due to the bias towards outer-dominating (high n) bulges in SDSS decomposition. As a whole, R_e measurements from each data source are effectively uncorrelated ($\rho = 0.09$). This implies that S11 and MegaCam 'bulges' are not measured from consistent galaxy structures. The disk components, however, remain moderately well-correlated ($\rho = 0.51$), consistent with the findings of Section 4.2.1, but with a factor of two greater scatter. However, this result is unsurprising given that the analysis sample contains galaxies with outer-dominant disks by definition.

As noted in Section 4.2.1, a population of extreme outliers in S11 bulge R_e (> 3 kpc; $N = 88$) exist for small MegaCam bulge R_e (< 1 kpc). These galaxy bulges are measured as systematically larger in S11 (with high R_e scatter), with higher bulge n, and B/T on average. The increased scatter is caused both by increased sensitivity to psf effects in S11 as bulge sizes approach the SDSS seeing limit ($1'' \equiv 0.5$ kpc), and poor disk measurement for SDSS imaging. Hence, trading of disk light into the bulge component yields larger, higher n bulges for S11. An equivalent additional population of outliers with high scatter in MegaCam R_e ($N = 75$) exists for small S11 R_e (< 2 kpc). Here, MegaCam-measured bulges are systematically larger, and more dominant (higher B/T), but consistent in Sérsic index with measurements from S11. However, unlike the S11 outlier galaxies, a significant offset is detected between the total galaxy magnitudes of MegaCam outliers ($\Delta M = -0.27$ mag for MegaCam $-$ S11,). This indicates that S11 models detect only $\sim 80\%$ of the galaxy flux measured from MegaCam. Hence, MegaCam Sérsic components (in these outliers) account for the central bulge plus additional outer structural components undetected in S11.

In summary, global (Sérsic-only model fit) galaxy properties measured from MegaCam and S11 are well-correlated. However, as with AGONII analysis of SDSS DR8 data (Section 4.2.1), component (bulge and disk) parameters measured from each dataset are moderately correlated at best, with greater measurement scatter. Notably, S11 bulges are systematically more centrally-concentrated (higher n) objects than MegaCam bulges, and exhibit no correlation in size. The outer structure measurement issues for SDSS data noted in Section 4.5 are also present in S11, yielding either systematically more dominant bulges at large radii (a consequence of trading outer disk light to the Sérsic component), or neglecting significant additional structures in the outer parts of galaxies. Galaxy and disk effective half-light radii are measured to be systematically smaller in S11 than MegaCam. As no such effect is detected in Section 4.5, this bias is attributed to sky-determination issues in the SDSS DR7 data of S11 (i.e. an overestimation of the sky flux yields a truncated outer galaxy profile). From the poor agreement with the results determined from MegaCam data, I conclude that the bulge-disk decomposition results of S11 are not measured from consistent galaxy structures as those reported in this thesis.

4.2.3 Comparison with Meert et al. (2014)

A recent study has emerged (Meert et al., 2014; 'M14') which revisits the SDSS DR7 imaging (as used in S11) with a more sophisticated decomposition pipeline using PyMorph (Vikram et al., 2010) and GALFIT. During pre-processing, M14 re-evaluates the DR7 sky background for each galaxy, finding values 0.25% lower on average than the SDSS sky values used in S11. In total, 456 galaxies are contained in both the CFHT Coma sample and M14, of which 167 galaxies are also contained in the analysis sample of the present work (i.e. are well-fit, archetypal bulge + disk systems). M14 also implements a system of galaxy fit assessment and flagging. Thus, 254 galaxies (out of the 456) are described as 'well-fit 2-component' systems in M14 ($N = 125$ in the CFHT analysis sample).

Here, I briefly compare the decomposition results of the present work to Coma cluster galaxies in M14. Since M14 uses r band imaging, I do not consider structural properties (due to wavelength dependence). Here, r band magnitudes for MegaCam are calculated as $r = g - 0.67(g-i) - 0.01$ for global and bulge measurements, and $r = g - 0.53(g-i) - 0.15$

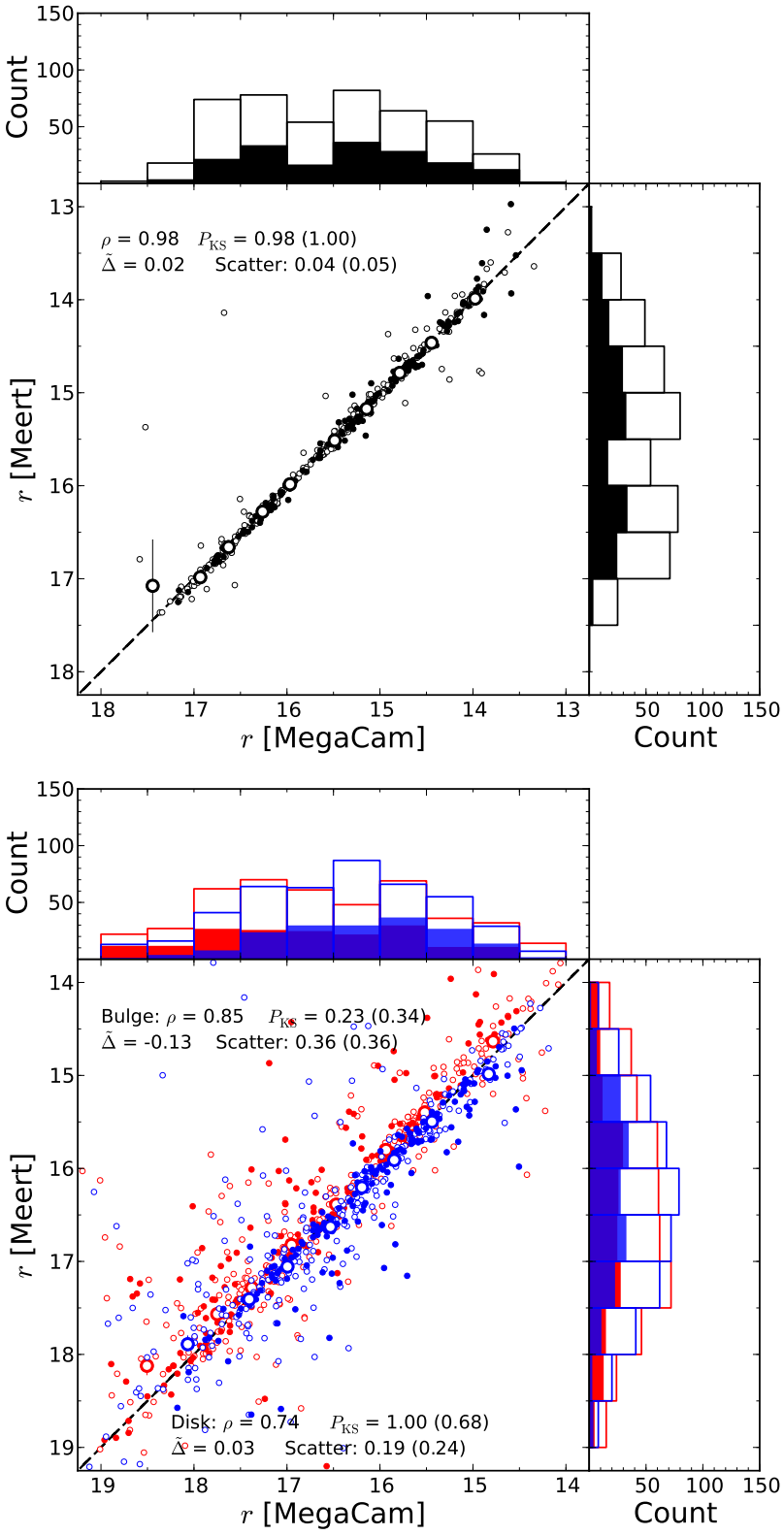

Figure 4.10: As Figure 4.1, displaying apparent (r band) Sérsic model magnitudes (**upper panel**), and 2-component model bulges and disks (**lower panel**; red and blue) for Coma cluster galaxies derived from MegaCam imaging (x), and measured from SDSS DR7 imaging (y) as presented in Meert et al. (2014). Regions of the lower plot histograms where both component distributions overlap are indicated in purple.

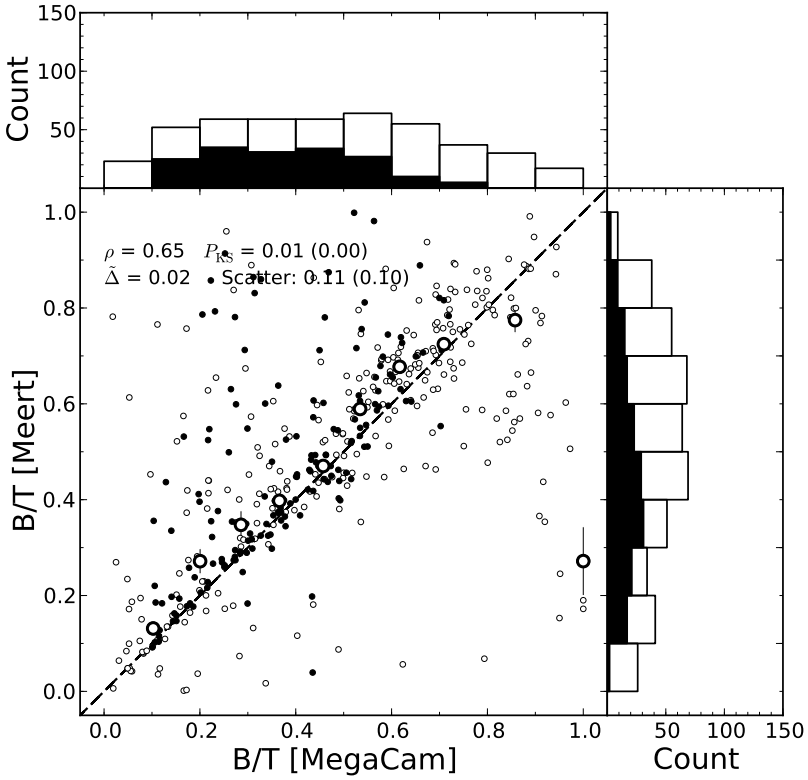

Figure 4.11: As Figure 4.1, displaying the (r band) B/T for Coma cluster galaxies as derived for the present work from g band component photometry (x), and from measurements of SDSS DR7 imaging (y) as presented in Meert et al. (2014).

for disks[4].

The resulting (r band) global (Sérsic-only fit) apparent magnitudes from MegaCam and M14 are presented in the upper panel of Figure 4.10. Here, both measures of galaxy magnitude are extremely-well correlated ($\rho = 0.98$), with low measurement scatter (0.05 mag), and a negligible average offset (M14 $-$ MegaCam; $\tilde{\Delta} = 0.02$ mag). These magnitudes are comparable (in terms of scatter, correlation, and offset) with the g band measurements of MegaCam and AGONII SDSS. However, the equivalent comparison with S11 yields a factor of eight greater scatter in (g band) galaxy magnitudes. This indicates a significant improvement in the reliability of global galaxy property measurements in M14 relative to S11.

Component (bulge and disk) apparent magnitudes (Figure 4.10 lower panel) exhibit a similar level of scatter to AGONII SDSS measurements (~ 0.35 mag for bulges, ~ 0.20 mag for disks) but are less well-correlated with MegaCam measurements ($\rho = 0.74$ for bulges, $\rho = 0.65$ for disks). Nevertheless, scatter from M14 component magnitudes remains a

[4]These magnitude conversions are determined empirically from SDSS aperture photometry in the appropriate colour ranges.

factor of $\sim 2\times$ less than equivalent measurements for S11. Furthermore, the bulges in M14 are significantly brighter on average than in MegaCam ($\tilde{\Delta} = -0.13$ mag), while disks are slightly fainter ($\tilde{\Delta} = 0.03$ mag). Thus, while measurement scatter is greatly reduced in M14, the trading of disk light to the bulge component (and hence disk measurement issues) remains a significant limitation of their decompositions.

Bulge fractions (B/T) in the r band from MegaCam (from the converted g band component magnitudes) and M14 are presented in Figure 4.11. As seen for component magnitudes, M14 B/T has similar measurement scatter to that found in AGONII SDSS (~ 0.1 mag), but is less well-correlated with MegaCam ($\rho = 0.65$). Relative to S11, M14 does not exhibit inverted 2-component models (i.e. systematically lower B/T) for the range $0.5 <$B/T$_{\rm MegaCam}< 0.8$, indicating improved assignment of model bulge and disk components to the corresponding galaxy structures. However, a significant population of high B/T scatter galaxies exists in M14 for B/T$_{\rm MegaCam} > 0.8$ (as also seen in S11), indicating that disk measurement issues remain in this bulge-dominated regime.

In summary, the r band decomposition study presented in M14 is a significant improvement (in terms of measurement reliability) over the previously-examined S11 catalogue, despite both studies using the same (SDSS DR7) imaging data. However, the measurement of outer surface brightness profile features (e.g. disks) remains significantly limited by the (lack of) observation depth. Hence, M14 fails to characterise galaxy component properties as well as the MegaCam decomposition of Coma presented in this thesis.

4.3 Hubble Space Telescope

The Hubble Space Telescope is a 2.4 m optical/near infrared space telescope, located in low Earth orbit. Due to the lack of atmospheric effects, the HST is capable of significantly better angular resolution than is possible from equivalently-sized ground-based observatories, and reduced contaminating sky flux (~ 1 mag fainter in g). However, for bulge-disk decomposition studies of low-redshift sources (e.g. Coma) this enhanced resolution can be a hindrance; fitting results are skewed by resolved structural sub-components (e.g. rings, shells, tidal tails).

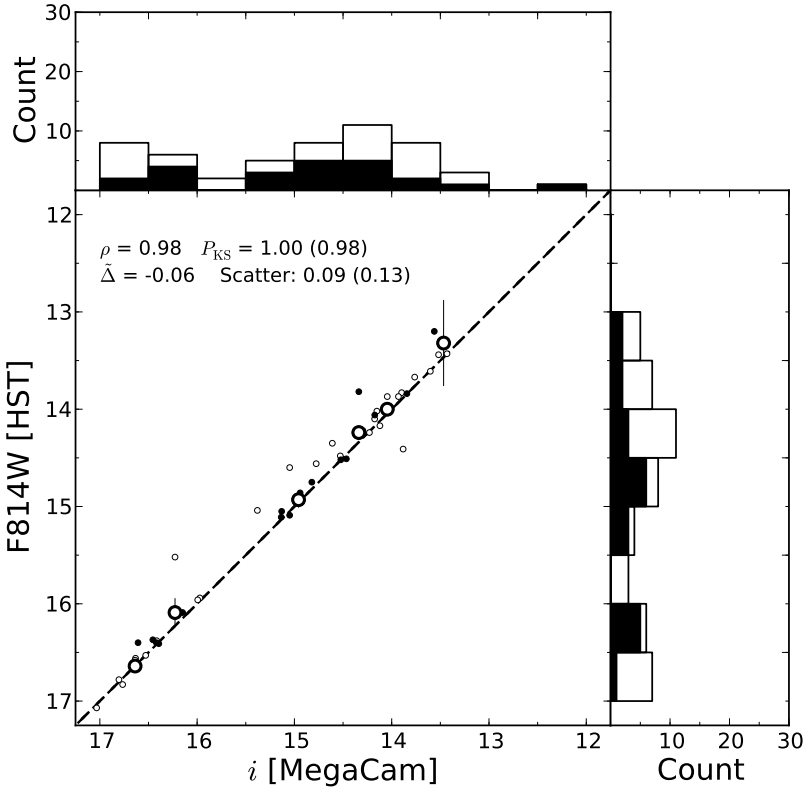

Figure 4.12: As Figure 4.1, plotting i band galaxy magnitudes for Coma cluster galaxies as measured from Sérsic model fits to MegaCam imaging (x) and the equivalent HST F814W magnitudes (y) as presented in Weinzirl et al. (2014).

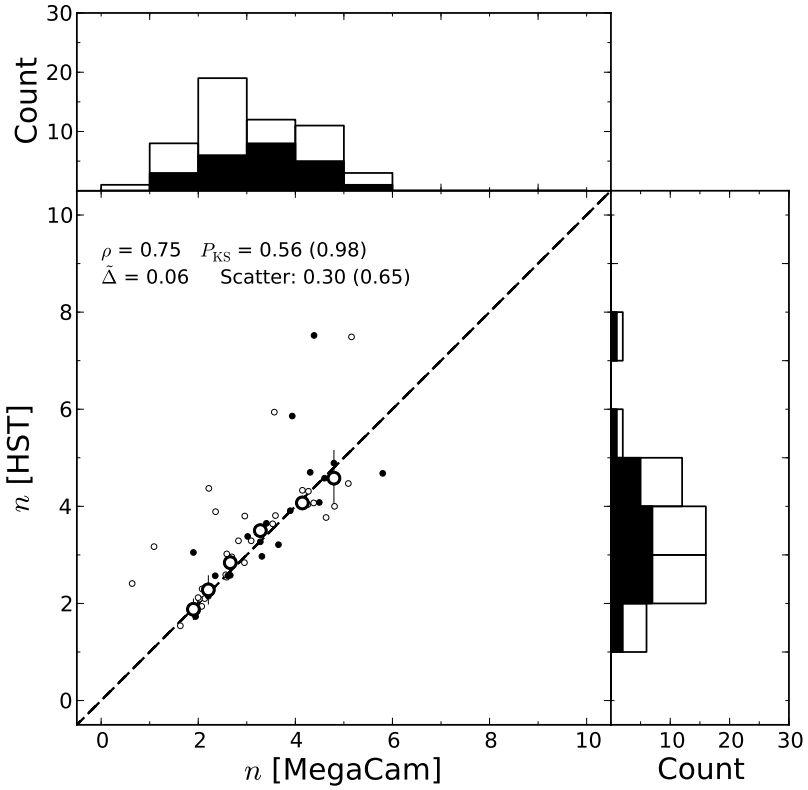

Figure 4.13: As Figure 4.1, plotting galaxy n for Coma cluster galaxies as measured from Sérsic model fits to (i band) MegaCam imaging (x) and from HST Sérsic fits (F814W; y) as presented in Weinzirl et al. (2014).

Weinzirl et al. (2014) presented GALFIT Sérsic fit parameters for 68 Coma galaxies (from a small, central area of the cluster) derived from the HST F814W ($\approx i$ band) imaging of the ACS Coma Cluster Treasury survey (Carter et al., 2008). 54 galaxies from the Hubble sample are also contained in the CFHT Coma sample, of which 23 are analysis sample galaxies. A comparison of the F814W/i Sérsic magnitudes is presented in Figure 4.12. Measurements from both data sources are extremely well correlated ($\rho = 0.98$), with a small offset ($\tilde{\Delta} = -0.06$ mag) such that MegaCam measurements are fainter than those from HST. However this variation may be due to differences between the HST F814W and MegaCam i filters.

Comparisons of Sérsic index and effective radii are presented in Figures 4.13 and 4.14. In both cases, the structural parameters measured from HST correlate well with those measured from MegaCam ($\rho = 0.75$ and 0.69 for n and R_e respectively), and both distributions (for all galaxies) are very likely to have been drawn from equivalent distributions ($P_{\rm KS} = 0.98$ for n and R_e). The HST-based measurements are systematically smaller (R_e: $\tilde{\Delta} = -0.10$ kpc), but more centrally concentrated (n: $\tilde{\Delta} = 0.06$) than MegaCam. These offsets are consistent

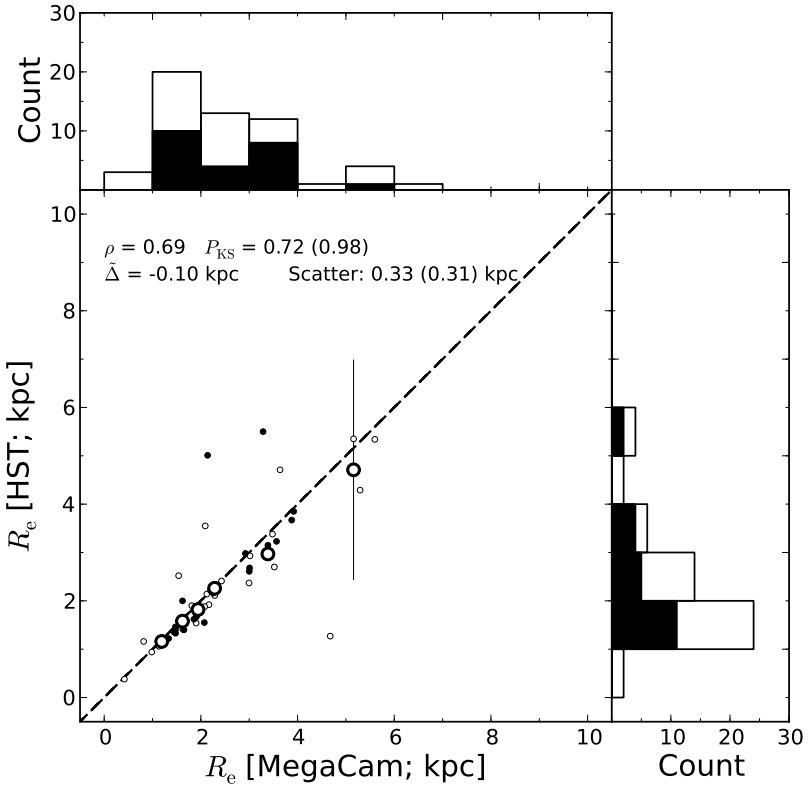

Figure 4.14: As Figure 4.1, plotting galaxy R_e for Coma cluster galaxies as measured from Sérsic model fits to (i band) MegaCam imaging (x) and from HST Sérsic fits (F814W; y) as presented in Weinzirl et al. (2014).

with those measured between S11 SDSS measurements and MegaCam (Section 4.2.2). As sky-subtraction is a negligible consideration in HST imaging, this offset is attributed to differences in psf between HST and MegaCam yielding more centrally peaked galaxy profiles (higher n), which in turn would require smaller R_e to fit the entire profile.

In summary, for the $\sim$50 galaxies in common with the MegaCam sample of the present work, our Sérsic-only structural parameters (n, R_e) correlate extremely well with the values reported in Weinzirl et al. (2014). Small structural offsets yield smaller, but higher n galaxies in HST relative to MegaCam, which is attributed to psf effects for the better-resolved HST fitting. Note that no comparison of HST B/T could be made, as only 14 galaxies (including six well-fit analysis sample galaxies) in T14 possess bulge and disk (but no bar) components.

4.4 Chapter Summary

In this chapter, I have compared the structural and colour measurements from the decomposition analysis of Coma cluster galaxies (using MegaCam imaging) to equivalent literature

measurements obtained from both SDSS and HST imaging. In addition, the decomposition routine presented in this thesis was applied to SDSS DR8 imaging data, allowing measurement differences to be analysed independent of the data reduction technique.
The main findings are summarised as follows:

i) Sérsic-model parameters, as determined from independent SDSS DR7 (S11 & M14), DR8 (with `AGONII`), and HST (Weinzirl et al., 2014) imaging, correlate well with the measurements of global structural and colour properties from MegaCam imaging data, and are distributed equivalently.

ii) Component (Sérsic bulge + exponential disk) properties measured from SDSS imaging data (Simard et al., 2011; Meert et al., 2014), however, are only moderately correlated with MegaCam measurements, with significant systematic offsets. Nevertheless, M14 shows a significant improvement in component and global measurement scatter relative to S11. SDSS decomposition measurements thus do not measure galaxy structures that are consistent with those measured from MegaCam data.

iii) Sérsic bulges measured from SDSS image data are larger, more centrally-concentrated, and dominate a greater proportion of galaxy surface brightness profiles. This is attributed to poor disk detection due to the shallower SDSS imaging.

iv) Exponential disks exhibit greater parameter scatter for the same reason, particularly for galaxies not identified as archetypal central bulge + outer disks.

v) Size measurements in S11 are systematically smaller on average than those measured in the present work from SDSS DR8. This is attributed to truncation of galaxy surface brightness profiles due to overestimation of the sky value in SDSS DR7 data by S11.

vi) Global size measurements derived from HST data (Weinzirl et al., 2014) are systematically smaller than those measured from MegaCam. This is attributed to differing Sérsic profile shapes at small radii due to psf differences (i.e. higher n for HST).

The relatively large scatter in galaxy component measurements from SDSS data (even for alternative reductions of the same images) indicates that SDSS-based decomposition studies are unreliable. Given that the considered (Coma) sample contains some of the closest,

most well-resolved galaxies in the SDSS catalogue, this calls into question the robustness of decomposition of galaxies based on SDSS imaging. The MegaCam decomposition analysis used in this thesis yields reliable bulge + disk measurements, agreeing favorably with measurements from deeper, better-resolved HST imaging data. Furthermore, the significant reduction in component parameter measurement scatter for analysis sample galaxies confirms that the filtering process selects a robust sample of well-fit (bulge + disk) galaxies.

Chapter 5

The Structural Properties of Coma *S0*s

5.1 Introduction

Galaxy quenching, and the formation of early-type morphologies is not a purely photometric change. The evolutionary pathways responsible for these changes also significantly alter galaxy structural morphology (e.g. Toomre & Toomre, 1972). Furthermore, the structural changes expected under the competing 'bulge enhancement' and 'disk fading' scenarios (see Section 1.2) would be highly distinct. Therefore, by investigating the structural properties of ETGs, the evolutionary mechanisms that acted upon these galaxies in the past can be constrained.

In this chapter, I present the (g band) Sérsic and exponential structural properties of Coma cluster red sequence galaxies (in the magnitude range $-17 > M_g > -22$) following the decomposition analysis detailed in Chapter 3. As noted previously, rather than forcing a bulge + disk morphology on all galaxies regardless of model suitability, I focus exclusively on a sample of galaxies with archetypal *S0* structural morphologies (central bulge + outer disk; i.e. the 'analysis sample'). Thus, the Sérsic and exponential components discussed in this chapter implicitly correspond to the bulges and disks of Coma ETGs (respectively).

First, I present the overall distributions in the structural parameters of the analysis sample. Secondly, I investigate structure variation along the red sequence via structural trends as a function of galaxy magnitude. Thirdly, the dependence of bulge and disk properties on clustercentric radius is used to investigate the role of the cluster environment in structural evolution. Finally, the structural results are summarised, and conclusions are drawn.

5.2 Structural Fitting Results

5.2.1 Parameter Distributions

In this section, I describe the distributions of bulge and disk structural parameters for galaxies in the analysis sample (as described in Section 3.6). A full catalogue of structural fitting measurements is presented in Table A.1 of Appendix A.

Galaxy bulges exhibit the full range of permitted Sérsic indices ($0.15 < n < 10$), although bulges with $n \gtrsim 4$ (i.e. more centrally concentrated) are rare, and the majority fall within the range $n \sim 1$ - 3 (Figure 5.1a), indicating that most archetypal *S0*s possess 'pseudobulges' ($n < 2$; Kormendy & Kennicutt, 2004), rather than classical ($n \sim 4$) bulges. The median bulge n is 1.86 ± 0.11. This distribution of Sérsic indices is similar to those reported in Krajnović et al. (2013) for ATLAS^{3D} 'fast rotator' galaxies in less dense environments ($\sim 75\%$ within $0.5 < n < 3$). Conversely, `GIM2D` bulge-disk decompositions of a broader sample of galaxies in Simard et al. (2011) yielded a more even spread of bulge n in the range $0.5 < n < 8$ (peaking at $n \sim 6$).

The measured bulge fractions of the sample are consistent with a relatively flat distribution in the range $0.1 < \mathrm{B/T} \leq 0.6$ (median B/T $= 0.38 \pm 0.01$), but the occupancy of bins above B/T~ 0.6 drops sharply (Figure 5.1b). This lack of bulge-dominated galaxies partially reflects an underlying deficit in the initial (i.e. unfiltered) distribution of B/T, but is exacerbated by sample filtering, which excludes galaxies wherein the bulge dominates the surface brightness profile at large radii. If 'atypical' fits are *included*, the combined bulge fraction distribution becomes consistent with the distribution measured for the initial (i.e. unfiltered) sample. The (B and R band) decompositions in Hudson et al. (2010; 'H10') for cluster galaxies exhibit a sharp peak for $0.4 <$B/T< 0.6, with greater occupancy of the $0.6 <$B/T< 1.0 bin, and lesser occupancy of the $0.0 <$B/T< 0.4 bin than in the present work. This lower median B/T reflects the higher magnitude limit (i.e. fainter galaxies) in this work relative to H10. ATLAS^{3D} B/T distributions exhibit a similar peak in the range $0.05 <$B/T< 0.40 for fast rotator galaxies (Krajnović et al., 2013), but are otherwise dominated by the $0.95 <$B/T< 1.00 bin ($\sim 36\%$).

The physical sizes of bulges are distributed across a narrow range of effective half-light

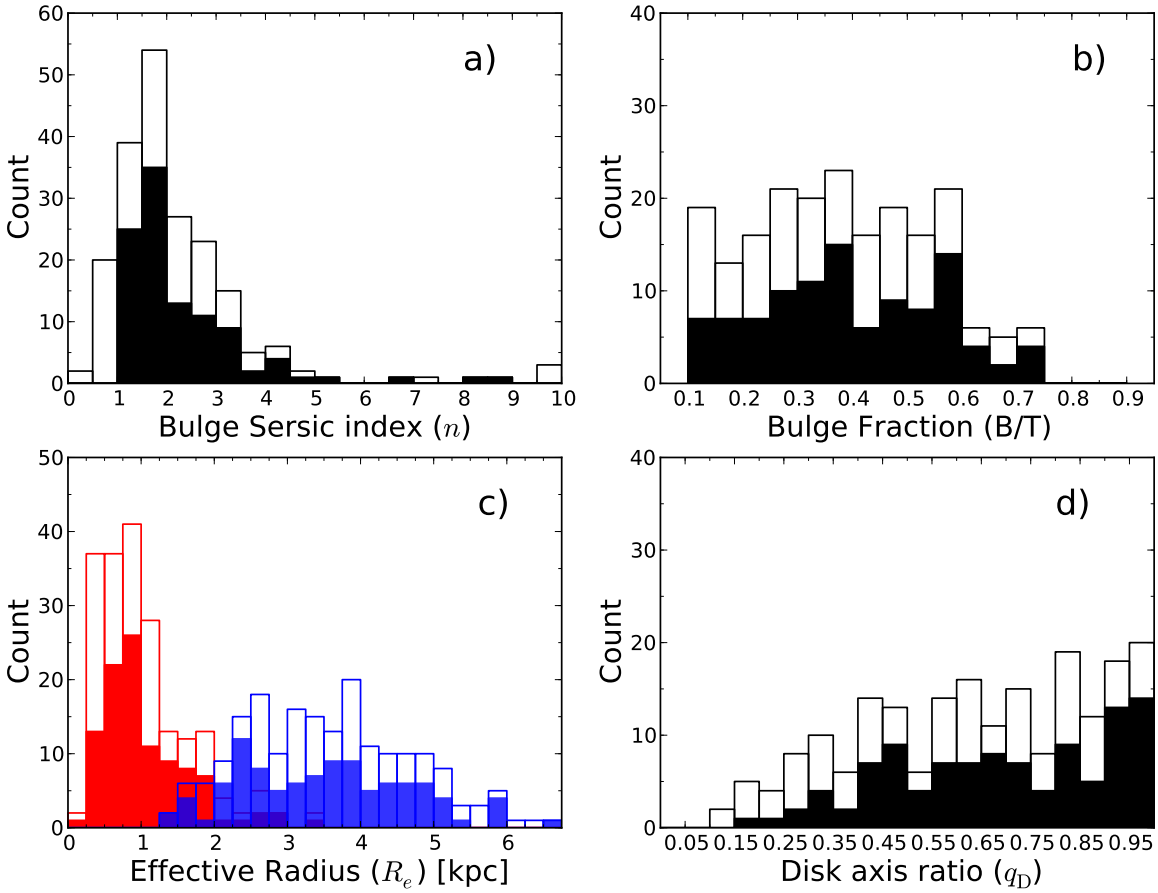

Figure 5.1: The measured (analysis sample) structural parameter distributions for the (freely-fit) g band galaxy models. The unfilled portion of each histogram bar corresponds to the number of 'flagged' fits (see Section 3.5) in that bin. **a):** Bulge Sérsic index, n. **b):** Bulge-to-total luminosity ratios, B/T (bulge fractions). **c):** Effective half-light radii of bulges ($R_{e,B}$; red) and disks ($R_{e,D}$; blue). Distribution overlap is indicated in purple. **d):** Disk axis ratio (b/a), $q_{\rm D}$.

radii ($0.5 \lesssim R_{e,B} \lesssim 1.5$ kpc), with a median value of 0.9 kpc (Figure 5.1c). Note that these sizes are not seeing-limited, as the half-width at half maximum (hwhm) of the MegaCam imaging ($\sim 0.4''$) corresponds to 0.2 kpc. Galaxy disks are larger (median $R_{e,D} = 3.6$ kpc), and spread over a wider range of effective radii ($2.0 \lesssim R_{e,D} \lesssim 6.0$ kpc)[1]. By comparison, Huang et al. (2013; hereafter H13) performed 3-component Sérsic fits to ~ 100 Carnegie-Irvine Galaxy Survey elliptical galaxies across a range of environments. The bulge Sérsic indices measured in our study are distributed similarly to the 'inner' (median $n \sim 2.0$) and 'outer' (median $n \sim 1.6$) H13 Sérsic structures, with sizes approximately consistent ($< 2\sigma$) with the former ($R_{e,B} \sim 0.6$ kpc). Coma disk sizes fall between the median value of 'middle' ($R_{e,B} \sim 2.5$ kpc) and 'outer' ($R_{e,B} \sim 10.5$ kpc) H13 structures. Thus the bulge components in our study are equivalent to the 'inner' H13 structures, while the disks in this work are a combination of the 'middle' and 'outer' components.

The $R_{e,B}$ and n values measured here for bulges ($n \sim 2$, $R_{e,B} \sim 1$ kpc) are similar to previous measurements of dwarf ellipticals (Graham & Guzmán, 2003) and the (pseudo)bulges of giant *S0*s and (early-type) spirals in Coma (Aguerri et al., 2004). A more general study of ETGs in the core of Coma (Gutiérrez et al., 2004) found a broader range of bulge sizes due to the presence of giant ellipticals in the sample. Nevertheless, this *E + S0* sample yielded average $R_{e,B}$ and n values consistent with the results of the present work. Additionally, as noted in other relevant works (Graham, 2013, H13), these bulges are comparable in structure with 'red nugget' galaxies (e.g. Buitrago et al., 2008; Damjanov et al., 2009) observed at $z > 1.5$ ($R_{e,B} \sim 1$ kpc, $n \sim 2$). This similarity between *S0* bulges and high-redshift, compact galaxies may indicate formation of *S0* progenitors via rapid disk-growth around pre-existing bulges between $z \approx 1.5$ and the epoch of quenching. However, current stellar mass estimates for red nuggets are approximately an order of magnitude larger than the mass of typical Coma galaxy bulges. Hence, a scenario in which disks are assembled around existing red nuggets is disfavoured.

The disks' apparent axis ratios are approximately equivalent to the cosine of their inclinations to the line-of-sight. The measured axis ratios are consistent with the expected flat distribution of inclinations down to $q_{\rm D} = 0.3$ (Figure 5.1d). Significantly fewer disks with

[1]The effective half-light radius of an exponential disk is related to the scale length parameter (R_s) used during fitting as $R_{e,D} = 1.678 R_s$

smaller axis ratios (more inclined) are detected, particularly for well-fit galaxies. This deficit of highly inclined galaxies is apparent even if the initial sample is not filtered, and a similar distribution of Sérsic-only axis ratios is measured. This indicates a systematic bias in the fitting against high ellipticity (i.e. edge-on) structures, and/or reflects the intrinsic thickness of *S0* disks.

In summary, archetypal *S0*s are disk-dominated (B/T~ 0.4) systems with compact ($R_e \sim 1$ kpc) 'pseudobulges' ($n \sim 2$). The exponential disks in these galaxies are larger (by construction), with a wider range of measured sizes ($R_e \sim 4$ kpc on average). A small deficit of high-ellipticity galaxies is apparent in the analysis sample, which is attributed to either fitting bias, or intrinsic *S0* disk thickness.

5.2.2 Trends with galaxy luminosity/mass

Variation of galaxy structure with luminosity indicates structural evolution due to the quenching mechanisms responsible for populating the red sequence. Conversely, detection of *equivalent* structural scaling relations for *S0*s and their (spiral-like) progenitors would indicate preservation of component structures during quenching. As such, trends in component structure can be used to distinguish between the bulge enhancement and disk fading scenarios. In this section, I investigate variation of archetypal *S0* bulge and disk structures as a function of total galaxy magnitude.

The measured structural parameters correlate with the total luminosity of the galaxy. More luminous *S0*s are more bulge-dominated (Figure 5.2), with more centrally concentrated (larger n) bulges (Figure 5.3), and larger disks (Figure 5.4). No significant size-luminosity trend is detected within galaxy bulges. Thus, the process(es) responsible for building mass in these galaxies caused significant disk growth, with relatively little change to their bulge sizes. No significant change is noted in the size-luminosity slopes if component sizes are compared to component magnitude instead of total magnitude. By comparison, Laurikainen et al. (2010) found a significant correlation between $R_{e,B}$ and (bulge) K band luminosity for *S0*s. However, their *S0* sample is intrinsically brighter (M_K (bulge) $< -21 \approx M_g$ (total) < -20) than the present work. Thus, the size-luminosity trend for *S0* bulges is flat for the range of galaxy luminosities studied here ($M_g > -20.5$) with a significant upturn for

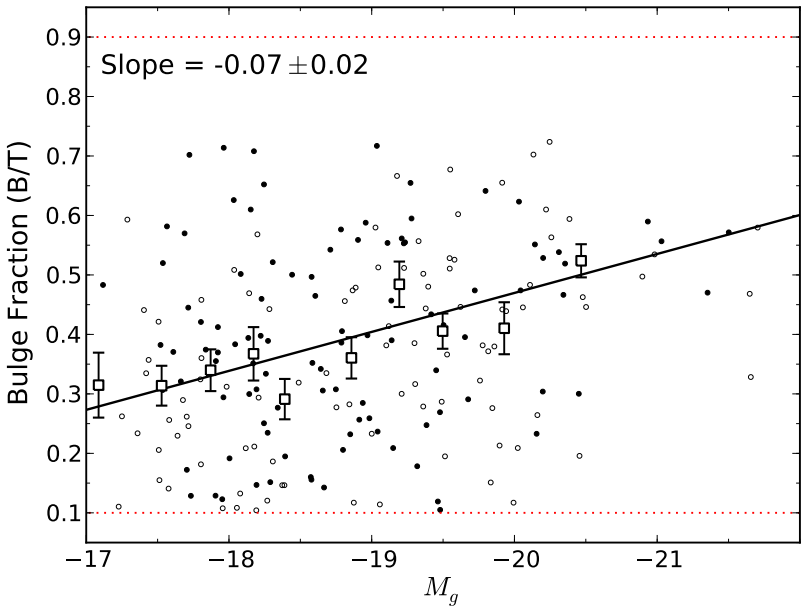

Figure 5.2: The galaxy bulge fractions (B/T) measured from g band (analysis sample) galaxy models plotted against the corresponding absolute (bulge + disk) magnitudes (M_g). Unfilled points indicate flagged fits (see Section 3.5). Best-fit linear trends (solid lines) are fit to median parameter values calculated in magnitude bins (large square points), weighted by the robust standard error in each bin (error bars). The slopes and their bootstrap errors (calculated from the unbinned data) are included in each plot. Dashed lines in each plot indicate any constraints on parameters values (green: hard limits imposed on GALFIT; red: sample filtering cuts).

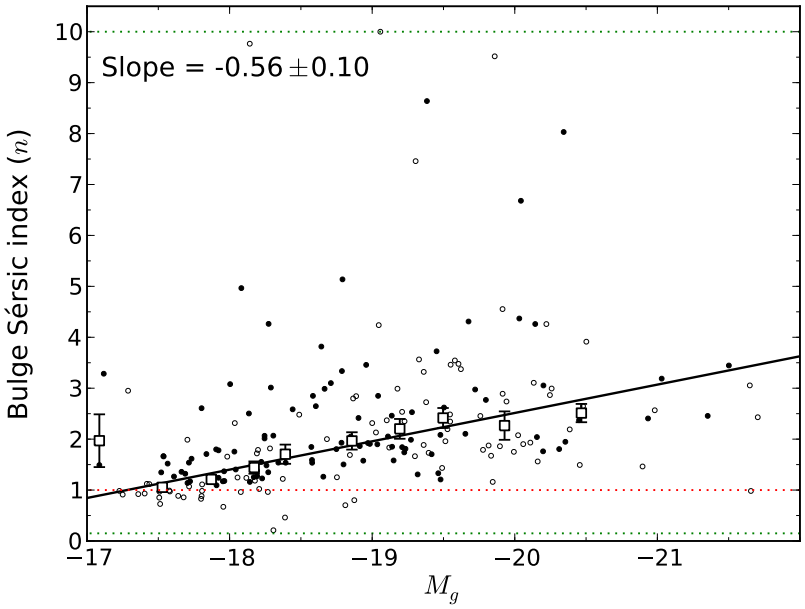

Figure 5.3: As Figure 5.2: the bulge Sérsic indicies (n) for g band (analysis sample) galaxy models plotted against the corresponding absolute (bulge + disk) magnitudes (M_g).

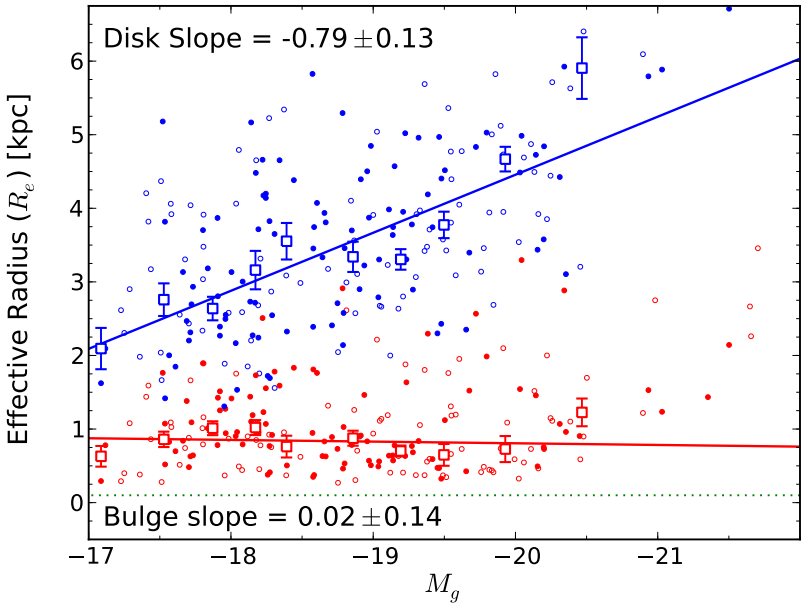

Figure 5.4: As Figure 5.2: bulge (red) and disk (blue) effective half-light radii (R_e; kpc) measured from g band (analysis sample) galaxy models plotted against the corresponding absolute (bulge + disk) magnitudes (M_g).

brighter *S0*s (see also Méndez-Abreu et al., 2008; Hyde & Bernardi, 2009; Allanson et al., 2009).

The disk size-luminosity slope ($R_{e,D}$ vs. M_g) measured in the present work is -0.85 ± 0.14 kpc mag^{-1}, consistent with the equivalent observed slope for star-forming spiral galaxies measured for the same magnitude range (-0.93 ± 0.06 kpc mag^{-1}; see Figure 5.5). This spiral sample was selected from Simard et al. (2011) using Galaxy Zoo morphology (Lintott et al., 2011), and MPA-JHU DR7 star formation rates. A marginal offset in total magnitude is noted between the best fit trends of *S0*s and spirals (-0.52 ± 0.20 mag; i.e. for a fixed disk size, 'archetypal' *S0* galaxies are 0.52 mag brighter than star forming spirals). If the size-luminosity trend is instead measured in terms of disk luminosity, the slopes for *S0*s and spirals do not change significantly, but the luminosity offset is reduced to -0.27 ± 0.12 mag (see Figure 5.6).

The slope of the B/T-luminosity trend measured here (-0.07 ± 0.02) is consistent with the R band slope in H10 (-0.069 ± 0.020) despite differing B/T distributions. This indicates a significant trend of increasing bulge dominance for brighter red sequence galaxies (or alternatively: fainter galaxies are more disk-dominated). This trend cannot be caused by fading of the disk component for more luminous galaxies due to shallowness of the B/T-M_g

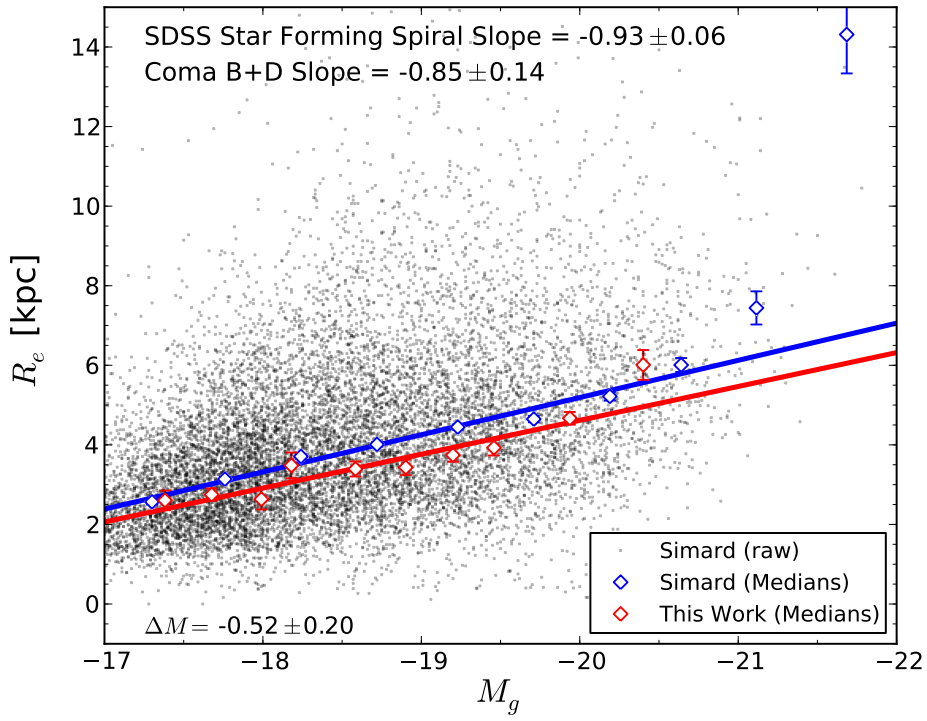

Figure 5.5: The size-luminosity relation ($R_{e,D}$ [kpc] vs. absolute bulge + disk g band magnitude) for the disks of *S0*s (this work; red) and star forming spirals (black). Spiral galaxies are plotted using bulge-disk decomposition parameters from Simard et al. (2011) for all galaxies at $z < 0.03$ where a debiased probability of spiral morphology (Galaxy Zoo, Lintott et al., 2011) is greater than 0.5. Star forming galaxies were selected using the MPA-JHU DR7 star formation catalogue (Brinchmann et al., 2004) where the specific star formation rate, $\log(M_\odot$ yr^{-1} $M_*^{-1}) > -10.5$. Median disk size values are measured in bins of absolute magnitude (0.5 mag width), to which best fit lines are fit. The slope uncertainties are bootstrap errors calculated from the unbinned data. This robust fitting is carried out over the same magnitude range for both datasets.

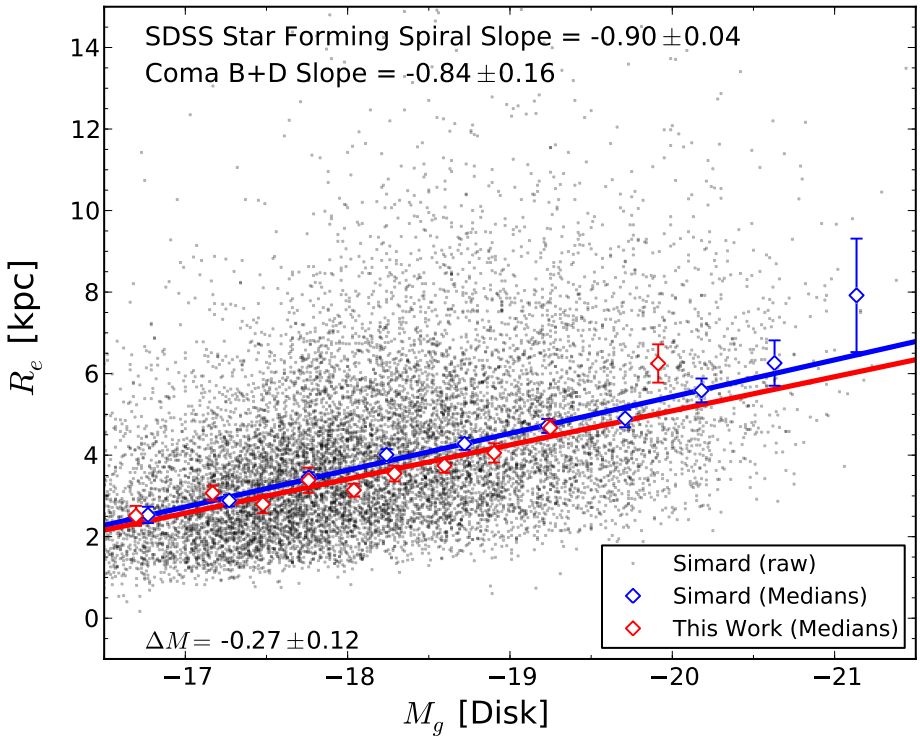

Figure 5.6: As Figure 5.5, the size-luminosity relation as a function of component luminosity ($R_{e,D}$ [kpc] vs. absolute disk g band magnitude).

slope[2]. Thus, *S0* galaxy luminosity is more strongly correlated with the luminosity of the component bulges, than with disk luminosity.

A significant variation in apparent inclination with total magnitude is noted (0.06 ± 0.02; Figure 5.7), suggesting that brighter galaxies are more likely to be inclined to the line-of-sight. However, this correlation results from the presence of 'flagged' galaxies ($q_{\rm D}$ biased by bar component), and the absence of 'atypical' galaxies (high $q_{\rm D}$ on average) towards the more luminous end. Removal of either bias results in no significant variation in axis ratio with luminosity. The apparent inclination of a galaxy does not correlate with its physical properties. Thus, the bias against detection of edge-on systems does not impede the analysis of the colour and luminosity distributions reported in later sections. However, galaxies more inclined than 60° ($q_{\rm D} < 0.5$) may contain additional undetectable structures (e.g. bars or spiral patterns seen edge-on). As such, these galaxies may yield unreliable model parameters.

In summary, with increasing galaxy luminosity, archetypal *S0*s become increasingly dominated by their bulge components (which in turn are higher n structures). Bulge size does not correlate with galaxy luminosity over the range studied, while disks exhibit a strong

[2] $\Delta {\rm B/T} \leq -0.6(1 - {\rm B/T})$ per mag indicates a reduction of disk luminosity.

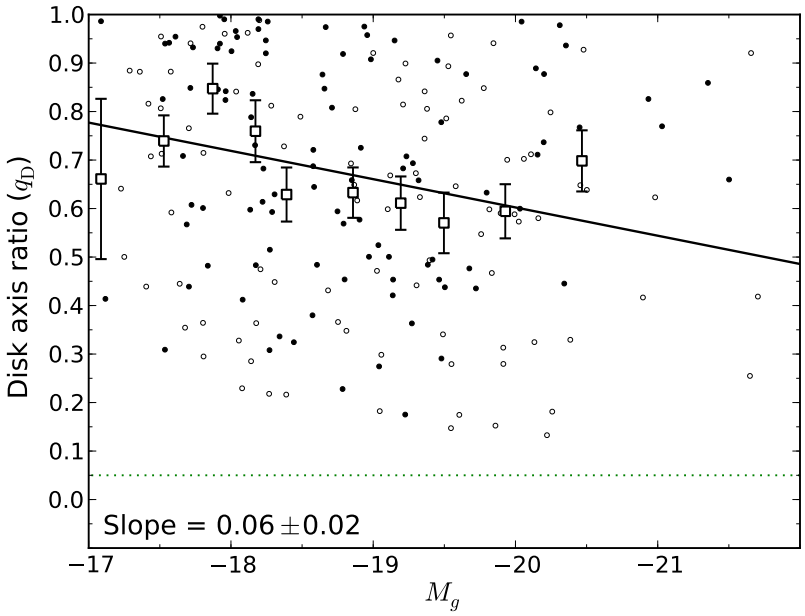

Figure 5.7: As Figure 5.2: disk component axis ratio ($q_{\rm D}$) measured from g band (analysis sample) galaxy models plotted against the corresponding absolute (bulge + disk) magnitudes (M_g).

size-luminosity trend consistent with the equivalent scaling relation for local (star-forming) spiral galaxies.

5.2.3 Structural trends with environment

With increasing projected distance from the cluster core, galaxies exhibit no significant correlation in bulge Sérsic index (Figure 5.8), disk axis ratio (Figure 5.9), or the half-light radii of either structural component (Figure 5.10). Thus, any contribution by bulge enhancement effects must have occurred prior to entering the cluster potential. Conversely, if *S0* formation is driven primarily by the cluster environment, then the quenching mechanism cannot significantly alter the structure of the bulge or disk components. Therefore, the offset in size-luminosity trends between *S0*s and spirals noted in Section 5.2.2 cannot be due to an (environment-driven) physical truncation of the disk component.

Galaxy bulge fraction increases towards the cluster core at a $\sim 2\sigma$ level (Figure 5.11). Thus, the relative luminosities of structural components in archetypal *S0*s vary significantly between the cluster outskirts and core. This implies either environment-driven enhancement of bulge luminosity or disk fading, despite consistent structures at all cluster radii. Since bulge enhancement mechanisms are less likely to be structure-preserving, this supports disk

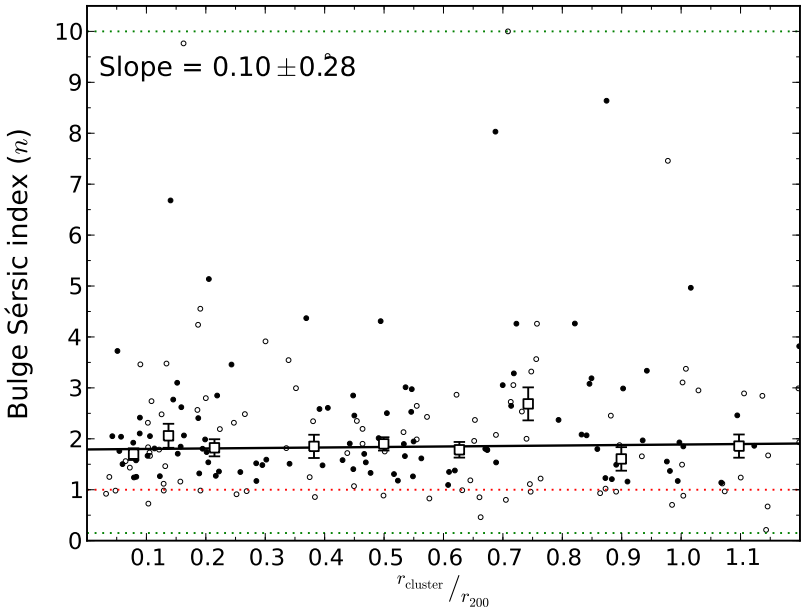

Figure 5.8: The measured (analysis sample) bulge Sérsic indices (n) for g band (analysis sample) galaxy models plotted against their radial distance from the cluster centre ($r_{\rm cluster}$; units of r_{200}). Unfilled points indicate flagged fits (see Section 3.5). Best-fit linear trends (solid lines) are fit to median parameter values calculated in magnitude bins (large square points), weighted by the robust standard error in each bin (error bars). The slopes and their bootstrap errors (calculated from the unbinned data) are included in each plot. Dashed lines in each plot indicate any constraints on parameters values (green: hard limits imposed on GALFIT; red: sample filtering cuts).

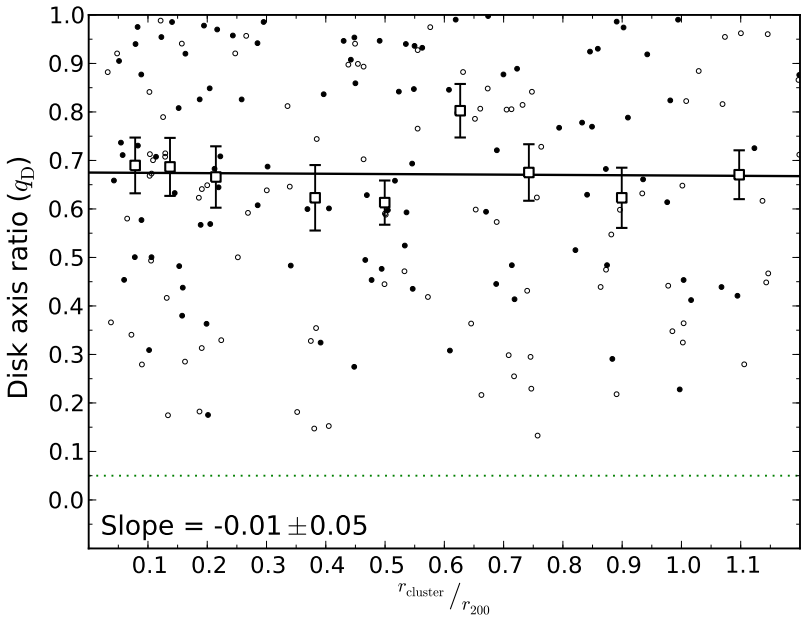

Figure 5.9: As Figure 5.8: disk component axis ratio ($q_{\rm D}$) measured from g band (analysis sample) galaxy models plotted against their radial distance from the cluster centre ($r_{\rm cluster}$; units of r_{200}).

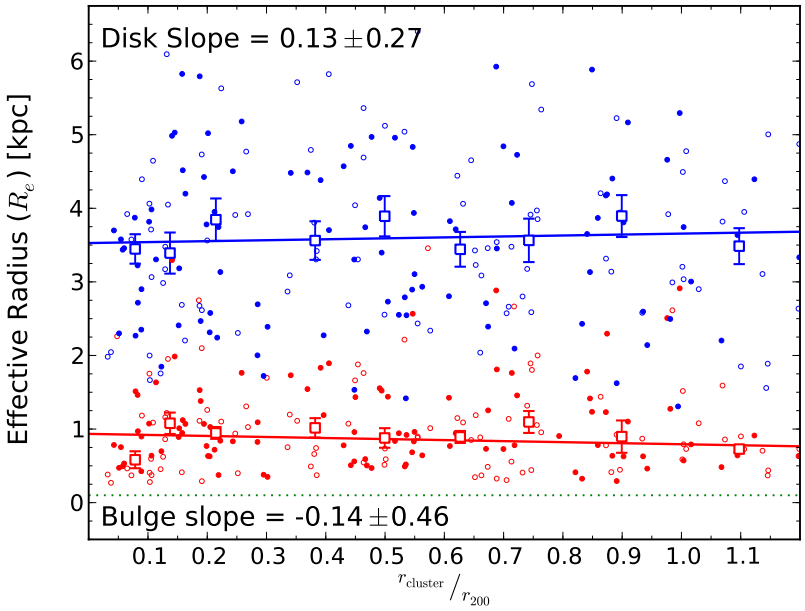

Figure 5.10: As Figure 5.8: bulge (red) and disk (blue) effective half-light radii (R_e; kpc) measured from g band (analysis sample) galaxy models plotted against their radial distance from the cluster centre ($r_{\rm cluster}$; units of r_{200}).

fading mediated by the cluster environment.

In summary, galaxy component structures do not vary between the Coma cluster outskirts and core. Nevertheless, bulge fraction increases with decreasing clustercentric radius. Since bulge enhancement mechanisms are unlikely to increase bulge luminosity without changing its structure, environment-driven fading of the disk component is favoured as the formation mechanism for archetypal *S0*s.

5.2.4 Fingerprints of quenching in the structural parameters of *S0*s

Different quenching mechanisms (see Section 1.2) cause distinctive changes to a galaxy's structure in addition to truncating its star formation. As such, the structural ensemble properties of the galaxy sample provide a fossil record of the physical mechanisms which have influenced their evolution. In this section, I investigate trends in bulge and disk structure with the aim of identifying the primary mechanism responsible for the formation of Coma cluster *S0*s. In particular, I focus on the B/T disparity between *S0*s and their less bulge-dominated, spiral-like progenitors (Dressler, 1980b; Lackner & Gunn, 2012). This apparent B/T increase is discussed in the context of either 'bulge-enhancement' (increased B/T from mass build-up in the bulge) or 'disk-fading' (increased B/T from decreased disk luminosity)

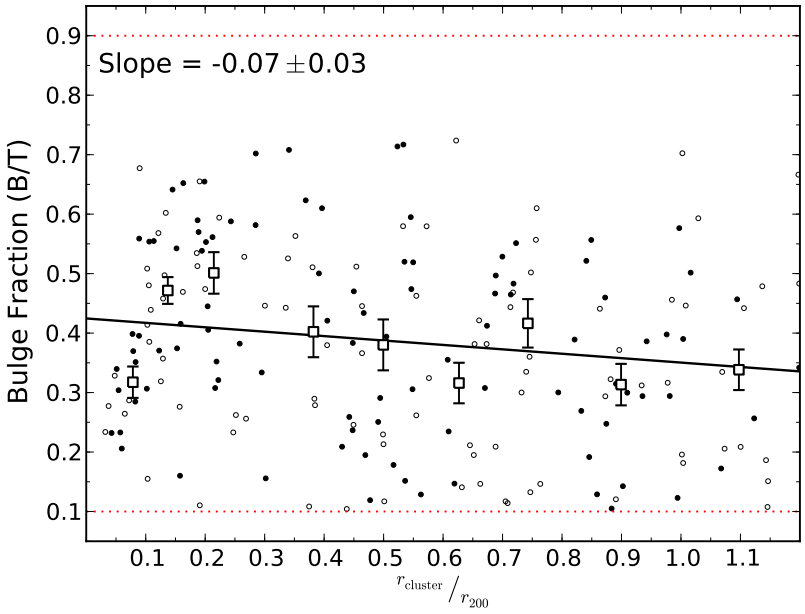

Figure 5.11: As Figure 5.8: galaxy bulge fraction (B/T) measured from g band (analysis sample) galaxy models plotted against their radial distance from the cluster centre ($r_{\rm cluster}$; units of r_{200}).

transformation mechanisms.

As discussed in Section 1.2.2, galaxy (minor/major) mergers cause bulge size growth, and may disrupt or destroy disk structures. Thus, if brighter (higher B/T) galaxies built a greater fraction of their present-day mass through merger events, then bulge $R_{e,B}$ should correlate with total galaxy luminosity. These predictions are incompatible with our observed size-luminosity relations; the measured physical sizes of these bulges do not vary significantly with luminosity over the galaxy luminosity range analysed in the present work (Figure 5.4). A correlation may exist for more luminous galaxies ($M_g < -20.5$), however the small number of galaxies in this luminosity range limits its detection in the present sample.

For galaxy disks, a strong correlation is measured between half-light radius and total galaxy luminosity, indicating that the disks survive after transformation. This trend is present even if the requirement that disks dominate the outer part of their galaxies (i.e. archetypal structures) is relaxed, and thus is not a consequence of our selection bias. Furthermore, when compared to the disks of local, star-forming spiral galaxies, the *S0*s in Coma have a similar size-luminosity slope (Figure 5.5), albeit with an offset in magnitude (see disk fading discussion below). Thus, the structural scaling relations of (spiral-like) progenitor galaxies are preserved for *S0* disks. Disk-destructive mechanisms (i.e. major mergers) are disfavoured

as the dominant process in *S0* formation.

Rawle et al. (2013) found that Coma *S0* galaxies are offset from the Tully-Fisher Relation (TFR) for spirals such that for a fixed rotation velocity, *S0*s are 1.1 ± 0.2 mag fainter in total galaxy luminosity than spirals in the g band. Assuming that this offset is a pure change in disk luminosity, then the progenitor of an 'average' Coma *S0* ($M_g = -18.8 \pm 0.1$ mag, B/T $= 0.38 \pm 0.01$) was brighter ($M_{g,0} = -19.9 \pm 0.2$ mag) and less bulge dominated (B/T$_0 = 0.14 \pm 0.02$). Hence, disk components were faded by 1.5 ± 0.2 mag on average in g. However, it has been shown that for a fixed disk size, Coma *S0*s are *brighter* (g band: 0.52 ± 0.20 mag globally, 0.27 ± 0.12 mag for disks) than local star-forming spiral galaxies (Figures 5.5 and 5.6). Thus, the simplest model of disk fading - wherein only disk *luminosity* is changed - is incompatible with the results of the present work.

To reconcile disk fading with the observed size-luminosity relations, either progenitor (exponential) disks must be intrinsically smaller (and/or brighter) than the disks of present-day spirals, or disks must have been truncated in size during transformation to *S0*s (as previously noted in Coma; Aguerri et al., 2004). This may be observed as e.g. 'Type II' surface brightness profiles (see Pohlen & Trujillo, 2006; Erwin et al., 2012; Roediger et al., 2012; see also Chapter 8). Physical truncation may result from the stripping of outer disk stars predicted from galaxy harassment (de Jong et al., 2004; Aguerri & González-García, 2009), however the lack of correlation between disk size and $r_{\rm cluster}$ disfavours environment-driven truncation. Fading the total galaxy luminosity of star-forming spirals by 1.1 mag requires a disk size offset (i.e. *S0* disks smaller than spiral disks) of 1.5 ± 0.3 kpc (at fixed galaxy luminosity) to be consistent with the observed global Coma *S0* size-luminosity trend. Repeating this analysis for size-luminosity as a function of disk luminosity yields a similar size offset (1.5 ± 0.2 kpc). From the average observed disk size for our sample ($R_s = 2.2 \pm 0.1$ kpc), *S0* disks are thus $41 \pm 6\%$ smaller on average than the equivalent disks of local spiral galaxies.

A progenitor size bias scenario (i.e. *S0* progenitors are intrinsically smaller than present-day spirals) is in qualitative agreement with Trujillo et al. (2006), who found low n objects at $z \sim 2.5$ with sizes $\sim 3\times$ smaller than local galaxies. If present-day spirals and *S0*s share a parent progenitor population, then the disk size offset can be explained as interruption of disk growth when *S0* progenitors were quenched, while spiral progenitor disks continued

to grow via star formation. Using the size growth predictions of Trujillo et al. (2006), the measured disk size offset corresponds to a quenching redshift of $z \sim 1.5$ for Coma cluster *S0*s. Note however, that galaxies at lower $r_{\rm cluster}$ entered dense environments (e.g. the Coma cluster or preceding galaxy groups) at earlier epochs. If the quenching formation mechanism for *S0*s was driven by the cluster environment (or by pre-processing in groups), then disk growth ended earlier for galaxies in the cluster core. However, as reported in Section 5.2.3 no trend in disk size was found with clustercentric radius. Thus, termination of disk growth cannot explain the spiral/*S0* size offset if quenching is driven by the cluster environment.

A disk-fading scenario is supported by the detection of a strong correlation between disk component and total galaxy colours (Lackner & Gunn, 2012)[3]. The (global) colour transition from blue [cloud] to red [sequence] galaxies was thus interpreted as driven by redder disk colours. Disk-fading was disputed by Burstein et al. (2005; see also Christlein & Zabludoff, 2004), who found that *S0*s have equal (or greater) K band luminosity than spirals, rather than less. However, this offset compares present-day *S0*s to present-day spirals, rather than to their progenitors. In addition, the measurement of *global* luminosity differences does not strictly rule out disk fading (i.e. if the bulge is brighter).

In summary, through analysis of the structural parameters of the bulges and disks of *S0*s, I have investigated the physical mechanisms responsible for their formation. The detection of a strong size-luminosity relation for disks - but not for bulges - does not support a bulge-enhancing origin for *S0*s, particularly for disk-disruptive (major) and bulge size growing (minor) mergers. While the probable importance of mergers in bulge mass assembly at early times has been previously noted (e.g. Fisher et al., 1996; Barway et al., 2009, 2013), here I am asserting that this process is not responsible for the final transformation which yields the observed *S0*s. This work therefore supports disk-fading as the dominant formation mechanism for *S0*s in the Coma cluster. However, as *S0*s are brighter (at a fixed disk size) than local spirals, *S0* disks must be significantly smaller than the disks of today's star-forming spirals. Therefore, either the disks of cluster *S0* progenitors were intrinsically smaller or brighter than local field spiral disks, or these disks were truncated during transformation to *S0*s.

[3]Lackner & Gunn also report an increase in 'bulge size' (from B/T) as galaxies transition onto the red sequence. However, it is not necessary to invoke bulge growth to explain an increase in B/T if disk fading is a dominant effect.

5.3 Summary

The bulge and disk structures of red-sequence galaxies (with $-17 > M_g > -22$) in the Coma cluster have been characterised using deep u, g, and i band imaging. Extensive sample vetting was carried out to isolate a sample of 200 galaxies well-described by an 'archetypal' *S0* (central) bulge + (outer) disk morphology. In this chapter, I have described the distributions and trends (as functions of total/component luminosity, and cluster-centric radius) of the g band structural bulge and disk parameters resulting from decomposition analysis.

The main results of this chapter are as follows:

i) ***S0* bulges have physical sizes, $R_{e,B} \sim$ 1 kpc, and profile shape, $n \sim$ 2, on average.**

Bulges are thus structurally similar to both dwarf ellipticals in Coma, and 'red nugget' galaxies observed at $z > 1.5$ (albeit an order of magnitude smaller in mass than the latter).

ii) **No significant correlation between bulge half-light radius and total galaxy luminosity is detected (for galaxies fainter than $M_g = -20.5$).**

This is inconsistent with predictions for a 'bulge-enhancement' scenario of *S0* formation via major mergers (R_e increases $\propto M$) or minor mergers ($R_e \propto M^2$).

iii) **No significant variation in bulge or disk structure (i.e. bulge n, bulge and disk R_e) is observed with projected distance from the Coma cluster centre.**

Thus, environmental quenching mechanisms (if present) do not affect galaxies structurally, implying a relatively gentle formation mechanism for *S0*s. Alternatively, environment mediated evolutionary pathways may cause galaxies to cease to be structurally archetypal.

iv) **Disk effective half-light radius is strongly correlated with total galaxy luminosity.**

The R_e-M slope for *S0* disks is consistent with the size-luminosity relation for today's star-forming disk galaxies. However, these trends are separated in luminosity such that *S0*s are brighter than such spirals. If *S0* galaxies are formed through disk fading, then their disks are 40% smaller on average than the disks of equally luminous local spirals. Thus, either their progenitor's disks were intrinsically smaller than the disks of today's

spirals (suggesting a quenching epoch of $z \sim 1.5$), or were truncated in size during transformation to *S0*s. However, as no trend in disk size was noted with clustercentric radius, neither scenario could be driven by environment-dependent mechanisms.

As this study focuses purely on galaxies with 'archetypal' bulge + disk structures, we do not rule out a merger-based formation scenario in *all* early-types. 'Atypical' *S0* galaxies in the present work represent the most bulge-dominated ETGs, and hence are the most likely candidates for 'traditional' ellipticals. The possibility of multiple evolutionary pathways for 'archetypal' and 'atypical' ETGs (e.g. due to a relatively quiet merger history for 'archetypal' *S0*s) is investigated through multi-component decomposition in Chapter 7.

In the next chapter, the colour characteristics of bulge and disk components will be described, including discussion of the colour-magnitude and colour-(cluster) radius trends. SSP models will be used to estimate the stellar population property differences which yield the measured offsets in component colour. In addition, variation of the colour properties with (visual) morphological classification will be investigated.

Chapter 6

Photometric Component Properties

6.1 Introduction

The photometric colour of an early-type galaxy is strongly correlated with the physical properties of its constituent stars. Through use of simple Synthetic Stellar Population (SSP) models, colours can be used to constrain the age (and metallicities) of galaxy stellar populations, and hence investigate their star formation history. Analysis of colours is thus an important tool when investigating the quenching and evolution of ETGs.

In this chapter, I report the separated photometry of Sérsic bulges and exponential disks following the decomposition analysis described in Chapter 3. A sample of 200 galaxies well-fit by an archetypal *S0* structure (central bulge + outer disk) was selected to ensure that dissonance between the models and underlying galaxy structure does not distort the measured component photometry. Through analysis of component colour-magnitude trends, I investigate whether Coma's *S0* red sequence is a consequence of global or component colour-magnitude trends (i.e. more luminous *S0* galaxies redder as a whole, or increasingly red in only one structural component). As such, I place photometric constraints on the quenching history of Coma *S0*s, based on estimates of component ages. Furthermore, variations of component colours as a function of cluster radius and with morphological types are investigated, yielding insight into the role of the Coma cluster environment in quenching, and any variation of quenching mechanisms with observed structural morphology.

The structure of this chapter is as follows: First, I present a comparison of the component colour magnitude results derived using both fixed multi-band, and internal gradient fitting

techniques. Analysis of the colour offsets between bulges and disks is performed using SSP models, yielding constraints on the age/metallicity differences between these components. Secondly, (cluster) radial trends of component colours are investigated, yielding estimates of age differences between the components of galaxies in the cluster core and outskirts. Thirdly, visual morphological classifications (where available) are investigated in the context of component photometry and photometric trends. Fourthly, I present a comparison between the (cluster-radial) photometric results of the present work, and those presented in similar literature decomposition studies. Finally, I summarise the conclusions drawn in this chapter.

6.2 Colour-magnitude trends

This section presents an analysis of the separated red sequences for bulge and disk components in the Coma cluster. The slopes and systematic colour offsets between these components are then used to constrain the stellar population properties of archetypal Coma *S0*s. A full catalogue of the u, g, and i band photometry measurements is presented in Tables A.1 (g) and A.2 (u, i) of Appendix A.

6.2.1 Fixed multi-band fitting

Here, I report on the results where the structural parameters measured in the g band were imposed on the galaxy images in the u and i bands. This results in a uniform colour for both the bulge and disk components at all radii ('fixed multi-band fitting'; see Section 3.7). Thus in this section, the galaxies' colour gradients are only interpreted as a colour difference between the bulge and disk.

The $g - i$ colours and colour differences between the two components are presented in Figure 6.1 (upper plot). Both the bulges and disks follow significant colour-magnitude trends, with more luminous *S0*s possessing both redder bulges and redder disks. This trend is significantly steeper for bulges. A median (bulge $-$ disk) $g - i$ colour offset of 0.097 ± 0.004 mag separates the two components, which increases significantly ($> 3\sigma$) for brighter galaxies. For example, an average $M_g = -18$ galaxy has a bulge $-$ disk separation of 0.080 mag in $g - i$, while the separation for an average $M_g = -21$ galaxy is 0.146 mag. The bulge

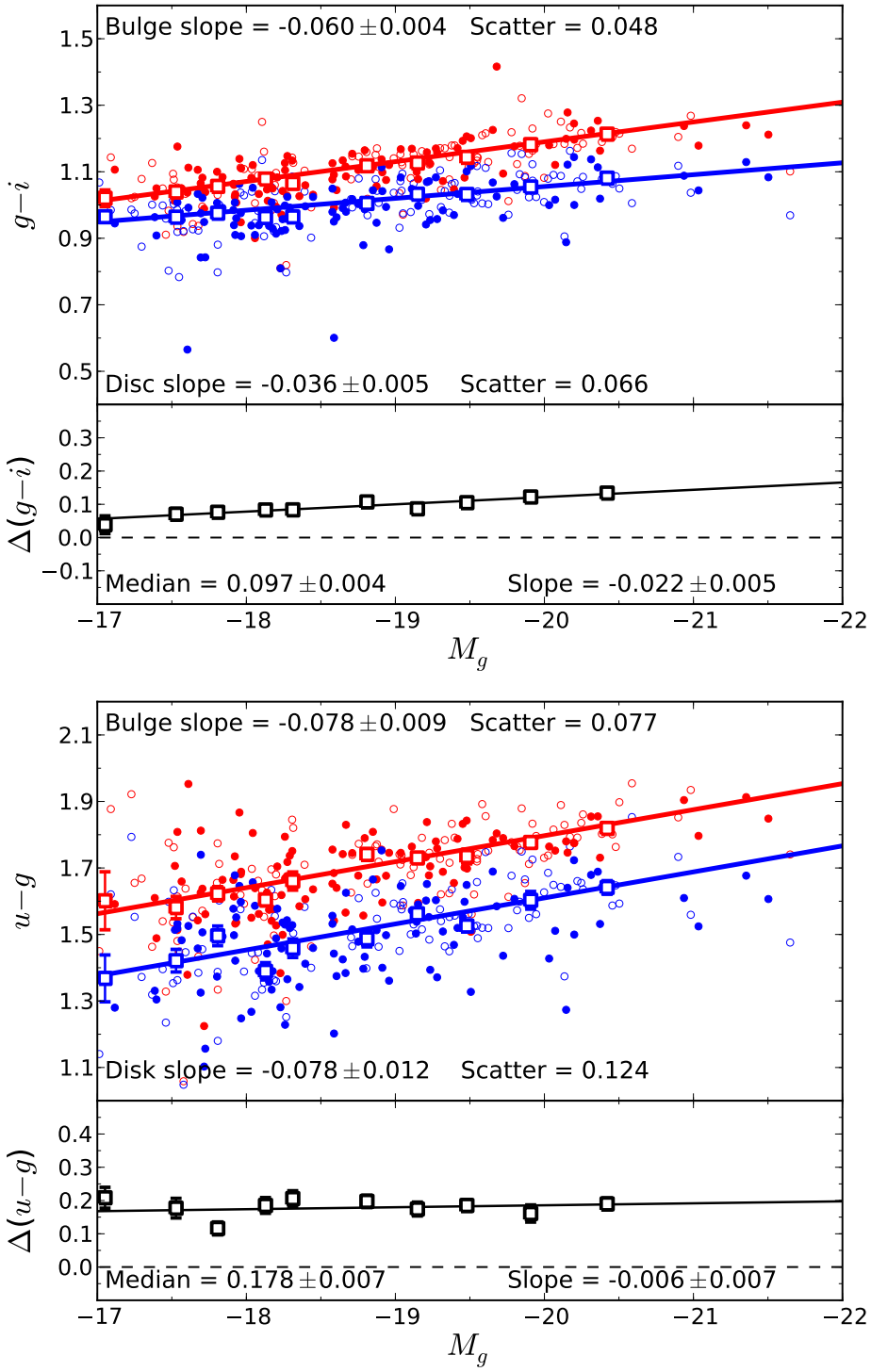

Figure 6.1: Colour-magnitude diagrams (**top:** $g-i$, **bottom:** $u-g$) for fixed multi-band structure. **Upper panels:** The bulge (red) and disk (blue) colours plotted against the absolute (bulge + disk) g band magnitudes of each galaxy. **Lower panels:** The colour difference (bulge − disk) plotted against absolute g band magnitude. Unfilled points indicate 'flagged' fits (containing weak extra components or asymmetries, see Section 3.5). Best-fit linear trends (solid lines) are fit to median colour values calculated in magnitude bins (large square points), weighted by the robust standard error in each bin (error bars). Slope uncertainties are bootstrap errors calculated from the unbinned data. A dashed black line at $\Delta(g-i)=0$ is included in the lower plot for comparison.

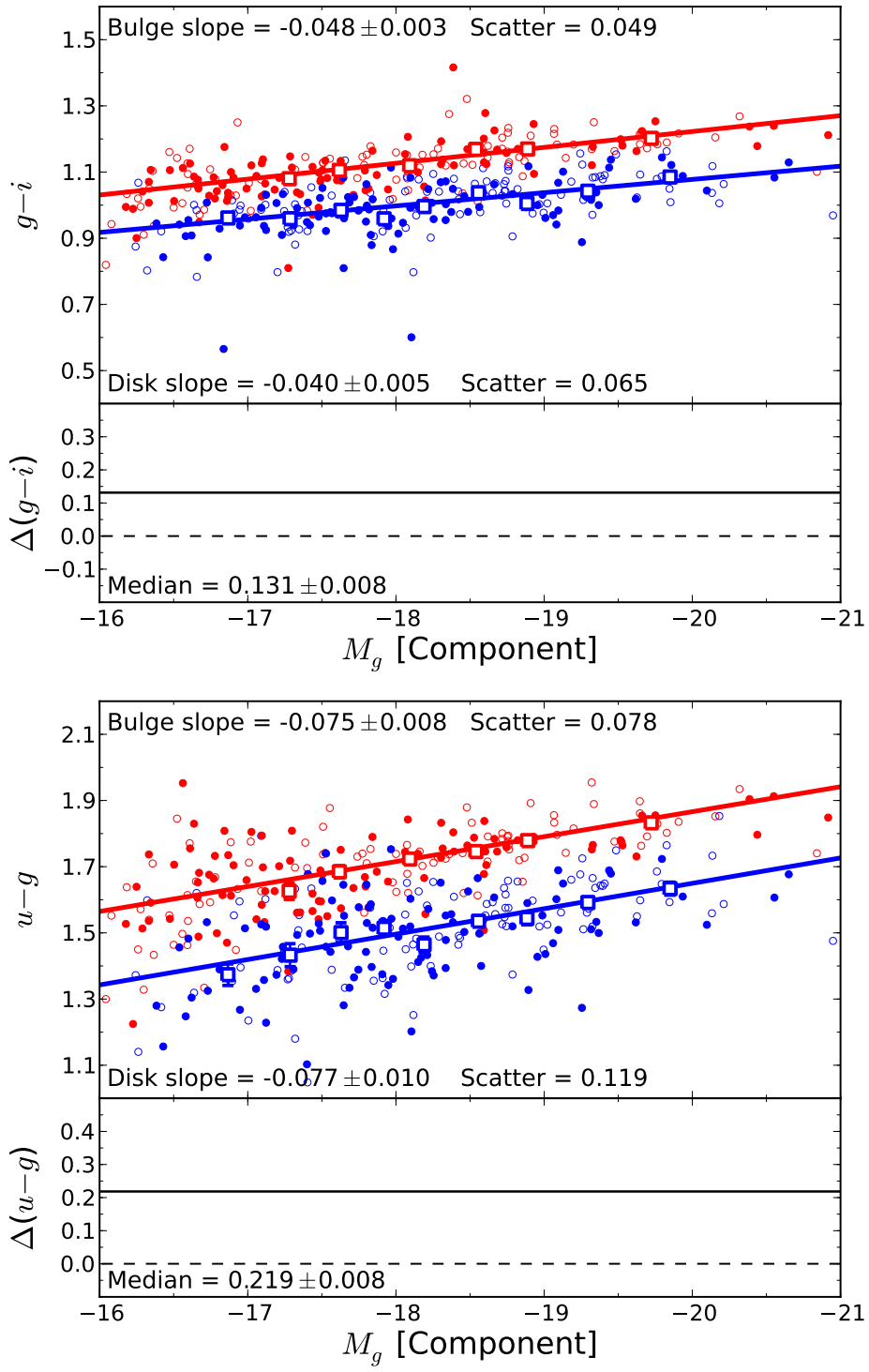

Figure 6.2: As Figure 6.1 for $g-i$ (**top**) and $u-g$ (**bottom**) colours and colour differences (bulges $-$ disks) as a function of component magnitude for fixed multi-band structure. Note that the slope of $\Delta(C)$ is zero by definition for component magnitudes.

colours have a slightly lower level of intrinsic scatter (i.e. additional scatter after removing measurement uncertainty) in $g-i$ relative to the colours of disks; 0.048 and 0.066 mag respectively.

The $u-g$ colour-magnitude trends (Figure 6.1; lower plot) are steeper than $g-i$, with no difference between the two components' slopes. Thus, the component colour offset in $u-g$ does not vary significantly with total luminosity. The median value of this offset is 0.178 ± 0.007 mag in $u-g$. Intrinsic scatter of component colours is significantly larger in $u-g$ than $g-i$. For bulges, the scatter relative to the $u-g$ colour magnitude trend is 0.077 mag, while the equivalent scatter for disks is 0.124 mag (i.e. an increase by a factor of 1.6 and 1.9 respectively, relative to $g-i$).

If the colour-magnitude trends are measured as a function of component (bulge or disk) magnitude (Figure 6.2), the colour-magnitude slopes of bulges and disks are consistent in both $g-i$ (bulges: -0.048 ± 0.003, disks: -0.040 ± 0.005) and $u-g$ (bulges: -0.075 ± 0.008, disks: -0.077 ± 0.010). The corresponding bulge $-$ disk colour separations at fixed component magnitudes are $\Delta(g-i) = 0.131 \pm 0.008$ mag and $\Delta(u-g) = 0.219 \pm 0.008$ mag. Here, a common colour-magnitude slope is assumed for both components such that colour differences are measured as a constant offset between the bulge and disk trends. Thus, $\Delta(g-i)$ and $\Delta(u-g)$ are significantly increased relative to the median (pairwise) separations at fixed total galaxy luminosity reported above.

A colour-colour plot depicting the bulge and disk $g-i$ colours is presented in the upper plot of Figure 6.3. The majority of galaxies form a broad sequence below the illustrative $y=x$ line. This indicates that galaxies with redder bulges have redder disks, and a galaxy's bulge is intrinsically redder than its disk. This is equivalent to the $B-R$ bulge/disk colour plot in MacArthur et al. (2004; see Figure 8). Converting component colours to $B-R$ ($\approx g-i+0.5$ using Jester et al., 2005), the *S0*s in the present work occupy the same region as the *S0* and *Sa* galaxies measured by MacArthur et al..

6.2.2 Models with Internal Gradients

Colour gradients were permitted in the model components to better reproduce the observed colour profiles of the galaxies. Thus in this section, the sample galaxies' colour gradients are

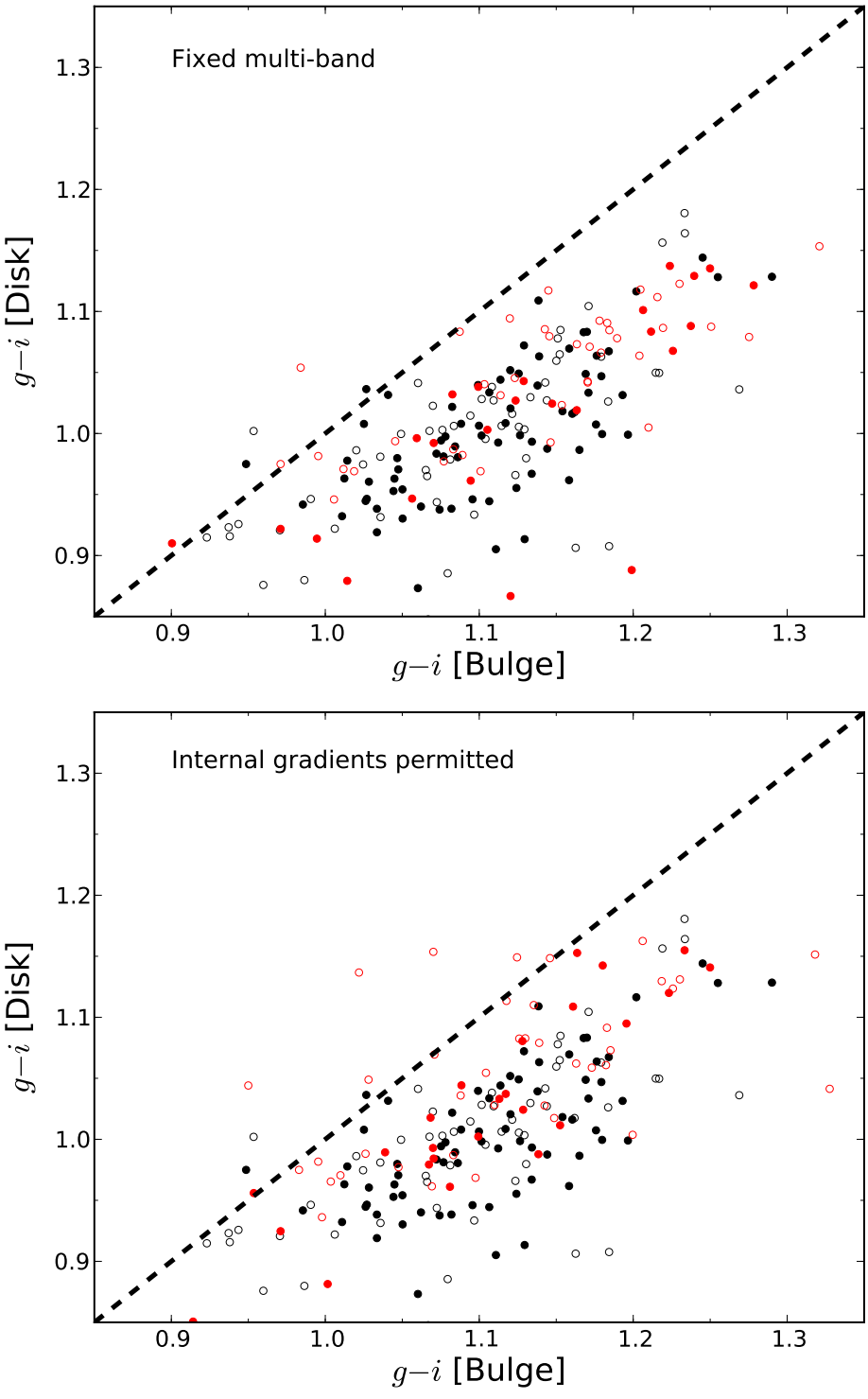

Figure 6.3: Colour-colour ($g - i$) diagrams of analysis sample bulges (x-axes) and disks (y-axes). **Top plot:** Fixed multi-band models. **Bottom plot:** Models where internal colour gradients are permitted. Unfilled points indicate 'flagged' galaxies, and red points highlight the galaxies which require internal gradients for at least one component. A line of $y = x$ (dashed line) is included in each plot for comparison.

interpreted as a combination of internal colour gradients *and* a colour difference between the bulge and disk.

Of the 200 galaxies in the analysis sample, 60 require component colour gradients (see Section 3.7.2). For these galaxies, the average (gradient $-$ no gradient) colour differences for bulge components are -0.022 ± 0.005 mag and -0.059 ± 0.009 mag in $g-i$ and $u-g$ (respectively), and 0.009 ± 0.005 mag and 0.023 ± 0.011 mag for disks. Thus, bulges are measured as systematically bluer when internal colour gradients are accounted for, while disks are redder (albeit at a marginal level). These systematic colour offsets result in the suppression of apparent bulge $-$ disk colour separations. For the 60 galaxies which require colour gradients, this decreases the apparent median $g-i$ colour separation from 0.104 ± 0.010 mag when internal gradients are ignored, to 0.073 ± 0.014 mag if those gradients are included. In $u-g$, this decrease in colour separation is even more pronounced (0.175 ± 0.013 without colour gradients; 0.104 ± 0.018 mag with).

The colour shifts measured when gradients were introduced highlights systematic biases in the measurement of bulge and disk colours if internal gradients are not accounted for. Hence, the exaggerated average bulge $-$ disk colour separations for fixed multi-band fitting is a consequence of attempting to account for complex colour profiles with offsets in component colour alone. In all subsequent sections, I report the 'best-fit' multi-band model results for the analysis sample ($N = 200$). Of these, 60 galaxies include internal gradients in at least one component, while 140 galaxies are adequately fit by a 'no component gradient' model.

The $g-i$ and $u-g$ colour-magnitude diagrams for the analysis sample when internal component gradients are permitted is presented in Figure 6.4. Here, the median $g-i$ colour separation for the sample as a whole is only ~ 0.01 mag smaller than was seen previously where component structures were held fixed from band to band (a difference of ~ 0.02 mag for $u-g$ separation). However, colour offsets are most evident towards the bright end of the galaxy magnitude distribution, where component gradients are required more frequently. This results in a larger decrease in the $g-i$ colour separation for brighter galaxies (0.03 mag at $M_g = -21.5$). For $u-g$, this is manifested as a steeper bulge colour-magnitude slope. However, this change is not significant ($\sim 1\sigma$).

As reported above for fixed multi-band fitting, the colour-magnitude slopes as a function

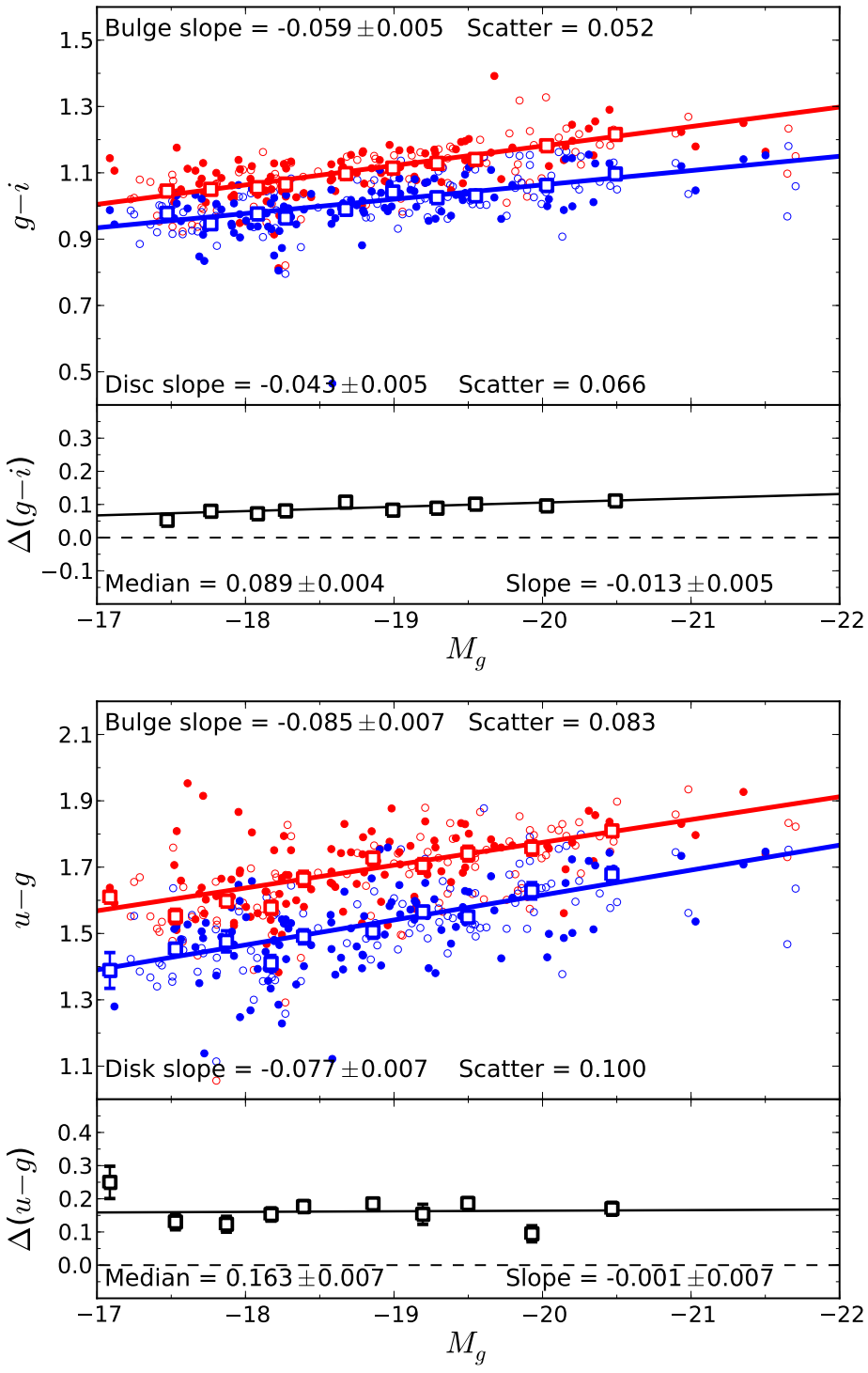

Figure 6.4: As Figure 6.1 for $g-i$ (**top**) and $u-g$ (**bottom**) colours and colour differences (bulges $-$ disks) when internal component gradients are permitted. 60 galaxies (out of 200) are affected by the inclusion of component gradients.

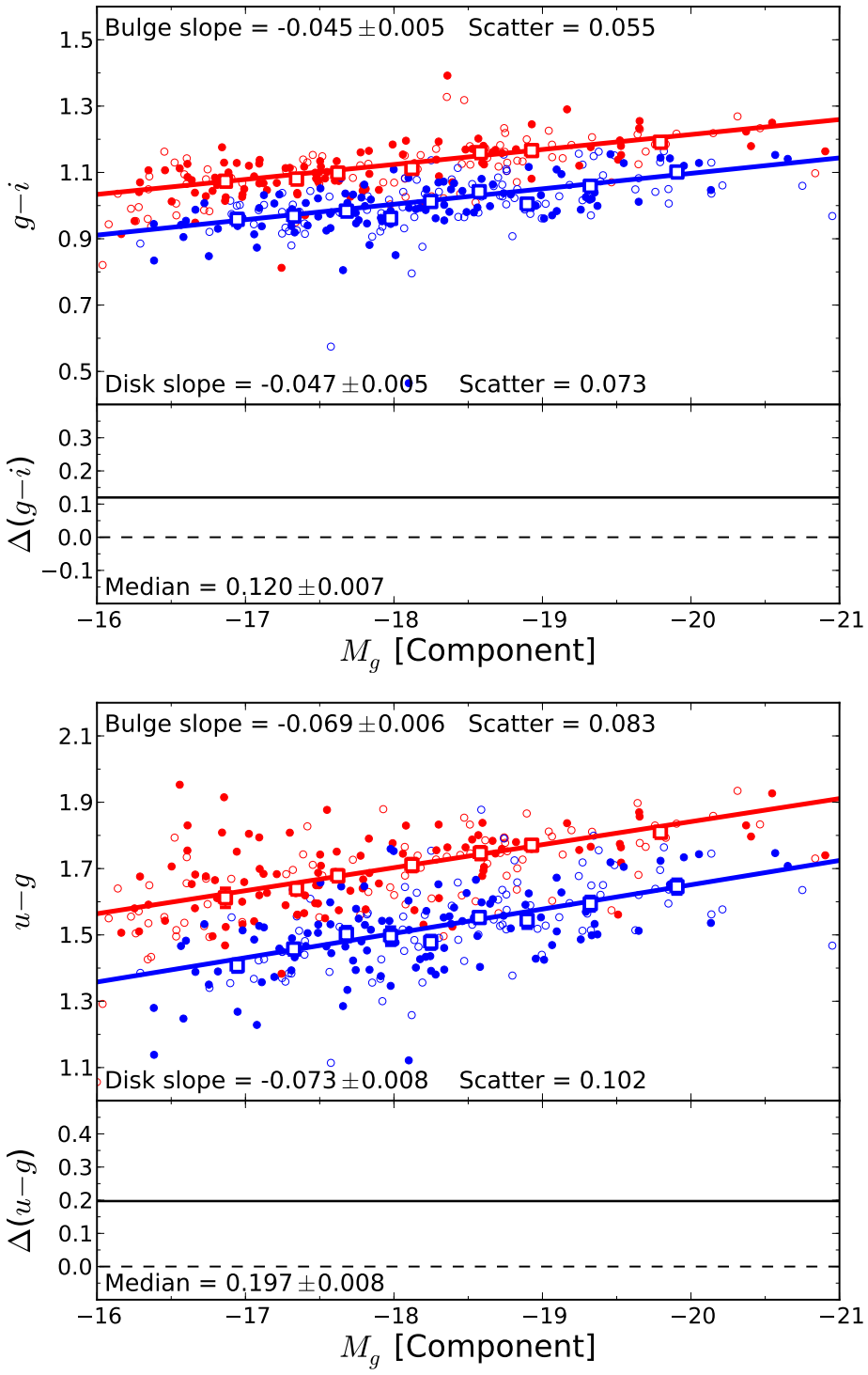

Figure 6.5: As Figure 6.1 for $g-i$ (**top**) and $u-g$ (**bottom**) colours and colour differences (bulges $-$ disks) as a function of component magnitude when internal component gradients are permitted. Note that the slope of $\Delta(C)$ is zero by definition for component magnitudes.

of component magnitude (Figure 6.5) for bulges and disks are consistent in $g-i$ (bulges: -0.045 ± 0.005, disks: -0.047 ± 0.005) and $u-g$ (bulges: -0.069 ± 0.006, disks: -0.073 ± 0.008). Here, the bulge $-$ disk colour offset at fixed component luminosity is 0.120 ± 0.007 mag in $g-i$, and 0.197 ± 0.008 mag in $u-g$. Thus, as with the component colour-magnitude results as a function of total magnitude, the $g-i$ and $u-i$ colour separations (bulge $-$ disk) are ~0.01 mag and ~0.02 mag smaller here than was measured for a fixed multi-band analysis.

Allowing for internal component gradients increases the number of free fitting parameters, and hence introduces additional fitting degeneracies. Thus, scatter in measured bulge and disk colours increases when component gradients are permitted. This effect is illustrated in Figure 6.3 by the increased scatter (0.09 mag from 0.07 mag) of gradient-requiring galaxies (red points) in the lower panel relative to the upper. Nevertheless, the increase in scatter due to additional free fitting parameters is substantially smaller than the resulting change in average component colours for the analysis sample.

6.2.3 Stellar population properties

The slope of the red sequence implies a luminosity dependence of the average stellar population properties (age and/or metallicity). From the bulge-disk decompositions of Hudson et al. (2010; H10), the global colour-magnitude slope was found to be a consequence of change in bulge colour in cluster galaxies. For the Coma *S0*s in the present work, I measure a bulge colour-magnitude slope of -0.059 ± 0.005 (Figure 6.4). This is consistent with the equivalent $B-R$ slope measured in H10 (-0.037 ± 0.014). However, I *also* measure a similar significant colour-magnitude slope for *S0* disks (-0.043 ± 0.005). By contrast, H10 reported no colour-magnitude slope for disk components (0.000 ± 0.010). This difference is not a consequence of selection bias: the colour-magnitude slopes measured in this work are not significantly altered if either the initial colour cut ($g-r>0.5$) or later sample vetting (see Section 3.5) are removed. Thus, I find that the red sequence of our archetypal Coma *S0* sample is due to similar trends towards redder colours for both structural components, rather than being driven only by the bulge colour-magnitude relation.

The colours of bulges and disks represent a fossil record of their star-formation history

and subsequent quenching. A $\Delta(B-R)$ colour separation ($\simeq \Delta(g-i)$) of ~ 0.25 between bulges and disks of L_* galaxies was previously reported in H10. Since most galaxies have a negative colour gradient, this colour offset reflects the radial positions of the bulge and disk structures in *S0*s. As such, bulge stellar populations are expected to be older (or more metal-rich) than disks.

The bulges of Coma *S0*s are measured in this work to be 0.089 ± 0.004 mag redder in $g-i$ than their disks on average, and 0.164 ± 0.007 mag redder in $u-g$ on average at fixed total galaxy luminosity. At a fixed component luminosity, bulges are 0.123 ± 0.008 mag redder in $g-i$ than disks on average, and 0.201 ± 0.009 mag redder in $u-g$ on average. Hence, bulges are significantly redder than disks in both colours when either measured between components of an average galaxy, or between equal luminosity components.

The average $\Delta(g-i)$ colour separation reported here at fixed total luminosity is thus $\sim 3\times$ smaller than the equivalent $\Delta(B-R)$ offset reported in H10, while the offset at fixed component luminosity is $\sim 2\times$ smaller. Removing the sample filters yields a significantly bluer median colour for galaxy bulges, although the median disk colours remain consistent with the filtered sample median. However, the average colour offsets are not changed significantly. Thus, the measurement of a smaller bulge $-$ disk colour offset for red sequence galaxies relative to H10 is a secure result, robust to the choice of sample selection criteria.

SSP models connect measured photometry to the underlying stellar population properties of a galaxy. Applying multi-linear fitting to Maraston (2005) SSP models (single burst star formation, Kroupa initial mass function) yields expressions for $g-i$ and $u-g$ colours as linear combinations of stellar population ages and metallicities. The bulge and disk colours, and colour separations measured above can thus be used to constrain the timescales involved in galaxy quenching. However, given the degenerate effects of age and metallicity on optical colours (Worthey, 1994), I do not attempt to attribute colour differences to exact values of either stellar population property.

If interpreted as purely an age difference, the 0.089 ± 0.004 mag bulge $-$ disk colour separation in $g-i$ (at a fixed galaxy magnitude) corresponds to a bulge age (t_B) $(1.9 \pm 0.1)\times$ larger than the disk age (t_D) on average. Using the $u-g$ colour separation, a larger age offset of $t_B = (3.0 \pm 0.5) t_D$ is measured. To estimate the absolute age difference between

bulges and disks, Δt, I assume $t_B = t_{\rm max} = 13.8$ Gyr. Using $\Delta(g-i)$, *S0* bulges are thus 6.4 ± 0.4 Gyr older than their disks on average. This is equivalent to disk formation at $z_{\rm disk} = 0.9 \pm 0.1$. From $\Delta(u-g)$, a significantly larger age offset, $\Delta t = 9.2 \pm 0.8$ Gyr ($z_{\rm disk} = 0.4 \pm 0.1$) is measured between the two components. The apparent discrepancy between these estimates is caused by increased sensitivity of $u-g$ to emission from young stars (i.e. disks are younger than detected in $g-i$). These disk ages are consistent with the presence of (relatively) recent star formation activity in a fraction of the measured Coma *S0*s. This may indicate contamination of the sample by red spiral galaxies which have been dust-reddened (e.g. Cibinel et al., 2013), or are currently undergoing truncation (e.g. Crossett et al., 2013).

Alternatively, if interpreted as only a difference in the metallicity, the $(g-i)$ colour separation between bulges and disks corresponds to a bulge metallicity (Z_B) $(2.2 \pm 0.1)\times$ greater than the metallicity of the disk (Z_D). From $u-g$, the metallicity difference would be $Z_B = (2.4 \pm 0.1) Z_D$ for fixed galaxy magnitude.

For typical ETGs, spectroscopic investigation of stellar populations report negative global metallicity gradients (Fisher et al., 1996; Moorthy & Holtzman, 2006; Morelli et al., 2008; Rawle et al., 2010; Johnston et al., 2012; La Barbera et al., 2012) indicating galaxy centres more metal-rich than than their outer regions. Global age gradients have been reported as either weakly negative/flat (Kuntschner et al., 2010; Rawle et al., 2010; Eigenthaler & Zeilinger, 2013), or positive (Bedregal et al., 2011; Johnston et al., 2012; La Barbera et al., 2012). If both age and metallicity gradients are negative, then the negative colour gradients measured in this work correspond to bulge $-$ disk age/metallicity offsets smaller than calculated above. Conversely, if age gradients are positive (i.e. centres of *S0*s younger than their outer regions), then a larger metallicity offset is required, relative to the (pure metallicity) values calculated above.

The measured bulge $-$ disk colour offsets can be interpreted as the difference in stellar population properties between the half light radii of the bulge and disk (with $R_{e,B} < R_{e,D}$ in archetypal *S0*s). On average, this corresponds to a 0.089 mag decrease in $g-i$ colour (0.164 mag decrease in $u-g$) across $\Delta\log(R) = -0.55$ dex in radius. A negative metallicity gradient and a weakly *negative* age gradient ($\Delta[Z/H]/\Delta\log(R) = -0.13 \pm 0.04$ and

$\Delta\log(\mathrm{age})/\Delta\log(R) = -0.02 \pm 0.06$ from Rawle et al., 2010) yield bulge $-$ colour offsets of $\Delta(g-i) = 0.022 \pm 0.013$ mag and $\Delta(u-g) = 0.036 \pm 0.017$ mag. These predicted colour offsets are significantly smaller than the observed $\Delta(g-i)$ and $\Delta(u-g)$, indicating that stellar population gradients alone are insufficient to explain the colour difference between bulges and disks. Further, the Rawle et al. (2010) sample is dominated by *E* or *E/S0* morphologies. The metallicity gradient for a sample of *S0*s would be shallower (e.g. Koleva et al., 2011), and thus the gradient-predicted colour offset would be even more discrepant with the measured values presented above. Alternatively, a negative metallicity gradient and positive age gradient ($\Delta[Z/H]/\Delta\log(R) = -0.6 \pm 0.5$ and $\Delta\mathrm{age}/\Delta\log(R) = 2.3 \pm 4.6$ Gyr dex^{-1} from Prochaska Chamberlain et al., 2011) yield bulge $-$ colour offsets of $\Delta(g-i) = 0.097 \pm 0.074$ mag and $\Delta(u-g) = 0.160 \pm 0.102$ mag, assuming a bulge age of $t_B = 13.8$ Gyr. These colour offsets are similar to the observed values, but the substantial uncertainty prevents a strong conclusion from being drawn.

To summarise, the colour-magnitude slopes of *S0* bulges and disks are similar, with an average colour separation of ~ 0.1 mag in $g-i$, and ~ 0.2 mag in $u-g$. Using SSP models, the redder colours of *S0* bulges can be calculated as a difference in either a stellar population age, or metallicity relative to *S0* disks. At a fixed galaxy luminosity, bulges are found to be $\sim$2-3$\times$ older than disks, or $\sim 2\times$ more metal rich. Alternatively, both age and metallicity may contribute to the colour-magnitude slopes. However, such combined stellar population property offsets cannot be quantified without additional (infra-red/spectroscopic) information.

6.3 Variation with Environment

In this section, I investigate variation of bulge and disk colour as a function of the (projected) distance from the Coma cluster centre, r_{cluster}. Observed r_{cluster} correlates with the time at which a galaxy first entered the cluster environment (Gao et al., 2004; Smith et al., 2012; De Lucia et al., 2012; Taranu et al., 2014), albeit with substantial scatter. A radial analysis therefore highlights variations of stellar population properties during cluster infall. By investigating the cluster-centric radial trends for bulges and disks, I thus trace the environment-mediated processes that have acted on these structural components, and hence the cluster

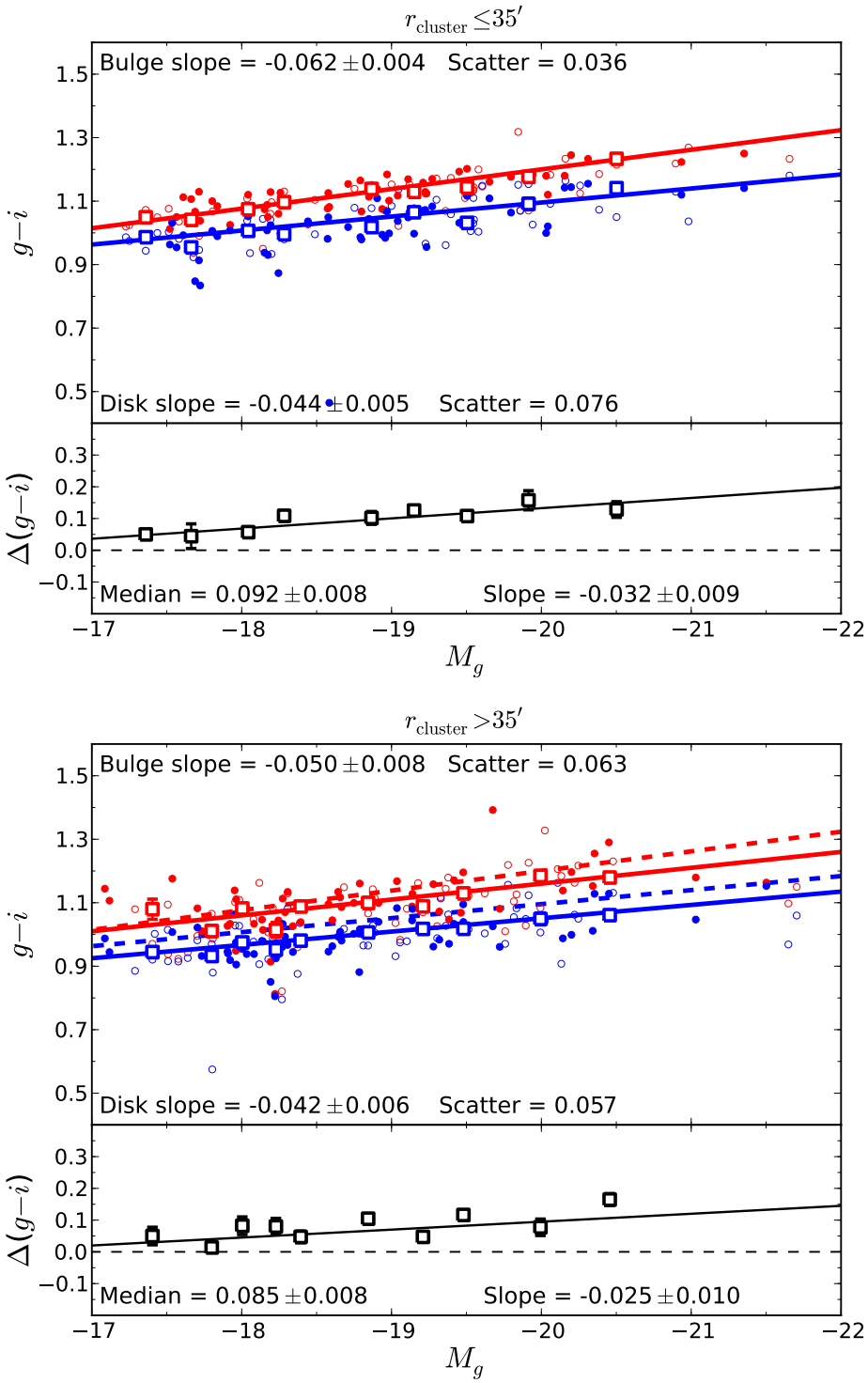

Figure 6.6: Colour-magnitude and colour-separation diagrams (gradients included). The sample is divided at $r_{\rm cluster} = 35'$ ($\equiv 0.46 r_{200}$), defining the inner (top plots) and outer (bottom plots) cluster samples. **Upper panels:** Bulge (red) and disk (blue) $g-i$ colours plotted against the absolute (bulge + disk) g band model magnitude. **Lower panels:** $g-i$ colour difference (bulge − disk) plotted against absolute magnitude. Unfilled points indicate 'flagged' fits (containing weak extra components or asymmetries, see Section 3.5). Best-fit linear trends (solid lines) are fit to median colour values calculated in magnitude bins (large square points), weighted by the robust standard error in each bin (error bars). Slope uncertainties are bootstrap errors calculated from the unbinned data. The best-fit bulge and disk trends for the inner sample are included in the upper panel of the outer sample plot as dashed lines for comparison.

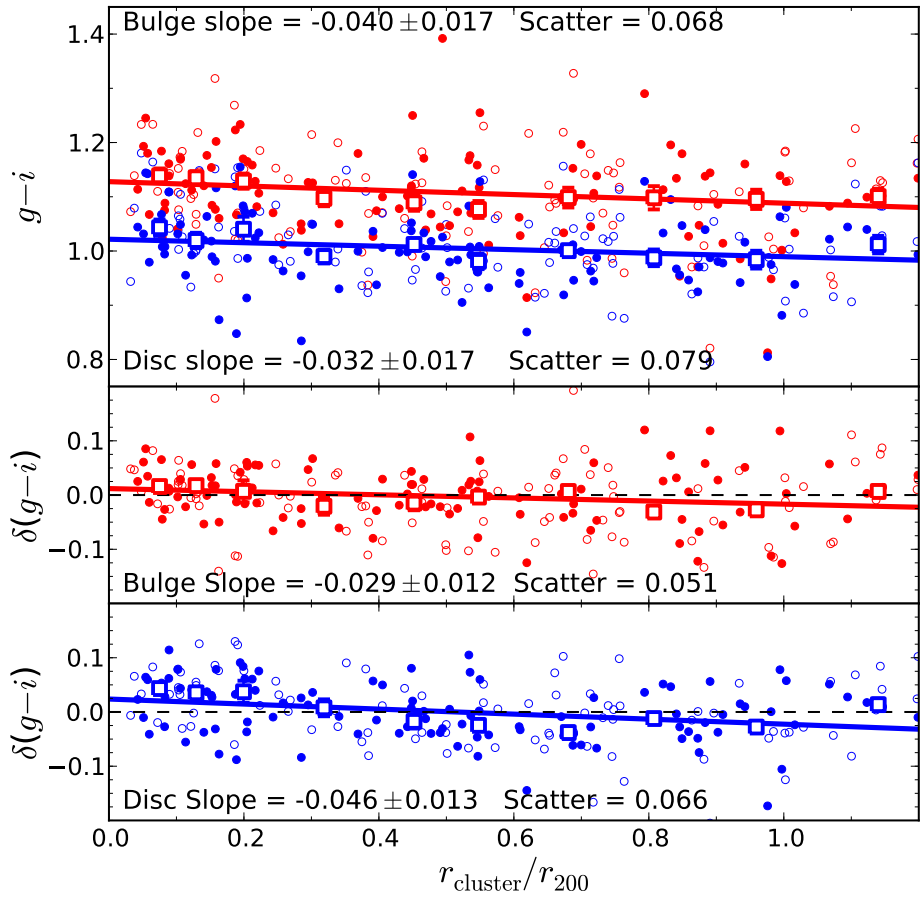

Figure 6.7: Colour-radius diagrams for Coma cluster galaxies (component gradients included). **Upper panels:** bulge (red) and disk (blue) $g-i$ colours plotted against the projected separation between the galaxy and the Coma cluster centre (in fractional units of r_{200}). **Middle panels:** Bulge $g-i$ colours after subtracting the equivalent colour-magnitude trend, $\delta(g-i)$, plotted against $r_{\rm cluster}$. **Lower panels:** disk $g-i$ colours after subtracting the equivalent colour-magnitude trend, $\delta(g-i)$, plotted against $r_{\rm cluster}$. Unfilled points indicate 'flagged' fits (containing weak extra components or asymmetries, see Section 3.5). Best-fit linear trends (solid lines) are fit to median colour values calculated in bins of projected radius (large square points), weighted by the robust standard error in each bin (error bars). Slope uncertainties are bootstrap errors calculated from the unbinned data.

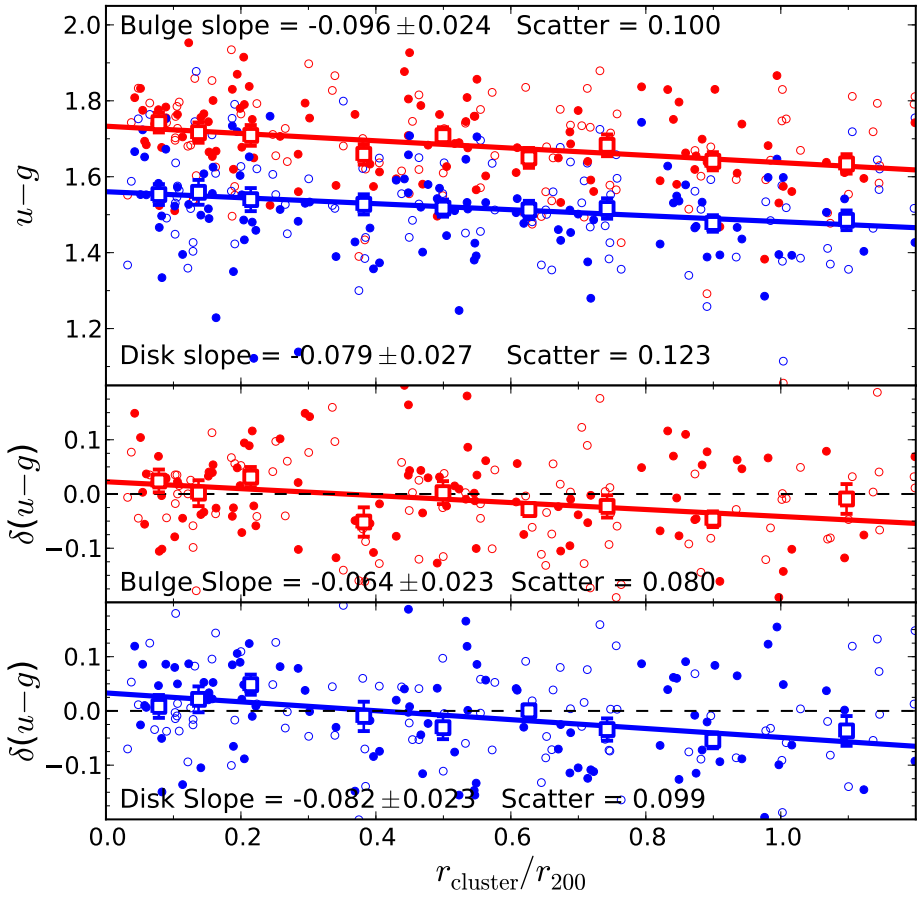

Figure 6.8: As Figure 6.7: Colour-radius diagrams for Coma cluster galaxies (component gradients included) displaying bulge (red) and disk (blue) $u-g$ colours and $\delta(u-g)$ colour residuals as a function of $r_{\rm cluster}$.

environment's role in star formation quenching and *S0* formation.

6.3.1 Cluster colour-radial results

First, galaxies are sub-divided into 'inner' and 'outer' cluster samples (Figure 6.6) based on a cut at $r_{\rm cluster} = 35'$ (~ 1.0 Mpc). This radial division is chosen such that each radial sub-sample contains $\sim 50\%$ of the analysis sample. Intrinsic scatter in the measured bulge colours around the corresponding colour-magnitude trend for galaxies in the cluster core is remarkably low (0.036 mag) relative to galaxies in the outer sample (0.063 mag). This difference in scatter is significant (from an F-test) at a very high confidence level ($\gg 99\%$). The scatter of disk colours in the cluster outskirts (0.057 mag) is comparable to this global colour scatter for all analysis sample galaxies (0.055 mag), but is significantly higher ($> 99\%$ confidence) for galaxies in the cluster core (0.076 mag). This increased scatter for disks may result from poorer disk detection at low $r_{\rm cluster}$ due to contamination by neighbouring galaxy haloes. The average bulge $-$ disk colour separations are similar for both samples, but bulge red sequence slopes are weakly ($\lesssim 2\sigma$) steeper for galaxies in the cluster core. In addition, a trend towards redder bulges and disk colours at smaller $r_{\rm cluster}$ is detected. Between the inner and outer samples, the average offset for bulges is ~ 0.03 mag in $g-i$ and ~ 0.05 mag in $u-g$. For disks, the offset is ~ 0.04 mag in both colours.

For the cluster sample as a whole, there exist marginal trends of redder galaxy bulges and disks towards the cluster centre (Figure 6.7). Disks have a colour-radius slope (-0.032 ± 0.017 mag r_{200}^{-1} in $g-i$) consistent with the trend for bulges (-0.040 ± 0.017 mag r_{200}^{-1}), but have greater intrinsic scatter (0.079 mag vs. 0.068 mag). However, the cores of galaxy clusters are populated by more luminous, bulge-dominated galaxies than the cluster outskirts. Thus, any observed colour-radius trends would need to be decoupled from the colour-magnitude relation. Instead, deviation from the observed (component) colour-magnitude trends, $\delta(g-i)$ and $\delta(u-g)$, as a function of radius is used as an unbiased probe of cluster-radial trends in stellar population properties.

The scatter in $\delta(g-i)$ is ~ 0.02 mag smaller (relative to the raw colour-radius results) for both components. However, the radial correlation slope is steeper for disks, and shallower for bulges. This change remains small for both components ($\sim 1\sigma$), but results in $\delta(g-i)$ slope

for disks (-0.046 ± 0.013 mag r_{200}^{-1}) which is significant at a 3.8σ level. The corresponding $\delta(g-i)$ slope for bulges is weakly significant (-0.029 ± 0.012 mag r_{200}^{-1}), but differs by less than 2σ from the disk result.

Colour-radius slopes in $u-g$ are significant at a $\sim 3\sigma$ level for both components (Figure 6.8). Compared to $g-i$, these correlations are steeper, and have greater scatter ($\sim 1.5\times$). Removing the best-fit component colour-magnitude trends results in shallower $\delta(u-g)$ slopes for both components (-0.064 ± 0.023 mag r_{200}^{-1} for bulges, -0.082 ± 0.023 mag r_{200}^{-1} for disks). As with $\delta(g-i)$, these residual trends are consistent but only significant at a $> 3\sigma$ level for disks. Scatter in $\delta(u-g)$ is ~ 0.02 mag smaller for both components (relative to scatter in $u-g$).

H10 previously noted a significant dependence of disk colours on projected cluster-centric radius (-0.103 ± 0.023 mag r_{200}^{-1} in $B-R$). This trend is steeper, but consistent at a $\sim 2\sigma$ level with the correlation reported above for $g-i$ disk colours. Similarly, H10 bulge colours were found to be invariant with radius (0.007 ± 0.038 mag r_{200}^{-1} in $B-R$), consistent with the (weak) correlation between $g-i$ bulge colour and $r_{\rm cluster}$ in this work. Conversely, Lackner & Gunn (2013) found that disk colours drove global colour-density trends, but only for galaxies in poor groups. In rich clusters, disk colours were measured as invariant with local density, while bulge colours were weakly anti-correlated with environment.

In summary, *S0* disks become significantly bluer in $g-i$ radially outwards from the cluster core. *S0* bulge $g-i$ colour, however, only correlates weakly with $r_{\rm cluster}$. Steeper colour-radial trends are measured in $u-g$ for both components, but at similar significance levels to $g-i$. These results are unchanged if instead multilinear fitting is used to investigate component colour as a function of component magnitude and cluster radius simultaneously.

6.3.2 Environmental Quenching

In this section, simple SSP models (from Maraston, 2005; see Section 6.2.3) are used to quantify variation of component stellar population properties with environment, and hence constrain the influence of environment-driven evolutionary pathways on Coma cluster *S0*s. The measured residual colour-radius slopes ($\delta(C)$; where C is either $g-i$ or $u-g$) are equivalent to colour offsets between galaxies with equal luminosities at $r_{\rm cluster} = 0$ and

$N = 200$		Fixed Multi-band		Internal Gradients	
		Bulge	Disk	Bulge	Disk
	M_g	$\mathbf{-18.842 \pm 0.072}$		$\mathbf{-18.842 \pm 0.072}$	
	B/T	$\mathbf{0.382 \pm 0.011}$		$\mathbf{0.382 \pm 0.011}$	
	$(u-g)$	$\mathbf{1.718 \pm 0.010}$	$\mathbf{1.520 \pm 0.010}$	$\mathbf{1.682 \pm 0.008}$	$\mathbf{1.524 \pm 0.009}$
	$(g-i)$	$\mathbf{1.112 \pm 0.006}$	$\mathbf{1.006 \pm 0.006}$	$\mathbf{1.108 \pm 0.006}$	$\mathbf{1.006 \pm 0.006}$
Median	$\Delta_T(u-g)$	$\mathbf{0.178 \pm 0.007}$		$\mathbf{0.164 \pm 0.007}$	
Value	$\Delta_T(g-i)$	$\mathbf{0.097 \pm 0.004}$		$\mathbf{0.089 \pm 0.004}$	
	$\Delta_C(u-g)$	$\mathbf{0.219 \pm 0.008}$		$\mathbf{0.197 \pm 0.008}$	
	$\Delta_C(g-i)$	$\mathbf{0.131 \pm 0.008}$		$\mathbf{0.120 \pm 0.007}$	
	$(u-g)$	$\mathbf{-0.078 \pm 0.009}$	$\mathbf{-0.078 \pm 0.012}$	$\mathbf{-0.085 \pm 0.007}$	$\mathbf{-0.077 \pm 0.007}$
Col-Mag	$(g-i)$	$\mathbf{-0.060 \pm 0.004}$	$\mathbf{-0.036 \pm 0.005}$	$\mathbf{-0.059 \pm 0.005}$	$\mathbf{-0.043 \pm 0.005}$
Slope	$\Delta_T(u-g)$	-0.006 ± 0.007		-0.001 ± 0.007	
	$\Delta_T(g-i)$	$\mathbf{-0.022 \pm 0.005}$		-0.013 ± 0.005	
	$(u-g)$	-0.039 ± 0.032	-0.055 ± 0.030	$\mathbf{-0.096 \pm 0.024}$	-0.079 ± 0.027
Col-Rad	$\delta(u-g)$	-0.010 ± 0.022	$\mathbf{-0.086 \pm 0.025}$	-0.064 ± 0.023	$\mathbf{-0.082 \pm 0.023}$
Slope	$(g-i)$	-0.003 ± 0.020	-0.044 ± 0.016	-0.040 ± 0.017	-0.032 ± 0.017
	$\delta(g-i)$	-0.015 ± 0.014	-0.028 ± 0.013	-0.029 ± 0.012	$\mathbf{-0.046 \pm 0.013}$

Table 6.1: Table of median absolute galaxy magnitudes, bulge fractions, and colour values for bulges and disks, and their corresponding colour-magnitude and colour-cluster radius [fractional units of r_{200}] trend slopes. $\Delta(C)$ denotes the bulge $-$ disk colour separation measured pairwise as a function of total galaxy luminosity ($\Delta_T(C)$), or as a constant offset between bulge and disk trends (sharing a common slope) as a function of component magnitude ($\Delta_C(C)$). The slope of $\Delta_C(C)$ with magnitude or radius is zero by definition. $\delta(C)$ refers to residual colour-radius trends after subtracting component colour-magnitude trends. Results are presented for the entire analysis sample ($N = 200$) for models with no internal gradients (left) and where internal component gradients are permitted (right). Significant values ($\geq 3\sigma$) are highlighted in bold.

$r_{\rm cluster} = r_{200}$ after removing the luminosity-(cluster) radius trend. Thus, the $\delta(C)$ slopes reflect structural component age and/or metallicity differences between *S0*s at Coma's virial radius (t_{200}, Z_{200}) and those in the cluster core (t_0, Z_0).

Interpreted as a pure age difference in *S0* disks with radius, the $\delta(u-g)$ slope of -0.082 ± 0.023 mag per r_{200} yields $t_{0,\rm D} = (1.6 \pm 0.2)t_{200,\rm D}$. Equivalently from the $\delta(g-i)$ slope, the disk age difference is estimated as $t_{0,\rm D} = (1.4 \pm 0.1)t_{200,\rm D}$. The stellar population age differences for *S0* bulges are $t_{0,\rm B} = (1.5 \pm 0.2)t_{200,\rm B}$ from $\delta(u-g)$, and $t_{0,\rm B} = (1.2 \pm 0.1)t_{200,\rm B}$ from $\delta(g-i)$. Upper limits can be placed on bulge age offsets by using $t_{0,B} = t_{\rm max} = 13.8$ Gyr. From $\delta(u-g)$, *S0* bulges in Coma's core are older than those found in the cluster outskirts by 4.6 ± 1.2 Gyr, while the equivalent age difference from $\delta(g-i)$ is 2.3 ± 1.0 Gyr. No corresponding limits can be placed on the ages of *S0* disks without an estimate for $t_{\rm max,D}$.

Alternatively, if a pure metallicity difference was responsible for the $\delta(u-g)$ component colour changes between the virial radius and cluster core, then $Z_{\rm C,B} = (1.4 \pm 0.2)Z_{200,\rm B}$ for bulges, and $Z_{\rm C,D} = (1.5 \pm 0.2)Z_{200,\rm D}$ for disks. From $\delta(g-i)$, the equivalent disk metallicity changes would be $Z_{\rm C,B} = (1.3 \pm 0.1)Z_{200,\rm B}$ and $Z_{\rm C,D} = (1.5 \pm 0.2)Z_{200,\rm D}$.

In summary, I confirm that the increasingly red global colours of *S0* galaxies towards the cluster centre are mainly driven by a cluster-radial trend in the colours of component disks. The detection of a weak trend in bulge colours with radius indicates that the environment-dependent bulge reddening contributes to the global colour-radius trend for red sequence galaxies. However, compared to the significant disk colour-radius trend, this bulge evolution is not the dominant factor in *S0* formation. Therefore, our component colour data favour *S0* formation via an environment-driven fading of the disks of spiral-like progenitors. Thus, information about the earlier formation history of *S0* bulges is largely preserved in their stellar population properties.

6.4 Variation with Morphology

In this section, the analysis sample ($N = 200$) is divided according to various (by-eye) morphological classification schemes. I thus explore how these traditional morphological classification schemes modify the reported colour-magnitude, and colour-radius characteristics

of galaxies in Coma. This enables quantification how the red sequence varies with classical morphology, and isolates any bimodality of galaxy structure due to differing evolutionary pathways. Hence, I investigate whether consideration of visual morphology provides additional information regarding galaxy properties which would be missed by analyses utilising photometric structure fitting alone (as used in this thesis).

6.4.1 Dressler (1980a) Morphologies

As described in Section 3.6.1, 204 galaxies (out of 247) with visual morphology classifications from the Dressler (1980a; D80) catalogue meet the Coma sample selection criteria (as described in Section 2.3). Of these, 65 have *E* or *E/S0* morphologies (32%), 120 have *S0*, *S0/a*, or *S0/E* morphologies (59%), and 19 (9%) have *Sa-Sc* and *S/S0* morphologies (see Table 3.5). To simplify the analysis, no distinction is made between barred and unbarred classifications.

Morphological subsamples are drawn from the analysis sample (i.e. where galaxies exhibit archetypal structures). These are described as the D80 'elliptical' ('D80 *E*'; $N = 20$), 'lenticular' ('D80 *S0*'; $N = 53$), and 'spiral' ('D80 *S*'; $N = 6$) samples hereafter. Note that most of the rejected D80 ellipticals (along with $\sim 50\%$ of rejected D80 *S0*s) were removed due to atypical surface brightness profiles (Type 5, and some Type 3). Hence, many of the 'traditional' D80 ellipticals (wherein the Sérsic component dominates the majority of the surface brightness profile) are removed from consideration in favour of ensuring meaningful interpretation of all 'bulge' and 'disk' parameters.

Rejected D80 spiral galaxies were removed primarily as badly-fit (i.e. due to asymmetry, contamination, or high χ^2). Hence, the remaining six analysis sample D80 spirals are 'anemic' spirals (see Figure 1.3 in Chapter 1) wherein the spiral pattern is too weak to disrupt the fitting process (due to asymmetry or high χ^2). However, the spiral sample is excluded from further analysis due to its insignificant sample size. The resulting (median) galaxy magnitudes, bulge fractions, and component colours, colour offsets, and trends with magnitude and cluster radius are presented in brief in Table 6.2.

Component bulges are redder on average in $u - g$ for D80 ellipticals compared to bulges in *S0*s ($\sim 3\sigma$ significance), while the disks of elliptical galaxies are only moderately redder

		D80 *S0* ($N = 53$)		D80 *E* ($N = 20$)	
		Bulge	Disk	Bulge	Disk
	M_g	$\mathbf{-19.462 \pm 0.084}$		$\mathbf{-19.277 \pm 0.253}$	
	B/T	$\mathbf{0.446 \pm 0.020}$		$\mathbf{0.542 \pm 0.029}$	
Median	$(u-g)$	$\mathbf{1.754 \pm 0.011}$	$\mathbf{1.576 \pm 0.015}$	$\mathbf{1.822 \pm 0.022}$	$\mathbf{1.646 \pm 0.029}$
Value	$(g-i)$	$\mathbf{1.143 \pm 0.010}$	$\mathbf{1.050 \pm 0.008}$	$\mathbf{1.161 \pm 0.012}$	$\mathbf{1.052 \pm 0.016}$
	$\Delta_T(u-g)$	$\mathbf{0.172 \pm 0.019}$		$\mathbf{0.186 \pm 0.021}$	
	$\Delta_T(g-i)$	$\mathbf{0.087 \pm 0.010}$		$\mathbf{0.106 \pm 0.011}$	
	$(u-g)$	$\mathbf{-0.057 \pm 0.013}$	$\mathbf{-0.102 \pm 0.019}$	-0.048 ± 0.019	$\mathbf{-0.095 \pm 0.023}$
Col-Mag	$(g-i)$	$\mathbf{-0.072 \pm 0.010}$	$\mathbf{-0.040 \pm 0.009}$	$\mathbf{-0.038 \pm 0.010}$	$\mathbf{-0.040 \pm 0.012}$
Slope	$\Delta_T(u-g)$	0.034 ± 0.024		0.017 ± 0.017	
	$\Delta_T(g-i)$	-0.021 ± 0.011		-0.010 ± 0.010	
	$(u-g)$	-0.108 ± 0.052	-0.228 ± 0.086	-0.042 ± 0.099	0.122 ± 0.146
	$\delta(u-g)$	-0.068 ± 0.047	-0.143 ± 0.065	0.010 ± 0.070	0.124 ± 0.118
Col-Rad	$(g-i)$	$\mathbf{-0.207 \pm 0.056}$	$\mathbf{-0.170 \pm 0.045}$	-0.094 ± 0.052	0.012 ± 0.081
Slope	$\delta(g-i)$	-0.067 ± 0.049	$\mathbf{-0.154 \pm 0.035}$	0.000 ± 0.046	0.006 ± 0.062
	$\Delta_T(u-g)$	0.072 ± 0.079		-0.135 ± 0.116	
	$\Delta_T(g-i)$	0.023 ± 0.042		-0.082 ± 0.058	

Table 6.2: As Table 6.1: the median absolute galaxy magnitudes, bulge fractions, and component colours, colour separations, and colour trend slopes for D80 elliptical and *S0* galaxies. Significant values ($\geq 3\sigma$) are indicated in bold.

($\sim 2\sigma$) in $u-g$. Neither component's $g-i$ colour varies significantly with morphology. Elliptical bulges display the least intrinsic scatter in $(g-i)$ colour (0.034 mag), while the $g-i$ scatter for all other *E* or *S0* components (and $u-g$ scatter for all components) are consistent with the equivalent measurements for the parent analysis sample (~ 0.06 mag for both components in $g-i$, ~ 0.07 mag for bulges and ~ 0.10 mag for disks in $u-g$).

Note, however, that the D80 ellipticals are intrinsically more bulge-dominated (ΔB/T $= 0.096 \pm 0.035$) than D80 *S0*s, if not significantly more luminous on average ($\Delta M = -0.185 \pm 0.267$ mag). Hence, the reduced scatter for D80 *E* bulges is a result of the increased bulge component S/N in these galaxies. Likewise, all component colour offsets between D80 *S0* and *E* morphologies are consistent ($\lesssim 1.5\sigma$ difference) with the expected colour increase for 0.185 mag brighter galaxies given the component colour-magnitude trends measured from the parent analysis sample.

All component colour trends in $u-g$ are consistent between D80 *S0* and *E* morphologies. Similarly, consistent colour-magnitude slopes are measured for *S0* and *E* disks in $g-i$. However, bulges in elliptical galaxies have a shallower $g-i$ colour-magnitude slope than *S0* component bulges (at $\sim 2.5\sigma$ significance). This suggests weak bimodality of the bulge red sequence for high/low B/T systems, with a sharper colour change per magnitude galaxy luminosity for disk dominated galaxies.

		GZ *S* ($N = 47$)		GZ *E* ($N = 140$)	
		Bulge	Disk	Bulge	Disk
	M_g	$\mathbf{-18.389 \pm 0.130}$		$\mathbf{-18.938 \pm 0.089}$	
	B/T	$\mathbf{0.335 \pm 0.025}$		$\mathbf{0.412 \pm 0.013}$	
Median	$(u-g)$	$\mathbf{1.619 \pm 0.015}$	$\mathbf{1.522 \pm 0.022}$	$\mathbf{1.730 \pm 0.010}$	$\mathbf{1.531 \pm 0.010}$
Value	$(g-i)$	$\mathbf{1.041 \pm 0.014}$	$\mathbf{0.988 \pm 0.016}$	$\mathbf{1.126 \pm 0.006}$	$\mathbf{1.016 \pm 0.006}$
	$\Delta_T(u-g)$	$\mathbf{0.102 \pm 0.012}$		$\mathbf{0.177 \pm 0.008}$	
	$\Delta_T(g-i)$	$\mathbf{0.057 \pm 0.009}$		$\mathbf{0.100 \pm 0.004}$	
	$(u-g)$	$\mathbf{-0.049 \pm 0.014}$	$\mathbf{-0.076 \pm 0.018}$	$\mathbf{-0.069 \pm 0.008}$	$\mathbf{-0.079 \pm 0.008}$
Col-Mag	$(g-i)$	$\mathbf{-0.049 \pm 0.012}$	$\mathbf{-0.039 \pm 0.010}$	$\mathbf{-0.045 \pm 0.006}$	$\mathbf{-0.041 \pm 0.005}$
Slope	$\Delta_T(u-g)$	0.009 ± 0.020		0.007 ± 0.008	
	$\Delta_T(g-i)$	0.008 ± 0.011		-0.008 ± 0.005	
	$(u-g)$	-0.078 ± 0.054	-0.097 ± 0.069	-0.083 ± 0.026	-0.070 ± 0.033
	$\delta(u-g)$	0.029 ± 0.055	0.008 ± 0.065	-0.064 ± 0.024	-0.034 ± 0.022
Col-Rad	$(g-i)$	-0.068 ± 0.044	0.014 ± 0.054	-0.011 ± 0.015	-0.033 ± 0.017
Slope	$\delta(g-i)$	-0.068 ± 0.042	0.072 ± 0.060	-0.027 ± 0.012	-0.030 ± 0.012
	$\Delta_T(u-g)$	0.012 ± 0.073		0.002 ± 0.025	
	$\Delta_T(g-i)$	0.004 ± 0.052		-0.001 ± 0.013	

Table 6.3: As Table 6.1: the median absolute galaxy magnitudes, bulge fractions, and component colours, colour separations, and colour trend slopes for GZ combined spiral and elliptical galaxies. Significant values ($\geq 3\sigma$) are indicated in bold.

Due to low sample size, and limited radial coverage of the cluster ($r < 0.7r_{200}$), the D80 morphologies are not suited for analysis of cluster-radial trends. This will instead be addressed in the next section from a wider catalogue of Coma cluster morphologies from Galaxy Zoo.

In summary, the photometric properties of galaxies do not differ significantly from the parent analysis sample for either D80 morphology (*E*, *S0*). Structural components in D80 *E* galaxies are slightly redder (in $u-g$ *only*) than the *S0* equivalents, however these colour offsets are not significant relative to the measured colour-magnitude trends. Conversely, a significant bulge fraction offset is noted between D80 elliptical and lenticular galaxies. Hence, D80 *E* and *S0* samples do not represent morphologically distinct galaxies in photometric structure, but rather represent the bulge-dominant/bulge-weak ends of the archetypal galaxy distribution. As such, the misclassification of archetypal bulge + disk galaxies as pure ellipticals in D80 is a consequence of poor disk detection for high B/T (i.e. faint disk) galaxies.

6.4.2 Galaxy Zoo Morphology

Galaxy Zoo (Lintott et al., 2008) is a citizen science morphological classification project based on SDSS Data Release 6 (DR6) imaging. Users are presented with monochrome

or three-colour image of target galaxies, and are asked to catagorise each as one of six broad morphological classes (elliptical, clockwise/anti-clockwise/other spiral, unknown, or merger). Galaxies are then assigned morphology classifications based on group consensus via the de-biased vote fraction ($f_{\rm vote}$). Since no distinct *S0* class is considered, lenticular galaxies are assigned to either the elliptical or (other/edge-on) spiral categories, depending on observed galaxy orientation.

Classifications from the Galaxy Zoo catalogue (Lintott et al., 2011; hereafter 'GZ') are available for 195 of the 200 Coma MegaCam analysis sample (i.e. well-fit, archetypal bulge + disk) galaxies. Of these, 78 are flagged[1] as ellipticals (40%), and 12 are flagged as (any type of) spirals (6%). If the required vote fraction threshold is relaxed to $f_{\rm vote} > 0.5$, then 140 galaxies are classified as ellipticals (72%; hereafter 'GZ *E*' sample), while 47 galaxies are classified as spirals (24%; hereafter 'GZ *S*' sample). These morphology fractions (for either f threshold) are not significantly changed if the entire CFHT Coma sample is considered.

GZ 'ellipticals' are more luminous, and more bulge-dominated than GZ spirals on average, with similar disk colours in both $u-g$ and $g-i$ (Table 6.3). However, GZ *S* bulges are 0.1 mag bluer than GZ *E* bulges in both colours (*S* − *E*: -0.11 ± 0.02 mag in $u-g$, -0.09 ± 0.02 mag in $g-i$). Given that the bulge and disk colour-magnitude trends are equivalent (Figure 6.4), this bulge colour offset cannot be explained by the luminosity offset of the GZ *S* and *E* samples. Furthermore, bulge colours do not vary with disk axis ratio ($q_{\rm D}$) for either morphology. Hence, the bulge colour offset is not a result of galaxy inclination bias (i.e. GZ *S* preferentially selected for edge-on *S0*s).

Colour magnitude trends for both GZ *E* and *S* galaxies are consistent with those measured for the entire analysis sample (see Table 6.1). Scatter in component colours for GZ ellipticals is likewise consistent with analysis sample measurements (~ 0.09 mag in $u-g$, ~ 0.05 mag in $g-i$ for both components). Conversely, while bulge colour scatter for GZ spirals is similar (0.05 mag in $g-i$) or lower (0.06 mag in $u-g$) than the parent sample, their disks exhibit a twofold increase in scatter (0.10 mag in $g-i$, 0.12 mag in $u-g$). However, this is unsurprising, given that the majority of GZ *S* galaxies (62%) have previously been flagged as poor fits (see Section 3.6). Hence, the Galaxy Zoo 'spiral' category includes systems poorly-suited to fitting due to faint spiral features, asymmetry, or high galaxy inclination.

[1] $\cong f_{\rm vote} > 0.8$

Conversely, the GZ *E* class preferentially selects galaxies with smooth isophotes, and hence is an amalgam of traditional elliptical and lenticular morphologies.

The residual trends in GZ spiral component colours with cluster-radius (after subtracting the best-fit colour-magnitude slope) are non-significant due to high scatter and poor radial coverage of the GZ *S* sample. The bulges of GZ ellipticals exhibit radial colour trends consistent with the parent analysis sample, while the trends for GZ elliptical disks are significantly shallower (~ -0.03 in both bands vs. -0.08 and -0.05 in $u-g$ and $g-i$ previously). This indicates a stronger environmental dependence of bulge colours than was seen previously, suggesting that environment-driven quenching affects both structural components.

In summary, rather than categorising morphologically distinct samples, Galaxy Zoo classifications identify galaxies with low-level deviations from a smooth, regular profile. Galaxy Zoo 'spirals' are thus fainter and more disk-dominated, but exhibit greater levels of scatter in (disk) colour measurements. Galaxy Zoo 'ellipticals' are primarily well-characterised lenticular galaxies and thus are consistent (in terms of median colours and colour trends) with the results of the entire analysis sample. Galaxy Zoo 2 (Willett et al., 2013) implements a more complex system of visual classification, involving multiple additional morphology subsamples. However, the majority of the new classification steps involve the description of spiral patterns or obvious structural features (e.g. bars, rings, and dust lanes). As such, there remains no means of distinguishing between elliptical and lenticular morphologies.

6.5 Comparison with Taranu et al. (2014)

In this section, the bulge + disk model photometry from the present work (hereafter 'Mega-Cam Coma') are compared to bulge-disk decomposition of SDSS imaging for a large galaxy sample from a set of rich ($\sigma_{\rm 1D} > 800$ km s^{-1}) clusters in a redshift range $0.04 < z \lesssim 0.10$ (Taranu et al., 2014; hereafter T14). Note that the Coma cluster is not included in the T14 sample. Note also that the T14 data is also drawn from the previously-examined (see Section 4.2.2) Simard et al. (2011; S11) decomposition catalogue.

For comparison with T14, we use our entire (unfiltered) Coma sample, as no such sample filtering is applied to the T14 galaxy sample to remove unsuitable model fits. The colour cut ($g-r > 0.5$) is removed from our sample for the same reason. The T14 selection criteria are

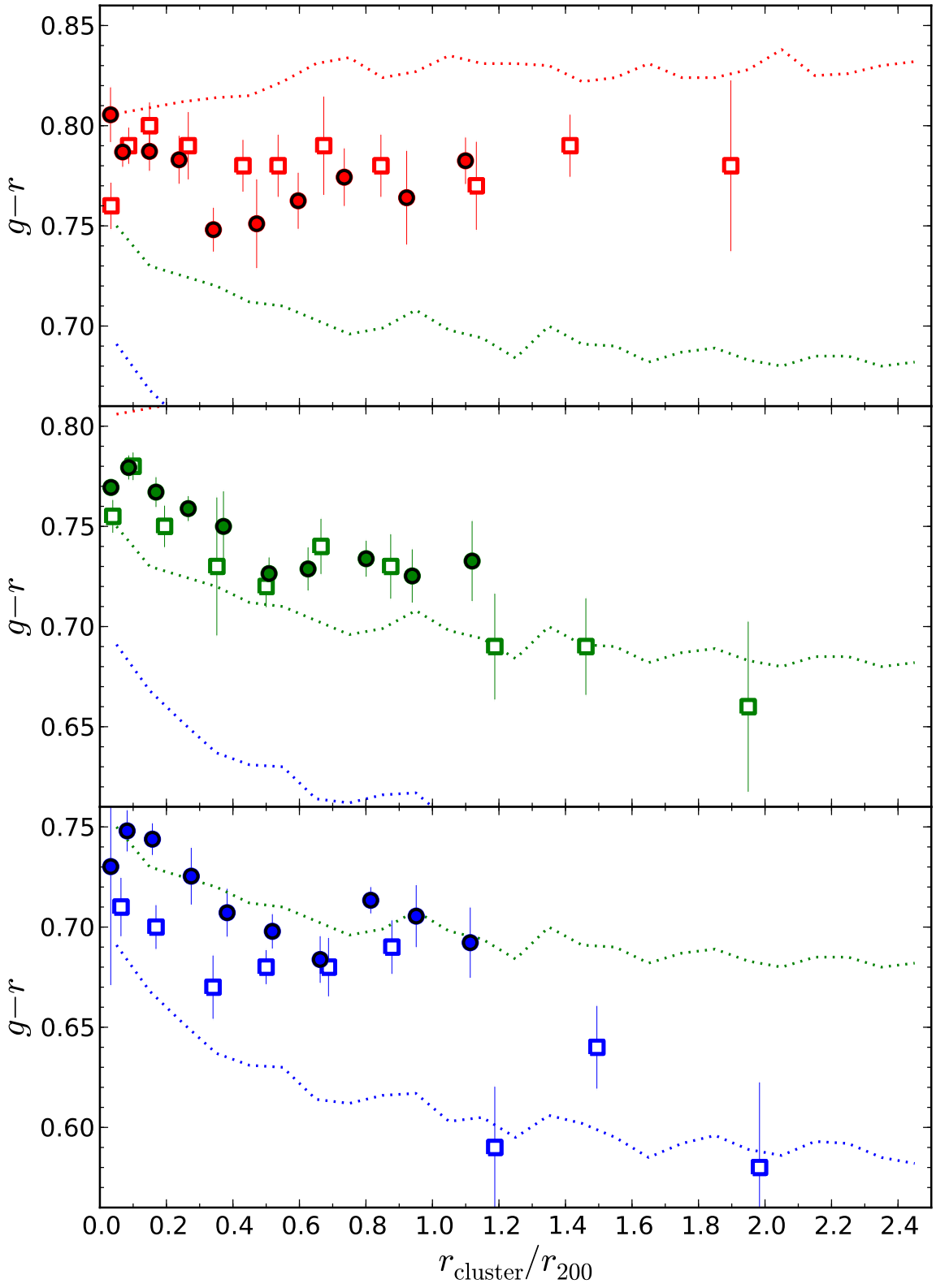

Figure 6.9: Colour-(cluster) radius plots for bulge (red, upper panel), total galaxy (green, middle panel), and disk (blue, bottom panel) $g-r$ colours. Filled circular points indicate the results of the present work (converted from $g-i$). Unfilled square points indicate the data from Simard et al. (2011) for Coma. The equivalent data for rich clusters from Taranu et al. (2014) are included as dotted lines in each panel for comparison. Plotted colour data (from all three sources) are median values measured in $r_{\rm cluster}$ bins.

then applied to our data to ensure equivalence of the compared samples: the magnitude limit for galaxies is thus set to $M_g < -19.3$ ($\approx M_R < -20.25$, i.e. ~ 2 mag brighter than our sample limit). In addition, a sample of Coma cluster galaxies were drawn from S11 using the same selection criteria for comparison (hereafter 'Coma SDSS').

Colour-cluster radius plots are displayed in Figure 6.9 for bulge, disk and total galaxy colours. As per T14, bulge data are only included if B/T > 0.2, and disk data are only included if B/T < 0.8. The $g - r$ colours are calculated for MegaCam Coma data using $(g - r) = 0.67(g - i) + 0.01$ for bulge and galaxy colours and $(g - r) = 0.53(g - i) + 0.15$ for disk colours. These conversion maps are measured empirically from SDSS aperture photometry in the appropriate colour ranges.

Coma bulges are found to be systematically bluer (from MegaCam and SDSS) than bulges in the full T14 cluster sample. This offset is less prominent in the cluster core, but increases with $r_{\rm cluster}$ due to a weakly positive radial trend in T14 and a weakly negative/flat trend for MegaCam/SDSS. On average, T14 bulges are ~ 0.04 mag redder in $g - r$. Total galaxy colours are marginally redder on average in Coma than in T14, albeit with equivalent radial trends in all three datasets. MegaCam galaxies are ~ 0.03 mag redder in $g - r$ than T14 on average, while SDSS galaxy colours are in agreement with both MegaCam and T14.

Disks in Coma galaxies are found to be systematically redder than T14 disks, although SDSS disk colours are consistent with T14 beyond r_{200}. MegaCam Coma disks are ~ 0.08 mag redder than T14 (~ 0.03 mag redder than SDSS in Coma), but follow a similar negative radial colour trend. Similarly, the disks of SDSS Coma galaxies are ~ 0.05 mag redder than T14 in $g - r$, with a noisy (negative) radial trend in colour. The discrepancy between Coma galaxy disk colours may be caused by the improved disk detection from MegaCam imaging due to increased depth relative to SDSS (as seen in Chapter 4). Disks measured from MegaCam dominate to lower galaxy-centric radii than in SDSS (i.e. lower B/T). Hence, inner galaxy flux is traded from the (SDSS) bulge to the (MegaCam) disk. As galaxies have redder centres, this makes the MegaCam disks redder on average.

To summarise, MegaCam colours agree well with the decomposition of SDSS data except for disk colours, which are systematically redder than SDSS. The bulges/disks of Coma galaxies are bluer/redder in $g - r$ on average than the same components measured from a

larger cluster galaxy sample. Discrepancy between Coma SDSS component colours and T14 (despite both using the same decomposition catalogue) implies that either the Coma cluster is not representative of the ensemble properties of the rich cluster considered, or the increase in size of the seeing disk in physical units (i.e. kpc; MegaCam Coma $<$ SDSS Coma $<$ SDSS higher z clusters) causes a systematic trend in structural component colours.

6.6 Conclusions and Chapter Summary

The bulge and disk structures of red-sequence galaxies in the Coma cluster have been characterised using deep u, g, and i band imaging. Extensive sample vetting (as described in Chapter 3) was carried out to isolate a sample of 200 galaxies well-described by an 'archetypal' (central) bulge + (outer) exponential disk morphology. Fitting was carried out using two approaches: i) where model structure does not vary from band-to-band; ii) internal component colour gradients were permitted in one or both components.

The component colours of archetypal galaxies in Coma have been reported as functions of galaxy luminosity and clustercentric radius. In addition, variation of component colours and colour trends were investigated for visual classifications of galaxy morphology.
The main results of this chapter are as follows:

i) **If either galaxy or component luminosity is fixed, the bulges of *S0*s are significantly redder than their disks (by $\sim$0.1 mag in $g-i$, $\sim$0.2 mag in $u-g$ on average).**

   Thus, bulge stellar populations are $\sim$2-3$\times$ older, and/or $\sim 2\times$ more metal rich than those found in disks.

ii) **Significant colour-magnitude slopes are detected for both the bulge and disk structural components in $g-i$ and $u-g$.**

   In either colour, the measured trend slopes for bulges and disks are consistent at a 2σ level. Hence, the global red sequence in Coma is a consequence of the increasingly red colours of bulges *and* disks in more luminous galaxies.

iii) **After subtracting the best-fit colour-magnitude trend, galaxy disks become bluer in both $g-i$ and $u-g$ with increasing projected distance from the centre of the**

Coma cluster.

Bulge component colours also become bluer with $r_{\rm cluster}$, but this trend is only marginally significant (2.5σ) and more sensitive to the treatment of component colour gradients. The global colour-radius trend for *S0*s is thus dominated by increasingly red disks in galaxies closer to the cluster core. Therefore, the environment-mediated mechanism which drives *S0* formation is a 'disk-fading' process (i.e. quenching acts primarily on the disk).

iv) **'*E*' and '*S0*' classifications from Dressler (1980a) represent the bulge-dominant and bulge-weak ends of the archetypal galaxy distribution rather than morphologically distinct galaxies.**

D80 ellipticals are significantly more bulge dominated, indicating poor disk detection for faint disks (high B/T). No significant difference in component colours are noted for morphology relative to predictions from the colour-magnitude trend.

v) **Galaxy Zoo classifications identify galaxies with low-level deviations from a smooth, regular profile, rather than categorising morphologically distinct samples.**

Galaxy Zoo 'spirals' are thus fainter and more disk-dominated, but exhibit greater levels of scatter in (disk) colour measurements. Galaxy Zoo 'ellipticals' are primarily well-characterised lenticular galaxies and thus are consistent (in terms of median colours and colour trends) with the results of the entire analysis sample.

These results are taken from analysis of galaxies where internal component colour gradients are permitted due to the significant exaggeration of bulge $-$ disk colour separation for fixed multi-band fitting. No significant change is noted (on average) due to either the inclusion of blue galaxies removed during the selection of the initial galaxy sample, or the removal of the *a posteriori* sample vetting used to select only well-fit, 'archetypal' galaxies.

From the results of fitting 'archetypal' bulge + disk galaxies, the red sequence is interpreted as a consistent shift towards redder colours for both the bulges and disks of more luminous galaxies. Significant trends towards bluer disks (but only marginally bluer bulges) further from the cluster core indicate that the colour-environment relation is caused by an environment-driven disk fading mechanism. To reconcile disk fading with more luminous

*S0*s (see Section 5.2.4), either the disks of *S0*s must be truncated in size during transformation, or their progenitors were intrinsically smaller and/or fainter than today's star-forming spirals.

In the next chapter, I will discuss the extension of the decomposition analysis to include a wider range of (2-3 component) candidate models structures. With this multi-component analysis, I will explore the range of galaxy structures present in the Coma cluster, including those galaxies which were not best described by archetypal bulge + disk structures.

Chapter 7

Multi-component Fitting, and Deviations from the Exponential Disk Profile

7.1 Introduction

The simple exponential model (Type I; Freeman, 1970) adopted in the preceding chapters does not fully represent of the true range of *S0* outer disk structures. Truncated or anti-truncated disks (Type II and III respectively; see Section 1.4 and Erwin et al., 2008) as detected in both cluster and field galaxies, result from the redistribution of stars due to evolutionary processes. For example, truncated (Type II) disks may be formed when stars are physically removed from a galaxy's outer regions (e.g. during tidal interaction), while anti-truncated (Type III) disks may result from major merger events (Borlaff et al., 2014). Investigation of these 'broken' disks reveals their environmental or secular origins, and thus provides a deeper understanding of the evolutionary history of Coma cluster *S0*s.

In this chapter, decomposition analysis is carried out using a wider suite of candidate models (including 2- and 3-component broken disk galaxies) in order to explore the diversity of galaxy structure in the Coma cluster. Thus, I reinvestigate the structural morphologies of the $\sim \frac{2}{3}$ of galaxies in the initial Coma sample which are not well-described by an archetypal bulge + disk model. While a primary goal of this analysis is the investigation of Type I, II, and III disks galaxy structures, the extended range of (multi-component) models is necessary to avoid mis-classification of additional component structures (e.g. bars or rings) as surface brightness profile breaks. Bayesian model selection and sample filtering are applied to avoid

overfitting, and to ensure that best fit models are reliable representations of the underlying galaxy structures.

The structure of this chapter is as follows: first, I describe the multi-component decomposition methodology, highlighting differences from the previously-described AGONII bulge-disk decomposition. The broken disk component model is also described in this section. Secondly, I present the broad fitting results, including investigation of morphological (model) fractions. Lastly, I summarise the findings and conclusions of this chapter.

A detailed analysis of this multi-component decomposition will be presented in Chapter 8. Therein, the structural properties and possible evolutionary formation scenarios of galaxies whose outer regions are not dominated by an *exponential* disk will be discussed.

7.2 Methodology

In this section, the fitting process is described for a range of multi-component galaxy models, including Sérsic + broken disk models. With the exception of this broken disk model (hereafter 'Dd'), all other models are combinations of the previously-discussed Sérsic (hereafter 'S', or 'B' when used to describe a central bulge) and exponential disk (hereafter 'D') profiles.

First, I outline the 1D surface brightness profile fitting that was used as an initial stage of disk break detection and parameterisation. Next, the analytical form of the broken disk component profile (used during 2D fitting) is presented, and its photometric properties are briefly discussed. Lastly, the 2D multi-component decomposition pipeline is described (highlighting changes to the AGONII fitting routines described in Section 3), including details of fitting techniques, model selection, and sample filtering (i.e. the selection of robustly-fit multi-component galaxies).

7.2.1 1D Break Parameterisation

A simple 1D (outer) profile fitting procedure was used as a preliminary method of disk break detection. This was used primarily to produce realistic input parameter values for the 2D broken disk model fitting (see Section 7.2.2), but also identifies a sample of candidate broken

disk galaxies.

Galaxy surface brightness profiles (as measured along the major axis in 45° wedges) were fit with a simple linear or broken linear model (analogous to exponential or broken exponential). Fitting was restricted to the range $3.54'' < r < r_{\rm sky}$ (where $r_{\rm sky}$ is the radius at which the total model surface brightness is equal to 4.94$\times$ the sky uncertainty, following the methodology in Erwin et al., 2012) to avoid contamination of the surface brightness profile by the bulge or low level sky background uncertainty. The inner limit ($3.54''$) comes from the radius at which the bulge contribution, B/T(r), of an average archetypal galaxy (as determined in preceding chapters) drops below 1%. The outer limit is increased relative to the analysis presented in previous chapters to allow the outer regions of galaxy surface brightness profiles to be characterised.

A 1D BIC (see Section 3.4) was used to identify cases where the additional degrees of freedom afforded by the profile break significantly improved the model goodness-of-fit. For such broken galaxies, inner and outer disk scale length values were calculated from the inner and outer slopes of the best-fit broken linear models. The break radius was measured directly from the point at which the linear model switches from the inner to the outer slope.

Following 1D break detection, 215 galaxies (from an initial sample of 631 Coma cluster galaxies) were selected as candidate broken disks. Subsequent analysis stages also include galaxies with no 1D-detected break, however such galaxies must use generic input parameter values for broken disk model fitting.

7.2.2 2D Broken Disk Model

Fitting a broken disk structure requires a model profile with distinct inner and outer exponential scale radii, connected via a smooth transition. In GALFIT, this profile is implemented by linking two exponential disk profiles ($\Sigma_{\rm in}$ and $\Sigma_{\rm out}$) with (hyperbolic) truncation functions at some break radius. This (pixel surface brightness) profile can be expressed as:

$$\Sigma(r) = T_1(r)\Sigma_{\rm in}(r) + T_2(r)\Sigma_{\rm out}(r) \tag{7.1}$$

where T_1 and T_2 are the outer and inner truncation functions available for GALFIT (see Peng et al., 2010). The full functional form of the broken disk profile is:

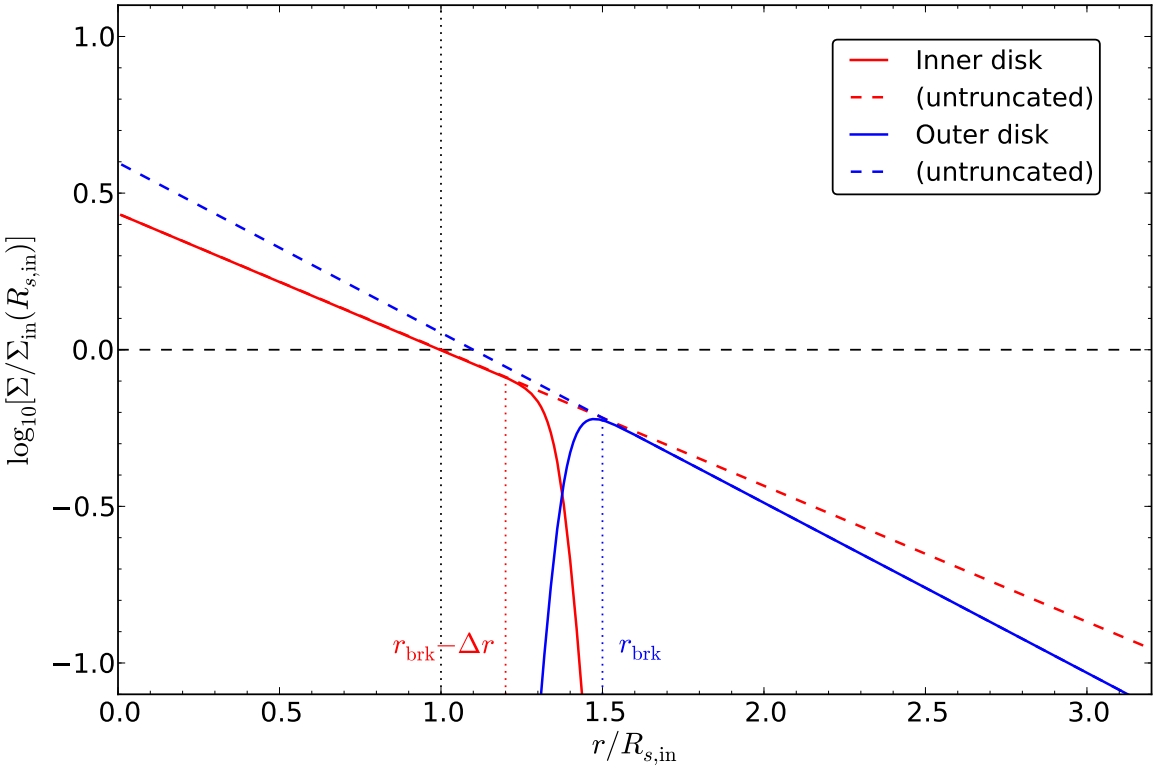

Figure 7.1: Cartoon example of the broken disk profile, indicating surface brightnesses of the inner (red) and outer (blue) disks (and their untruncated forms). r is normalised to the inner disk scale length, $R_{s,\rm in}$ (black dotted line), and Σ is normalised to the inner disk surface brightness at $R_{s,\rm in}$ (black dashed line). The inner ($r_{\rm brk}-\Delta r$) and outer ($r_{\rm brk}$) truncation radii are indicated by red and blue dotted lines. In this example, $R_{s,\rm out}=0.8R_{s,\rm in}$, $r_{\rm brk}=1.5R_{s,\rm in}$, and $\Delta r=0.3R_{s,\rm in}$.

$$\Sigma(r)=\frac{1}{2}\left(1-\tanh\left[(2-B)\frac{r}{r_{\rm brk}}+B\right]\right)\Sigma_{0,\rm in}\exp\left(\frac{-r}{R_{s,\rm in}}\right) + \frac{1}{2}\left(\tanh\left[(2-B)\frac{r}{r_{\rm brk}}+B\right]+1\right)\Sigma_{0,\rm out}\exp\left(\frac{-r}{R_{s,\rm out}}\right) \quad (7.2)$$

where $R_{s,\rm in}$ and $R_{s,\rm out}$ are the inner and outer disk scale radii, $\Sigma_{0,\rm in}$ and $\Sigma_{0,\rm out}$ are the (untruncated) central surface brightnesses of the inner and outer disks, and $r_{\rm brk}$ is the break radius. Here, $r_{\rm brk}$ is defined as the radius at which the inner and outer disk surface brightnesses are 1% and 99% of their untruncated values respectively. Dimensionless parameter B is defined as $B=2.65-4.98\left(\frac{r_{\rm brk}}{\Delta r}\right)$, where Δr is the break softening radius (radial difference within which the truncated flux drops from 99% to 1%). An example of the broken disk profile is presented in Figure 7.1 for a truncated (Type II) disk with a greatly exaggerated Δr.

The surface brightness of this model component can be fully described by a single

GALFIT input parameter: surface brightness at the break radius, $\mu(r = r_{\rm brk})$. The value of $\mu(r = r_{\rm brk})$ is constrained to be identical for the inner and outer disk structures, ensuring continuity of the total component profile. Additionally, the axis ratios and position angle parameters of both disks are coupled for structural consistency, and Δr is fixed at 0.1 pixel ($0.02''$). Hence, the broken disk profile includes only two more free fitting parameters ($R_{s,\rm out}$, and $r_{\rm brk}$; $k = 6$) than the usual exponential disk model ($k = 4$; see Table 7.1).

Fitting using a truncation function with GALFIT yields a component's surface brightness at $r_{\rm brk}$, rather than the total component magnitude. Integrating Equation 7.2 to infinity, however, is non-trivial due to the tanh function. Instead the total broken disk profile luminosity can be approximated using:

$$L_{\rm tot} = \int_0^{r_{\rm brk}} \Sigma_{\rm in}(r) 2\pi dr + \int_{r_{\rm brk}}^{\infty} \Sigma_{\rm out}(r) 2\pi dr \tag{7.3}$$

which approximates the truncation as a step function at $r_{\rm brk}$. The corresponding total profile magnitude is thus:

$$\begin{aligned} m_{\rm tot} = m_{\rm zp} &- 2.5{\rm log}_{10}[2\pi q] \\ &- 2.5{\rm log}_{10}\left[\Sigma_{0,\rm in} R_{s,\rm in}^2 \gamma(2, \frac{r_{\rm brk}}{R_{s,\rm in}}) + \Sigma_{0,\rm out} R_{s,\rm out}^2 \left(1 - \gamma(2, \frac{r_{\rm brk}}{R_{s,\rm out}})\right)\right] \end{aligned} \tag{7.4}$$

where q is the common disk axis ratio, and γ is the incomplete gamma function.

7.2.3 Processing Differences from AGONII

Fitting is carried out on i band[1] thumbnails using GALFIT with an automated python wrap-around derived from AGONII. Sérsic-only (hereafter 'S') and bulge + disk (hereafter 'BD') models are carried forward from the previous analysis. In addition, I also consider boxy bulge + disk (hereafter 'CD'), double Sérsic (hereafter 'BS'), bulge + broken disk (hereafter 'BDd'), boxy bulge + broken disk (hereafter 'CDd'), bulge + double disk (hereafter 'BDD'), bulge + bar + disk (hereafter 'BSD'), bulge + double Sérsic (hereafter 'BSS') and bulge +

[1]The i band imaging is selected for this structural investigation as it has the best seeing of all the MegaCam bands.

Component	Label	k	Parameters
Model centre	-	2	x, y
Sérsic (bulge)	B	5	$m_{\rm B}, R_{e,{\rm B}}, n_{\rm B}, q_{\rm B}$,PA$_{\rm B}$
Sérsic (general)	S	5	$m_{\rm S}, R_{e,{\rm S}}, n_{\rm S}, q_{\rm S}$,PA$_{\rm S}$
Boxy (Sérsic) bulge	C	6	$m_{\rm S}, R_{e,{\rm S}}, n_{\rm S}, q_{\rm S}$,PA$_{\rm S}, C_0$
Exponential (disk)	D	4	$m_{\rm D}, R_{s,{\rm D}}, q_{\rm D}$,PA$_{\rm D}$
Broken exponential	Dd	6	$m_{\rm D}, R_{s,{\rm in}}, R_{s,{\rm out}}, q_{\rm D}$,PA$_{\rm D}, r_{\rm brk}$

Table 7.1: Table of model component types used during multi-component decomposition analysis, including the number of free parameters, k.

bar + broken disk (hereafter 'BSDd') models. Note that usage of 'bar'/'barred' throughout this chapter is loose terminology referring to galaxies with two distinct (inner) Sérsic components, rather than explicitly requiring a stellar bar structure. As such, a 'bar' may correspond also to a distinct lens structure (i.e. high intrinsic axis ratio spheroids with flat inner surface brightness profiles, dying rapidly at larger radii; Kormendy & Kennicutt, 2004). A full description of these model components is provided in Table 7.1, and the candidate models are described in Table 7.2.

The fitting procedure in this chapter is not exhaustive (i.e. the search through parameter space is not extended) as such an approach becomes computationally expensive (and highly sensitive to parameter degeneracies) for 3+ component models. Thus, the results of each input model are the product of one `GALFIT` cycle. Instead, greater care is taken to generate sensible initial parameter values: in addition to building model complexity iteratively, multiple input models are generated for a single model type if the prior model's components could be interpreted ambiguously. For example, a best-fit BD model's bulge (or disk) structure can be used as the basis for the bulge, bar, or disk for an input BSD model. This build-up of model complexity is illustrated in Figure 7.2.

Extended Profile Typing

Models with two structural components are classified by Allen et al. (2006) surface brightness profile types as before. In addition, models including broken disks (BDd, CDd) can be assigned a subscript '+' /'$-$' where the surface brightness profiles of the two components cross more/fewer times than if their inner structures were unmodified (e.g. a Type II BDd model wherein truncation causes the disk profile to become fainter than the bulge at large

Model	Label	k	$n_{\rm comp}$
Sérsic	S	7	1
Sérsic + exponential	BD	11	2
Boxy Sérsic + exponential	CD	12	2
Double Sérsic	BS	12	2
Sérsic + broken exponential	BDd	13	2
Boxy Sérsic + broken exponential	CDd	14	2
Sérsic + double exponential	BDD	15	3
Double Sérsic + exponential	BSD	16	3
Triple Sérsic	BSS	17	3
Double Sérsic + broken exponential	BSDd	18	3

Table 7.2: Table of the multi-component models used during decomposition analysis, including the number of independent structural components, $n_{\rm comp}$, and number of free parameters, k. The individual components are described in Table 7.1.

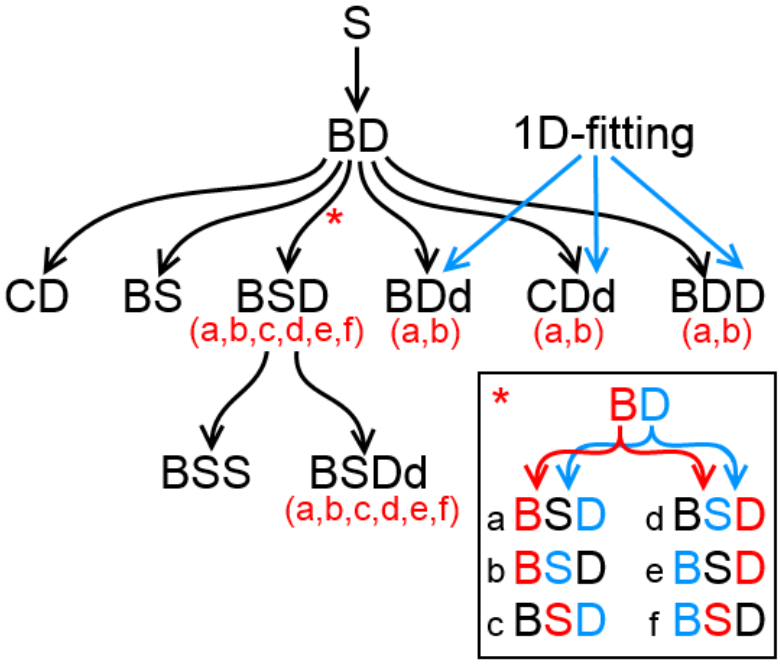

Figure 7.2: Graphical illustration of the relation between the models during multi-component decomposition. Black arrows indicate which models take input parameter values from the best fit of a simpler model. Blue arrows indicate models which also take input parameter values from external sources. Models with multiple input variants (differing in their interpretation of progenitor model components) are noted in red. The inset illustrates multiple input generation for BSD models from the best fit BD components.

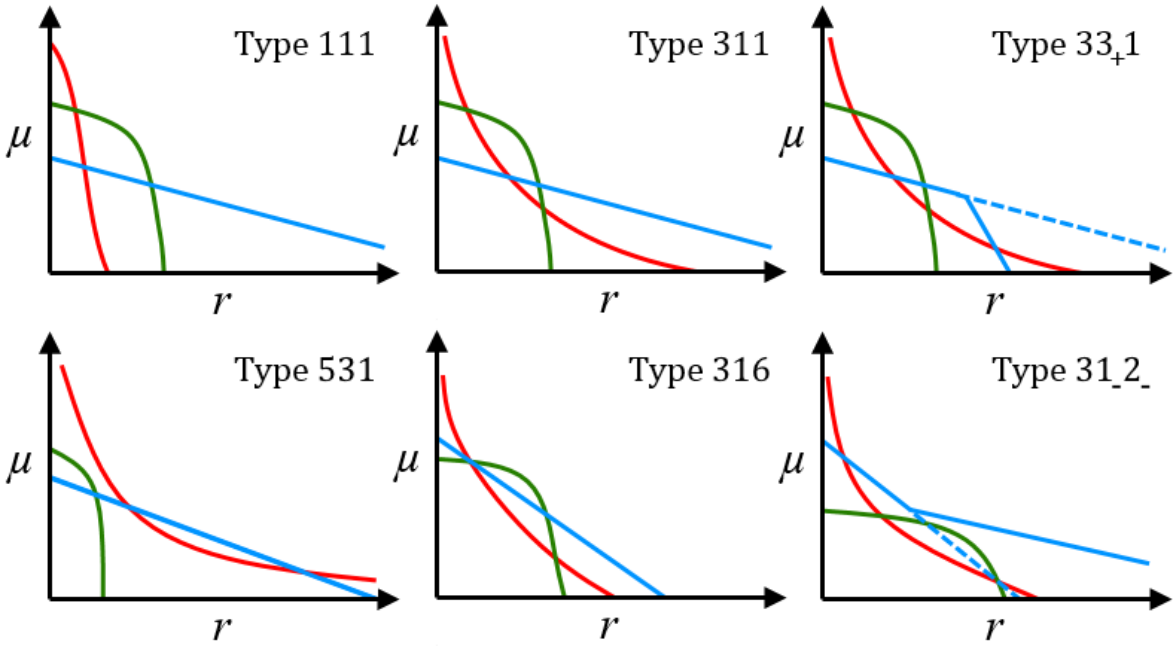

Figure 7.3: Cartoon surface brightness profiles for 3-component galaxies with profile Types 111 (**top left**), 311 (**top middle**), 33_+1 (**top right**), 531 (**bottom left**), 316 (**bottom middle**), and $31\_2\_$ (**bottom right**), indicating the bulge (red), bar (green), and disk (blue) component surface brightnesses as a function of distance from the galaxy centre. The Type 33_+1 profile is identical to the Type 311 example, except for the disk truncation which causes the bulge to dominate at large radii. Likewise, the Type $31\_2\_$ profile is equivalent to the Type 316 profile, except the outer Type III disk does not cross the bulge or bar profiles.

radii would be assigned Type3_+; a Type III CDd model wherein the disk profile is never fainter than the bulge due to the outer disk would be assigned Type2_-).

3-component model surface brightness profiles cannot be completely described by Allen types (i.e. the relative brightnesses of the bulge and disk component alone). Instead, I assign each 3 component model a three digit surface type ('Type abc') based on the interaction of all its components. For a generalised model with components A, B, and C, a corresponds to the Allen type for A/B, b corresponds to the Allen type for A/C, and c corresponds to the Allen type for B/C. For example, a BSD model of Type311 has bulge and bar surface brightness profiles which are brighter than the disk at all radii ($b = 1, c = 1$), but the bulge is dominated by the bar at intermediate radii ($a = 3$). For BSDd models, both b and c can be modified by the $+/-$ subscript as described above. Cartoon examples of three of the most common 3-component profiles types (Types 111, 311, and 331) are presented in Figure 7.3, including one profile wherein a broken (Type II) disk modifies the profile type (Type 33_+1 rather than 311).

Filtering

Sample filtering is applied to the fitting results (similar to Section 3.5) in order to isolate a sample of accurately-fit galaxies. A key step in this process is the selection of best-fit models which are meaningful descriptions of each galaxy's underlying morphological structure. Hence, galaxy models are assessed on both goodness-of-fit (i.e. ensuring that a galaxy is neither underfit nor overfit), and suitability of component structures (i.e. rejecting components with unrealistic parameters, or which do not measure the intended target substructure). By removing such instances of structural dissonance between the galaxy and model, the reliability of multi-component analysis results is vastly improved.

The filtering process for multi-component fits is illustrated in Figure 7.4, and summarised as follows:

1. Galaxies are excluded if contaminated by nearby sources (using $f_{\rm mask}(a_{\rm target}, q_{\rm target}) \geq 0.4$ and $f_{\rm mask}(a_{\rm target}/2, q_{\rm target}) \geq 0.3$ as before).

2. Asymmetrical galaxies are also removed ($A > 0.2$), but the threshold for removing galaxies based on BD-residual asymmetry was raised to $A_{\rm res} > 0.5$, as moderate residual asymmetry may simply indicate the presence of unfitted structural components.

3. For models with multiple variants (e.g. $\text{BSD}_{\rm a-f}$), a single (best fit) model is selected for analysis based on a simple χ^2 test. However, for models with broken disks (BDd, CDd, BSDd) model variants are excluded from consideration if $0.4r_{\rm brk} > 1.678R_{s,\rm out}$ (i.e. the outer disk contributes less than 8% of its total flux) or $0.2r_{\rm brk} > 1.678R_{s,\rm in}$ (i.e. less than 0.3% of the inner disk's total flux is truncated). These cuts remove anomalous model structures resulting from the broken disk component fitting to unintended structures.

4. For broken disk (Dd) models, galaxies are removed if $R_{s,\rm out} < 0.1r_{\rm brk}$ as a bug in `GALFIT`'s truncation yields an additional (strong) central point source in this regime.

5. Additionally, broken disks with $r_{\rm brk} < 5''$ are removed, as the inner disk of such systems behave like point sources.

6. A BIC test is applied to select the best-fit model, which introduces the least extra

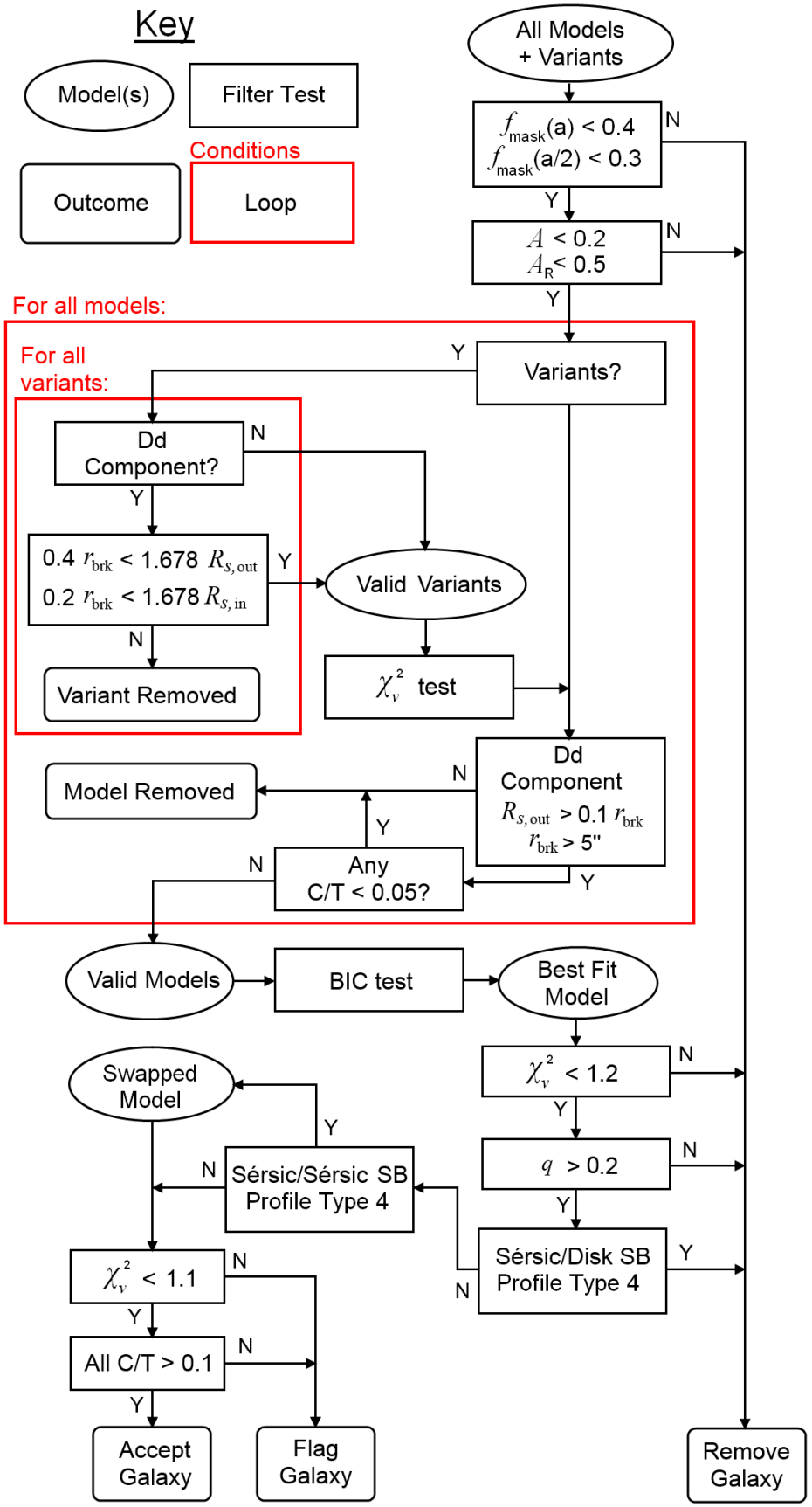

Figure 7.4: Flow chart illustrating multi-component fitting model selection for models S, BD, CD, BS, BDd, CDd, BDD, BSD, BSS, and BSDd. For profile type definitions, refer to Section 1.4 and Allen et al. (2006).

fitting parameters. To provide a more stringent model selection test, the psf area ($N_{\rm psf}$) used for Equation 3.2 is increased to the area within two Gaussian σ (a factor of ~ 3 increase). Conversely, the scatter in psf area ($\sigma_{\rm res}$) is measured here from the individual psf images (typically $\sim 3\%$).

7. Models with (one or more) component-to-total ratios, C/T< 0.05 are removed from consideration during the BIC test due to high parameter uncertainty. This is similar to the B/T cut for the selection of Sérsic-only models in Section 3.5, but does not make assumptions regarding the preferred 'simpler' model.

8. The χ^2_ν limit for (BIC-selected) models is lowered to $\chi^2_\nu > 1.2$, while galaxies are now flagged if $1.1 < \chi^2_\nu < 1.2$. This more critical cut in model χ^2_ν has been calibrated through visual examination of model residuals.

9. Galaxies with disk/outer component axis ratios, $q < 0.2$ are removed, as multi-component decomposition cannot be meaningfully applied to edge-on systems.

10. Models with Type 4 Sérsic/disk profiles (i.e. Type 4, $x4x$, $xx4$) are removed due to swapping of the bulge/bar and disk roles of the structural components.

11. Models with Type 4 Sérsic/Sérsic profiles (e.g. Type 4, $4xx$) have their components swapped (e.g. bar and bulge swap) to maintain the 'inner' role of the bulge component (or 'inner'/'middle'/'outer' roles for components 1, 2, and 3 in BSS models). Galaxy models modified in this way are not removed or flagged.

12. Remaining models with $0.05 < {\rm C/T} < 0.1$ are flagged as unreliable.

13. Galaxies are no longer flagged via cuts based on the relative sizes (R_e), axis ratios (q), or position angles (PA) of any two components (as in Section 3.5). Likewise, Sérsic components are no longer flagged if $n < 1$. Such tests were intended to identify underfit 3-component systems, which are now explicitly identified via the BIC test.

14. As no colour analysis will be carried out, galaxies are also no longer removed for possessing blue cores.

7.3 Overview of Results

7.3.1 Best-fit Models

A wide mix of best-fit model morphologies are found for the 631 galaxies (570 Coma sample + 61 blue Coma galaxies) considered for 2D multi-component fitting. Figure 7.5 presents an illustrative example galaxy best fit by a Sérsic-only model (upper panels), and the corresponding (overfit) bulge + disk model (lower panels). Surface brightness plots (μ_i) and model residuals (image $-$ model in counts) are included for both model fits (top left), as measured from the galaxy and model thumbnails in wedges of elliptical annuli (angle $\cos^{-1}(e^2)$, where e is the eccentricity of the galaxy's target ellipse). The i band residual images (including only the central quarters) are presented in the bottom right corners (black border) for each model fit. In addition, component residual images (i.e. the residual image after all model components *except* the target component are subtracted) are included along the bottom in panels bordered by their μ_i plot line colours (i.e. red and blue for Sérsic and exponential components respectively). Here, the addition of a disk component improves the goodness of fit (lower χ^2_ν), but this improvement is not statistically significant given the increased number of fitting parameters (increased BIC).

Equivalent example plots for galaxies best fit by all other model types (except CD, and CDd due to small sample sizes) are presented in Figures 7.6-7.12. Each best fit model (upper panels) is compared to its next simplest equivalent (lower panels). Hence, best-fit BD (Figure 7.6) and BS (Figure 7.7) models are compared to (underfit) S models; best-fit BDd (Figure 7.8), BDD (Figure 7.9), BSD (Figure 7.10), and BSS (Figure 7.11) models are compared to (underfit) BD models; and the best-fit BSDd model (Figure 7.12) is compared to an (underfit) BSD model.

The fractions of Coma cluster galaxies best fit by each candidate multi-component model are illustrated in Figure 7.13. From the initial sample of 631 galaxies, 162 are best fit by a Sérsic-only model (26%), 102 are best fit by BD (16%), 43 are best fit by BS (7%), three are best fit by CD ($< 1\%$), 18 are best fit by BDd (3%), three are best fit by CDd ($< 1\%$), 43 are best fit by BDD (7%), 97 are best-fit by BSD (15%), 98 are best fit by BSS (16%), and 62 are best fit by BSDd (10%). Thus, the majority of Coma cluster galaxies (58%) have

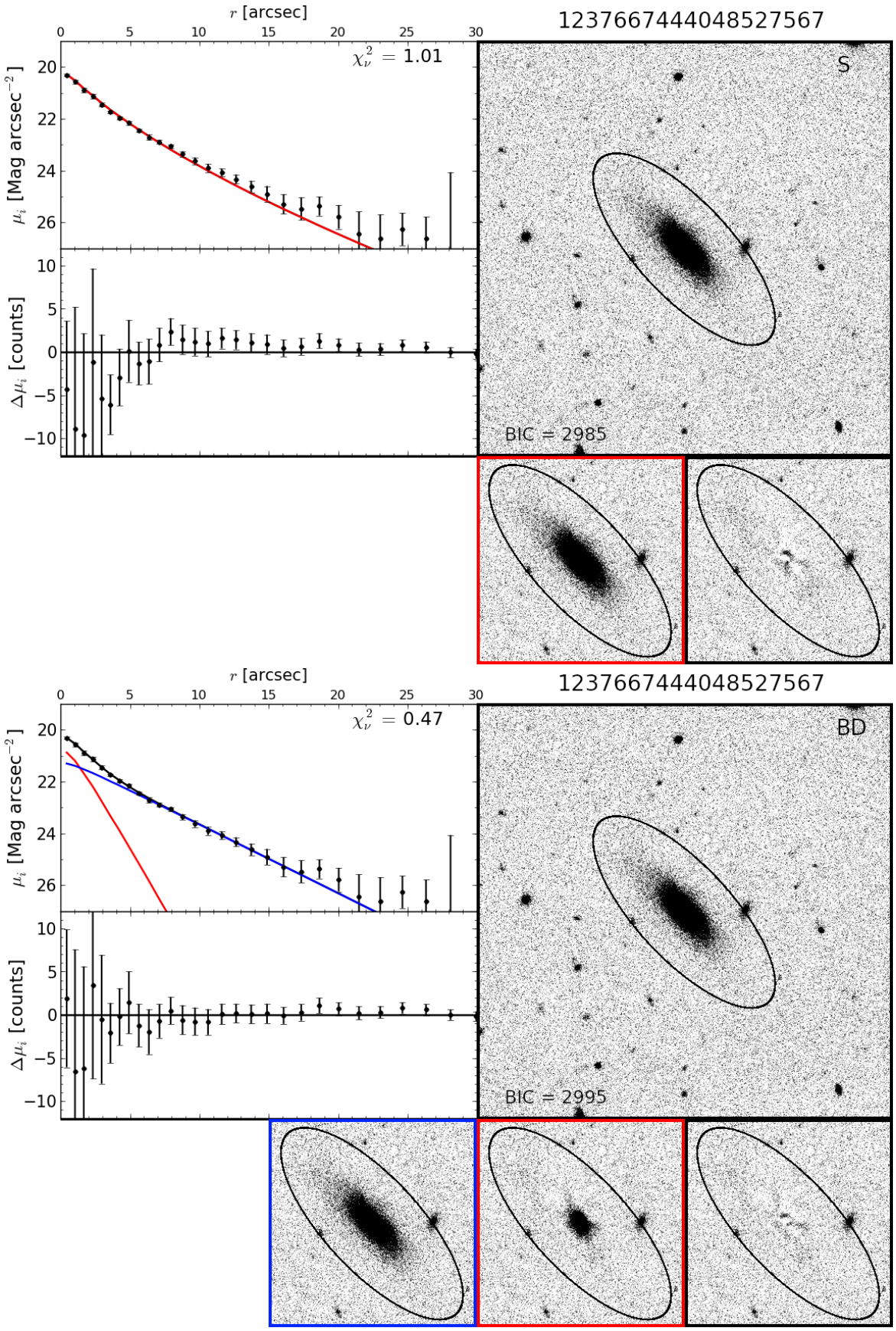

Figure 7.5: An example galaxy best fit by an S model (DR8 ObjID 1237667444048527567): Surface brightness profiles (μ_i), residuals ($\Delta\mu_i$), and i band thumbnails for the S model (**top:** Sérsic = red), and the corresponding BD model (**bottom:** bulge = red, disk = blue). Small images depict isolated model components (border colours $\equiv$ μ_i plot), and the total residual (black borders). The target ellipse is noted in black in all thumbnails, and 1D χ^2_ν (major axis) and 2D BIC values are included for both models.

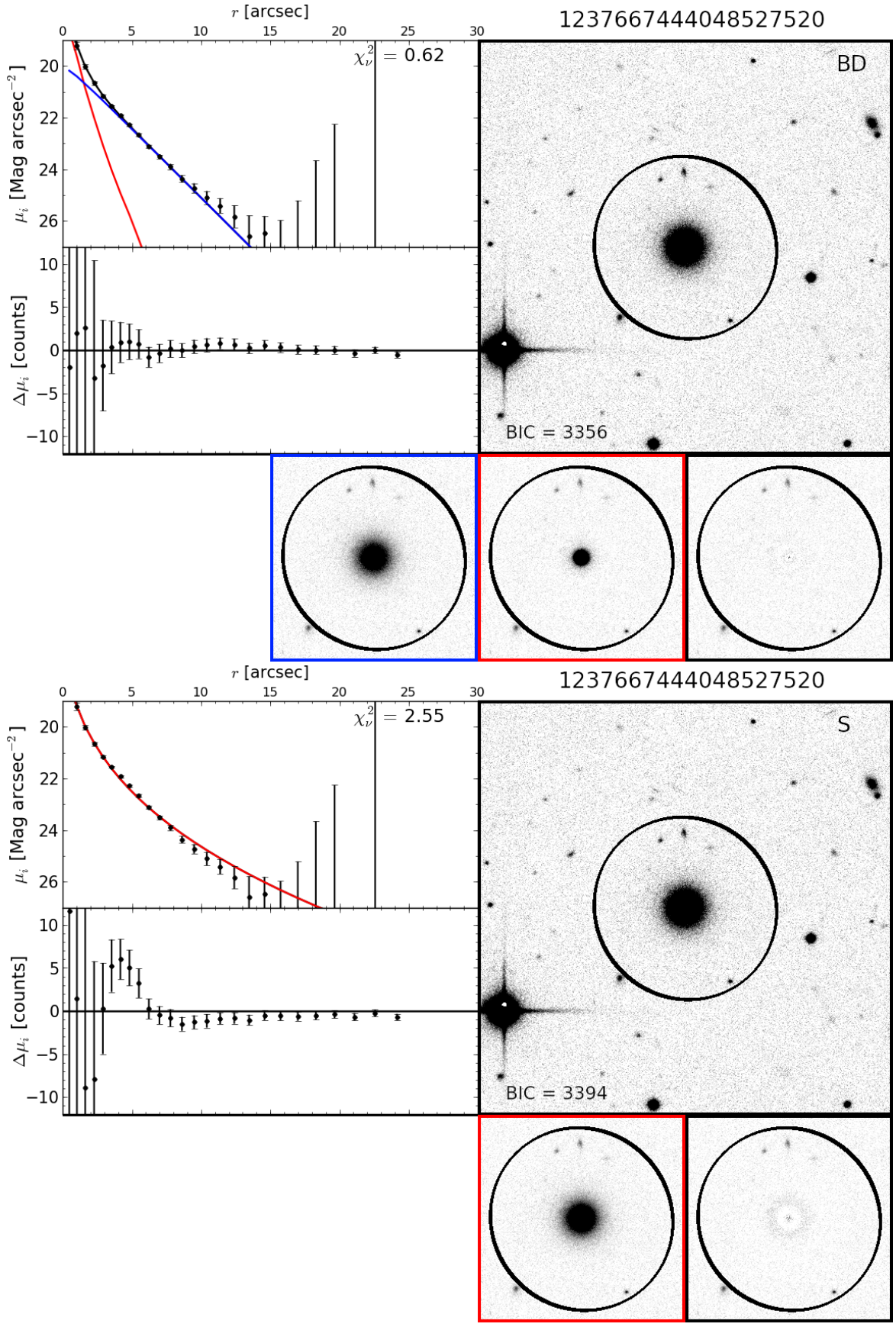

Figure 7.6: An example galaxy best fit by a BD model (DR8 ObjID 1237667444048527520). As Figure 7.5 for a BD model (**top:** bulge = red, disk = blue), and the corresponding S model (**bottom:** Sérsic = red).

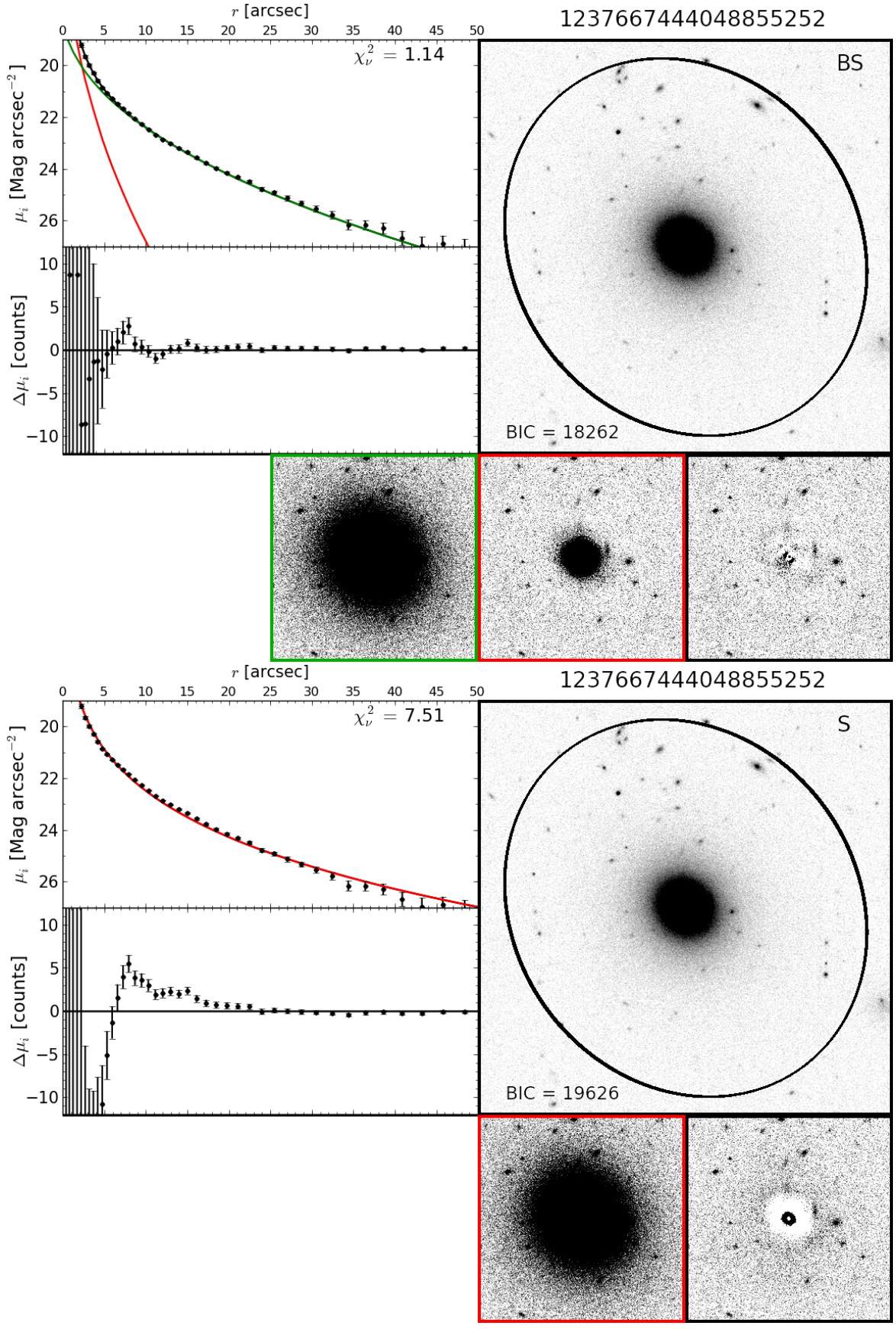

Figure 7.7: An example galaxy best fit by a BS model (SDSS DR8 ObjID 1237667444048855252). As Figure 7.5 for a BS model (**top:** bulge = red, Sérsic = green), and the corresponding S model (**bottom:** Sérsic = red).

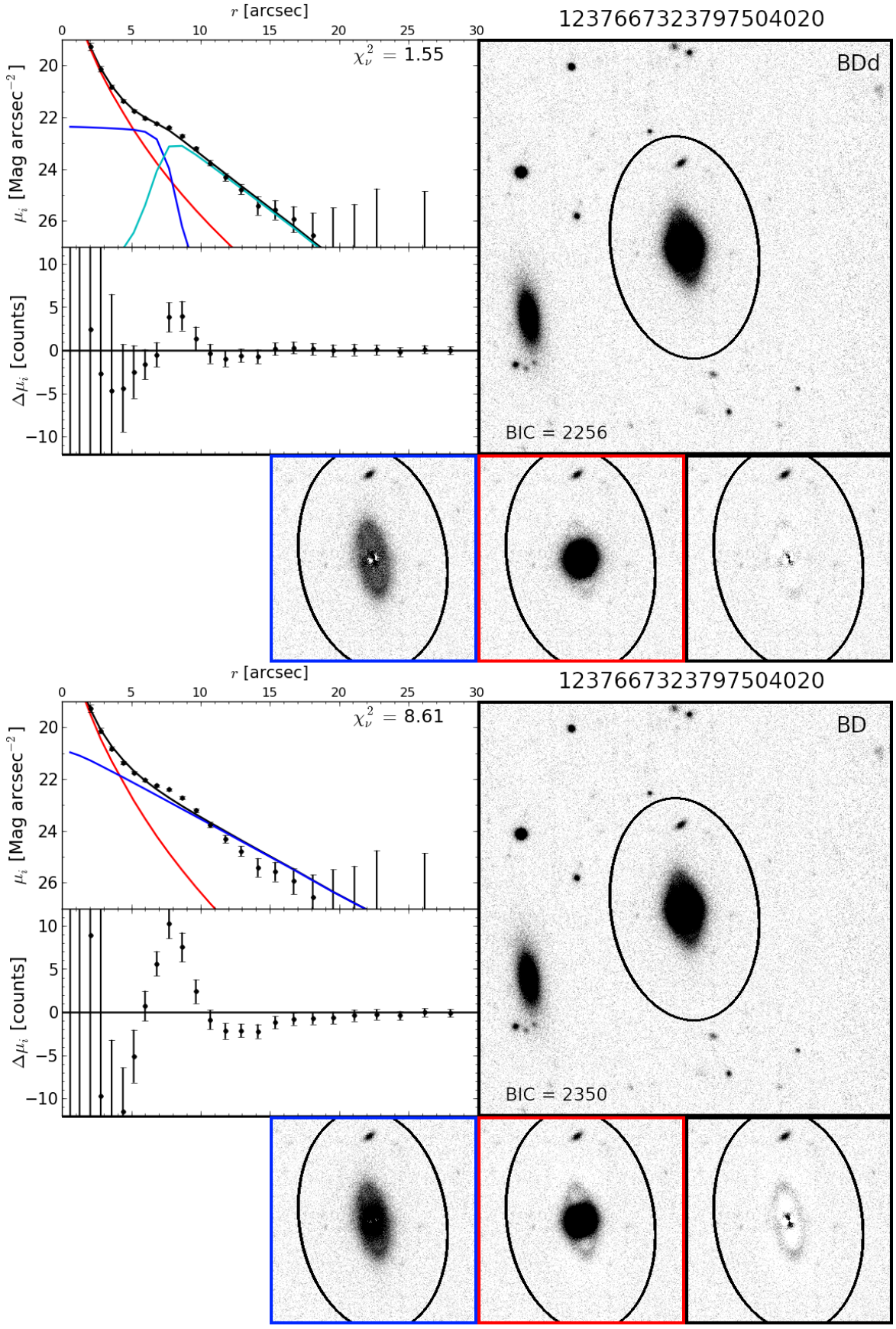

Figure 7.8: An example galaxy best fit by a BDd model (SDSS DR8 ObjID 1237667323797504020). As Figure 7.5 for a BDd model (**top:** bulge = red, inner/outer disk = blue/cyan), and the corresponding BD model (**bottom:** bulge = red, disk = blue).

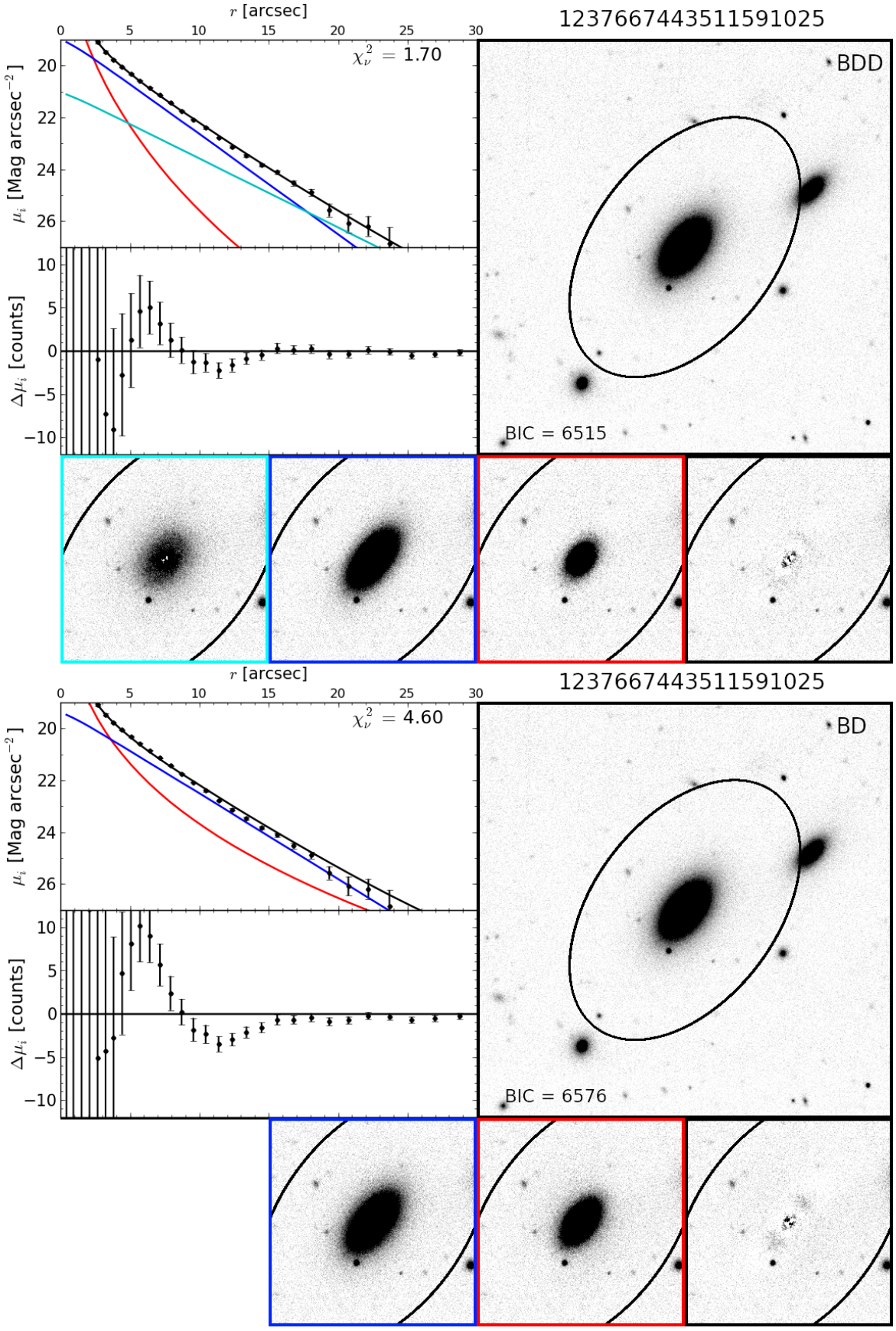

Figure 7.9: An example galaxy best fit by a BDD model (SDSS DR8 ObjID 1237667443511591025). As Figure 7.5 for a BDD model (**top:** bulge = red, disk1 = blue, disk2 = cyan), and the corresponding BD model (**bottom:** bulge = red, disk = blue).

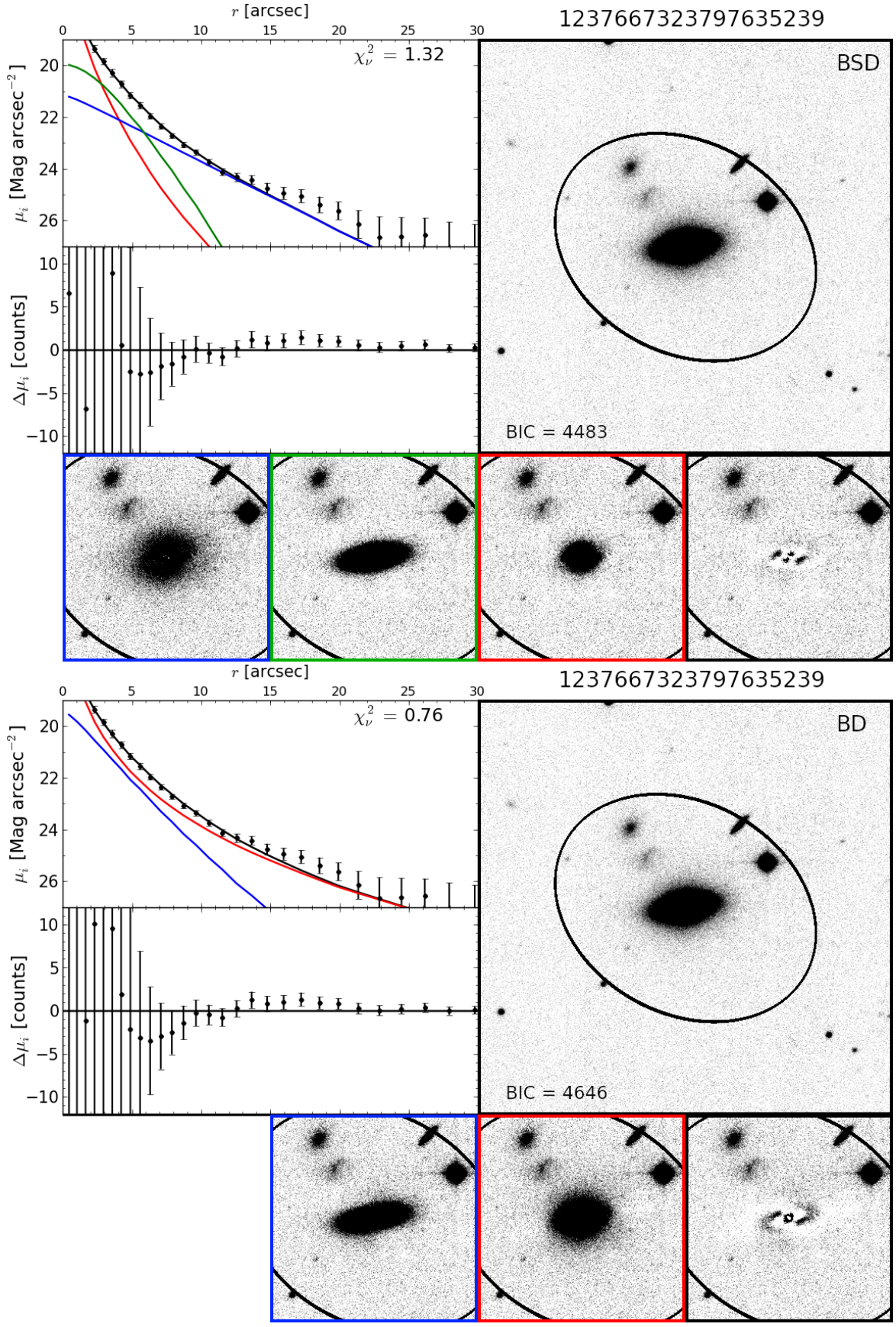

Figure 7.10: An example galaxy best fit by a BSD model (SDSS DR8 ObjID 1237667323797635239). As Figure 7.5 for a BSD model (**top:** bulge = red, bar = green, disk = blue), and the corresponding BD model (**bottom:** bulge = red, disk = blue).

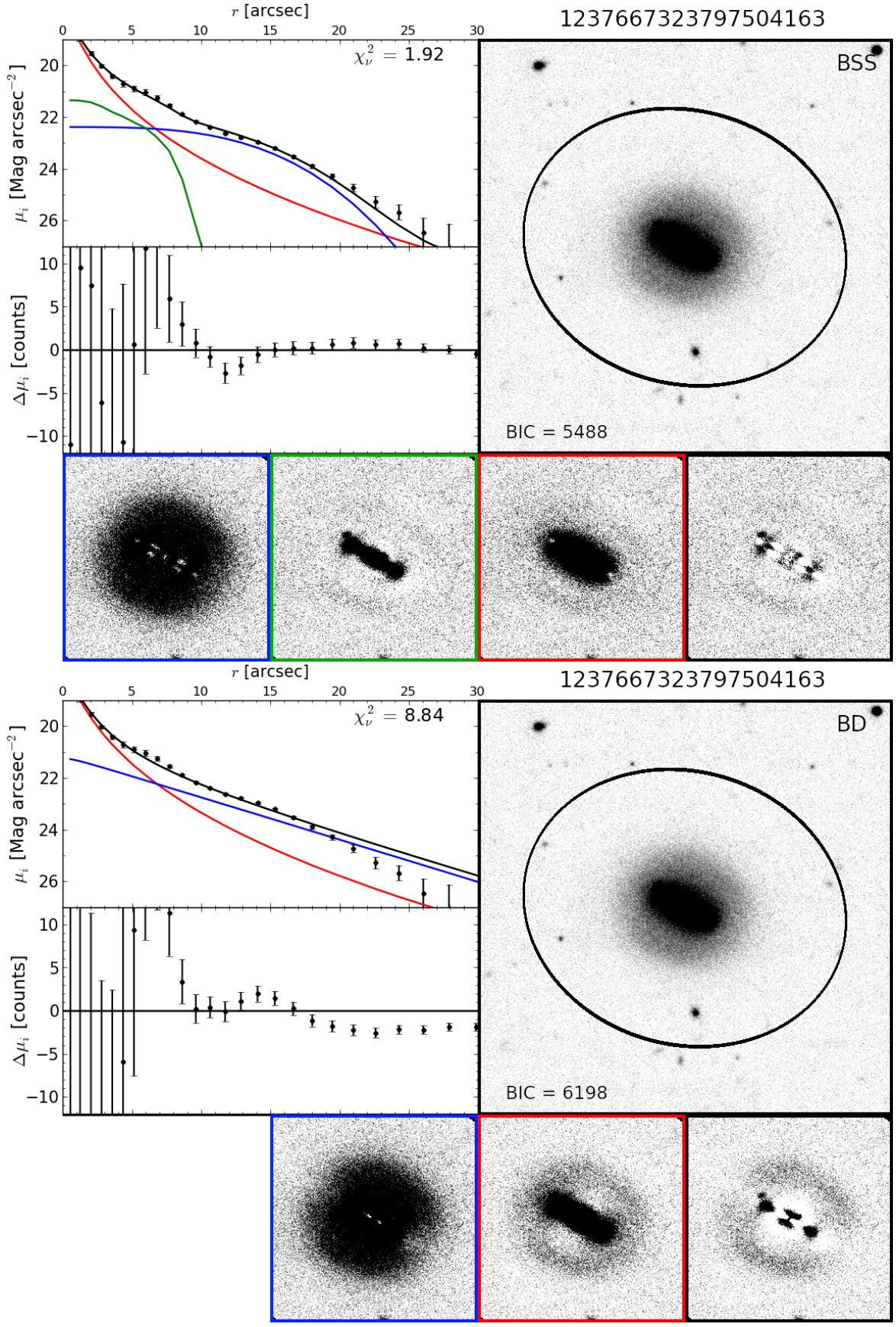

Figure 7.11: An example galaxy best fit by a BSS model (SDSS DR8 ObjID 1237667323797504163). As Figure 7.5 for a BSS model (**top:** bulge = red, Sérsic1 = green, Sérsic2 = blue), and the corresponding BD model (**bottom:** bulge = red, disk = blue).

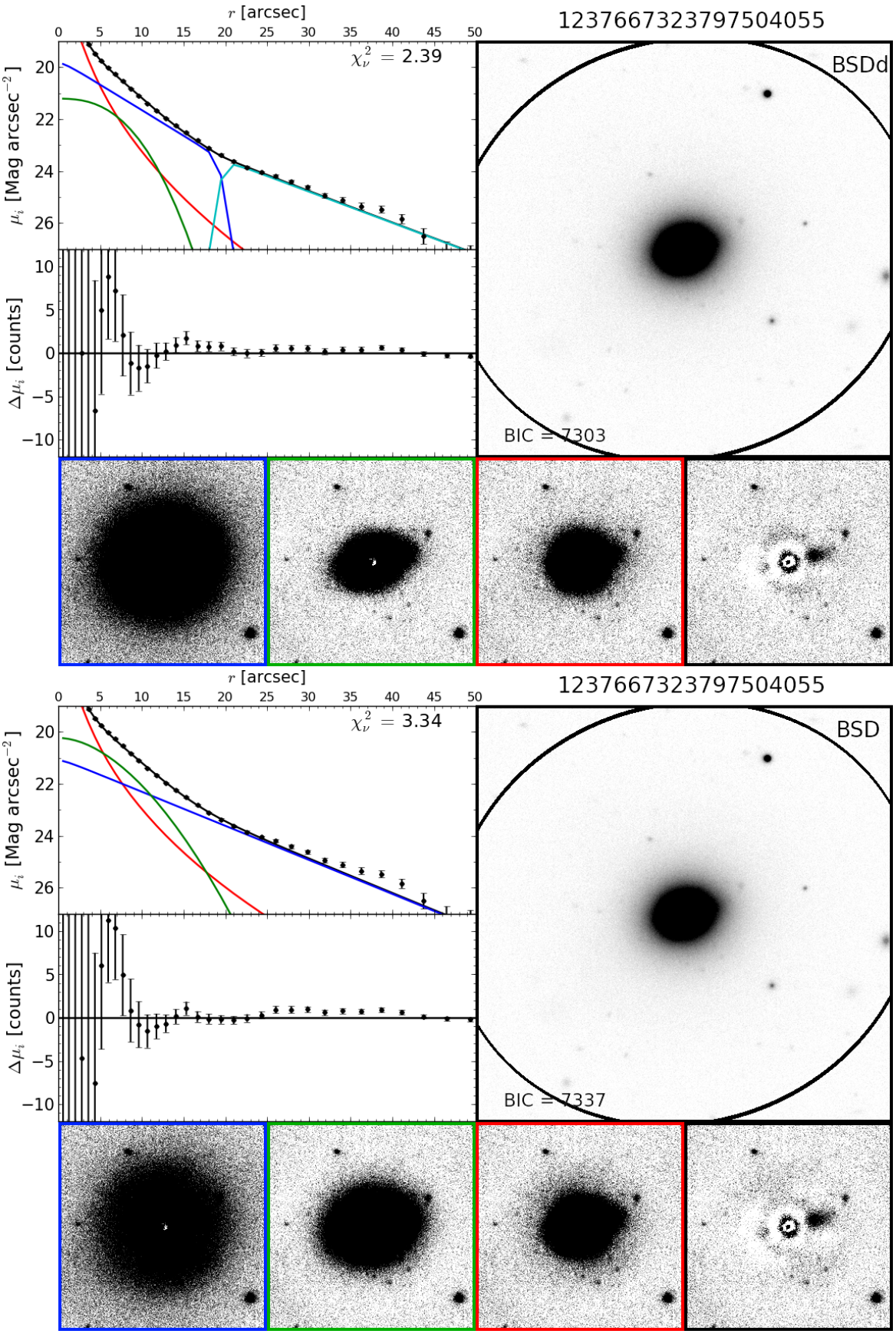

Figure 7.12: An example galaxy best fit by a BSDd model (SDSS DR8 ObjID 1237667323797504055). As Figure 7.5 for a BSDd model (**top:** bulge = red, bar = green, inner/outer disk = blue/cyan), and the corresponding BSD model (**bottom:** bulge = red, bar = green, disk = blue).

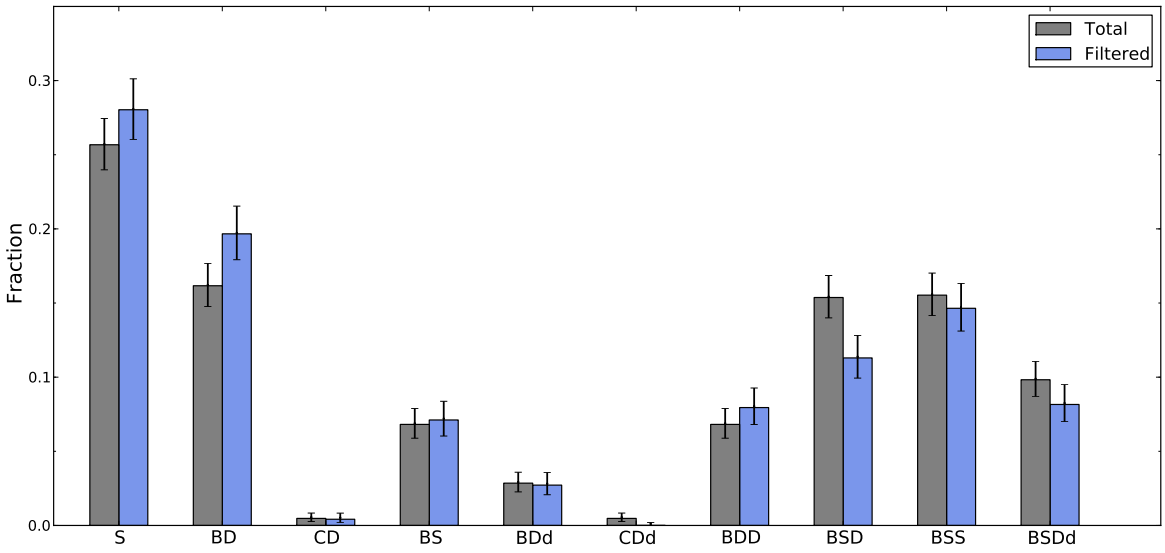

Figure 7.13: Histogram of best-fit model type fractions for the initial ($N = 631$) and filtered ($N = 515$) samples. Error bars are 68% confidence limits.

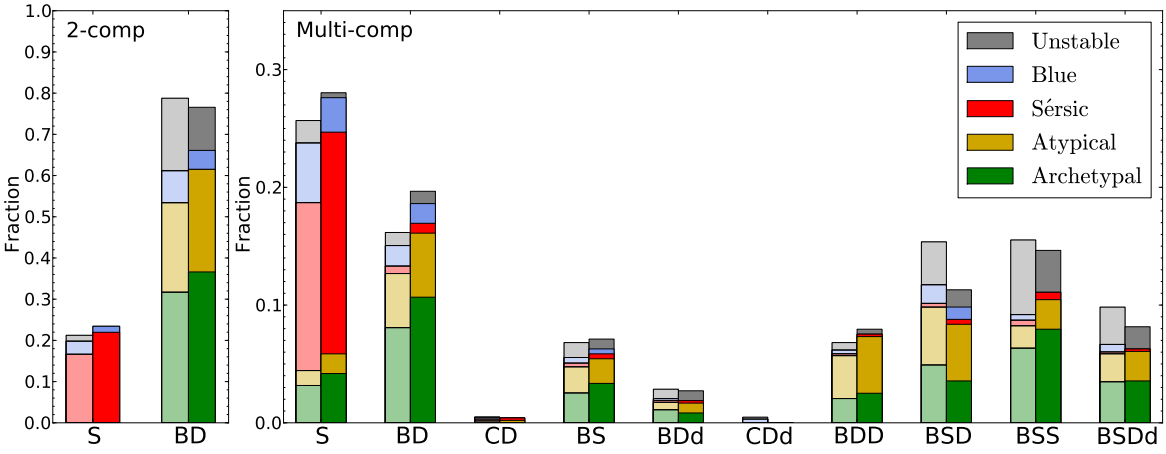

Figure 7.14: Histograms of best-fit model numbers (as fractions of the initial sample, $N = 631$) for 2-component decomposition (**left:** AGONII, see Chapter 3) and multi-component decomposition (**right:** this chapter). Bar colours indicate the filtered sub-samples from AGONII (see Section 3.5), and the additional sample of blue Coma galaxies ($g - r < 0.5$) considered in this chapter. Faint bars indicate the model fractions prior to applying the multi-component sample filter described in Section 7.2.3.

Model	Total	Removed A, $f_{\rm mask}$	Removed χ^2_ν	Removed $q_{\rm D}$	Removed $r_{\rm brk}$ Errors	Removed Type 4	Filtered Sample
S	162	28	0	0	-	-	134
BD	102	4	0	2	-	2	94
CD	3	1	0	0	-	0	2
BS	43	5	1	3	-	-	34
BDd	18	2	0	0	3	0	13
CDd	3	2	1	0	0	0	0
BDD	43	4	0	1	-	0	38
BSD	97	11	6	2	-	24	54
BSS	98	12	12	4	-	-	70
BSDd	62	11	3	1	2	6	39
All	**631**	**80**	**23**	**13**	**5**	**32**	**478**

Table 7.3: The distribution of model types resulting from multi-component fitting (including the number removed by sample filtering). Dashes indicate models for which a particular sample filter is not valid.

morphologies more complex than the simple S and BD models considered previously.

Many of these complex structure galaxies were considered to be (archetypal *S0*) bulge + disk systems previously (see Figure 7.14). In total, 51 'archetypal' galaxies (from $N = 200$; 25.5%) remain best-fit by a BD model, while 129 (64.5%) require more complex models and 20 (10.0%) are demoted to a single-Sérsic model (due to the more stringent model selection tests in this chapter). The fractions of prior 'atypical bulge + disks' adequately fit by a BD model (21.1% of 137), requiring more complex models (73.0%), and demoted to S (5.8%) are similar. Note that many galaxies classed as 'unstable' previously are best-fit here by complex 3-component models (68% of 128). This is due to significant reductions in χ^2_ν as additional structural components are accounted for.

7.3.2 Filtering Results

After filtering, 478 galaxies from the sample of 631 (76%) remain. The 153 galaxies removed by filtering comprise: 80 galaxies removed due to asymmetry or contamination, 23 galaxies with high χ^2, 13 highly-inclined galaxies, three galaxies with anomalous outer disks due to $R_{s,\rm out} > 0.1 r_{\rm brk}$, two galaxies with anomalous inner disks due to $r_{\rm brk} < 5''$, and 32 galaxies removed due to inverted Sérsic/disk components (Type 4, $4xxx$ etc.). Of the remaining filtered galaxies, 134 are best fit by a Sérsic-only model (28.0%), 94 are best fit by BD (19.7%), 34 are best fit by BS (7.1%), two are best fit by CD (0.4%), 13 are best fit by

BDd (2.7%), none are best fit by CDd (0.0%), 38 are best fit by BDD (7.9%), 54 are best-fit by BSD (11.3%), 70 are best fit by BSS (14.6%), and 39 are best fit by BSDd (8.2%). The number of galaxies best fit by each model type (before and after sample filtering) are summarised in Table 7.3.

Note that in total, 93 galaxies ($19.5^{+2.0}_{-1.8}\%$) are well-described by 'barred' models (BSD, BSDd). This barred fraction for Coma is significantly lower than the value reported in Lansbury et al. (2014) from either decomposition ($72^{+5}_{-6}\%$) or ellipse ($48^{+6}_{-6}\%$) analyses. This difference cannot be reconciled, even if BSS models are included in the 'barred' sample (yielding $34.1^{+2.6}_{-2.3}\%$ bar fraction). However, if the present sample is restricted to only contain galaxies with D80 morphological classifications (as in Lansbury et al., 2014), then the barred fraction (including BSS galaxies) rises to $62.5^{+4.1}_{-4.3}\%$. This fraction rises further if only D80 *S0*s (including *S0/a*, *E/S0*) galaxies are considered, yielding bars in $70.5^{+4.6}_{-5.0}\%$ of galaxies. As the D80 catalogue only covers the bright end of the Coma sample ($M_g \lesssim -18$), the bar fraction increase for D80 galaxies indicates a significantly decreasing bar detection rate for faint galaxies. However, the lower bar detection rate relative to Lansbury et al. (2014), particularly if BSS galaxies are not considered 'barred', reflects the more stringent conditions for accepting a more complex model in the present work.

Based on the results of model selection in the filtered sample, I note the following results:

- 215 galaxies (45% of total) are selected by 1D fitting to have a disk break. Of these, only 37 are also detected as containing breaks from 2D analysis (17%). In total, 52 galaxies (11%) have 2D-selected disk breaks. Thus, 1D fitting correctly identifies (71%) of all broken disk galaxies.

  Thus: **A 1D break detection method detects 71% of (2D-detected) broken disk galaxies, but reports a false positive result (i.e. breaks reported in unbroken profiles) 83% of the time.**

- If only 1- or 2-component models (excluding double Sérsic models; i.e. S, BD, CD, BDd, CDd) are considered for 2D analysis, a broken disk model (BDd, CDd) is preferred for 152 galaxies (32% of total). Of these, 53 galaxies would be better-fit by a double Sérsic model.

  Thus: **A 2-component 2D analysis falsely reports broken disk models 35% of the**

time if only (2-component) models with exponential disks are considered.

- Alternatively, if all 1-, 2-, and 3-component models are considered (excluding double/triple Sérsic models) for 2D analysis, a broken disk model (BDd, CDd, BSDd) is selected for 94 galaxies (20% of total). Of these, 42 galaxies would be better-fit by a double or triple Sérsic model.

  Thus: **A 2D analysis falsely reports broken disk models 45% of the time if only models with exponential disks are considered.**

- If 3-component models are excluded from consideration for 2D analysis, a 2-component model is preferred in 342 galaxies (72% of total). However, 199 of these galaxies would be better fit by a 3-component model[2].

  Thus: **A 2D analysis selects an overly-simplistic 2-component model 58% of the time if 3-component models are not considered.**

- Of all 141 galaxies with 2-component structures, 82 galaxies (58%) exhibit Type 1 (i.e. 'archetypal' inner + outer component) profiles, while 44 Type 3 profile galaxies (recurrent bulge; 31%) make up the second most common structural type. For 3-component galaxies ($N = 201$), the three most common profile types are Type $31x$ ('archetypal' bulge + disk, with bar-like Sérsic ; $N = 87$; 43%), Type $33x$ (recurrent bulge with bar-like Sérsic ; $N = 36$; 18%), and Type $11x$ ('archetypal' bulge + disk, with 'archetypal' bulge + Sérsic; $N = 31$; 18%).

  Thus: **2D analysis selects 2- and 3-component galaxies with archetypal disk structures in the majority of cases, with recurrent bulges (dominant over their disks at large radii) being the second most common structure.**

- Of the 478 galaxies in the filtered sample, 214 (62%) yield a Type 1 (archetypal) profile if fitted by a BD model, with 72 galaxies (21%) corresponding to Type 3 (recurrent bulge) profiles. If 2- and 3-component galaxies are considered separately, no significant differences in (imposed BD model) Type 1 and 3 profile fractions are detected (Type 1/3: $66\%/20\%$ for 2-component galaxies, $59\%/22\%$ for 3-component galaxies).

[2]Disparity between this value and the 201 3-component models reported above is due to two galaxies which would be better fit by a single Sérsic model, if 3-component models are excluded.

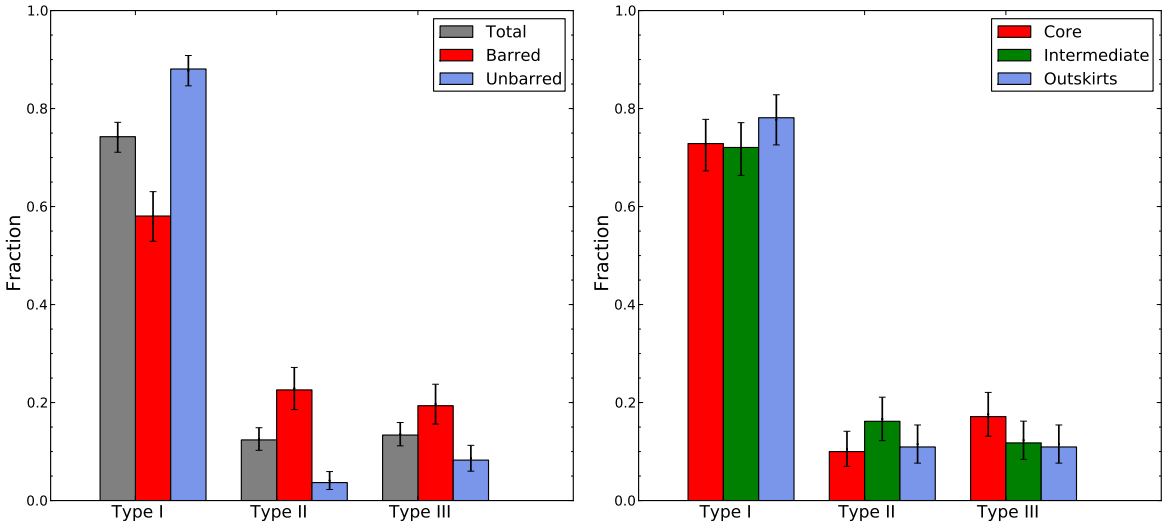

Figure 7.15: Histogram of outer disk type fractions for **Left:** barred (BSD, BSDd) and unbarred (BD, BDd) bulge + disk models, **Right:** galaxies in the core ($r_{\rm cluster} < 800$ kpc), intermediate ($0.8 < r_{\rm cluster} < 1.6$ Mpc), and outskirts ($r_{\rm cluster} > 1.6$ Mpc) cluster samples. Types I, II, and III refer to unbroken, truncated, and anti-truncated disks respectively. Error bars are 68% confidence limits.

Thus: **Type 3 BD profiles do not intrinsically represent underfit galaxy structures, but rather a structural morphology distinct from archetypal bulge + disk systems.**

7.3.3 Freeman Disk Type Fractions

Galaxies with single disk-like outer profiles (BD, CD, BDd, CDd, BSD, BSDd) were categorised by their disk types (i.e. Type I, II, or III). In total, 202 valid disk galaxies are contained within the sample after filtering. Of these, 150 galaxies ($74.3^{+2.9}_{-3.2}\%$) have Type I (untruncated) disks, 25 galaxies ($12.4^{+2.5}_{-2.1}\%$) have Type II (truncated) disks, and 27 galaxies ($13.4^{+2.6}_{-2.2}\%$) have Type III (anti-truncated) disks (Figure 7.15, left panel). Compared to the disk type fractions reported in Erwin et al. (2012), I detect significantly more Type I and II disks in Coma than are reported in the Virgo cluster ($45.8^{+10.1}_{-9.5}\%$ and $0^{+4}_{-0}\%$ respectively), but fewer Type III disks than Virgo ($54.2^{+9.7}_{-10.1}\%$). By comparison, the field *S0* sample in Erwin et al. (2012) yields significantly fewer Type I disks ($26.0^{+6.6}_{-5.7}\%$), but greater Type II ($28.0^{+6.7}_{-5.7}\%$) and III ($46.0^{+7.0}_{-6.9}\%$) fractions than the Coma sample.

If considered separately, Type I disks are found more frequently in unbarred (BD, CD, BDd, CDd; $88.1^{+2.7}_{-3.4}\%$) galaxies than those containing bars (BSD, BSDd; $58.1^{+5.0}_{-5.1}\%$). Consequently, barred galaxies have a greater fraction of Type II and III disks ($22.6^{+4.6}_{-4.0}\%$ and

$19.4^{+4.4}_{-3.7}\%$) than galaxies without bars ($3.7^{+2.2}_{-1.4}\%$ and $8.3^{+3.0}_{-2.3}\%$). Erwin et al. also reported a decrease in the Type I fraction for barred Virgo galaxies ($23.3^{+8.5}_{-6.8}\%$), however the increased barred Type II fraction in this work only widens the disparity between Coma and Virgo Type II disk detection.

To test the variation of disk type with environment, the filtered Coma sample was subdivided into core, intermediate, and outskirts samples based on galaxy distance from the cluster centre ($r_{\rm cluster} < 800$ kpc, $0.8 < r_{\rm cluster} < 1.6$ Mpc, and $r_{\rm cluster} > 1.6$ Mpc respectively; Figure 7.15, right panel). These clustercentric radial ranges are selected such that each sample has approximately equal occupancy ($N = 70$, 68, and 64). In all three samples, Type I disks form the vast majority, with a slightly increased Type I disk fraction for outskirt galaxies ($72.9^{+4.9}_{-5.6}\%$, $72.1^{+5.1}_{-5.7}\%$, and $78.1^{+4.7}_{-5.6}\%$ for core, intermediate, and outskirt galaxies). Type II and III disk fractions are consistent across all radial samples (Type II: $10.0^{+4.1}_{-3.0}\%$, $16.2^{+4.9}_{-4.0}\%$, $10.9^{+4.5}_{-3.3}\%$; Type III: $17.1^{+4.9}_{-4.0}\%$, $11.8^{+4.4}_{-3.3}\%$, $10.9^{+4.5}_{-3.3}\%$) although slight peaks in Type II and Type III disk fractions are apparent in the intermediate and core samples (respectively).

In summary, thorough 2D decomposition analysis reveals a rich range of galaxy structures in the Coma cluster, with 3(+) structural components required in a significant proportion of cases. Archetypal central bulge + outer disk structures were detected most frequently ($N = 202$), with 52 galaxies possessing broken outer disk profiles. This broken disk fraction would be overestimated, however, if double/triple Sérsic models were excluded, or if 1D analysis was applied alone. Greater fractions of Freeman Type I (untruncated) and Type II (truncated) disks were detected in the present work than have been reported previously in Virgo, with fewer Type III (anti-truncated) disks. These Type II and III disks were detected significantly more frequently in barred galaxies than those without bars, but no significant variation in Type I/II/III fraction was detected with local environment within Coma.

7.4 Conclusions and Chapter Summary

In this chapter, I have extended the decomposition analysis for the Coma galaxy sample to include a wider range of candidate model structures. An analysis pipeline was developed (based on the previously-described `AGONII`) to perform thorough (if not exhaustive) fitting of

2- and 3-component models based on combinations of Sérsic, boxy Sérsic, and exponential structural components. In addition, a broken exponential profile was developed for this work for the detection and parameterisation of (Freeman) Type II and III disk galaxies. This model component comprised an exponential disk with a smooth transition between inner and outer scale lengths at a break radius.

Sample filtering was applied to remove unreliable fits, and select the most statistically meaningful model (from Bayesian analysis) of the underlying galaxy structures (i.e. to ensure galaxies are neither under- or overfit). After filtering, a total of 478 galaxies remain for analysis from the initial sample.

The main findings of this chapter are as follows:

i) **The variety, and complexity of galaxy structure in the Coma cluster is far greater than has previously been reported from bulge-disk decomposition studies from shallow imaging data.**

Only $48 \pm 3\%$ of galaxies are best-represented by simple Sérsic, or Sérsic + exponential models, and a 3(+) component structure is necessary to fully describe $42 \pm 3\%$ of galaxies. The remaining 10% are 2-component systems requiring more complex outer profiles (e.g. Sérsic, or broken disk).

ii) **Galaxies with archetypal *S0* structures (central bulge + outer disk; N =202) are most frequently untruncated exponential disks ($74 \pm 3\%$). Similar numbers of 'truncated' ($12^{+3}_{-2}\%$) and 'anti-truncated' ($13^{+3}_{-2}\%$) disks are detected.**

Compared to the (cluster galaxy) results of Erwin et al. (2012), a significantly higher truncated disk fraction, and lower anti-truncated disk fraction are measured in the present work for the Coma cluster.

iii) **Detection of genuine broken disk galaxies is significantly limited if too narrow a range of models are considered.**

False positive broken disk detection (i.e. the fraction of reported 'broken disk' galaxies revealed to have more complex, *unbroken* structures via a more mature analysis) can exceed 50% if 3-component and/or multi-Sérsic models are not considered for decomposition analysis.

iv) **The fraction of barred galaxies detected in the present work ($20 \pm 2\%$) is significantly lower than previously reported for the Coma cluster.**

However, if triple Sérsic galaxies are considered 'barred', and analysis is limited to galaxies with morphological classifications from Dressler (1980b), then this value rises to $71 \pm 5\%$, consistent with previous measurements.

In the next chapter, the structural characteristics of these multi-component galaxies will be described in detail. In particular, the properties of galaxies with Type II and Type III (broken) disks will be investigated, constraining their formation mechanisms (and hence the evolutionary pathways for galaxies observed in the Coma cluster).

Chapter 8

The Structural Properties of Multi-component Galaxies

8.1 Introduction

Evolutionary pathways will not necessarily preserve archetypal bulge + disk galaxy morphologies. Depending on the specific nature of the mechanism involved, disks may cease to be simple exponential structures (e.g. disk truncation) or may be entirely disrupted, shifting the global morphology towards that of classic (i.e. pure spheroid) ellipticals. Thus, investigation of galaxies with a wider range of structural morphologies provides a more complete picture of the ETG formation mechanisms relevant to the Coma cluster.

Following the decomposition procedure presented in Chapter 7, I explore here the (i band) structural characteristics of Coma cluster red sequence galaxies with a range of multi-component structures (in the magnitude range $-17 > M_g > -22$). Particular emphasis is placed on disk galaxies with outer structures which deviate from the simple exponential disk profile (truncated or anti-truncated; i.e. Freeman Types II and III), with an aim to constrain the evolutionary histories of such galaxies. Note that discussion of 'disk galaxies' here refers specifically to systems where an exponential (or broken exponential) component dominates the surface brightness profile at large radii *only*. This ensures that the resulting properties measured from these 'disk components' are meaningful measurements of astrophysical disk structures. A full catalogue of the best-fit multi-component model structural measurements discussed in this chapter is presented in Table A.6 of Appendix A.

Model	Parameter	Comp. 1	Comp. 2	Comp. 3
S	n	1.90 ± 0.05	-	-
$N = 134$	R_e [kpc]	1.99 ± 0.07	-	-
$m_i = 16.58 \pm 0.03$	C/T	1.0	-	-
BS	n	2.12 ± 0.30	0.66 ± 0.10	-
$N = 34$	R_e [kpc]	5.27 ± 0.90	14.57 ± 0.90	-
$m_i = 15.76 \pm 0.12$	C/T	0.35 ± 0.04	0.65 ± 0.04	-
BSS	n	2.17 ± 0.23	0.43 ± 0.13	0.55 ± 0.04
$N = 70$	R_e [kpc]	4.20 ± 0.55	12.68 ± 0.76	25.80 ± 1.75
$m_i = 14.45 \pm 0.08$	C/T	0.42 ± 0.02	0.26 ± 0.02	0.27 ± 0.02

Table 8.1: Table of the median structural parameter values for multi-Sérsic model galaxies (S, BS, BSS), indicating the half-light radii, Sérsic indices, and component fraction (C/T) of each model component. In addition, the median total apparent magnitude (m_i), and number of galaxies (N) are given for each model type.

This investigation will address four main questions regarding galaxy evolution: Does the multi-component structure of giant ellipticals suggest the 'puffing-up' of a compact progenitor, or the accumulation of additional structures around a compact spheroid? Are broken disks structures (truncated or anti-truncated) correlated with the properties of the bulge/bar components? Do the structures of Freeman Type II galaxies indicate physical truncation of disks? Does such a truncation scenario explain the apparent size offset of *S0* disks relative to star-forming spirals reported in Chapter 5?

The structure of this chapter is as follows: First, I describe the overall structural properties of multi-component galaxies for which a Sérsic component ($n \neq 1$) is a better description of their outer profiles than an exponential disk (i.e. S, BS, and BSS). Secondly, I investigate the influence of bar structures on galaxies with broken disk profiles. This explores whether barred and unbarred broken disk galaxies are equivalent structures, and thus can be compared as a singular class. Thirdly, I contrast the bulge, disk, and break properties (where applicable) of outer-disk galaxies with Freeman Type I, II, and III profiles. The resulting structural trends are then discussed in the context of the evolutionary histories, and formation mechanisms of each disk type. Finally, I summarise the key results of this analysis.

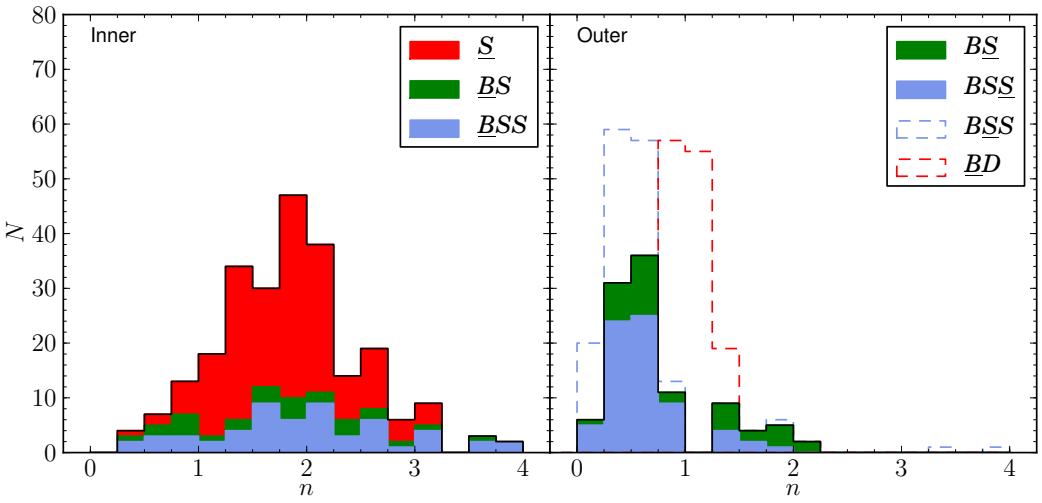

Figure 8.1: Histograms of Sérsic index, n, for multi-component Sérsic galaxies. **Left:** the n distribution for inner-dominant Sérsic structures (**S**, **B**S, **B**SS), divided by best-fit model type. **Right:** the n distribution of outer-dominant Sérsic structures (**B**S, BSS) divided by best-fit model type. The equivalent distributions including middle Sérsic structures (BSS) or outer Sérsic n for BS fits to galaxies best-fit by a BD model are included as dashed blue and red histograms respectively.

8.2 Multi-Sérsic Systems

From the initial sample of 478 galaxies (filtered to exclude badly-fit galaxies; see Section 7.2.3), $\sim$50% were best-fit by a model comprising one or more Sérsic components (28% S; 7% BS; 15% BSS). In this section, I briefly discuss the structural results for these multi-component Sérsic galaxies (Table 8.1). Note that average galaxy luminosity increases with number of model components, highlighting the strong S/N and spatial size dependence of multi-component structure detection.

In all Sérsic model variants, the central structure is compact and has a 'pseudobulge-like' ($n \sim 2$) profile (Figure 8.1, left panel). For S model galaxies, the Sérsic structure is equivalent to a 'naked' bulge for BD galaxies, albeit a factor of 2$\times$ larger ($R_e \sim 2$ kpc). The central 'bulges' of both BS and BSS galaxies are consistent in size, but larger on average than a single Sérsic ($R_e \sim 4$ kpc). Note that very few inner structures refer to a classic $n = 4$ (de Vaucouleur's) profile. If BSS (or other 3-component) galaxies were force fit by a single Sérsic structure, however, the resulting n distribution would extend to $n \sim 8$, peaking strongly for $n =$ 3-4. Hence, de Vaucouleur's profile arises from underfitting more structurally complex systems.

Outer Sérsic structures have Gaussian-like profiles ($n \sim 0.5$) on average, although a weak

tail exists in the n distribution towards higher values (Figure 8.1, right panel). Since an outer component with $n = 1$ would be described by a BD model, the $1.00 < n < 1.25$ bin is empty for outer structures. If the disk n is allowed to vary for these bulge + disk galaxies (i.e. fitting a BS model), then a continuous distribution of outer structure Sérsic index becomes apparent (red dashed histogram in Figure 8.1). The resulting 'disk' n distribution covers the range $0.5 < n < 1.5$, but peaks strongly at $n = 1$ (median value: 1.00, standard deviation: 0.24)[1]. Hence, the outer structures considered in this section may represent (non-exponential) disks. However, this hypothesis cannot be confirmed without information regarding the kinematics of these multi-component Sérsic galaxies. As a practical choice, only $n = 1$ disks will be considered in discussion of disk structure in later sections due to the uncertain nature of outer Sérsic structures.

The outer and middle Sérsic structures of BS and BSS galaxies are both $\gtrsim 10$ kpc larger than 'bulges', but represent drastically different fractions of their parent galaxy's total luminosity ($\sim \frac{2}{3}$ and $\sim \frac{1}{4}$ respectively). Conversely, the outer structure of BSS galaxies is comparable in luminosity to the middle Sérsic , but is an additional 10 kpc larger. As such, BSS galaxies are structurally equivalent to BS galaxies with the addition of an outer Sérsic structure. The outer Sérsic structures may be the remnants of past merger events. As such, the distinction between BS and BSS may be a difference in the number of major merger events experienced in the past.

By comparison, the triple Sérsic structures measured by Huang et al. (2013; H13) in a small sample of nearby ellipticals consist of a faint, compact central object ($R_e < 1$ kpc), a middle component ($R_e \sim 2.5$ kpc), and a dominant outer envelope ($R_e \sim 10$ kpc). If the compact structure is neglected, the H13 structures are comparable with the BS models in the present work, albeit with smaller bulges, different component profiles ($n \sim$1-2 in H13), and C/T for the outer structure (~ 0.6 in H13). Given that the galaxy sample in H13 comes from a less dense environment on average, the increased detection rate of weak outer Sérsic structures in the present work may reflect a more active merger history of present-day Coma cluster galaxies. This is supported by the higher average bulge size in the present work, as mergers will also increase bulge R_e.

[1]Recall however, that these changes in outer profile n do not yield statistically significant improvements to the goodness-of-fit relative to fixing $n = 1$.

If the models considered in this section represent the multi-component structures of traditional elliptical galaxies, then such galaxies comprise a (relatively) compact pseudobulge ($\sim$ 5 kpc) around which large ($\sim$ 10-20 kpc) outer (Gaussian) structures have been assembled. These compact central structures are 2-3$\times$ larger than 'red nugget' objects ($\sim$ 1-2 kpc) detected at high redshift ($z \sim 2$; Damjanov et al., 2009). Thus, if the multi-component Sérsic galaxies observed in Coma in the present work evolved from red nuggets, then their bulge structures must have experienced significant size growth ('puffing up'). However, the *total* effective radii for BS and BSS galaxies (estimated from the combined luminosities of all model components, assuming alignment of component PAs) is $\sim$ 10-11 kpc on average[2], suggesting an even more drastic growth mechanism ($\sim 6\times$, consistent with van Dokkum et al., 2014).

8.3 Barred/Unbarred Broken Disk Systems

In this section, I contrast the properties of galaxies with 'bar' components (specifically, *any* inner Sérsic component in addition to the bulge; hereafter 'barred') with the equivalent galaxies lacking these structures (hereafter 'unbarred'). This analysis will determine whether barred and unbarred galaxies are the same class of object, or whether the observed bar component implies an intrinsically distinct galaxy structure and evolutionary history. As such, I aim to determine whether galaxy disks can be categorised solely by Freeman type (unbroken, truncated, anti-truncated), or whether the presence/absence of a bar must also be accounted for.

Here, the distributions and trends in structural parameters for galaxies with (single) disk-dominated outer regions (BD, CD, BDd, BSD, BSDd; see Figures 7.6, 7.8, 7.10, 7.12) are investigated. In order to ensure that model parameters are measured from consistent structures (i.e. exponential/broken exponential components measure galaxy disk properties), I only consider galaxies with archetypal bulge/disk models (i.e. Type 1 for 2-component galaxies, Type $x1x$ for 3-component galaxies), or those which become/cease to be archetypal due to disk breaks (Types 1_{-}, 3_{+}, $x1_{-}x$, $x3_{+}x$). This reduces the sample of analysed galaxies to

[2]Even if the outermost structures in BSS galaxies were dismissed as fitting artefacts, the total R_e of such systems would remain in excess of 7 kpc.

146 (67 2-component galaxies, 79 3-component galaxies), of which 97 galaxies have Type I disks, 25 have Type II disks, and 24 have Type III disks. As a convenient shorthand, I hereafter use the phrase 'Type I/II/III galaxy' to refer to galaxies containing Freeman Type I/II/III disks.

The sizes and Sérsic indices of bulges and bars (where present) of galaxies with broken disks (models BDd and BSDd) are presented in Figure 8.2. On average, unbarred galaxies are fainter (median $M_i = -19.8 \pm 0.2$) than galaxies with bars (median $M_i = -20.6 \pm 0.1$), and have smaller bulge sizes ($R_e = 0.81 \pm 0.06$ kpc for barred, $R_e = 0.63 \pm 0.05$ kpc for unbarred) at a $\sim 2.5\sigma$ level. However, the bulge Sérsic indices are consistent for both barred ($n = 2.06 \pm 0.15$) and unbarred ($n = 2.04 \pm 0.27$) galaxies.

With increasing galaxy luminosity, all galaxy bulges increase weakly in size (~ -0.2 kpc per magnitude). For unbarred galaxies, bulge Sérsic index sharply increases with total luminosity (-1.91 ± 0.76 per mag), but no trend is detected for barred galaxies (0.01 ± 0.25 per mag). This apparent disparity in bulge profile shape should be treated with skepticism, given the small samples sizes involved. Indeed, if both barred and unbarred bulges are considered together, then neither trend (n or R_e) differs significantly from those measured from barred galaxies alone. Hence, the bulge components of barred and unbarred galaxies are the same class of structure, albeit with greater scatter in the properties of unbarred bulges.

In contrast with bulges, galaxy bars exhibit a narrow range of (low) n profiles ($n = 0.43 \pm 0.04$ on average), but are systematically larger structures ($R_e = 2.65 \pm 0.18$ kpc on average). Note that this is not an artefact of selecting archetypal galaxies in this section, as no constraints are placed on the bulge/bar or bar/disk profile types (i.e. bars are not required to dominate bulges at large radii). Low n profiles are expected for bar-like systems (Gadotti, 2011), yielding approximately constant brightness towards the galaxy centre, but fading rapidly at larger radii. Galaxy bars exhibit no significant trends in n (0.02 ± 0.36) or size (0.14 ± 0.59 kpc per mag) with luminosity.

The sizes of inner and outer disks (the structures inside and beyond $r_{\rm brk}$) for barred and unbarred galaxies are presented in Figure 8.3. With the exception of the inner disks of barred galaxies, all inner and outer disks exhibit similar R_e-M_i trends (slope ~ -1.5 kpc per mag), consistent with the strong size-luminosity trend detected for disks in Chapter 5.

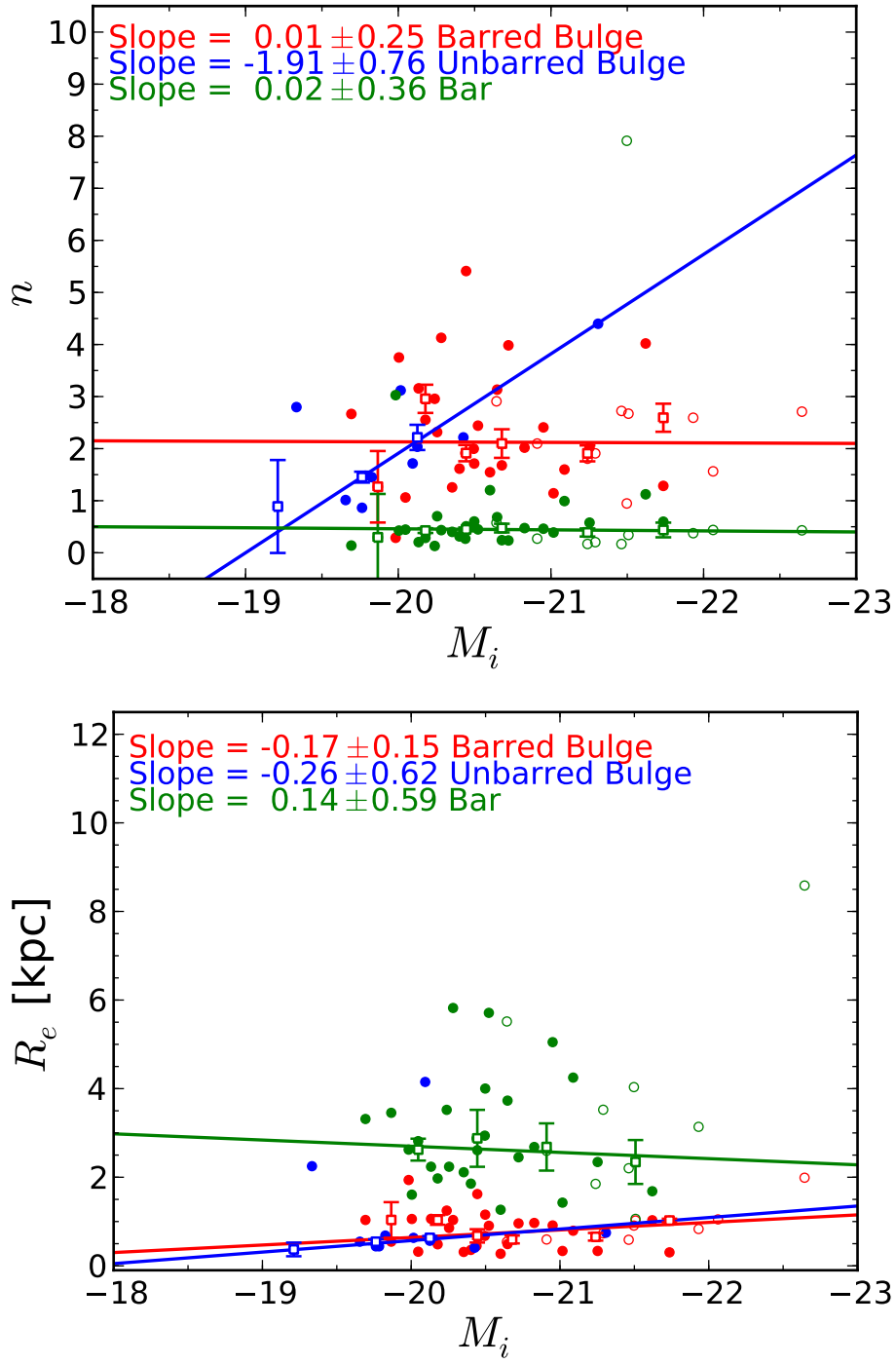

Figure 8.2: Sérsic component structural parameters for BDd, CDd, and BSDd models as a function of total absolute i band model magnitude. **Upper plot:** Sérsic index for barred and unbarred bulges (red and blue), and bars (green). **Lower plot:** Effective half-light radii for barred and unbarred bulges (red and blue), and bars (green). Unfilled data points indicated flagged galaxies. Large square points are median parameter values in bins of M_i, to which a linear trend has been fit.

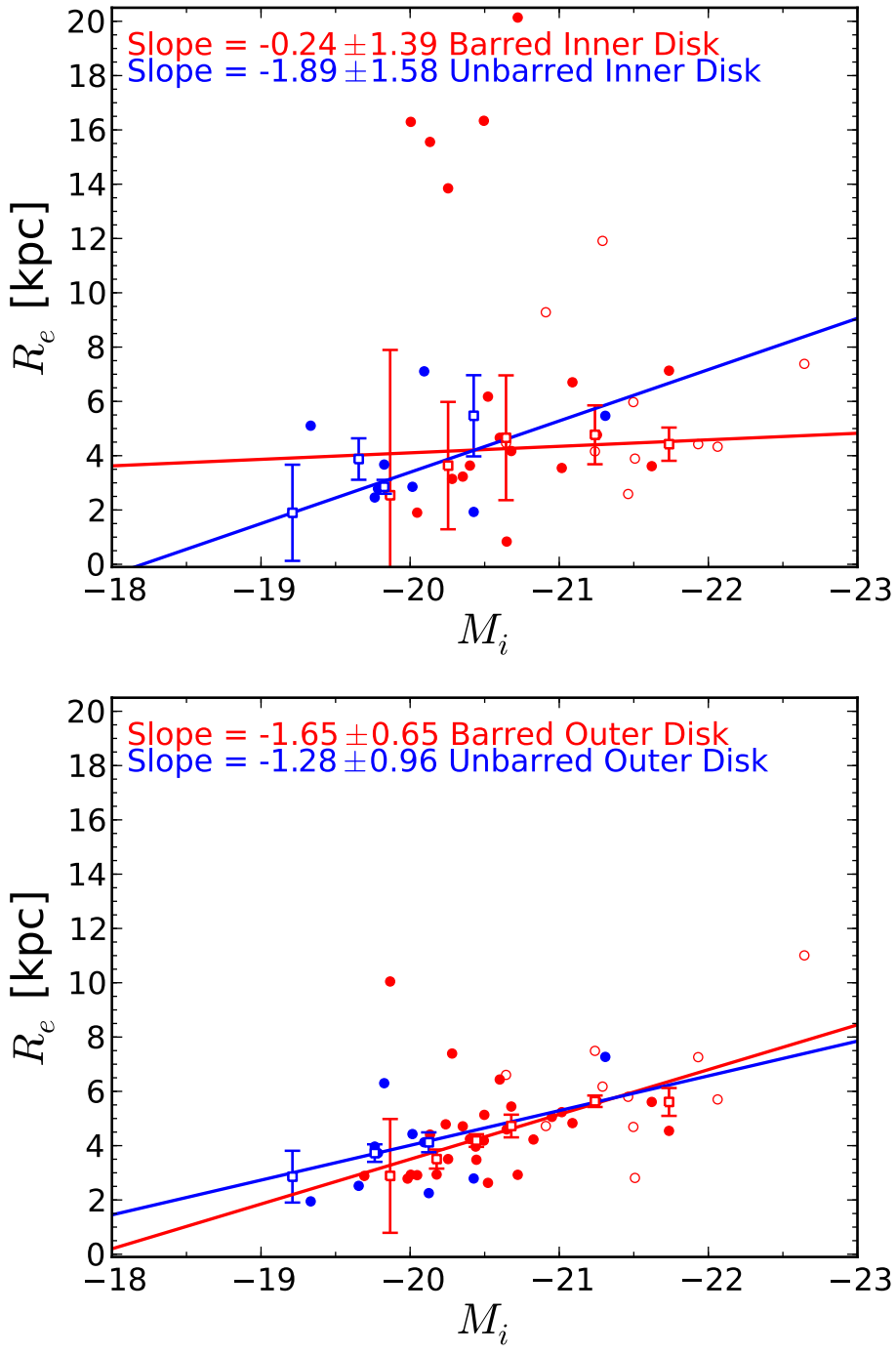

Figure 8.3: Disk structural parameters for BDd, CDd, and BSDd models as a function of total absolute i band model magnitude. **Upper plot:** Inner disk effective half-light radii for barred and unbarred bulges (red and blue). **Lower plot:** Outer disk effective half-light radii for barred and unbarred bulges (red and blue). Unfilled data points indicated flagged galaxies. Large square points are median parameter values in bins of M_i, to which a linear trend has been fit.

However, these trends are non-significant due to high scatter in size measurement. Unbarred (inner/outer) disks are visually consistent (i.e. lie on the same best-fit trend) with barred galaxies, with similar levels of scatter. As such, the (broken) disk components of barred and unbarred galaxies form a single family of consistent galaxy sub-structures.

On average, inner disks are smaller (barred: $R_e = 4.66 \pm 0.99$ kpc, unbarred: $R_e = 3.26 \pm 0.56$ kpc) than outer disks (barred: $R_e = 4.72 \pm 0.28$ kpc, unbarred: $R_e = 3.97 \pm 0.29$ kpc), reflecting the greater proportion of Type III disks in the sample. Since Type II and III disks are considered together in this comparison, however, this difference is not significant. Disks in barred galaxies are systematically larger than unbarred disks, but since barred galaxies are also systematically *brighter*, this size offset reflects the overall size-luminosity trend for disks. Hence, for a fixed galaxy luminosity, the sizes of barred and unbarred galaxies are consistent (as in Courteau et al., 2003).

In summary, the bulges of broken disk models have an order of magnitude weaker size-luminosity trend than their disks. This is consistent with the strong and negligible luminosity-dependence for disk and bulge sizes (respectively) for the BD analysis in Chapter 5. No significant differences are detected between the broken disks of galaxies with or without bars. As such, barred and unbarred broken disks are concluded to form the bright and faint end (respectively) of a continuous sequence of consistent structures. Similarly, the bulges of barred and unbarred galaxies are structurally consistent. I conclude that barred and unbarred (archetypal; inner bulge, outer disk) disk galaxies belong to the same family of structurally consistent objects, differing only in the presence/absence of a bar component.

8.4 Freeman Type I, II, and III disks

In this Section, the galaxy sample is divided by Freeman type to investigate differences in structure for galaxies with untruncated (Type I), truncated (Type II), or anti-truncated (Type III) disks. I consider all models with a single (exponential) disk component which dominates (relative to the bulge) at large galaxy-centric radii (BD, CD, BDd, BSD, BSDd). As in the previous section, only galaxies with archetypal disks (and those which cease to be archetypal due to a broken disk; Allen Types 1, 1_{-}, 3_{+}, $x1x$, $x1_{-}x$, and $x3_{+}x$) are considered for this analysis.

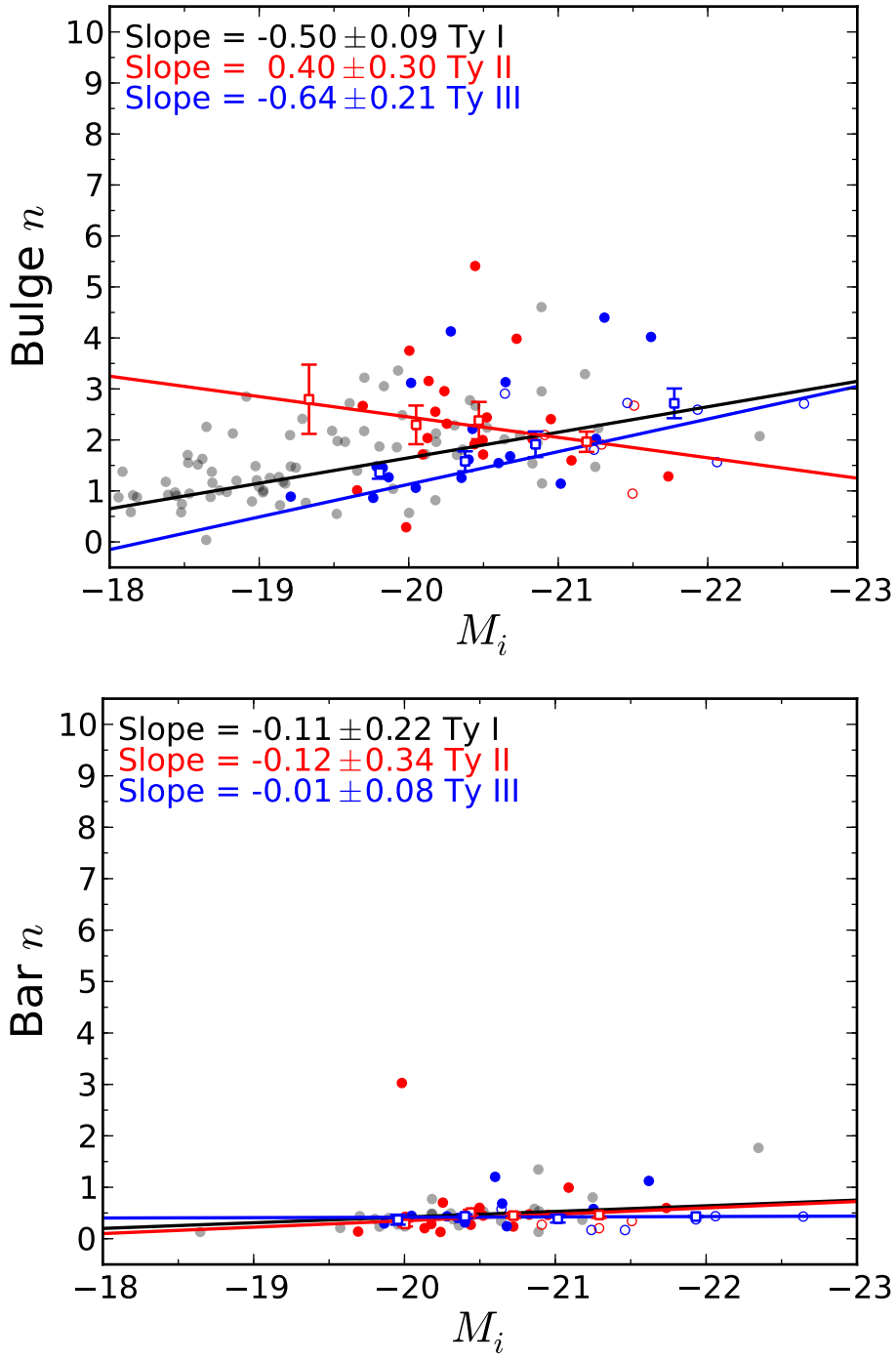

Figure 8.4: Bulge and bar Sérsic indices (n) for BD, CD, BDd, CDd, BSD, and BSDd model galaxies with Type I (black), II (red), and III (blue) disks as a function of total absolute i band model magnitude. **Upper plot:** Bulge Sérsic index. **Lower plot:** Bar Sérsic index. Unfilled data points indicate flagged galaxies. Large square points are median parameter values in bins of M_i, to which a linear trend has been fit. Type I galaxies are indicated by faint grey points.

8.4.1 Central component properties

The bulge and bar Sérsic indices for galaxies of each disk type are presented in Figure 8.4. Bulge n is smaller (on average) in Type I (1.89 ± 0.08) galaxies those with Type II (2.32 ± 0.14) broken disks, and consistent with the bulges of Type III galaxies (1.74 ± 0.19). By comparison, *bar* Sérsic index is consistent across all Freeman types (0.44 ± 0.04 for Type I, 0.44 ± 0.04 for Type II, and 0.43 ± 0.03 for Type III). Thus, while consistent bar profiles are measured independent of disk type, the bulge profile shape depends on disk structure. Note that the Type I averages are calculated from galaxies in the magnitude range $-19 < M_i < -22$ for consistency with the range of Type II and III galaxy luminosities

With increasing galaxy luminosity, no significant variation in bar n is detected for any galaxy type. However, the bulges of both Type I and Type III galaxies become more centrally-concentrated (higher n) for more luminous galaxies. Similar n-M_i slopes are measured for both galaxy types (consistent with the equivalent trend measured previously for archetypal BD models in Chapter 5). The reverse trend (lower n for higher galaxy luminosity) is measured for Type II galaxies. While this trend is not significant ($\sim 1.5\sigma$), it remains discrepant with the measured Type I/III trends at a 3σ level. Thus, the bulges of galaxies with truncated disks are structurally distinct from those found in galaxies with untruncated, or anti-truncated disks. This is analogous to the distinct n-luminosity trends measured in the previous section for barred and unbarred galaxies. However, as barred galaxies comprise approximately equal numbers of Type II ($23^{+5}_{-4}\%$) and III disks ($19 \pm 4\%$), this apparent bulge n bimodality is not strongly related to the presence of a bar component.

Half light radii for the bulges and bars of Type I, II, and III galaxies are presented in Figure 8.5. The bulges of Type I and III galaxies show no significant size difference on average (Type I: 0.57 ± 0.05 kpc, Type III: 0.54 ± 0.05 kpc), while Type II galaxies have systematically larger bulges (0.96 ± 0.07 kpc). No notable trends in bulge size with galaxy luminosity is noted for galaxies of any Freeman type.

The bars in Type II galaxies are systematically larger on average (2.91 ± 0.22 kpc) than those found in Type I galaxies (1.95 ± 0.18 kpc), but similar to the bars of Type III galaxies (2.82 ± 0.49 kpc). As with bulge components, no significant size-luminosity trends are noted for galaxy bars. Thus, large galaxy bars are found more frequently in galaxies with broken

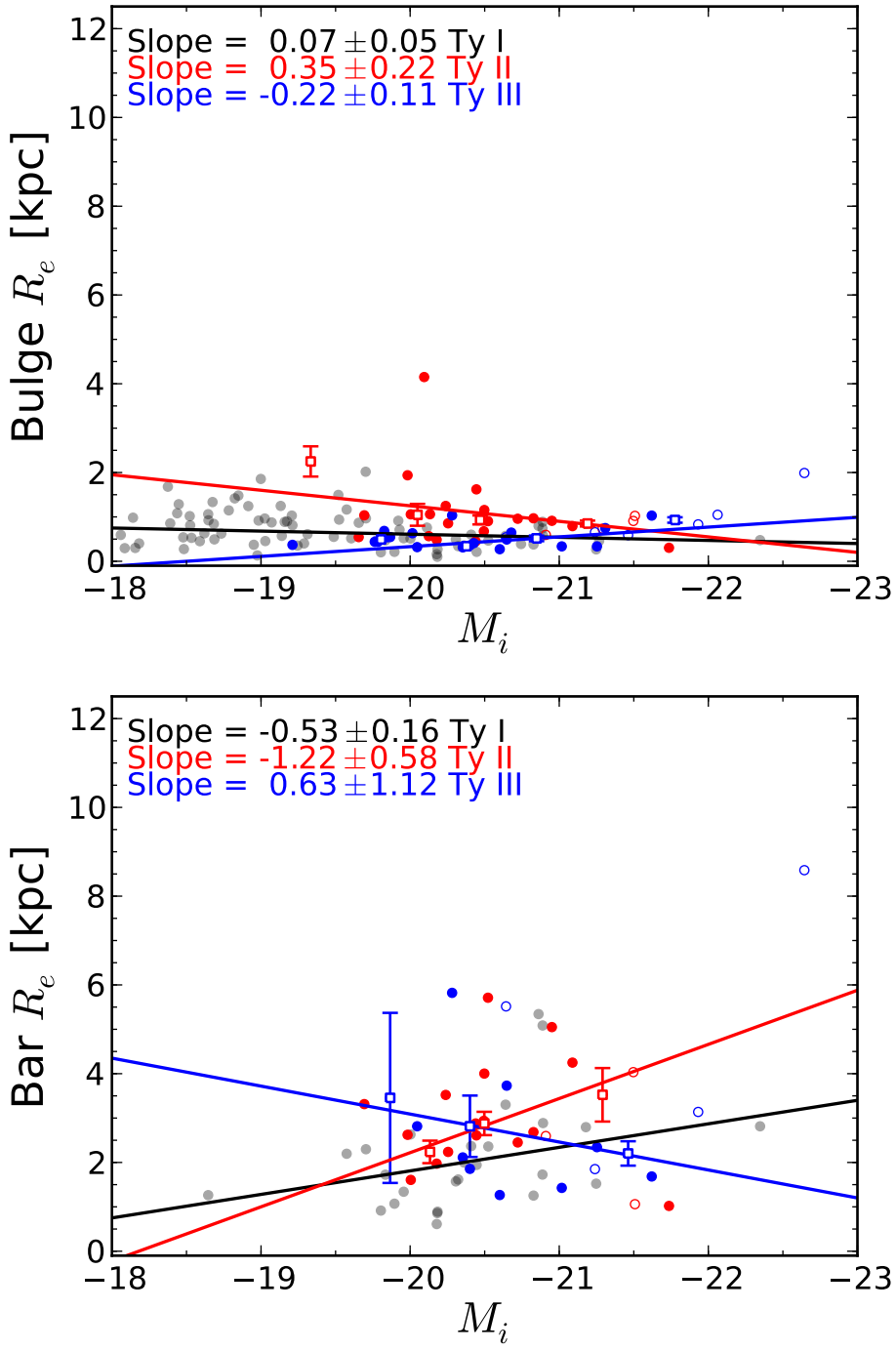

Figure 8.5: Bulge and bar effective half-light radii (R_e) for BD, CD, BDd, CDd, BSD, and BSDd model galaxies with Type I (black), II (red), and III (blue) disks as a function of total absolute i band model magnitude. **Upper plot:** Bulge R_e. **Lower plot:** Bar R_e. Unfilled data points indicate flagged galaxies. Large square points are median parameter values in bins of M_i, to which a linear trend has been fit. Type I galaxies are indicated by small grey points for clarity.

(truncated/anti-truncated) disks, regardless of total galaxy luminosity.

In summary, the bulges of galaxies with Type II disks have systematically larger n and R_e than the bulges of Type I or III galaxies. In addition, no significant bulge n-luminosity trend is detected for Type II galaxies. Thus, the bulges of galaxies with truncated disks are distinct in structure and origin from the equivalent components in galaxies with either untruncated or anti-truncated disks. Galaxy bars are consistent in profile shape across all Freeman types, but have systematically larger R_e in galaxies with Type II or III broken disks.

8.4.2 Disk Properties

The effective half-light radii for the inner and outer disks (i.e. the disks internal and external to the break radius, $r_{\rm brk}$) of Type II (truncated) and III (anti-truncated) galaxies are presented in Figure 8.6, with the disk R_e for Type I galaxies included in both panels. Note that by definition, the inner R_e of Type II/III galaxies is larger/smaller than the outer R_e, yielding a shallower disk surface brightness profile within/beyond $r_{\rm brk}$. On average, Type III inner disks are consistent in size (3.58 ± 0.20 kpc) with Type I disks (3.68 ± 0.18 kpc), and have a consistent size-luminosity relation (despite a $\sim 2\times$ difference in slope). By contrast, Type II inner disks are *substantially* larger (than Type I disks) on average (9.28 ± 1.44 kpc), with an extremely steep trend (4.76 ± 3.09 kpc per mag) of *decreasing* inner disk size with increasing galaxy luminosity, albeit at low significance ($\sim 1.5\sigma$).

The outer disks of Type II galaxies have scale lengths (4.12 ± 0.20 kpc) consistent with Type I disks (for galaxies in the range $-19 < M_i < -22$) on average, while Type III outer disks are systematically larger (5.62 ± 0.34 kpc). Outer disk size-luminosity relations are similar for both Type II and III disks, yielding size increases for more luminous galaxies a factor of approximately two times greater than the measured trend for Type I disks. However, this difference relative to Type I disks is only significant (at a $\sim 2.5\sigma$ level) for Type II galaxies. The detection of consistent scale lengths (and similar size-luminosity relations) for Type I disks, Type II outer disks, and Type III inner disks (in agreement with Laine et al., 2014) suggests that the outer/inner structures of Type II/III disks preserve the structural properties of their progenitor disks.

The break radius, $r_{\rm brk}$, is plotted in Figure 8.7 for Type II and III disks as a fraction of

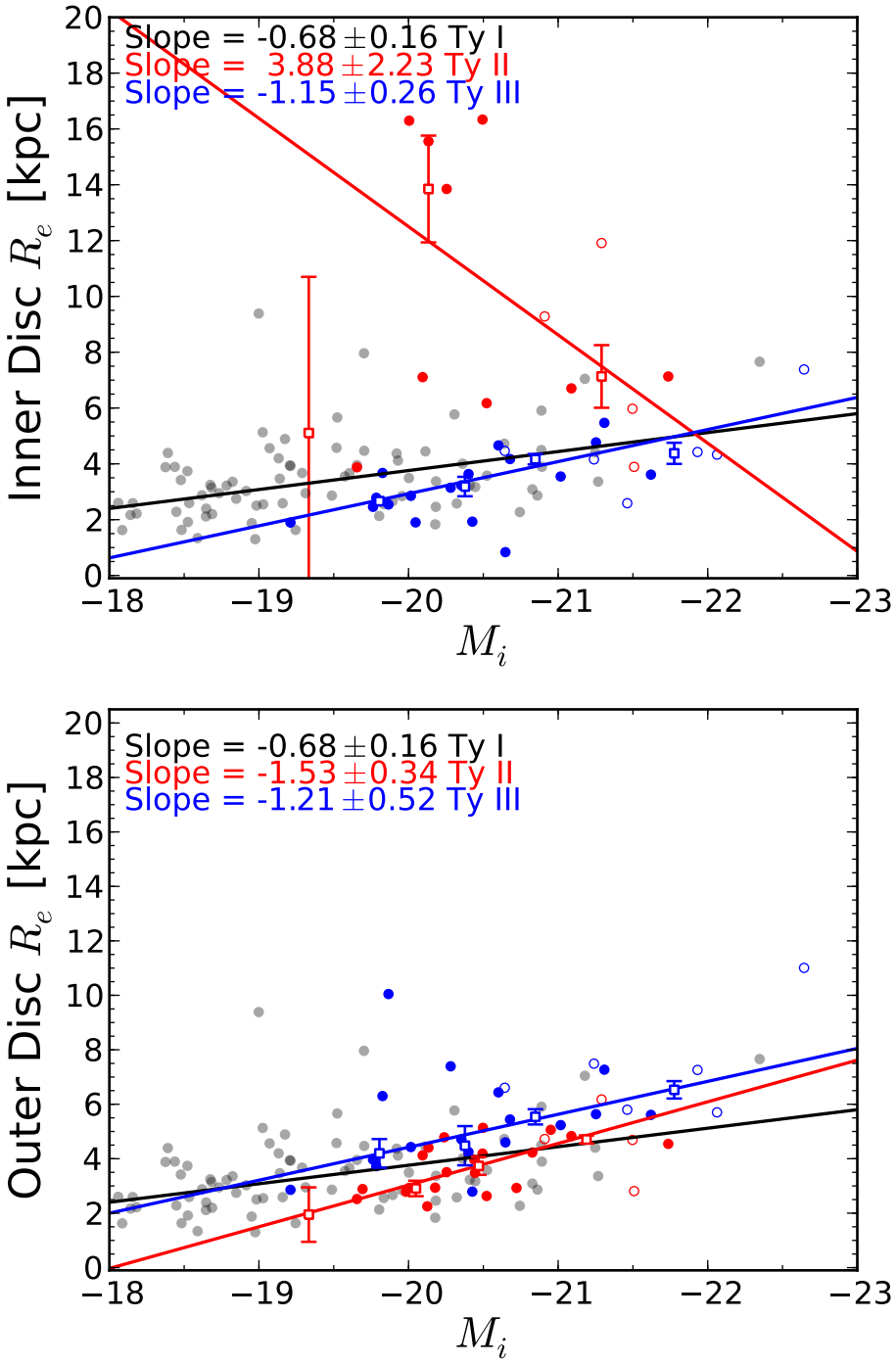

Figure 8.6: Inner and outer disk effective half-light radii (R_e) for BD, CD, BDd, CDd, BSD, and BSDd model galaxies with Type I (black), II (red), and III (blue) disks as a function of total absolute i band model magnitude. **Upper plot:** Inner disk R_e. **Lower plot:** Outer disk R_e. Unfilled data points indicate flagged galaxies. Large square points are median parameter values in bins of M_i, to which a linear trend has been fit. Type I galaxies are indicated by faint grey points.

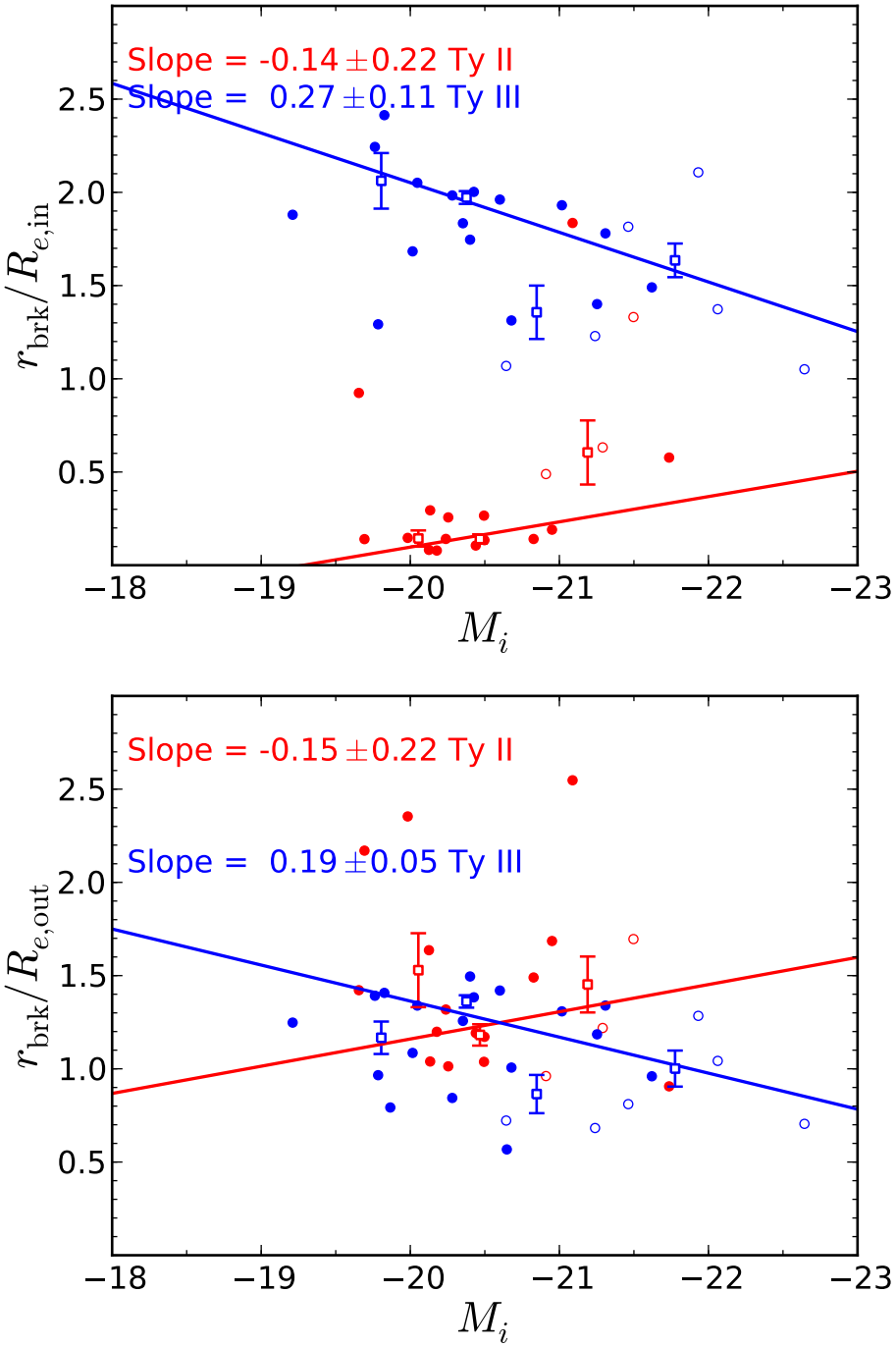

Figure 8.7: Break radius, $r_{\rm brk}$, as a function of the total absolute i band model magnitude for galaxies with Type II (red) and III (blue) disk models relative to the inner (**top**) and outer (**bottom**) disk R_e. Unfilled data points indicate flagged galaxies. Large square points are median parameter values in bins of M_i, to which a linear trend has been fit.

both inner and outer disk R_e. For Type II disks, the break radius is a small fraction of the inner disk size (~ 0.25). However, since R_e is large for these structures, the contribution of the (flat) inner disk to the total disk luminosity is non-negligible. By comparison, Type III disk break radii are significantly beyond the inner disk half-light radius ($r_{\rm brk} \sim 2R_e$), indicating that only the outer wings of Type III inner disk structures are modified by the profile break. Alternatively, both Type II and III profile breaks are comparable in size to the *outer* disk R_e. Thus, in both cases, the outer structure of broken disks contribute $\sim 50\%$ of the light of an equivalently-sized untruncated disk.

In comparison to either disk, Type III breaks occur at smaller fractions of disk R_e for increasingly luminous galaxies. Note, however, that this correlation is significant at a $> 3\sigma$ level for outer disk R_e, but only significant at a $\sim 2.5\sigma$ level for inner disk R_e. A decreased fractional break radius indicates that a Type III disk contains a smaller proportion of the primordial disk. Conversely, Type II break radii exhibit a non-significant increase (as fractions of both R_e) with galaxy luminosity. Thus, the break radius of a Type II disk is approximately the same fraction of the inner/outer disk size for any galaxy. Note that if Type II disks where $R_{e,\rm in}$ reaches the `GALFIT` limit are excluded, the trend in $r_{\rm brk}$ relative to $R_{e,\rm out}$ is made considerably shallower. Hence, $r_{\rm brk}$ increases in size at a similar rate to outer disk R_e with total galaxy luminosity.

In summary, the inner disks of anti-truncated (Type III) galaxies are consistent in size with the disks of unbroken (Type I) galaxies. Conversely, Type III outer disks are systematically larger than unbroken disks. Both inner and outer Type III disks exhibit a size-luminosity relation consistent with Type I disks. Thus, the inner disks of Type III galaxies preserve the properties of the unbroken progenitor disk. The inner disks of truncated (Type II) galaxies are not consistent in size or size-luminosity trend with unbroken disks. This rules out a formation scenario in which physical truncation preserves the primordial disk within the break radius. Conversely, the outer disks of Type II galaxies have sizes (and size-luminosity relations) consistent with untruncated disk structures.

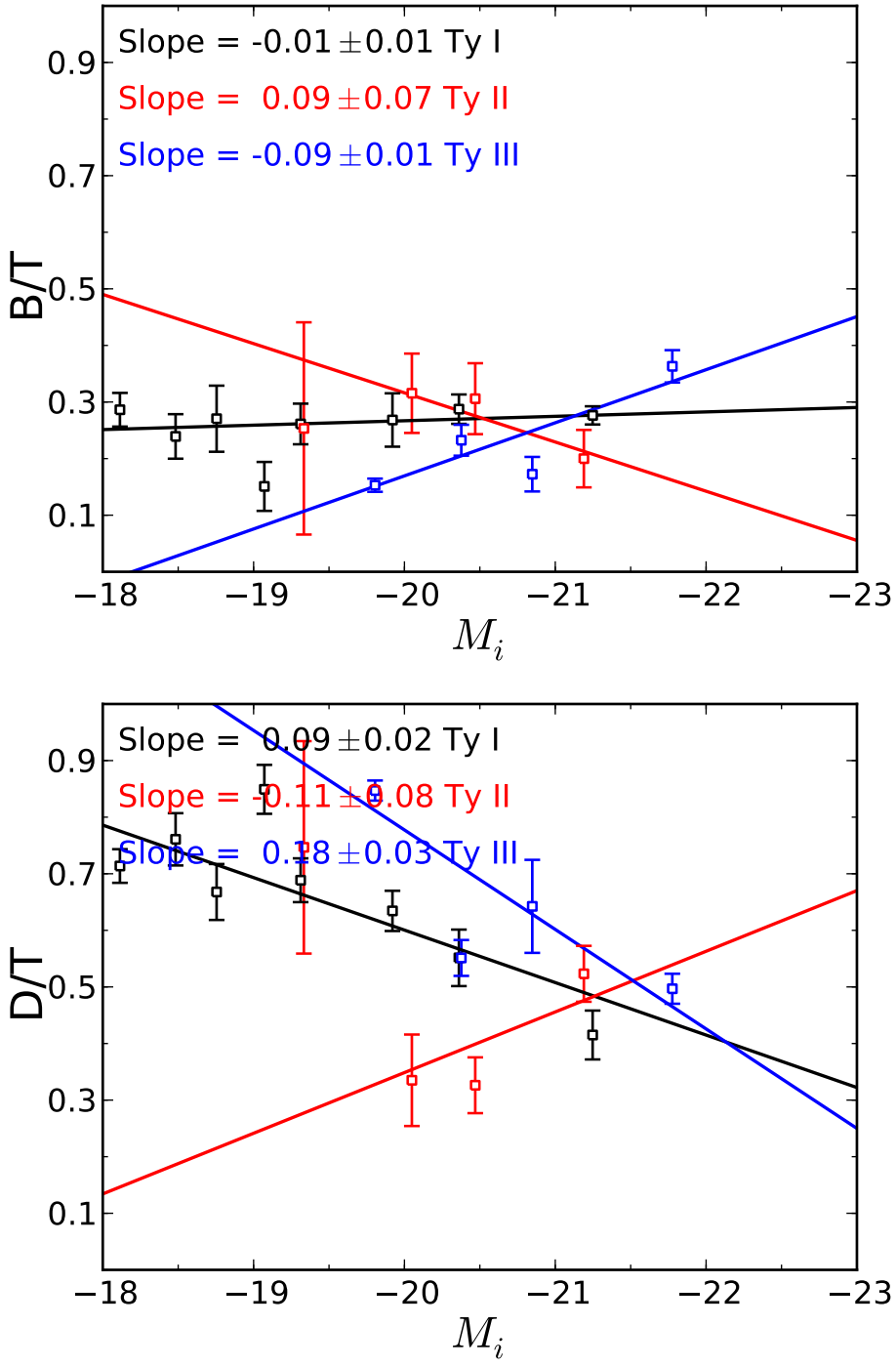

Figure 8.8: Component fraction (C/T) as a function of total absolute i band model magnitude for galaxies with Type I (black), Type II (red) and Type III (blue) disk models. **Upper plot:** bulge fraction (B/T). **Lower plot:** disk fraction (D/T). Note that due to the presence of bar components in some galaxies, B/T + D/T $\neq 1$. Square points are median parameter values in bins of M_i, to which linear trends have been fit.

		N	$\Delta_{\rm B/T}$	$\Delta_{\rm S/T}$	$\Delta_{\rm D/T}$
2-comp.	Type I	56	-0.01 ± 0.03	-	0.01 ± 0.03
	Type II	4	-0.10 ± 3.65	-	0.10 ± 3.65
	Type III	7	-0.12 ± 0.11	-	0.12 ± 0.11
3-comp.	Type I	41	-0.04 ± 0.03	-0.10 ± 0.03	0.12 ± 0.04
	Type II	21	0.11 ± 0.07	0.01 ± 0.05	-0.22 ± 0.06
	Type III	17	-0.14 ± 0.02	0.07 ± 0.03	0.05 ± 0.03

Table 8.2: Table of best-fit component light fraction-luminosity trends ($\Delta_{\rm C/T}$; C/T per magnitude galaxy luminosity) measured for 2-component (**top**) and 3-component (**bottom**) galaxies. Here, a negative value indicates increasing C/T with luminosity.

	N	x_B/x_T	x_S/x_T	x_D/x_T
Type I	41	1.16 ± 0.12	1.41 ± 0.13	0.76 ± 0.08
Type II	21	0.65 ± 0.23	0.96 ± 0.20	1.51 ± 0.15
Type III	17	1.56 ± 0.09	0.66 ± 0.16	0.91 ± 0.06

Table 8.3: Table of approximate fractional component luminosity changes for 3-component Type I, II, and III galaxies as total galaxy luminosity increases ($x_T = 2.5$).

8.4.3 Component fractions (C/T)

In this Section, I discuss the component flux fractions (B/T, S/T, and D/T for bulges, bars, and disks respectively) for galaxies with Type I, II, and III disks.

Measured across all (2- and 3-component) galaxies, Type I galaxies are strongly disk-dominated (median D/T $= 0.62 \pm 0.02$), with (sub-dominant) bulges (B/T $= 0.28 \pm 0.02$) and weak bar components (S/T $= 0.10 \pm 0.01$). The corresponding component fractions for Type III galaxies are measured to be consistent with Type I galaxies (D/T$= 0.62 \pm 0.03$, B/T $= 0.24 \pm 0.02$, S/T $= 0.14 \pm 0.03$). By contrast, Type II galaxies have a diminished disk light fraction on average (D/T$= 0.46 \pm 0.04$), with corresponding increases in bulge (B/T$= 0.33 \pm 0.04$) and bar (S/T$= 0.21 \pm 0.03$) fractions. Note, however, that these averages are heavily biased by the lack of a bar (i.e. S/T$= 0.00$) in 2-component galaxies. If the average is calculated from only 3-component galaxies, then bar light fraction (S/T) increases significantly for all three disk types (Type I: 0.24 ± 0.02; Type II: 0.25 ± 0.02; Type III: 0.20 ± 0.03). The corresponding disk light fractions (D/T) decrease on average for 3-component galaxies (Type I: 0.51 ± 0.03; Type II: 0.43 ± 0.04; Type III: 0.55 ± 0.03), while average bulge fractions (B/T) are not significantly changed (Type I: 0.25 ± 0.02; Type II: 0.31 ± 0.04; Type III: 0.20 ± 0.03).

Bulge and disk fractions (for the combined 2- and 3-component galaxy sample) are plotted as a function of total galaxy luminosity in Figure 8.8 for Type I, II, and III galaxies. For increasingly luminous Type II/Type III galaxies, bulge light fraction decreases/increases, while disk light fraction increases/decreases. These trends are significant for Type III galaxies, but only marginal for Type II galaxies. Unbroken disk galaxies (Type I) exhibit no luminosity dependence of B/T, but are significantly less disk-dominated (lower D/T) for more luminous galaxies. This is caused by the increased frequency of barred galaxies at higher galaxy luminosities.

The corresponding best-fit component light fraction trends with galaxy luminosity (2-component and 3-component galaxies considered separately) are presented in Table 8.2. For 2-component galaxies, no significant trends are noted in Type I galaxy B/T or D/T, while no conclusions can be drawn for Type II and III galaxies due to small sample sizes. However, with increasing luminosity, 3-component Type I galaxies become significantly more bar-dominated (-0.10 ± 0.03), and less disk-dominated (0.12 ± 0.04). Conversely, 3-component Type II galaxy disk light fraction and Type III galaxy bulge light fraction increases with galaxy luminosity (-0.22 ± 0.06 and -0.14 ± 0.02 respectively).

These component light fraction-luminosity trends can be used to estimate whether the distinction between faint and bright galaxies is dominated by the luminosity difference of one particular component. This can characterise, for example, whether the difference between an average galaxy and an equivalent galaxy one magnitude brighter is primarily due to an increase in bulge or disk luminosity. Hence, we will determine whether the apparent differences in C/T trends between Freeman Types corresponds to intrinsically different component light scaling relations.

For two galaxies separated in total galaxy luminosity by one magnitude ($M_0 - M = 1.0$), the fractional difference in the luminosity of a particular component ('C') can be parametrised as $x_C = L_C/L_{C,0}$. For example, if the galaxy luminosity difference in Type I galaxies at $M_{i,0} = -20$ and $M_i = -21$ was caused by the bulge and disk components being $3\times$ brighter at $M_i = -21$ (but bars being as luminous in both cases), then $x_B = 3$, $x_S = 1$, and $x_D = 3$.

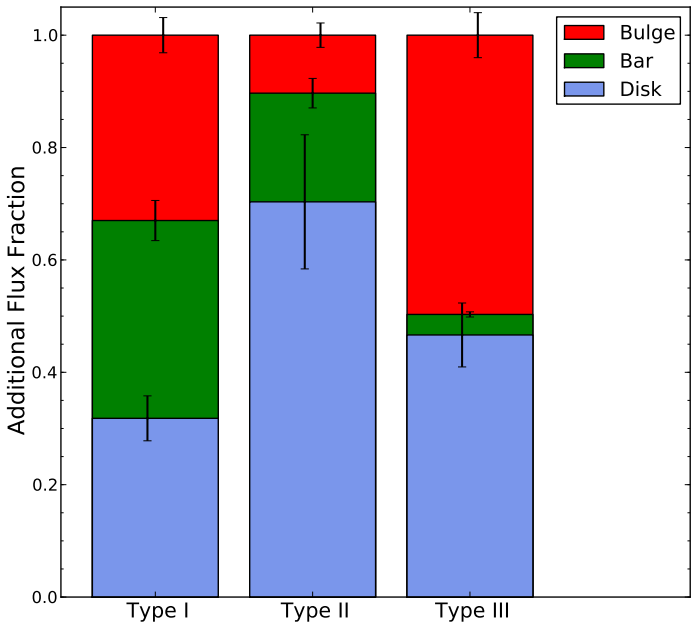

Figure 8.9: 'Additional' component light fractions (i.e. the proportions of the luminosity difference for each component structure per unit galaxy luminosity) for average galaxies with Freeman Type I, II and III disk components. Indicates the fraction of light added to the bulge (red), disk (blue) or bar (green) per unit galaxy luminosity increase. Type I galaxies - bulge: $33 \pm 3\%$, disk: $35 \pm 3\%$, bar: $32 \pm 4\%$; Type II galaxies - bulge: $10 \pm 2\%$, bar: $19 \pm 2\%$, disk: $70 \pm 12\%$; Type III galaxies - bulge: $50 \pm 4\%$, bar: $4 \pm 1\%$, disk: $47 \pm 6\%$.

The reported C/T slopes ($\Delta_{\mathrm{C/T}}$; Table 8.2) can be expressed as:

$$\Delta_{\mathrm{C/T}} = \mathrm{C}_0/\mathrm{T}_0 - \mathrm{C/T} = \mathrm{C}_0/\mathrm{T}_0 \left(1 - \frac{x_C}{x_T}\right), \tag{8.1}$$

where fractional difference in total luminosity, $x_T = 2.5$ across one magnitude. Note that x_C/x_T is greater than unity if component luminosity increases at a greater rate than galaxy luminosity. The component luminosity difference relative to an average galaxy can be estimated as:

$$x_C = \left(1 - \frac{\Delta_{\mathrm{C/T}}}{\langle \mathrm{C/T} \rangle}\right) x_T \tag{8.2}$$

where $\langle \mathrm{C/T} \rangle$ is the mean value of C/T.

Table 8.3 presents x_C values relative to a galaxy of average luminosity and C/T (i.e. $\mathrm{C}_0/\mathrm{T}_0 = \langle \mathrm{C/T} \rangle$). For a galaxy brighter than the average by an arbitrary magnitude difference ($M_{\mathrm{tot}} = M_{\mathrm{tot},0} + \Delta M_{\mathrm{tot}}$), the proportion of the total luminosity difference (ΔL_{tot}; where $L_{\mathrm{tot},0} = L_{\mathrm{tot}} + \Delta L_{\mathrm{tot}}$) attributed to each photometric component (ΔL_C) can be estimated using:

$$\frac{\Delta L_C}{\Delta L_{\rm tot}} = {\rm C/T}\frac{(x_T - 1) - x_T \Delta_{\rm C/T}}{x_T - 1}. \tag{8.3}$$

The resulting component fractions of the additional galaxy luminosity is illustrated in Figure 8.9 for Type I, II and III galaxies.

For Type I galaxies, bars become more luminous at a significantly greater rate than the overall galaxy luminosity (bar luminosity doubles for a 42% increase in total luminosity), while disks increase in luminosity at a slower rate (52% increase in disk luminosity as galaxy luminosity doubles). However, the luminosity difference for Type I galaxies arbitrarily brighter than the average is distributed equally between all three structural components (from Equation 8.3; Figure 8.9). For example, an average Type I galaxy ($\langle M_i \rangle = -20.3$) has a total luminosity of $8.6 \times 10^9\ L_\odot$. Relative to this average, a $9.6 \times 10^9\ L_\odot$ Type I galaxy (i.e. $10^9\ L_\odot$ brighter) would have a bulge more luminous by $(3.3 \pm 0.4) \times 10^8 L_\odot$, a bar more luminous by $(3.5 \pm 0.3) \times 10^8\ L_\odot$, and a disk $(3.2 \pm 0.4) \times 10^8 L_\odot$ more luminous.

For Type II galaxies, the disk component is the dominant contribution to luminosity growth ($70 \pm 12\%$ of $\Delta L_{\rm tot}$), doubling in luminosity for each 32% increase in galaxy luminosity. Hence, the disk-total luminosity trend is significantly steeper for Type II disks than Type I, indicating a larger difference in disk luminosity between faint and bright Type II galaxies than for Type I galaxies. This implies that fainter Type II galaxies have experienced a greater truncation (of light) than intrinsically more luminous galaxies.

For Type III galaxies, the bulge is the dominant component (doubling in luminosity for a 28% increase in global luminosity). For an average Type III galaxy, the bulge component's contribution to galaxy luminosity is approximately equal to the (intrinsically more luminous) disk. The corresponding bar light contribution is minimal ($3.7 \pm 0.4\%$ of $\Delta L_{\rm tot}$), indicating approximately equally-luminous bars in all Type III galaxies, independent of total galaxy luminosity.

No other components (bulges in Type I galaxies, bulges and bars in Type II galaxies, and bars and disks in Type III galaxies) differ significantly from increasing in luminosity proportional to the galaxy ($x_C \sim 1$). Note that since $x_T = 2.5$, no component in Type I, II, or III galaxies decreases in luminosity in brighter galaxies.

In summary, 3-component archetypal (central bulge + outer-dominant disk + any bar)

galaxies are disk-dominated on average, with approximately equal bulge and bar light fractions, independent of Freeman disk/galaxy type. The measured trends in component light fraction with total magnitude were used to quantify the contributions of each structural component to galaxy luminosity. All three structural components contribute equally on average to the increasing total luminosity in galaxies unbroken disks (Type I). However, the bar component exhibits the largest fractional increase in luminosity. disks were found to dominate truncated (Type II) galaxy luminosities. The corresponding disk-total luminosity trend is steeper than for Type I galaxies, which may indicate disk (luminosity) truncation. Increasing anti-truncated disk (Type III) galaxy luminosities correlate strongly with both their bulges and disks. Hence, bar luminosity in Type III galaxies is independent of galaxy luminosity.

8.5 Disk break formation scenarios

In this section, I investigate the evolutionary origins of archetypal broken disk (truncated/anti-truncated; Freeman Type II/III) galaxies through comparison of their structural and component photometric properties to unbroken (Type I) galaxies. As a working hypothesis, I assume a break formation scenario in which Type II and III galaxies had Type I disks at some point in the past. While the observed present-day Type I disks cannot be the progenitors of present-day broken disks, all three Freeman type galaxies must have evolved from a common population of primordial galaxies with (Type I) disks. Thus, features of the structural/photometric distributions unique to galaxies of a particular Freeman type can be used to constrain the evolutionary pathways that acted exclusively on them.

Significant increases in bulge luminosity for more luminous Type III galaxies ($x_B = 1.5x_T$; see Table 8.3), and moderate increases in bulge size supports a paradigm of forming anti-truncated disks through merger events (in which the disk is preserved), as in Borlaff et al. (2014). Such a merger event would add mass ($\equiv$luminosity) to the galaxy, and would grow the bulge component ($\propto M^{\alpha}$, as discussed in Section 1.2.2), thus creating a correlation between R_e and total luminosity. Additionally, Type III bulge n is systematically larger than the bulges in Type I (i.e. $n_{\rm III} \sim 1.7$ vs. $n_{\rm I} \sim 1.5$) galaxies, and correlates strongly with galaxy luminosity. This suggests that starburst events (induced during merging via gravitational torques) contribute to Type III galaxy formation, as increasing n indicates greater

concentration of profile light (e.g. due to an additional starburst remnant at radii $\ll R_e$). The resulting increase in bulge light concentration with luminosity would lower the reported R_e for higher n structures. This explains the relatively weak size-luminosity relation for Type III bulges.

Consistency in component scale-lengths (and size-luminosity trends) between Type III and Type I galaxies implies that the Type III inner disks may correspond to undisturbed primordial (Type I) disks. Conversely, the (significantly larger) outer disk represents an extended merger remnant structure. Nevertheless, the outer disk maintains a disk-like size-luminosity relation. An evolutionary scenario from Type I (or Type I *progenitors*) to Type III is supported by the consistent bulge and disk component light fractions for both disk types, despite Type III galaxies being a factor of $1.9\times$ brighter on average (Type I: $m_T = 14.8 \pm 0.1$, Type III: $m_T = 14.1 \pm 0.2$). This implies that both components increase in luminosity proportional to the whole galaxy. For bulges, this would correspond to bulge growth during a merger, while the increased disk light corresponds to an additional merger remnant (i.e. the outer disk). If brighter galaxies assembled more mass via mergers, then the observation of decreasing $r_{\rm brk}/R_{e,\rm in}$ with increasing Type III galaxy luminosity can be understood as a decreasing fraction of the primordial disk surviving increasing mass ratio mergers.

Systematically larger disk scale lengths (and inconsistent size-luminosity relations) compared to untruncated Type I galaxies indicates that the inner/outer disk of Type II galaxies are not structures equivalent to Type I disks. This disfavours a scenario in which Type II disks represent a truncated system in which the outer disk is suppressed relative to the surviving primordial inner disk. Furthermore, while D/T is systematically lower in Type II galaxies compared to Type I, the fractional change in disk light does not differ significantly from unity ($x_D/x_T = 0.9 \pm 0.1$ as in Equation 8.1, where x_T is the galaxy luminosity change between Type I and Type II galaxies). Hence, assuming an evolutionary scenario in which Type II galaxies evolve from from Type I, disk luminosity increases proportional to the $\sim 40\%$ increase in total galaxy luminosity (Type I: $m_T = 14.8 \pm 0.1$, Type II: $m_T = 14.5 \pm 0.1$). Intrinsically brighter Type II disks rule out a formation mechanism in which Type I disks are physical truncated. This conclusion is not compromised by the the comparison of present-day truncated and untruncated disks unless evolution from primordial to present-day Type I

galaxies also involves reduction of disk luminosity while preserving their untruncated profiles.

Rather than a truncation of the outer disk profile, Type II disk light has been redistributed from the inner region, such that the profile is flattened inside the break radius. Correspondingly, the outer disk represents a remnant more structurally reminiscent of the primordial (Type I disk). These effects may be enhanced via interaction with a bar potential, yielding steeper inner/outer disk size trends with luminosity due to the strong bar size - galaxy luminosity relation.

Bulge sizes in Type II galaxies are systematically larger than for untruncated galaxies, implying that bulge enhancement effects are significant for the formation of Type II galaxies. Consistency of average bulge n and R_e, and bar R_e with Type III galaxies may indicate that Type II galaxies have a similar, merger-based evolutionary origin. If true, then evolutionary distinction between Type II and III disks may purely result from differing trajectories of the merging progenitor galaxies (e.g. a difference between aligned/misaligned merging disks). Consistency of $r_{\rm brk}$ and $R_{e,\rm out}$ growth for brighter Type II galaxies implies that, in contrast to Type III galaxies, the Type II break always contains a consistent fraction of the progenitor disk.

Bar structures appear to be very important for the formation of Type II and III galaxies: while one half of all Type I galaxies contain a bar ($42^{+5}_{-5}\%$ barred, $58^{+5}_{-5}\%$ unbarred), the bar fraction is considerably higher for Type II ($89^{+5}_{-9}\%$) and Type III ($71^{+8}_{-10}\%$) galaxies. Furthermore, galaxy bars are significantly larger if their host galaxy has a truncated/anti-truncated disk than if the galaxy disk remains untruncated. This implies that either the truncation mechanism induces bar growth, or that bars stabilise the disk during truncation, such that the detection of a disk break for bright galaxies is more likely if a bar is present. For Type II galaxies, the bar also increases in size significantly for more luminous galaxies. This may imply that destabilisation of the inner disk causes significant migration of stars into the bar.

8.6 Conclusions and Chapter Summary

In this chapter, I have discussed the structural properties beyond the simple bulge + (exponential) disk morphology. This has allowed investigation into the multi-component structure

of classic ellipticals, and the role of galaxy bars in the evolution of disk-dominated galaxies. Furthermore, the properties of broken disk structures (Freeman Types II and III) have been contrasted with the previously-considered (unbroken) exponential disk (Freeman Type I), allowing investigation of the formation mechanisms (and hence evolutionary history) of galaxies containing such structures.

The key findings of this chapter are summarised as follows:

i) Galaxies best fit by double ($N = 34$; 7% of the filtered sample of 478) and triple Sérsic ($N = 70$; 15%) profiles have $n \sim 2$ bulges twice as large as single Sérsic galaxies ($N = 134$; 28%), with additional, significantly larger Gaussian ($n \sim 0.5$) outer structures. The total (combined) half-light radii for these multi-component Sérsic galaxies are typically ~ 11 kpc.

   Thus, **multi-component Sérsic galaxies resemble a compact core, surrounded by large Gaussian structures. If formed from the compact 'red nuggets' detected at high redshifts, these objects require a factor of $\sim 6\times$ growth in size.**

ii) If truncated (Freeman Type II) galaxies evolve directly from the observed untruncated (Type I) disk galaxies, then disk luminosity increases despite a significant reduction in D/T. Enhanced bulge/bar size and luminosity implies a bulge-enhancement origin (e.g. mergers) for truncated disk galaxies.

   Thus, **'truncated' disks may not be physically truncated. Rather, inner disk surface brightness is suppressed in these structures, while the outer disk approximately preserves the progenitor disk properties. However, Type II disk luminosity trends are steeper than untruncated disks, suggesting luminosity truncation in fainter galaxies.**

iii) Significant growth of bulge size and luminosity implies a bulge enhancement origin for anti-truncated (Freeman Type III) galaxies, while the inner disk ($r < r_{\rm brk}$) remains structurally consistent with that of untruncated galaxies.

   Thus, **'anti-truncated' disks are likely to result from (disk-preserving) merger events, causing bulge growth, and the addition of a disk-like remnant structure (the outer disk; $r > r_{\rm brk}$).**

iv) $89^{+5}_{-9}\%$ of truncated galaxies, and $71^{+8}_{-10}\%$ of anti-truncated galaxies are barred, compared to only $42 \pm 5\%$ untruncated galaxies. Furthermore, bar sizes are found to correlate with the inner/outer disk structures of truncated and anti-truncated galaxies. Thus, **galaxy bars play an important role in the formation or stabilisation of Freeman Type II and III disk structures.**

The evolutionary origins of truncated and anti-truncated galaxies may differ only in the orientation of progenitor merging systems. Structural similarities in nuclear components, and equivalent size-luminosity relations imply a common, bulge-enhancing origin for both disk types.

Further investigation into this subject will require analysis of a far wider galaxy sample to better constrain the structural trends reported in this work. Additionally, the measurement of component colours (via analysis of additional photometric bands) would provide valuable information regarding the stellar populations in inner and outer broken disks. In both cases, deeper imaging data would greatly improve the reliability with which the multi-component structures of galaxies can be measured.

Chapter 9

Summary and Conclusions

In this thesis I have presented detailed decomposition analyses (both bulge-disk and more complex, multi-component models) of Coma cluster red sequence galaxies (in the luminosity range $-17 > M_g > -22$) using MegaCam ugi imaging data. As this data is $\gtrsim 12\times$ deeper than SDSS, fitting accuracy and reliability was substantially improved relative to studies based on SDSS imaging data. This work focused on early-type galaxies (notably outer disk-dominated galaxies, i.e. *S0*s). The key aim has been to constrain the evolutionary pathways which lead to the formation of these galaxies, and the role of the rich cluster environment therein.

A particular emphasis has been placed on ensuring that the (best fit) models are structurally consistent with the true underlying morphologies of the studied galaxies. As such, galaxies which cannot be reliably fit by simple, symmetric models, or where the models do not accurately represent the galaxies' structures were removed from analysis. This approach is a significant improvement over a naïve enforcement of an assumed model structure on all galaxies regardless of propriety, wherein measurement scatter would be increased by the effect of structural dissonance. Furthermore, model selection via visual examination - employed in many previous studies - is purely subjective, and hence limits repeatability of results relative to clearly-defined parametric methods. Here, rigorous statistical tests were applied to ensure that each structural component of every best-fit model provides a statistically significant improvement to the goodness-of-fit (i.e. neither overfitting, nor underfitting of the data takes place). Result filtering is implemented (via thresholds in acceptable parameter values) to reject erroneous fits wherein model components do not correspond to the

intended target galaxy structures.

Throughout this thesis, I made use of the following notation conventions: Galaxy morphologies (see Section 1.1) were indicated in italics (e.g. '*Sa*') to distinguish them from fitted model structures (see Section 7.2.3; e.g. 'S'). Disk break types (i.e. Freeman types; untruncated, truncated, anti-truncated, see Section 1.4) were denoted with Roman numerals (e.g. 'Type II'), and galaxies containing such structures were referred to as Type I, Type II, or Type III galaxies. Conversely, galaxy types using Arabic numerals (e.g. 'Type 2') referred to Allen et al. (2006) surface brightness profile types (see Sections 1.4 and 7.2.3). The Type 1 profile is a special case describing a central bulge and an outer disk, and was referred to as an 'archetypal *S0*' profile ('archetypal', or '*S0*' as shorthand). All other Allen et al. (2006) types were referred to as 'atypical *S0*' profiles (or simply 'atypical').

9.1 Chapter Summaries

The content and conclusion of the chapters contained within this thesis are as follows:

- In Chapter 2, I described the deep MegaCam imaging of Coma used for decomposition throughout this thesis, including details of the selection criteria for the initial galaxy sample, and the data products derived from the raw imaging to ensure reliable `GALFIT` analysis.
  - In total, 570 (spectroscopically selected) Coma cluster members were identified as sufficiently bright ($M_g < -17$), red sequence galaxies for decomposition analysis.
- Chapter 3 provided details of the `AGONII` (Automated Galfitting of Optical and Near Infrared Imaging) data reduction pipeline used for robust bulge-disk decomposition in this thesis. This included a description of the thorough sample filtering criteria and tests used to detect and remove cases of structural dissonance, yielding a sample containing only smooth, symmetrical galaxies well described by an archetypal central (Sérsic) bulge and outer (exponential) disk model. Model selection tests based on the Bayesian Information Criterion (BIC; assessed over independent resolution elements) ensured that only galaxies in which the disk component provided a statistically

significant improvement to the goodness-of-fit are analysed as 2-component systems. Multi-band fitting was carried out with the model structure either entirely fixed from band-to-band, or partially allowed to vary, in order to reproduce the observed internal component colour gradients.

a) A stable, 2-component fitting solution was found in 337 galaxies (59%) of the initial sample, from which an analysis sample of 200 galaxies (35%) was drawn where model structures were consistent with an archetypal bulge + disk morphology.

b) The remaining 370 Coma cluster members include 106 galaxies well-fit by a pure Sérsic model, and 137 galaxies with atypical *S0* profiles (e.g. bulge components which dominate at small *and* large radii).

c) Internal component colour gradients provides a significant improvement to the colour profile fitting for 60 (30%) of the analysis sample galaxies. The component gradient fraction decreases with luminosity, suggesting that the detection of internal component gradients is magnitude limited.

- A comparison of the bulge-disk decomposition results in the present work with equivalent studies using SDSS (both using the `AGONII` pipeline, and from literature) and HST data was presented in Chapter 4.

  a) The pure Sérsic model parameters reported in the present work are in good agreement with measurements from independent HST and SDSS imaging data (independent of the reduction pipeline).

  b) Large measurement scatter in galaxy (bulge and disk) component properties is detected between results derived from MegaCam and SDSS imaging. Inconsistency of of SDSS-derived measurements (even for alternative reductions of the same images) is attributed to the shallow image data of SDSS, which limits reliable disk detection and measurement.

- In Chapter 5, I described the structural properties of archetypal (central) bulge + (outer) disk galaxies, which are labeled as '*S0*s'. This included a description of structural trends with galaxy luminosity and distance from the Coma cluster core.

a) *S0* bulges have physical sizes, $R_{e,B} \sim 1$ kpc, and profile shape, $n \sim 2$, on average. Bulges are thus structurally similar to both dwarf ellipticals in Coma, and 'red nugget' galaxies observed at $z > 1.5$ (albeit an order of magnitude smaller in mass than the latter).

b) Disk effective half-light radius is strongly correlated with total galaxy luminosity. The slope of the size-luminosity relation for *S0* disks is consistent with that of today's star-forming disk galaxies. However, these trends are separated in luminosity such that *S0*s are brighter than such spirals. If *S0* galaxies are formed through disk fading, then their disks are 40% smaller (on average) than the disks of equally luminous local spirals. Thus, either their progenitor's disks were intrinsically smaller than the disks of today's spirals (suggesting a quenching epoch of $z \sim 1.5$), or were truncated in size during transformation to *S0*s.

c) No significant correlation between bulge half-light radius and total galaxy luminosity is detected (for $M_g > -20.5$). This is inconsistent with predictions for a 'bulge-enhancement' scenario of *S0* formation via major mergers (R_e increases $\propto M$) or minor mergers ($R_e \propto M^2$).

d) Archetypal galaxy structure does not vary with radial position in the Coma cluster. Thus, either environmentally-driven evolution does not significantly alter galaxy structure (if present), or environmental effects cause evolution to atypical (i.e. not archetypal) structural morphologies.

- Chapter 6 presented the photometric colour properties of bulges and disks in archetypal galaxies, including colour-magnitude and colour-cluster radial trends for both the whole analysis sample, and for subsamples with different morphological types. Simple SSP models were used to convert the measured colour offsets (e.g. colour differences between bulges and disks within each galaxy, galaxies at different clustercentric radii, or with different morphologies) into estimated differences in stellar population properties (i.e. age or metallicity).

  a) If either galaxy or component luminosity is fixed, the bulges of *S0*s are significantly redder than their disks (by ~ 0.1 mag in $g - i$, ~ 0.2 mag in $u - g$ on

average). Thus, bulge stellar populations are $\sim$2-3$\times$ older, and/or $\sim 2\times$ more metal rich than those found in disks.

b) Significant colour-magnitude slopes are detected for both structural components in $g-i$ and $u-g$. In either colour, the measured trend slopes for bulges and disks are consistent at a 2σ level. Hence, the global red sequence is a consequence of the increasingly red colours of bulges *and* disks in more luminous galaxies.

c) After subtracting the best-fit colour-magnitude trend, galaxy disks become bluer in both $g-i$ and $u-g$ with increasing projected distance from the centre of the Coma cluster. Bulge component colours also become bluer with $r_{\rm cluster}$, but this trend is only marginally significant (2.5σ) and more sensitive to the treatment of component colour gradients. The global colour-radius trend for *S0*s is thus dominated by increasingly red disks in galaxies closer to the cluster core. Therefore, the environment-mediated mechanism which drives *S0* formation is primarily a 'disk-fading' process.

d) '*E*' and '*S0*' classifications from Dressler (1980a) represent the bulge-dominant and bulge-weak ends of the archetypal galaxy distribution rather than morphologically distinct galaxies. D80 ellipticals are significantly more bulge dominated, indicating poor disk detection for faint disks (high B/T). No significant difference in component colours are noted for morphology relative to predictions from the colour-magnitude trend.

e) Galaxy Zoo classifications from Lintott et al. (2008) identify galaxies with low-level deviations from a smooth, regular profile, rather than categorising morphologically distinct samples.

- In Chapter 7, the decomposition analysis was extended to a wider range of candidate models including 3-component and/or broken disk models. The `AGONII` decomposition pipeline was modified, with more rigorous model selection testing to ensure no dissonance exists between galaxy and (best-fit) model structure, ensuring reliable results.

  a) Only $48 \pm 3\%$ of galaxies ($N = 230$) are well-described by a Sérsic, or Sérsic +

exponential model, with 3(+) component models required to describe $42 \pm 3\%$ of galaxies. Coma cluster galaxies structure is thus more complex and varied than has previously been considered.

b) Archetypal (central bulge + outer disk) structures are most frequently untruncated exponential disks ($74 \pm 3\%$), with equal numbers of truncated ($12 \pm^{+3}_{-2}$ %) and anti-truncated ($13^{+3}_{-2}\%$) disks. This corresponds to a significantly higher truncated disk fraction, and lower anti-truncated disk fraction than has previously been detected for cluster galaxies.

c) Detection of genuine broken disk galaxies is significantly limited if too narrow a range of models are considered. False positive broken disk detection (i.e. the fraction of reported 'broken disk' galaxies revealed to have more complex, *unbroken* structures via a more mature analysis) can exceed 50% if 3-component and/or multi-Sérsic models are not considered for decomposition analysis.

d) The fraction of barred galaxies detected in the present work ($20 \pm 2\%$) is significantly lower than previously reported for the Coma cluster. However, if triple Sérsic galaxies are considered 'barred', and analysis is limited to galaxies with morphological classifications from Dressler (1980a), then this value rises to $71 \pm 5\%$, consistent with previous measurements.

- Finally, Chapter 8 described the structural properties of multi-component Sérsic galaxies (i.e. galaxies comprised only of Sérsic components with $n \neq 1$), and archetypal galaxies containing disk breaks. This included a discussion of possible formation mechanisms for truncated and anti-truncated disks (Freeman Types II and III), for a scenario in which such galaxies were formed from primordial untruncated disks (Type I).

  a) Multi-component Sérsic galaxies were resolved into a compact core (with $n \sim 2$), surrounded by large Gaussian structures. The total (combined) half-light radii for these multi-component Sérsic galaxies are typically ~ 11 kpc. Thus, if formed from the compact 'red nuggets' detected at high redshifts, these objects require a factor of $\sim 6\times$ growth in size.

b) 'Truncated' (Freeman Type II) disks may not be physically truncated. Rather, inner disk surface brightness may be suppressed in these structures, while the outer disk approximately preserves the progenitor disk properties. However, Type II disk luminosity trends are steeper than untruncated disks, suggesting luminosity truncation in fainter galaxies.

c) Significant growth of bulge size and luminosity implies a bulge enhancement origin (e.g. mergers) for anti-truncated (Freeman Type III) galaxies, while the inner disk ($r < r_{\rm brk}$) remains structurally consistent with that of untruncated galaxies. Thus, 'anti-truncated' disks are likely to result from (disk-preserving) merger events, causing bulge growth, and the addition of a disk-like remnant structure (the outer disk; $r > r_{\rm brk}$).

d) Disk breaks are found overwhelmingly in barred galaxies (truncated: $89^{+5}_{-9}\%$, anti-truncated: $71^{+8}_{-10}\%$ vs. untruncated: $42 \pm 5\%$), and are structurally correlated with bar size. Such structures therefore play an important role in the formation or stabilisation of Type II and Type III broken disks.

9.2 Future Directions and Concluding Remarks

Confirmation of the complex galaxy structures detected in Coma via independent, deep(er) imaging data (e.g. existing Surbaru imaging; Okabe et al., 2014) is an important short-term extension to this project. In particular, improved imaging depth would allow galaxy surface brightness profiles to be traced to a greater number of R_e, allowing the Type 1 (central bulge, outer disk)/Type 3 (central and outer bulge, intermediate disk) dichotomy to be investigated (e.g. do all bulges re-dominate if sufficiently high radii are considered?). Likewise, extension of multi-component analysis to additional target fields (e.g. SDSS Stripe 82; see e.g. Kaviraj, 2010) would allow differences in this structural diversity to be assessed across alternative (high and low density) environments. The analysis of additional photometric bands (e.g. NIR J or K bands) would also yield valuable information; breaking the age-metallicity degeneracy (i.e. are colour differences between the measured structural components caused primarily by age or metallicity differences between their stellar populations?), and allowing

the stellar population properties of broken disks to be investigated (e.g. have inner Type II/Type III disks traded stars with their bars or bulges?).

Furthermore, the addition of Integrated Field Unit (IFU) spectrograph data (e.g. from the CALIFA; Sánchez et al., 2012, MaNGA; Law & MaNGA Team, 2014, or SAMI; Bryant et al., 2014 surveys) to the existing imaging decomposition results would provide valuable (spatially resolved) spectroscopic information for the analysed galaxies. This would allow the galaxy kinematics to be investigated, confirming or refuting galaxy rotation, and hence disk structures (e.g. are outer-dominant Sérsic components with $0.5 < n < 1.5$ disks?). Relative to typical centralised or long-slit spectroscopic measurements, IFU data would allow a thorough investigation of stellar population properties in all structural components across all radii. Thus, component colour gradients could be analysed in parallel with gradients in stellar population properties (similar to Johnston et al., 2012, 2014). In addition, spectroscopic constraints would break the age/metallicity degeneracy present in this work for SSP analysis, allowing precise offsets in stellar population properties to be measured (e.g. between components, or between galaxies at differing cluster radii). As the component stellar population properties of cluster red sequence galaxies become more well-constrained, comparison with the predictions of simple quenching model scenarios (e.g. Smith et al., 2012; Taranu et al., 2014) would provide a valuable means of characterising their quenching histories (e.g. can the observed colour scatter be explained by instantaneous quenching upon cluster infall?).

In the intermediate-term, the multi-component decomposition routines developed in this thesis can be applied to artificial 'observations' drawn from simulations of galaxy structure (e.g. EAGLE; Schaye et al., 2014, Illustris; Vogelsberger et al., 2014). This would not only test whether such simulations reproduce the range of structure seen in real galaxies, but would also reveal the evolutionary histories of the star particles in such structures. Hence, galaxy simulations can reveal candidate progenitor galaxies for the multi-component galaxies observed in the Coma cluster.

The long-term direction of research into galaxy structure and evolution will be shaped by the advent of cutting-edge wide surveys such as the Panoramic Survey Telescope And Rapid Response System (Pan-STARRS; Kaiser et al., 2002), and the Large Synoptic Survey Telescope (LSST; Ivezic et al., 2008). These projects will yield immense catalogues of galaxies

over a wide range of environments and redshifts with greater imaging quality and depth than pioneer wide area studies such as SDSS or 2MASS. However, the resulting large datasets will require automated reduction pipelines capable of consistently robust measurements of structural and photometric galaxy properties. Furthermore, these wide galaxy surveys would be significantly devalued if efforts are not made to remove or least limit (even at the cost of sample size) the additional measurement scatter caused by model/galaxy structural dissonance.

While the sample filtering techniques presented in this thesis lay considerable groundwork towards a conclusive, robust prescription of model selection, further development is required before any singular test (or series of tests) can be considered the final word on the subject. In particular, the *a posteriori* approach taken in the present work (via the nevertheless promising BIC statistic) is not suitable for the reduction of larger datasets due to the necessity of fitting and comparing a multitude of possible models. Rather, an additional *a priori* test (e.g. the residual flux fraction test of Lansbury et al., 2014) capable of identifying the required model structure (or narrowing the range of candidate models) is necessary to keep require processor time per galaxy at a reasonable level. A smaller, focused pool of candidate models would thus enable exhaustive multi-component fitting to be carried out on large datasets.

To conclude, galaxy classification and model selection via visual morphologies is neither objective nor repeatable, while goodness-of-fit (considered in isolation) is not good enough. Instead, *propriety*-of-fit (assessed via clearly-defined parameter cuts and statistical model selection tests) is essential in decomposition studies to avoid disagreement between the *intended* target galaxy components and the stellar structures which are actually fitted. This structural dissonance (e.g. fitting an exponential model to a bulge structure, and interpreting the resulting parameters as a disk) is a major contribution to measurement scatter, but can also cause systematic biases in measured parameters if the 'true' galaxy structural form is not in the range of candidate models. As such, it is time to re-examine (or abandon outright) the morphological tropes (e.g. 'ellipticals are pure spheroids') and empirical models (e.g. 'disks have exponential profiles') inherited from 30+ year old observational studies which still shape the current paradigm of internal galaxy structures.

Appendix A

Supplementary Data Tables

The fitting results for the entire Coma cluster sample ($N = 571$) are presented for Sérsic-only ('S') and Sérsic + exponential ('BD') g band models in Table A.1 (column descriptions in Table A.3), and for (dependent) Sérsic + exponential u and i band models in Table A.2 (column descriptions in Table A.4). Independent fitting was carried out in the g band. Thus, the g band structural parameters were used for u and i band models except where internal component gradients are included. The best-fit multi-band fitting model (see Sections 3.5 and 3.7.2) have either no internal component colour gradients ('N'), or internal colour gradients in the bulge ('B'), disk ('D'), or both components ('BD'). This is indicated by column (xxxvi) in Table A.2. The results of sample filtering (see Section 3.5) are included in Table A.1, along with some of the key parameters involved in the filtering process (asymmetry, masking fraction, χ^2_ν. The meaning of the filtering sample codes used in Table A.1 are summarised in Table A.5. Erroneous parameter values (e.g. in fits which failed to converge) are set to 999.0 in both tables.

Multi-component i band fitting results for the extended Coma cluster sample ($N = 631$, including blue galaxies) are presented in Table A.6 (column descriptions in Table A.7). The structural parameters of the best-fit model (indicated by column (ab)) are presented for each galaxy, including values for the total luminosity and combined half-light radius[1]. A value of 999.0 indicates a parameter is not present in the relevant best-fit model (e.g. disk break radius in an unbroken BD galaxy). Fit quality flags (column (ad)) are explained in Table A.8.

[1]This value is an upper bound to the true value based on the assumption that major axes of all model components are aligned on the sky.

(1)	(2)	(3)	(4)	(5)	(6)	(7)	(8)	(9)	(10)	(11)	(12)
(13)	(14)	(15)	(16)	(17)	(18)	(19)	(20)	(21)	(22)	(23)	(24)
(25)	(26)	(27)	(28)	(29)	(30)	(31)	(32)	(33)	(34)	(35)	(36)
1237665427552927881	194.8755	28.7001	44.19	0.024	-17.483	0.012	-15.777	0.146	-17.128	0.021	-17.403
0.037	0.215	0.023	2.628	0.048	2.121	0.026	0.843	0.006	1.066	0.224	2.614
0.034	10.000	0.929	0.826	0.034	0.839	0.014	20.0	0.98	0.94	3	U4
1237665427552993436	195.0183	28.6035	38.22	0.023	-19.280	0.003	-16.369	0.114	-19.000	0.005	-19.092
0.010	0.075	0.007	10.058	0.057	2.150	0.009	0.783	0.002	1.310	0.217	8.422
0.025	1.375	0.120	0.571	0.023	0.796	0.003	154.6	1.07	0.91	1	S7
1237665427552993478	195.0946	28.5745	37.01	0.022	-18.446	0.007	-16.778	0.072	-17.920	0.014	-18.245
0.021	0.251	0.013	9.734	0.109	2.589	0.020	0.801	0.003	3.232	0.323	8.608
0.072	2.013	0.101	0.575	0.013	0.947	0.011	60.1	0.98	0.95	1	A11
1237665427553124587	195.4493	28.6602	48.74	0.029	-17.415	0.015	-16.184	0.129	-16.979	0.033	-17.405
0.047	0.315	0.026	4.412	0.102	1.579	0.024	0.730	0.006	2.076	0.379	6.384
0.127	1.046	0.083	0.779	0.028	0.685	0.018	2.0	0.96	0.95	1	S6
1237665427553189967	195.4972	28.7095	52.59	0.020	-17.171	0.017	-17.094	0.049	-14.386	0.129	-17.180
0.046	0.921	0.009	2.525	0.065	2.172	0.036	0.665	0.006	2.673	0.173	1.490
0.108	2.153	0.065	0.743	0.011	0.261	0.023	0.3	0.95	0.94	5	S6
1237665427553255498	195.7906	28.5835	57.10	0.023	-20.197	0.001	-19.695	0.005	-19.183	0.007	-20.222
0.004	0.610	0.002	6.144	0.014	2.874	0.005	0.294	0.000	4.158	0.025	8.009
0.028	4.259	0.020	0.605	0.002	0.133	0.001	0.4	2.87	1.26	1	A8
1237665427553321028	195.8325	28.6173	60.10	0.020	-18.434	0.004	-18.294	0.013	-16.372	0.033	-18.465
0.012	0.850	0.004	4.965	0.036	2.869	0.015	0.284	0.001	4.815	0.077	5.683
0.099	3.359	0.033	0.349	0.002	0.125	0.003	1.0	1.01	0.98	5	U4
1237665427553321062	195.9368	28.5459	61.91	0.026	-18.393	0.005	-17.270	0.030	-17.725	0.013	-18.274
0.014	0.389	0.007	2.887	0.022	3.553	0.020	0.477	0.001	0.858	0.034	3.520
0.026	4.263	0.096	0.367	0.004	0.515	0.005	0.8	1.13	0.99	1	A11
1237665427553452095	196.2053	28.6612	77.54	0.026	-18.244	0.007	-16.529	0.088	-17.947	0.013	-18.207
0.021	0.205	0.013	5.854	0.066	1.784	0.014	0.307	0.001	2.094	0.261	6.919
0.053	0.961	0.059	0.265	0.008	0.325	0.003	1.2	0.95	0.95	1	S6
1237665427553452170	196.3231	28.5827	80.63	0.026	-17.404	0.015	-16.261	0.116	-16.962	0.033	-17.420
0.045	0.335	0.025	6.264	0.140	1.741	0.026	0.567	0.005	3.307	0.542	7.940
0.158	1.123	0.081	0.432	0.014	0.816	0.021	164.5	0.94	0.92	1	A10

Table A.1: The structural and photometric parameters of Sérsic and Sérsic + exponential models fits (g band) for the entire galaxy sample. The column headings are described in Table A.3. This table displays the first ten data rows only; the complete version is available in Head et al. (2014).

(i) (xiii) (xxv)	(ii) (xiv) (xxvi)	(iii) (xv) (xxvii)	(iv) (xvi) (xxviii)	(v) (xvii) (xxix)	(vi) (xviii) (xxx)	(vii) (xix) (xxxi)	(viii) (xx) (xxxii)	(ix) (xxi) (xxxiii)	(x) (xxii) (xxxiv)	(xi) (xxiii) (xxxv)	(xii) (xxiv) (xxxvi)
1237665427552927881	-14.034	0.173	-15.624	0.051	-15.850	0.052	0.181	0.025	1.066	0.269	1.558
0.019	0.917	-16.936	0.133	-18.156	0.016	-18.461	0.035	0.236	0.022	1.066	0.202
1.558	0.021	0.930	-0.193	0.133	-0.056	0.018	-0.338	0.151	-0.078	0.019	N
1237665427552993436	-14.697	0.130	-17.473	0.013	-17.554	0.015	0.065	0.007	1.310	0.251	5.019
0.015	0.933	-17.450	0.107	-20.012	0.004	-20.110	0.010	0.079	0.007	1.310	0.203
5.019	0.015	0.935	-0.047	0.073	-0.048	0.004	-0.072	0.079	-0.066	0.004	N
1237665427552993478	-15.282	0.069	-16.377	0.034	-16.715	0.031	0.260	0.014	3.232	0.310	5.130
0.044	0.943	-17.823	0.068	-18.873	0.012	-19.222	0.021	0.267	0.012	3.232	0.302
5.130	0.044	0.921	0.064	0.148	0.029	0.007	0.017	0.111	-0.023	0.007	N
1237665427553124587	-14.727	0.135	-15.612	0.064	-16.010	0.061	0.302	0.029	2.076	0.397	3.805
0.074	0.969	-17.149	0.122	-17.856	0.026	-18.311	0.045	0.333	0.025	2.076	0.357
3.805	0.078	0.987	-0.110	0.141	-0.048	0.011	-0.167	0.142	-0.137	0.009	N
1237665427553189967	-15.692	0.047	-11.933	0.284	-15.726	0.046	0.969	0.008	2.673	0.164	0.888
0.071	0.951	-18.065	0.049	-15.467	0.093	-18.160	0.046	0.912	0.008	2.673	0.175
0.888	0.063	0.936	-0.351	0.167	-0.140	0.018	-0.442	0.195	-0.192	0.012	N
1237665427553255498	-17.930	0.005	-17.587	0.015	-18.524	0.007	0.573	0.004	4.158	0.027	5.391
0.017	1.158	-20.858	0.005	-20.245	0.005	-21.347	0.004	0.631	0.001	4.158	0.025
4.542	0.016	1.646	-0.176	0.107	-0.172	0.012	-0.313	0.068	-0.245	0.010	D
1237665427553321028	-16.653	0.013	-14.984	0.076	-16.865	0.017	0.820	0.010	4.815	0.080	4.708
0.077	0.971	-19.350	0.013	-17.414	0.023	-19.519	0.011	0.851	0.003	4.815	0.077
3.076	0.054	1.044	-0.077	0.202	-0.227	0.014	-0.229	0.158	-0.301	0.010	D
1237665427553321062	-15.681	0.033	-16.302	0.030	-16.788	0.023	0.354	0.009	1.040	0.046	2.142
0.015	0.979	-18.383	0.029	-18.758	0.009	-19.339	0.013	0.406	0.007	0.835	0.032
2.029	0.016	1.055	-0.421	0.197	-0.209	0.031	-0.565	0.167	-0.376	0.025	BD
1237665427553452095	-15.038	0.085	-16.419	0.026	-16.687	0.028	0.212	0.014	2.094	0.251	4.123
0.032	0.983	-17.534	0.080	-18.815	0.010	-19.106	0.020	0.226	0.013	2.094	0.234
4.123	0.033	1.010	-0.027	0.132	0.025	0.016	-0.050	0.092	-0.058	0.015	N
1237665427553452170	-14.757	0.122	-15.551	0.069	-15.977	0.061	0.320	0.028	3.307	0.570	4.732
0.092	0.952	-17.215	0.120	-17.964	0.023	-18.405	0.043	0.324	0.025	3.307	0.561
4.732	0.092	0.922	-0.031	0.223	-0.054	0.011	0.005	0.171	-0.019	0.011	N

Table A.2: The multi-band fitting parameters of Sérsic + exponential models fits (u and i bands) for the entire galaxy sample. Any deviations from the g band structures (see Table A.1) are included (i.e. where internal component gradients are necessary). The column headings are described in Table A.4. This table displays the first ten data rows only; the complete version is available in Head et al. (2014).

Column name	(n)	Description
ObjID	(1)	SDSS DR8 Object ID
RA	(2)	Object Right Ascension [degrees]
Dec	(3)	Object Declination [degrees]
$R_{\rm proj}$	(4)	Projected distance from Coma cluster centre [arcmin]
z	(5)	Object SDSS Redshift
$M_{g,\rm S}$	(6)	Rest-frame Sérsic magnitude (g band S model)
$e_{M_{g,\rm S}}$	(7)	Uncertainty in $M_{g,\rm S}$
$M_{g,\rm B}$	(8)	Rest-frame bulge magnitude (g band BD model)
$e_{M_{g,\rm B}}$	(9)	Uncertainty in $M_{g,\rm B}$
$M_{g,\rm D}$	(10)	Rest-frame disk magnitude (g band BD model)
$e_{M_{g,\rm D}}$	(11)	Uncertainty in $M_{g,\rm D}$
$M_{g,\rm T}$	(12)	Rest-frame total magnitude (g band BD model)
$e_{M_{g,\rm T}}$	(13)	Uncertainty in $M_{g,\rm T}$
$\rm B/T_{\it g}$	(14)	g band bulge fraction (BD model)
$e_{\rm B/T_{\it g}}$	(15)	Uncertainty in $\rm B/T_{\it g}$
$R_{e,{\rm S},g}$	(16)	Effective Sérsic half-light radius (g band S model) [arcsec]
$e_{R_{e,{\rm S},g}}$	(17)	Uncertainty in $R_{e,{\rm S},g}$
$n_{{\rm S},g}$	(18)	Sérsic index (g band S model)
$e_{n_{{\rm S},g}}$	(19)	Uncertainty in $n_{{\rm S},g}$
$q_{{\rm S},g}$	(20)	Sérsic axis ratio (b/a,g band S model)
$e_{q_{{\rm S},g}}$	(21)	Uncertainty in $q_{{\rm S},g}$
$R_{e,{\rm B},g}$	(22)	Effective bulge half-light radius (g band BD model) [arcsec]
$e_{R_{e,{\rm B},g}}$	(23)	Uncertainty in $R_{e,{\rm B},g}$
$R_{e,{\rm D},g}$	(24)	Effective disk half-light radius (g band BD model) [arcsec]
$e_{R_{e,{\rm D},g}}$	(25)	Uncertainty in $R_{e,{\rm D},g}$
$n_{\rm B}$	(26)	Bulge S index (BD model)
$e_{n_{\rm B}}$	(27)	Uncertainty in $n_{\rm B}$
$q_{\rm B}$	(28)	Bulge axis ratio (b/a, BD model)
$e_{q_{\rm B}}$	(29)	Uncertainty in $q_{\rm B}$
$q_{\rm D}$	(30)	Disk axis ratio (b/a, BD model)
$e_{q_{\rm D}}$	(31)	Uncertainty in $q_{\rm D}$
$\Delta({\rm PA})$	(32)	Absolute position angle difference between components [Degrees]
$\chi^2_{\nu,{\rm s},g}$	(33)	Reduced χ^2 (g band, Sérsic model)
$\chi^2_{\nu,g}$	(34)	Reduced χ^2 (g band, BD model)
ProfType	(35)	Major axis surface brightness profile type (see Allen et al., 2006)
FiltSamp	(36)	Filtering sample (Table A.5)

Table A.3: This table describes the column headings (1-36) for Table A.1. Fitting results are presented for Sérsic-only ('S') and bulge + disk ('BD') models in the g band.

Column name	(n)	Description
ObjID	(i)	SDSS DR8 Object ID
$M_{u,\mathrm{B}}$	(ii)	Rest frame bulge magnitude (u band)
$e_{M_{u,\mathrm{B}}}$	(iii)	Uncertainty in $M_{u,\mathrm{B}}$
$M_{u,\mathrm{D}}$	(iv)	Rest frame disk magnitude (u band)
$e_{M_{u,\mathrm{D}}}$	(v)	Uncertainty in $M_{u,\mathrm{D}}$
$M_{u,\mathrm{T}}$	(vi)	Rest frame total magnitude (u band)
$e_{M_{u,\mathrm{T}}}$	(vii)	Uncertainty in$M_{u,\mathrm{T}}$
$\mathrm{B/T}_u$	(viii)	u band bulge fraction
$e_{\mathrm{B/T}_u}$	(ix)	Uncertainty in $\mathrm{B/T}_u$
$R_{e,\mathrm{B},u}$	(x)	Effective bulge half-light radius (u band) [arcsec]
$e_{R_{e,\mathrm{B},u}}$	(xi)	Uncertainty in $R_{e,\mathrm{B},u}$
$R_{e,\mathrm{D},u}$	(xii)	Effective disk half-light radius (u band) [arcsec]
$e_{R_{,\mathrm{D},u}}$	(xiii)	Uncertainty in $R_{e,\mathrm{D},u}$
$\chi^2_{\nu,u}$	(xiv)	Reduced χ^2 (u band)
$M_{i,\mathrm{B}}$	(xv)	Rest frame bulge magnitude (i band)
$e_{M_{i,\mathrm{B}}}$	(xvi)	Uncertainty in $M_{i,\mathrm{B}}$
$M_{i,\mathrm{D}}$	(xvii)	Rest frame disk magnitude (i band)
$e_{M_{i,\mathrm{D}}}$	(xviii)	Uncertainty in $M_{i,\mathrm{D}}$
$M_{i,\mathrm{T}}$	(xix)	Rest frame total magnitude (i band)
$e_{M_{i,\mathrm{T}}}$	(xx)	Uncertainty in$M_{i,\mathrm{T}}$
$\mathrm{B/T}_i$	(xxi)	i band bulge fraction
$e_{\mathrm{B/T}_i}$	(xxii)	Uncertainty in $\mathrm{B/T}_i$
$R_{e,\mathrm{B},i}$	(xxiii)	Effective bulge half-light radius (i band) [arcsec]
$e_{R_{e,\mathrm{B},i}}$	(xxiv)	Uncertainty in $R_{e,\mathrm{B},i}$
$R_{e,\mathrm{D},i}$	(xxv)	Effective disk half-light radius (i band) [arcsec]
$e_{R_{,\mathrm{D},i}}$	(xxvi)	Uncertainty in $R_{e,\mathrm{D},i}$
$\chi^2_{\nu,i}$	(xxvii)	Reduced χ^2 (i band)
$\Delta(u-g)$	(xxviii)	Radial gradient in galaxy $(u-g)$
$e_{\Delta(u-g)}$	(xxix)	Uncertainty in $\Delta(u-g)$
$\Delta(u-g)_{\mathrm{m}}$	(xxx)	Radial gradient in model $(u-g)$
$e_{\Delta(u-g)_{\mathrm{m}}}$	(xxxi)	Uncertainty in $\Delta(u-g)_{\mathrm{m}}$
$\Delta(g-i)$	(xxxii)	Radial gradient in galaxy $(g-i)$
$e_{\Delta(g-i)}$	(xxxiii)	Uncertainty in $\Delta(g-i)$
$\Delta(g-i)_{\mathrm{m}}$	(xxxiv)	Radial gradient in model $(g-i)$
$e_{\Delta(g-i)_{\mathrm{m}}}$	(xxxv)	Uncertainty in $\Delta(g-i)_{\mathrm{m}}$
MultiType	(xxxvi)	Best-fit multi-band model

Table A.4: This table describes the column headings (i-xxxvi) for Table A.2. Results are presented for bulge + disk models in the u and i bands.

Sample	Subsample	Reason for filtering
Unsuitable (U)	1	Masking fraction
	2	Asymmetry
	3	High χ^2_ν
	4	SB profile type
	5	Blue core
Sérsic (S)	6	BIC
	7	B/T
Analysis (A)	8	Flagged (χ^2)
	9	Flagged (Bar-like structure)
	10	Flagged (Forced swap)
	11	Regular fit

Table A.5: Filtering sample/subsample codes for Table A.1.

(a) (p)	(b) (q)	(c) (r)	(d) (s)	(e) (t)	(f) (u)	(g) (v)	(h) (w)	(i) (x)	(j) (y)	(k) (z)	(l) (aa)	(m) (ab)	(n) (ac)	(o) (ad)
1237665427552927881 0.826	194.875 121.312	28.7 999.0	0.024 999.0	-18.364 999.0	1.1 999.0	-16.449 999.0	0.233 999.0	6.96 999.0	0.8 0.171	118.556 0.829	0.0 0.0	-18.16 BD	1.237 3	1.0 0
1237665427552927902 0.769	195.926 13.057	28.906 -19.488	0.022 7.865	-19.763 1.0	502.0 0.824	-17.618 79.766	0.53 2.417	1.008 5.914	0.955 0.139	97.153 0.085	0.0 0.776	-17.089 BSDd	4.686 312	0.128 1
1237665427552993436 0.838	195.018 8.609	28.603 -19.303	0.023 6.369	-20.068 0.486	3.73 0.706	-18.354 21.469	1.221 999.0	1.927 999.0	0.68 0.206	167.424 0.299	0.0 0.495	-18.758 BSS	2.917 311	0.374 0
1237665427552993478 0.858	195.095 111.1	28.574 999.0	0.022 999.0	-19.109 999.0	3.3 999.0	-18.388 999.0	2.162 999.0	2.124 999.0	0.659 0.515	29.906 0.485	0.0 0.0	-18.324 BS	4.354 3	0.44 0
1237665427553124587 999.0	195.449 999.0	28.66 999.0	0.029 999.0	-18.288 999.0	2.143 999.0	-18.288 999.0	2.143 999.0	1.649 999.0	0.723 1.0	137.698 0.0	0.0 0.0	999.0 S	999.0 5	999.0 0
1237665427553189967 999.0	195.497 999.0	28.709 999.0	0.02 999.0	-18.071 999.0	1.154 999.0	-18.071 999.0	1.154 999.0	2.139 999.0	0.675 1.0	163.726 0.0	0.0 0.0	999.0 S	999.0 5	999.0 0
1237665427553255498 0.118	195.791 37.438	28.584 -20.291	0.023 5.003	-21.264 1.604	2.7 0.334	-20.016 38.009	0.662 999.0	2.382 999.0	0.698 0.317	36.852 0.275	0.0 0.408	-19.862 BSS	3.442 311	0.77 0
1237665427553321028 0.139	195.833 89.733	28.617 -18.832	0.02 3.31	-19.367 1.0	2.1 0.308	-17.539 88.911	0.407 999.0	1.038 999.0	0.576 0.186	87.345 0.204	0.0 0.611	-17.639 BDD	1.51 111	1.0 0
1237665427553321062 0.352	195.937 157.637	28.546 -17.387	0.026 2.075	-19.311 0.347	1.18 0.779	-18.78 160.077	0.632 999.0	4.136 999.0	0.483 0.613	156.929 0.217	0.0 0.17	-17.653 BSS	1.653 353	0.408 0
1237665427553321118 0.717	195.926 90.75	28.906 999.0	0.022 999.0	-19.1 999.0	3.7 999.0	-17.482 999.0	1.988 999.0	0.858 999.0	0.574 0.225	124.893 0.775	0.0 0.0	-18.823 BS	4.281 1	0.516 0
1237665427553386581 0.216	195.926 109.335	28.906 -19.334	0.022 2.881	-19.756 1.0	1.9 0.542	-18.303 88.491	1.116 999.0	0.329 999.0	0.525 0.262	85.592 0.06	0.0 0.678	-16.699 BDD	0.669 611	1.0 1
1237665427553386633 999.0	195.926 999.0	28.906 999.0	0.022 999.0	-17.793 999.0	2.586 999.0	-17.793 999.0	2.586 999.0	1.321 999.0	0.441 1.0	18.602 0.0	0.0 0.0	999.0 S	999.0 5	999.0 1
1237665427553452095 999.0	196.205 999.0	28.661 999.0	0.026 999.0	-19.125 999.0	2.771 999.0	-19.125 999.0	2.771 999.0	1.904 999.0	0.311 1.0	116.33 0.0	0.0 0.0	999.0 S	999.0 5	999.0 0
1237665427553452110 999.0	195.926 999.0	28.906 999.0	0.022 999.0	-17.894 999.0	2.366 999.0	-17.894 999.0	2.366 999.0	0.908 999.0	0.263 1.0	119.769 0.0	0.0 0.0	999.0 S	999.0 5	999.0 1
1237665427553452138 0.376	195.926 87.237	28.906 -17.823	0.022 2.119	-18.646 1.0	502.0 0.433	-17.298 87.338	1.062 999.0	0.039 999.0	0.149 0.289	81.445 0.242	0.0 0.469	-17.107 BSD	1.263 116	0.131 0

Table A.6: The structural and photometric parameters of multi-component models fits (i band) for the entire galaxy sample. The column headings are described in Table A.7. This table displays the first 15 data rows only; the complete version will be made available in Head et al, (2015).

Column name	(n)	Description
ObjID	(a)	SDSS DR8 Object ID
RA	(b)	Object Right Ascension [degrees]
Dec.	(c)	Object Declination [degrees]
z	(d)	Object SDSS Redshift
$M_{i,\mathrm{tot}}$	(e)	Total rest-frame magnitude
$R_{e,\mathrm{tot}}$	(f)	Upper limit total half-light radius [kpc]
$M_{i,1}$	(g)	Component 1 rest-frame magnitude
$R_{e,1}$	(h)	Component 1 half-light radius [kpc]
n_1	(i)	Component 1 Sérsic index
q_1	(j)	Component 1 axis ratio (b/a)
PA_1	(k)	Component 1 position angle [degrees]
$C0_1$	(l)	Component 1 boxiness
$M_{i,2}$	(m)	Component 2 rest-frame magnitude
$R_{e,2}$	(n)	Component 2 half-light radius [kpc]
n_2	(o)	Component 2 Sérsic index
q_2	(p)	Component 2 axis ratio (b/a)
PA_2	(q)	Component 2 position angle [degrees]
$M_{i,3}$	(r)	Component 3 rest-frame magnitude
$R_{e,3}$	(s)	Component 3 half-light radius [kpc]
n_3	(t)	Component 3 Sérsic index
q_3	(u)	Component 3 axis ratio (b/a)
PA_3	(v)	Component 3 position angle [degrees]
$R_{e,\mathrm{out}}$	(w)	Outer disk half-light radius [kpc]
r_{brk}	(x)	Disk break radius [kpc]
C_1/T	(y)	Component 1 light fraction
C_2/T	(z)	Component 2 light fraction
C_3/T	(aa)	Component 3 light fraction
Model	(ab)	Best-fit model
Profile	(ac)	(Extended) Allen et al. (2006) type
Flag	(ad)	Fitting flag

Table A.7: This table describes the column headings (a-ad) for Table A.6, presenting multi-component fitting results in the i band. Best-fit model types are described in Section 7.2.3, extended Allen et al. (2006) types are described in Section 7.2.3, and fitting flags are described in Table A.8.

Flag code	Description	Condition
0	Normal fit	N/A
1	Bad fit (removed)	See Figure 7.4
2	High chi-squared	$1.1 < \chi^2_\nu < 1.2$
3	Low component fraction	Any $0.05 < \mathrm{C/T} < 0.10$
4	Small break radius	$r_{\mathrm{brk}} < 5''$

Table A.8: This table describes the multi-component fitting flag codes, as used in Table A.6.

Bibliography

Abadi M. G., Moore B., Bower R. G., 1999, MNRAS, 308, 947

Aguerri J. A. L., Balcells M., Peletier R. F., 2001, A&A, 367, 428

Aguerri J. A. L., González-García A. C., 2009, A&A, 494, 891

Aguerri J. A. L., Iglesias-Paramo J., Vilchez J. M., Muñoz-Tuñón C., 2004, AJ, 127, 1344

Aguerri J. A. L., Iglesias-Páramo J., Vílchez J. M., Muñoz-Tuñón C., Sánchez-Janssen R., 2005, AJ, 130, 475

Ahn C. P., Alexandroff R., Allende Prieto C., Anderson S. F., Anderton T., Andrews B. H., Aubourg É., Bailey S., Balbinot E., Barnes R., et al. 2012, ApJS, 203, 21

Aird J., Coil A. L., Moustakas J., Blanton M. R., Burles S. M., Cool R. J., Eisenstein D. J., Smith M. S. M., Wong K. C., Zhu G., 2012, ApJ, 746, 90

Akaike H., 1974, IEEE Transactions on Automatic Control, 19, 716

Allanson S. P., Hudson M. J., Smith R. J., Lucey J. R., 2009, ApJ, 702, 1275

Allen P. D., Driver S. P., Graham A. W., Cameron E., Liske J., de Propris R., 2006, MNRAS, 371, 2

Aragón-Salamanca A., Bedregal A. G., Merrifield M. R., 2006, A&A, 458, 101

Balogh M. L., Baldry I. K., Nichol R., Miller C., Bower R., Glazebrook K., 2004, ApJ, 615, L101

Balogh M. L., Navarro J. F., Morris S. L., 2000, ApJ, 540, 113

Barden M., Häußler B., Peng C. Y., McIntosh D. H., Guo Y., 2012, MNRAS, 422, 449

Barnes J. E., Hernquist L. E., 1991, ApJ, 370, L65

Barway S., Wadadekar Y., Kembhavi A. K., Mayya Y. D., 2009, MNRAS, 394, 1991

Barway S., Wadadekar Y., Vaghmare K., Kembhavi A. K., 2013, MNRAS, 432, 430

Bedregal A. G., Cardiel N., Aragón-Salamanca A., Merrifield M. R., 2011, MNRAS, 415, 2063

Begelman M. C., Blandford R. D., Rees M. J., 1984, Reviews of Modern Physics, 56, 255

Bekki K., 1998, ApJ, 502, L133+

Bekki K., Couch W. J., 2011, MNRAS, 415, 1783

Bell E. F., McIntosh D. H., Katz N., Weinberg M. D., 2003, ApJS, 149, 289

Bendo G. J., Barnes J. E., 2000, MNRAS, 316, 315

Bertin E., Arnouts S., 1996, A&AS, 117, 393

Bertin E., Mellier Y., Radovich M., Missonnier G., Didelon P., Morin B., 2002, in Bohlender D. A., Durand D., Handley T. H., eds, Astronomical Data Analysis Software and Systems XI Vol. 281 of Astronomical Society of the Pacific Conference Series, The TERAPIX Pipeline. p. 228

Best P. N., Kaiser C. R., Heckman T. M., Kauffmann G., 2006, MNRAS, 368, L67

Best P. N., Kauffmann G., Heckman T. M., Brinchmann J., Charlot S., Ivezić Ž., White S. D. M., 2005, MNRAS, 362, 25

Bois M., Emsellem E., Bournaud F., Alatalo K., Blitz L., Bureau M., Cappellari M., Davies R. L., Davis T. A., de Zeeuw P. T., Duc P.-A. e. a., 2011, MNRAS, 416, 1654

Borlaff A., Eliche-Moral M. C., Rodríguez-Pérez C., Querejeta M., Tapia T., Pérez-González P. G., Zamorano J., Gallego J., Beckman J., 2014, ArXiv e-prints

Boulade O., Charlot X., Abbon P., Aune S., Borgeaud P., Carton P.-H., Carty M., Da Costa J., Deschamps H., Desforge D., et al. 2003, in Iye M., Moorwood A. F. M., eds, Instrument

Design and Performance for Optical/Infrared Ground-based Telescopes Vol. 4841 of Society of Photo-Optical Instrumentation Engineers (SPIE) Conference Series, MegaCam: the new Canada-France-Hawaii Telescope wide-field imaging camera. pp 72–81

Bournaud F., Jog C. J., Combes F., 2005, A&A, 437, 69

Bournaud F., Jog C. J., Combes F., 2007, A&A, 476, 1179

Bower R. G., Lucey J. R., Ellis R. S., 1992, MNRAS, 254, 601

Boylan-Kolchin M., Ma C.-P., Quataert E., 2005, MNRAS, 362, 184

Brinchmann J., Charlot S., White S. D. M., Tremonti C., Kauffmann G., Heckman T., Brinkmann J., 2004, MNRAS, 351, 1151

Brodwin M., Stanford S. A., Gonzalez A. H., Zeimann G. R., Snyder G. F., Mancone C. L., Pope A., Eisenhardt P. R., Stern D., Alberts S. e. a., 2013, ApJ, 779, 138

Bryant J. J., Owers M. S., Robotham A. S. G., Croom S. M., Driver S. P., Drinkwater M. J., Lorente N. P. F., Cortese L., Scott N., Colless M., et al 2014, ArXiv e-prints

Buitrago F., Trujillo I., Conselice C. J., Bouwens R. J., Dickinson M., Yan H., 2008, ApJ, 687, L61

Burstein D., Ho L. C., Huchra J. P., Macri L. M., 2005, ApJ, 621, 246

Capaccioli M., 1989, in Corwin Jr. H. G., Bottinelli L., eds, World of Galaxies (Le Monde des Galaxies) Photometry of early-type galaxies and the R exp 1/4 law. pp 208–227

Cappellari M., 2013, ApJ, 778, L2

Cappellari M., Emsellem E., Krajnović D., McDermid R. M., Serra P., Alatalo K., Blitz L., Bois M., Bournaud F., Bureau M., Davies R. L., et al. 2011, MNRAS, 416, 1680

Carter D., Goudfrooij P., Mobasher B., Ferguson H. C., Puzia T. H., Aguerri A. L., Balcells M., Batcheldor D., Bridges T. J., Davies J. I., et al. 2008, ApJS, 176, 424

Cen R., 2014, ApJ, 790, L24

Chen C.-T. J., Hickox R. C., Alberts S., Brodwin M., Jones C., Murray S. S., Alexander D. M., Assef R. J., Brown M. J. I., Dey A., Forman W. R., Gorjian V., Goulding A. D., Le Floc'h E., Jannuzi B. T., Mullaney J. R., Pope A., 2013, ApJ, 773, 3

Chilingarian I. V., Melchior A.-L., Zolotukhin I. Y., 2010, MNRAS, 405, 1409

Chilingarian I. V., Zolotukhin I. Y., 2012, MNRAS, 419, 1727

Christlein D., Zabludoff A. I., 2004, ApJ, 616, 192

Cibinel A., Carollo C. M., Lilly S. J., Bonoli S., Miniati F., Pipino A., Silverman J. D., van Gorkom J. H., Cameron E., Finoguenov A., Norberg P., Peng Y., Rudick C. S., 2013, ApJ, 777, 116

Coelho P., Gadotti D. A., 2011, ApJ, 743, L13

Courteau S., Andersen D. R., Bershady M. A., MacArthur L. A., Rix H.-W., 2003, ApJ, 594, 208

Crossett J. P., Pimbblet K. A., Stott J. P., Jones D. H., 2013, ArXiv e-prints

Damen M., Labbé I., Franx M., van Dokkum P. G., Taylor E. N., Gawiser E. J., 2009, ApJ, 690, 937

Damjanov I., McCarthy P. J., Abraham R. G., Glazebrook K., Yan H., Mentuch E., Le Borgne D., Savaglio S., Crampton D., Murowinski R., Juneau S., Carlberg R. G., Jørgensen I., Roth K., Chen H.-W., Marzke R. O., 2009, ApJ, 695, 101

Danielson A. L. R., Lehmer B. D., Alexander D. M., Brandt W. N., Luo B., Miller N., Xue Y. Q., Stott J. P., 2012, MNRAS, 422, 494

de Jong R. S., Simard L., Davies R. L., Saglia R. P., Burstein D., Colless M., McMahan R., Wegner G., 2004, MNRAS, 355, 1155

De Lucia G., Weinmann S., Poggianti B. M., Aragón-Salamanca A., Zaritsky D., 2012, MNRAS, 423, 1277

de Vaucouleurs G., 1948, Annales d'Astrophysique, 11, 247

Di Matteo P., Haywood M., Combes F., Semelin B., Snaith O. N., 2013, A&A, 553, A102

Di Matteo T., Springel V., Hernquist L., 2005, Nature, 433, 604

Dressler A., 1980a, ApJS, 42, 565

Dressler A., 1980b, ApJ, 236, 351

Dressler A., Oemler Jr. A., Couch W. J., Smail I., Ellis R. S., Barger A., Butcher H., Poggianti B. M., Sharples R. M., 1997, ApJ, 490, 577

Driver S. P., Popescu C. C., Tuffs R. J., Liske J., Graham A. W., Allen P. D., de Propris R., 2007, MNRAS, 379, 1022

Eigenthaler P., Zeilinger W. W., 2013, A&A, 553, A99

Eliche-Moral M. C., González-García A. C., Aguerri J. A. L., Gallego J., Zamorano J., Balcells M., Prieto M., 2012, A&A, 547, A48

Emsellem E., Cappellari M., Krajnović D., Alatalo K., Blitz L., Bois M., Bournaud F., Bureau M., Davies R. L., Davis T. A., de Zeeuw P. T., et al. 2011, MNRAS, 414, 888

Erwin P., Debattista V. P., 2013, MNRAS, 431, 3060

Erwin P., Gutiérrez L., Beckman J. E., 2012, ApJ, 744, L11

Erwin P., Pohlen M., Beckman J. E., 2008, AJ, 135, 20

Feldmann R., Carollo C. M., Mayer L., 2010, ArXiv e-prints

Ferland G. J., Fabian A. C., Hatch N. A., Johnstone R. M., Porter R. L., van Hoof P. A. M., Williams R. J. R., 2008, MNRAS, 386, L72

Ferland G. J., Fabian A. C., Hatch N. A., Johnstone R. M., Porter R. L., van Hoof P. A. M., Williams R. J. R., 2009, MNRAS, 392, 1475

Ferrarese L., Merritt D., 2000, ApJ, 539, L9

Fisher D., Franx M., Illingworth G., 1996, ApJ, 459, 110

Franx M., Illingworth G., 1990, ApJ, 359, L41

Freeman K. C., 1970, ApJ, 160, 811

Fujita Y., 2004, PASJ, 56, 29

Fukugita M., Ichikawa T., Gunn J. E., Doi M., Shimasaku K., Schneider D. P., 1996, AJ, 111, 1748

Gadotti D. A., 2009, MNRAS, 393, 1531

Gadotti D. A., 2011, MNRAS, 415, 3308

Gao L., De Lucia G., White S. D. M., Jenkins A., 2004, MNRAS, 352, L1

Gavazzi G., 1989, ApJ, 346, 59

Gavazzi G., Fumagalli M., Cucciati O., Boselli A., 2010, A&A, 517, A73

Gavazzi R., Adami C., Durret F., Cuillandre J.-C., Ilbert O., Mazure A., Pelló R., Ulmer M. P., 2009, A&A, 498, L33

Giaretta D. L., Currie M. J., Rankin S., Draper P., Berry D. S., Gray N., Taylor M., 2004, in Ochsenbein F., Allen M. G., Egret D., eds, Astronomical Data Analysis Software and Systems (ADASS) XIII Vol. 314 of Astronomical Society of the Pacific Conference Series, Starlink Software. p. 832

Governato F., Brook C. B., Brooks A. M., Mayer L., Willman B., Jonsson P., Stilp A. M., Pope L., Christensen C., Wadsley J., Quinn T., 2009, MNRAS, 398, 312

Graham A. W., 2013, Elliptical and Disk Galaxy Structure and Modern Scaling Laws. p. 91

Graham A. W., Driver S. P., 2005, PASA, 22, 118

Graham A. W., Guzmán R., 2003, AJ, 125, 2936

Gunn J. E., Gott III J. R., 1972, ApJ, 176, 1

Gutiérrez C. M., Trujillo I., Aguerri J. A. L., Graham A. W., Caon N., 2004, ApJ, 602, 664

Guzman R., Lucey J. R., Carter D., Terlevich R. J., 1992, MNRAS, 257, 187

Harrison C. M., Alexander D. M., Mullaney J. R., Altieri B., Coia D., Charmandaris V., Daddi E., Dannerbauer H., Dasyra K., Del Moro A., Dickinson M., Hickox R. C., Ivison R. J., et al. 2012, ApJ, 760, L15

Harrison C. M., Alexander D. M., Swinbank A. M., Smail I., Alaghband-Zadeh S., Bauer F. E., Chapman S. C., Del Moro A., Hickox R. C., Ivison R. J., Menéndez-Delmestre K., Mullaney J. R., Nesvadba N. P. H., 2012, MNRAS, 426, 1073

Haynes M. P., Giovanelli R., Kent B. R., 2007, ApJ, 665, L19

Head J. T. C. G., Lucey J. R., Hudson M. J., Smith R. J., 2014, MNRAS, 440, 1690

Herschel W., 1785, Philosophical Transactions of the Royal Society of London, 75, pp. 213

Hester J. A., 2010, ApJ, 720, 191

Hilz M., Naab T., Ostriker J. P., Thomas J., Burkert A., Jesseit R., 2012, MNRAS, 425, 3119

Hogg D. W., Blanton M. R., Brinchmann J., Eisenstein D. J., Schlegel D. J., Gunn J. E., McKay T. A., Rix H.-W., Bahcall N. A., Brinkmann J., Meiksin A., 2004, ApJ, 601, L29

Homeier N. L., Postman M., Menanteau F., Blakeslee J. P., Mei S., Demarco R., Ford H. C., Illingworth G. D., Zirm A., 2006, AJ, 131, 143

Hopkins P. F., Cox T. J., Younger J. D., Hernquist L., 2009, ApJ, 691, 1168

Huang S., Ho L. C., Peng C. Y., Li Z.-Y., Barth A. J., 2013, ApJ, 766, 47

Hubble E. P., 1926, ApJ, 64, 321

Hudson M. J., Stevenson J. B., Smith R. J., Wegner G. A., Lucey J. R., Simard L., 2010, MNRAS, 409, 405

Hyde J. B., Bernardi M., 2009, MNRAS, 394, 1978

Imanishi M., Saito Y., 2014, ApJ, 780, 106

Irwin J. A., Seaquist E. R., Taylor A. R., Duric N., 1987, ApJ, 313, L91

Ivezic Z., Tyson J. A., Acosta E., Allsman R., Anderson S. F., Andrew J., Angel R., Axelrod T., Barr J. D., Becker A. C., et al 2008, ArXiv e-prints

Jester S., Schneider D. P., Richards G. T., Green R. F., Schmidt M., Hall P. B., Strauss M. A., Vanden Berk D. E., Stoughton C., Gunn J. E., Brinkmann J., Kent S. M., Smith J. A., Tucker D. L., Yanny B., 2005, AJ, 130, 873

Johnston E. J., Aragón-Salamanca A., Merrifield M. R., 2014, MNRAS, 441, 333

Johnston E. J., Aragón-Salamanca A., Merrifield M. R., Bedregal A. G., 2012, MNRAS, 422, 2590

Jørgensen I., 1999, MNRAS, 306, 607

Kaiser N., Aussel H., Burke B. E., Boesgaard H., Chambers K., Chun M. R., Heasley J. N., Hodapp K.-W., Hunt B., Jedicke R., et al 2002, in Tyson J. A., Wolff S., eds, Survey and Other Telescope Technologies and Discoveries Vol. 4836 of Society of Photo-Optical Instrumentation Engineers (SPIE) Conference Series, Pan-STARRS: A Large Synoptic Survey Telescope Array. pp 154–164

Kannappan S. J., Guie J. M., Baker A. J., 2009, AJ, 138, 579

Karouzos M., Im M., Trichas M., Goto T., Malkan M., Ruiz A., Jeon Y., Kim J. H., Lee H. M., Kim S. J., Oi N., Matsuhara H., Takagi T., Murata K., Wada T., Wada K., Shim H., Hanami H., Serjeant S., White G. J., Pearson C., Ohyama Y., 2014, ApJ, 784, 137

Kaviraj S., 2010, MNRAS, 406, 382

Kaviraj S., Ting Y.-S., Bureau M., Shabala S. S., Crockett R. M., Silk J., Lintott C., Smith A., Keel W. C., Masters K. L., Schawinski K., Bamford S. P., 2012, MNRAS, 423, 49

Kawata D., Mulchaey J. S., 2008, ApJ, 672, L103

Kelvin L. S., Driver S. P., Robotham A. S. G., Hill D. T., Alpaslan M., Baldry I. K., Bamford S. P., Bland-Hawthorn J., Brough S., Graham A. W., et al. 2012, MNRAS, 421, 1007

King A., 2005, ApJ, 635, L121

Knapen J. H., Shlosman I., Peletier R. F., 2000, ApJ, 529, 93

Kocevski D. D., Faber S. M., Mozena M., Koekemoer A. M., Nandra K., Rangel C., Laird E. S., Brusa M., Wuyts S., Trump J. R., Koo D. C., Somerville R. S., Bell E. F., Lotz J. M., Alexander D. M., Bournaud F., Conselice C. J., Dahlen T., et al. 2012, ApJ, 744, 148

Koleva M., Prugniel P., de Rijcke S., Zeilinger W. W., 2011, MNRAS, 417, 1643

Komatsu E., Smith K. M., Dunkley J., Bennett C. L., Gold B., Hinshaw G., Jarosik N., Larson D., Nolta M. R., Page L., Spergel D. N., Halpern M., Hill R. S., Kogut A., 2011, ApJS, 192, 18

Kormendy J., 1979, ApJ, 227, 714

Kormendy J., Bender R., 2012, ApJS, 198, 2

Kormendy J., Kennicutt Jr. R. C., 2004, ARA&A, 42, 603

Krajnović D., Alatalo K., Blitz L., Bois M., Bournaud F., Bureau M., Cappellari M., Davies R. L., Davis T. A., de Zeeuw P. T., Duc P.-A., Emsellem E., Khochfar S., 2013, MNRAS, 432, 1768

Kuntschner H., Emsellem E., Bacon R., Cappellari M., Davies R. L., de Zeeuw P. T., Falcón-Barroso J., Krajnović D., McDermid R. M., Peletier R. F., Sarzi M., Shapiro K. L., van den Bosch R. C. E., van de Ven G., 2010, MNRAS, 408, 97

La Barbera F., Ferreras I., de Carvalho R. R., Bruzual G., Charlot S., Pasquali A., Merlin E., 2012, MNRAS, 426, 2300

Lackner C. N., Gunn J. E., 2012, MNRAS, p. 2423

Lackner C. N., Gunn J. E., 2013, MNRAS, 428, 2141

Laine J., Laurikainen E., Salo H., Comerón S., Buta R. J., Zaritsky D., Athanassoula E., Bosma A., Muñoz-Mateos J.-C., Gadotti D. A., et al. 2014, MNRAS, 441, 1992

Lansbury G. B., Lucey J. R., Smith R. J., 2014, MNRAS, 439, 1749

Larson R. B., Tinsley B. M., Caldwell C. N., 1980, ApJ, 237, 692

Laurikainen E., Salo H., Buta R., Knapen J. H., Comerón S., 2010, MNRAS, 405, 1089

Law D. R., MaNGA Team 2014, in American Astronomical Society Meeting Abstracts 223 Vol. 223 of American Astronomical Society Meeting Abstracts, Mapping Nearby Galaxies at APO: The MaNGA IFU Galaxy Survey. p. 254.31

Lewis I., Balogh M., De Propris R., Couch W., Bower R., Offer A., Bland-Hawthorn J., Baldry I. K., Baugh C., Bridges T., et al. 2002, MNRAS, 334, 673

Lintott C., Schawinski K., Bamford S., Slosar A., Land K., Thomas D., Edmondson E., Masters K., Nichol R. C., Raddick M. J., Szalay A., Andreescu D., Murray P., Vandenberg J., 2011, VizieR Online Data Catalog, 741, 166

Lintott C. J., Schawinski K., Slosar A., Land K., Bamford S., Thomas D., Raddick M. J., Nichol R. C., Szalay A., Andreescu D., Murray P., Vandenberg J., 2008, MNRAS, 389, 1179

Liu X., Shen Y., Strauss M. A., Hao L., 2011, ApJ, 737, 101

Lucey J. R., Guzman R., Carter D., Terlevich R. J., 1991, MNRAS, 253, 584

MacArthur L. A., Courteau S., Bell E., Holtzman J. A., 2004, ApJS, 152, 175

Magnier E. A., Cuillandre J.-C., 2004, PASP, 116, 449

Magorrian J., Tremaine S., Richstone D., Bender R., Bower G., Dressler A., Faber S. M., Gebhardt K., Green R., Grillmair C., Kormendy J., Lauer T., 1998, AJ, 115, 2285

Maraston C., 2005, MNRAS, 362, 799

Marinova I., Jogee S., 2007, ApJ, 659, 1176

Masters K. L., Mosleh M., Romer A. K., Nichol R. C., Bamford S. P., Schawinski K., Lintott C. J., Andreescu D., Campbell H. C., Crowcroft B., Doyle I., Edmondson E. M., Murray P., Raddick M. J., Slosar A., Szalay A. S., Vandenberg J., 2010, MNRAS, 405, 783

Masters K. L., Nichol R. C., Hoyle B., Lintott C., Bamford S. P., Edmondson E. M., Fortson L., Keel W. C., Schawinski K., Smith A. M., Thomas D., 2011, MNRAS, 411, 2026

Meert A., Vikram V., Bernardi M., 2014, ArXiv e-prints

Méndez-Abreu J., Aguerri J. A. L., Corsini E. M., Simonneau E., 2008, A&A, 478, 353

Mihos J. C., Hernquist L., 1994, ApJ, 425, L13

Moore B., Katz N., Lake G., Dressler A., Oemler A., 1996, Nature, 379, 613

Moore B., Lake G., Katz N., 1998, ApJ, 495, 139

Moore B., Lake G., Quinn T., Stadel J., 1999, MNRAS, 304, 465

Moorthy B. K., Holtzman J. A., 2006, MNRAS, 371, 583

Morelli L., Pompei E., Pizzella A., Méndez-Abreu J., Corsini E. M., Coccato L., Saglia R. P., Sarzi M., Bertola F., 2008, MNRAS, 389, 341

Naab T., Johansson P. H., Ostriker J. P., 2009, ApJ, 699, L178

Okabe N., Futamase T., Kajisawa M., Kuroshima R., 2014, ApJ, 784, 90

Oman K. A., Hudson M. J., Behroozi P. S., 2013, MNRAS, 431, 2307

Orban de Xivry G., Davies R., Schartmann M., Komossa S., Marconi A., Hicks E., Engel H., Tacconi L., 2011, MNRAS, 417, 2721

Peng C. Y., Ho L. C., Impey C. D., Rix H., 2010, AJ, 139, 2097

Perez J., Tissera P., Padilla N., Alonso M. S., Lambas D. G., 2009, MNRAS, 399, 1157

Pohlen M., Trujillo I., 2006, A&A, 454, 759

Prochaska Chamberlain L. C., Courteau S., McDonald M., Rose J. A., 2011, MNRAS, 412, 423

Quilis V., Moore B., Bower R., 2000, Science, 288, 1617

Quinn P. J., Hernquist L., Fullagar D. P., 1993, ApJ, 403, 74

Rawle T. D., Lucey J. R., Smith R. J., Head J. T. C. G., 2013, MNRAS, 433, 2667

Rawle T. D., Smith R. J., Lucey J. R., 2010, MNRAS, 401, 852

Rees M. J., Begelman M. C., Blandford R. D., Phinney E. S., 1982, Nature, 295, 17

Rix H.-W., White S. D. M., 1990, ApJ, 362, 52

Robaina A. R., Bell E. F., van der Wel A., Somerville R. S., Skelton R. E., McIntosh D. H., Meisenheimer K., Wolf C., 2010, ApJ, 719, 844

Roberts M. S., Haynes M. P., 1994, ARA&A, 32, 115

Roediger J. C., Courteau S., MacArthur L. A., McDonald M., 2010, ArXiv e-prints

Roediger J. C., Courteau S., Sánchez-Blázquez P., McDonald M., 2012, ApJ, 758, 41

Roškar R., Debattista V. P., Loebman S. R., 2013, MNRAS, 433, 976

Sánchez S. F., Kennicutt R. C., Gil de Paz A., van de Ven G., Vílchez J. M., Wisotzki L., Walcher C. J., Mast D., Aguerri J. A. L., Albiol-Pérez S., et al. 2012, A&A, 538, A8

Sandage A., Binggeli B., Tammann G. A., 1985, AJ, 90, 1759

Schawinski K., Dowlin N., Thomas D., Urry C. M., Edmondson E., 2010, ApJ, 714, L108

Schawinski K., Khochfar S., Kaviraj S., Yi S. K., Boselli A., Barlow T., Conrow T., Forster K., Friedman P. G., Martin D. C., et al. 2006, Nature, 442, 888

Schawinski K., Thomas D., Sarzi M., Maraston C., Kaviraj S., Joo S.-J., Yi S. K., Silk J., 2007, MNRAS, 382, 1415

Schaye J., Crain R. A., Bower R. G., Furlong M., Schaller M., Theuns T., Dalla Vecchia C., Frenk C. S., McCarthy I. G., Helly J. C., et al. 2014, ArXiv e-prints

Schechter P., 1976, ApJ, 203, 297

Schlafly E. F., Finkbeiner D. P., 2011, ApJ, 737, 103

Schwarz G., 1978, The annals of statistics, 6, 461

Sellwood J. A., 2014, Reviews of Modern Physics, 86, 1

Sellwood J. A., Wilkinson A., 1993, Reports on Progress in Physics, 56, 173

Semenov V., Dyadechkin S., Punsly B., 2004, Science, 305, 978

Sérsic J. L., 1963, Boletin de la Asociacion Argentina de Astronomia La Plata Argentina, 6, 41

Shapley H., 1934, Harvard College Observatory Bulletin, 896, 3

Sil'chenko O. K., 2011, ArXiv e-prints

Silk J., Rees M. J., 1998, A&A, 331, L1

Simard L., Mendel J. T., Patton D. R., Ellison S. L., McConnachie A. W., 2011, ApJS, 196, 11

Simard L., Willmer C. N. A., Vogt N. P., Sarajedini V. L., Phillips A. C., Weiner B. J., Koo D. C., Im M., Illingworth G. D., Faber S. M., 2002, ApJS, 142, 1

Simien F., de Vaucouleurs G., 1986, ApJ, 302, 564

Smith J. A., Tucker D. L., Kent S., Richmond M. W., Fukugita M., Ichikawa T., Ichikawa S.-i., et al. 2002, AJ, 123, 2121

Smith R., Davies J. I., Nelson A. H., 2010, MNRAS, 405, 1723

Smith R. J., Lucey J. R., Hammer D., Hornschemeier A. E., Carter D., Hudson M. J., Marzke R. O., Mouhcine M., Eftekharzadeh S., James P., Khosroshahi H., Kourkchi E., Karick A., 2010, MNRAS, 408, 1417

Smith R. J., Lucey J. R., Price J., Hudson M. J., Phillipps S., 2012, MNRAS, 419, 3167

Springel V., Di Matteo T., Hernquist L., 2005, MNRAS, 361, 776

Stewart K. R., Bullock J. S., Wechsler R. H., Maller A. H., Zentner A. R., 2008, ApJ, 683, 597

Struble M. F., Rood H. J., 1999, ApJS, 125, 35

Taranu D. S., Hudson M. J., Balogh M. L., Smith R. J., Power C., Oman K. A., Krane B., 2014, MNRAS, 440, 1934

Tecce T. E., Cora S. A., Tissera P. B., Abadi M. G., Lagos C. D. P., 2010, MNRAS, pp 1443–+

Toomre A., Toomre J., 1972, ApJ, 178, 623

Tran K., van Dokkum P., Franx M., Illingworth G. D., Kelson D. D., Schreiber N. M. F., 2005, ApJ, 627, L25

Trujillo I., Förster Schreiber N. M., Rudnick G., Barden M., Franx M., Rix H.-W., Caldwell J. A. R., McIntosh D. H., Toft S., Häussler B. e. a., 2006, ApJ, 650, 18

Tully R. B., Fisher J. R., 1977, A&A, 54, 661

Vader J. P., Vigroux L., Lachieze-Rey M., Souviron J., 1988, A&A, 203, 217

van den Bergh S., 1976, ApJ, 206, 883

van den Bergh S., 1990, ApJ, 348, 57

van den Bergh S., 2009a, ApJ, 702, 1502

van den Bergh S., 2009b, ApJ, 694, L120

van den Bosch F. C., Aquino D., Yang X., Mo H. J., Pasquali A., McIntosh D. H., Weinmann S. M., Kang X., 2008, MNRAS, 387, 79

van der Wel A., Bell E. F., Holden B. P., Skibba R. A., Rix H., 2010, ApJ, 714, 1779

van Dokkum P. G., Bezanson R., van der Wel A., Nelson E. J., Momcheva I., Skelton R. E., Whitaker K. E., Brammer G., Conroy C., Förster Schreiber N. M., et al. 2014, ApJ, 791, 45

van Dokkum P. G., Whitaker K. E., Brammer G., Franx M., Kriek M., Labbé I., Marchesini D., Quadri R., Bezanson R., Illingworth G. D., Muzzin A., Rudnick G., Tal T., Wake D., 2010, ApJ, 709, 1018

Vika M., Bamford S. P., Häußler B., Rojas A. L., Borch A., Nichol R. C., 2013, MNRAS, 435, 623

Vikram V., Wadadekar Y., Kembhavi A. K., Vijayagovindan G. V., 2010, MNRAS, 409, 1379

Vogelsberger M., Genel S., Springel V., Torrey P., Sijacki D., Xu D., Snyder G. F., Nelson D., Hernquist L., 2014, ArXiv e-prints

Vollmer B., Balkowski C., Cayatte V., van Driel W., Huchtmeier W., 2004, A&A, 419, 35

Walker I. R., Mihos J. C., Hernquist L., 1996, ApJ, 460, 121

Weinmann S. M., van den Bosch F. C., Yang X., Mo H. J., Croton D. J., Moore B., 2006, MNRAS, 372, 1161

Weinzirl T., Jogee S., Neistein E., Khochfar S., Kormendy J., Marinova I., Hoyos C., Balcells M., den Brok M., Hammer D., Peletier R. F., Kleijn G. V., Carter D., Goudfrooij P., Lucey J. R., et al. 2014, MNRAS, 441, 3083

Wielen R., 1977, A&A, 60, 263

Willett K. W., Lintott C. J., Bamford S. P., Masters K. L., Simmons B. D., Casteels K. R. V., Edmondson E. M., Fortson L. F., Kaviraj S., Keel W. C., Melvin T., Nichol R. C., Raddick M. J., Schawinski K., Simpson R. J., Skibba R. A., Smith A. M., Thomas D., 2013, MNRAS, 435, 2835

Wolf M., 1902, Publikationen des Astrophysikalischen Instituts Koenigstuhl-Heidelberg, 1, 125

Worthey G., 1994, ApJS, 95, 107

Wu H., Shao Z., Mo H. J., Xia X., Deng Z., 2005, ApJ, 622, 244

York D. G., Adelman J., Anderson Jr. J. E., Anderson S. F., Annis J., Bahcall N. A., Bakken J. A., Barkhouser R., Bastian S., Berman E., SDSS Collaboration 2000, AJ, 120, 1579

Zhang X., 1998, ApJ, 499, 93

Zhang X., 1999, ApJ, 518, 613

Zinn P.-C., Middelberg E., Norris R. P., Dettmar R.-J., 2013, ApJ, 774, 66